

Development of Fluorogenic Probes for Reaction Screening: From Design and Synthesis, to Reactivity and Live Cell Imaging

By Lana Elizabeth Corkum Greene

*A thesis submitted to McGill University in partial fulfillment of the
requirements for the degree of*

Doctor of Philosophy

Department of Chemistry

McGill University

Montreal, Quebec, Canada

May, 2017

© Lana Greene, 2017

I dedicate this thesis
to my family and the best parents in the ‘whole wild world’
and to the memory of my grandmother: “be strong my darlings and keep the faith”

Abstract

This thesis describes our progress in developing fluorogenic probes for reaction screening, with the purpose of answering vexing problems in chemistry and biology. The work, motivated by our interest in reactive oxygen species (ROS) and associated by-products, focuses on two major goals: 1) the design and development of fluorogenic bio-molecule analogues to report on antioxidant status and 2) the design of fluorogenic electrophilic probes and new fluorescence based assays. The newly developed probes described are comprised of 2 segments: a boron-dipyrromethene (BODIPY) reporter fluorophore (emissive segment), and a trap segment to sense a reaction of interest (quencher/switch). The library of trap segments explored as part of this work encompasses the structure of naturally occurring substrates (ubiquinone: Chapter 2, α -tocopherol: Chapters 3 and 4, and electrophilic aldehydes in general: Chapter 5). Upon reaction of interest at the trap site (e.g. oxidation/reduction), the fluorescence of the BODIPY fluorophore is restored providing a highly sensitive and chemoselective sensing mechanism.

The development of a fluorogenic analogue of ubiquinone (H_2B-Q) is first described to reversibly report on redox reactions. H_2B-Q undergoes a 200-fold fluorescence enhancement upon reduction of the ubiquinone moiety. We show that by replacing the isoprenoid tail of ubiquinone with a BODIPY fluorophore, the expected redox behaviour of the ubiquinone head group remains intact. Formation of H_2B-Q from its reduced dihydroquinone form is both chemically and electrochemically reversible.

Fluorogenic analogues of α -tocopherol based on photoinduced electron transfer is next described where we specifically tackled the effects of BODIPY substitution and linker length on PeT efficiency within the context of Marcus Theory of electron transfer. We showed how through judicious choice of linker and substitution of the BODIPY core, we may increase the sensitivity dynamic range from 20 to 1,000, in state-of-the art fluorogenic antioxidants based on α -tocopherol. Armed with a newly prepared highly sensitive fluorogenic analogue of tocopherol, H_4BPMHC , we next demonstrate how optimum sensitivity/large dynamic range allowed us to detect and quantify lipid peroxidation at basal levels and in the presence of

additional antioxidant within HeLa cells. Our results show indisputable evidence of the antioxidant role of Vitamin E *in vitro*.

The development of a fluorescence assay and reactivity palette to study nucleophilic addition based on *meso*-formyl BODIPY dyes is then discussed. Quenching of the BODIPY core by the *meso*-formyl is deactivated upon the addition of a nucleophile. We demonstrate how the exploration of fluorescence parameters including fluorescence lifetime and quantum yields, may provide us with reaction rates, yields, and reaction mechanism.

We conclude this thesis with an outlook on future probe development, methodology, and application. With novel and highly sensitive probes in hand, we may take advantage of the advancement of spectroscopy techniques to aid in the unraveling of complex redox reactions occurring in living systems.

Résumé

Cette thèse décrit nos résultats envers le développement de sondes fluorogènes dans le but de répondre à des problématiques importantes dans la recherche en chimie et en biologie. Ce travail est motivé, en particulier, par notre intérêt dans la réactivité des espèces réactives d'oxygène (ROS) et leurs sous-produits associés. Notre approche se concentre sur deux objectifs majeurs: 1) la synthèse et l'application d'analogues de biomolécules avec modifications fluorogènes pour signaler un état antioxydant, et 2) la conception de fluorogène agissant comme sondes électrophiles. Les sondes développées sont composées de 2 segments: un fluorophore rapporteur de bore-dipyrométhène (BODIPY) (segment émissif) et un segment réactif pour détecter une réaction d'intérêt, par exemple un extincteur ou interrupteur. La bibliothèque de segments réactifs explorés dans le cadre de ce travail englobe la structure des substrats naturels (ubiquinone: chapitre 2, α -tocophérol: chapitres 3 et 4 et aldéhydes électrophiles en général: chapitre 5). Lorsque la réaction d'intérêt aie lieu au site réactif (par exemple, oxydation / réduction), la fluorescence du fluorophore BODIPY est restaurée, fournissant un mécanisme de détection hautement sensible et chimiosélectif.

Le développement d'un analogue fluorogène de l'ubiquinone (H2B-Q) est d'abord décrit comme rapporteur réversible sur les réactions redox. H2B-Q subit une augmentation de l'intensité de fluorescence de 200 fois suite à la réduction de la fraction ubiquinone. Nous démontrons qu'en remplaçant la queue d'isoprénoïde de l'ubiquinone par un fluorophore BODIPY, le comportement redox attendu du groupe de tête ubiquinone demeure intact. La formation de H2B-Q à partir de sa forme de dihydroquinone réduite est à la fois chimiquement et électrochimiquement réversible.

Les analogues fluorogènes de l' α -tocophérol à base de transfert d'électrons photoinduits (PeT) sont ensuite décrits. Pour cette approche, nous avons spécifiquement abordé les effets de la substitution du groupe fluorescent BODIPY et de la proximité entre le fluorophore et la partie réactive sur l'efficacité de PeT dans le contexte de la Théorie de Marcus sur le transfert d'électrons. Un choix judicieux de la liaison entre les segment fluorescent et réactifs, la substitution du noyau BODIPY, et l'utilisation de technologies avancées basée sur l' α -tocophérol, nous a permis d'augmenter la sensibilité des mesures de 20 à 1000. Avec cet

analogue fluorogène hautement sensible du tocophérol, H4BPMHC, nous démontrons ensuite comment une sensibilité optimale et la grande plage dynamique nous a permis de détecter et de quantifier la peroxydation lipidique pour des systèmes non-perturbés et pour des systèmes de cellules HeLa en présence d'antioxydants supplémentaires. Nos résultats montrent une preuve incontestable du rôle antioxydant de la vitamine E in vitro.

Le développement d'un dosage de fluorescence et d'une palette de réactivité pour étudier l'addition nucléophile basée sur les fluorophores méso-formyl BODIPY est ensuite discuté. Le noyau BODIPY éteint par la méso-insaturation devient fluorescent lorsqu'une addition nucléophile survient. Nous démontrons comment l'exploration des paramètres de base de la fluorescence, y compris la durée de vie de la fluorescence et les rendements quantiques, peuvent nous fournir des taux de réaction, des pourcentage de rendements et des mécanismes de réaction.

Nous concluons cette thèse avec une perspective sur le développement futur de la sonde, sa méthodologie et son application. Avec telles sondes novatrices et très sensibles, nous pourrions profiter de l'avancement des techniques de spectroscopie pour aider à démêler les réactions redox complexes survenant dans les systèmes vivants.

Acknowledgements

“With mirth and laughter let old wrinkles come.”

-William Shakespeare, The Merchant of Venice

My time at McGill University has truly been an unforgettable experience and I am very grateful to the many people who helped me, supported me and provided multiple sources of encouragement, inspiration, and laughter during my PhD. First, I would like to thank my research supervisor, Gonzalo Cosa, for his constant motivation, guidance and support. You inspired me to be critical in my own work, yet open to new ideas and pursuits. Your excitement in results was often contagious, and you also helped me appreciate the interesting stories often found in disappointing results (or rather “making lemonade out of lemons”). I will be forever grateful to your mentorship in forming me into the scientist I am now, and am growing into.

I would also like to thank Profs Jean-Philip Lumb, Karine Auclair, and Nicolas Moitessier for being involved in my committee, giving me positive and critical feedback and pushing me to achieve my best.

Special thanks to the support staff of McGill Chemistry. Thanks to Chantal Marotte for helping me adjust in my first year at McGill, and taking care of all the complexities of grad school, to Fred Morin for helping me run 2D and NOESY NMR as well as for keeping up the NMR facilities along with Robin Stein, to Nadim Saade and Alex Wahba for running my samples for HRMS and to Collen McNamee and Jean-Marc Gauthier for taking care of Pulp and Paper and my complaints.

I also am grateful to Katerina Krumova, (KK, or the angry Bulgarian) who helped me start off on the right foot and for being one of my first Montreal friends. Your guidance from setting up reactions, to living life in general has been invaluable. Your training has been instrumental in giving me confidence. You will always be an idol to me! Thank you also for encouraging me to join the softball team, frisbee team and hockey team! Without joining I may have never met so many friends. Thanks for going on trips to Tim’s, Sushi, and dress

shops with me. And most importantly, thanks for teaching me not ski across a bare parking lot...

I am also grateful to the entire Cosa group, present and past members. I'm sure we are the most envied group at McGill for our special and bizarre group dynamic. I'm also not sure any other group would have been able to endure the horrors and haunts of Pulp and Paper like we could. Every disaster makes me appreciate what a wonderful group I am a part of. We are such a varied group of people who work on a wide array of projects, making advice on projects truly unique. Thanks to Dr. Robert Godin (Bobzilla) for the scientific discussions, hockey advice, and introducing me to the wonders of chocolate milk and amaretto; to Richard Lincoln (Rick-meister, the Trickster) for the in-depth chats about life, science, and video games, for organizing massive movie nights, for helping me proof-read my thesis, and for reminding me of the dangers of getting Rick-ied; to Yasser Gidi (Yassman) for the microscope advice (it's so simple) and being part of the Cosa Hockey team; to Dr. Pierre Karam for such a warm welcome to the Cosa lab on my first day and teaching me Arabic; to Dr. Andres Durantini for always willing to go play some shinny outside and helping with electrochem; to Ryan Marko for always being available for ranting purposes; and to Dr. Mathieu Frenette (Old Man) for always finding the fun in science and helping me with my French abstract. Also a special thanks to the ladies of the Cosa Lab: Thanks to the beautiful Mei-Ni Belzile (our very own Dwight Shrute) for the countless source of laughter, head rubs in the park, and movie snuggles; to the lovely snack fairy, Casey Platnich, for the Milk Bar snack making, our unforgettable nights of spooning, and making me delicious risotto; to the formidable General Dr. Amani Hariri for the wo(man) power inspiration and The Plan; to Dr. Mayra Martinez for talking with me en Español over beers; and to Viktorija Glembockyte (Viki, Vickles Pickles) for the chats about food and science, the delicious scones, toonie Tuesday, dancing to fiddlers in plaid pants and being liquor soft with me. I especially want to thank my lovely Christina "Stineman" Calver (the Beast from the West). Our affection began upon our mutual love of skiing the "purity" and our love for doing (skiing) Ryan. Stineman, don't ever be normal.

I am also grateful to the Mittermaier Lab whose office and lab space we share. Thanks to Justin Ditrani (Dtrain, Sargent Spankles) for the liquoring and ski trips in the witches' twine,

and to Robert Harkness (Robbie-san) for his laughter, foodie discussions and docking ‘experiments.’

I am also grateful to a number of fellow McGill students for making these last few years a fun, silly and wonderful experience. Thanks to Master Mitch Huot, for allowing me to play on Nice Snatch even with 0 softball experience, for making some sweet bro-beef tacos, and giving me the secret strategy to win Race for the Galaxy. Thanks also to my splendiferous friend and his amazing fiancée, Danielle Vlaho (Sweet Dee, “Dee’s HERE!”) for our chats, rants, shopping trips, wine drinking, eating and board game tomfooleries. There’s also that time you stayed at the hospital with me until 6 am, and still rallied and made it to your softball game, what a friend and champ. You are truly a gem of a friend and one I hope to have forever and so verrry generous...

I also must thank Kunal Tiwarni? Tiwari? Deeply sorry. I think the first time I met you, you shoved your stinky softball glove in my face. From that moment, I knew we would be friends. Because of the implication that is... Thanks for hosting the sweet trips to Maine, giving a rockin’ Bris, and making some sick Calzones. Thanks for the farm wars in Carcassonne, captaining the Boner Patrol, and introducing me to Maggie. Wherever we end up in the world, I’m sure we’ll bump heads again.

Thanks also to Dr. Katie Castor (Moon Moon) and Dr. Graham Hamblin (Gary). From discussing ponies with Katie, to the multitude of “sober” shenanigans with Gary, there’s never a dull moment. You guys always make for a blast, and like Samwise, are the true heroes of the fellowship of the burrito. Thanks for hosting in SoCal, and we’ll be sure to come back for some more tandem adventures! #Mandem. #Outandproud.

Thanks also to my hockey team, the Degenerate Orbitals and in particular to fellow captain Dr. Josh Pottel for “making hockey fun” and David Polcari for coaching/complaining. The DOs made Montreal winters something to look forward to.

Thanks to my fellow New Scotsman, Dr. Michelle Bezanson. We were just innocent small townies when we came to Montreal. Having you by my side throughout undergrad, and grad school made it that much easier. Thank you for being my hero, as well as my constant cheerleader.

My family has been one of the biggest supports in my life, and without you I would still be crying on the grade 3 classroom floor playing with tiny plastic horses. Thank you to Joe, Nannie, Nana, and Auntie Barb. Thank you, Mom, for always pushing me to be better and not accepting the minimum. You are the strongest woman I know, and from you I get my strength. Thanks for teaching me to be kind, loving, and respectful, but not a pushover. Thanks for bringing horses into my life and providing the riding lessons, drives to the barn at wee hours, and coaching. Thank you as well for instilling a love of Science and curiosity from the very beginning. Thanks Dad for teaching me to be a critical thinker, to laugh at my own mistakes, and to find love and laughter in the small things. Thank you also for pushing me to try new things be it learning to play the trumpet or moving to Montreal for grad school. You both are the best parents in the whole wild world, and make me a very lucky girl.

Last of all, thanks to my wonderful fiancé, William Curtis (Honourable Sir William of Halifax). Thank you for being my biggest cheerleader. From supporting me on the hard nights from the lab, to making posters to bring to my hockey games, it is your smile in the stands that keeps me going. Life is easier with you. This whole PhD thing was hard enough, I can't even imagine it without you. Thanks for being there through the tears and the angry rants, for doing all the chores and cooking when I had my finger surgery, for nursing me when I was ever sick, for giving me head rubs when I had a headache, and for generally looking out for me. I feel like keeping a smile on my face is one of your life missions (except when we're playing tennis). Thanks for running with me, for pushing me to do better, and for the science advice and advice in general. Thanks for the days we do nothing, the bike trips, the ski trips, the snowball fights, the pillow fights, the painting, the cooking adventures, the laughing over silly youtube videos (wink wink), the surprise Juliette et Chocolat brownies, the Laniam-McGreentis, the daydreaming in the park, and the trips to the market. I always find changes in life scary, but having you by my side makes me confident, and if anything, excited to take on the coming challenges.

Table of Contents

ABSTRACT.....	III
RÉSUMÉ	V
ACKNOWLEDGEMENTS	VII
LIST OF FIGURES.....	XVI
LIST OF SCHEMES	XXIV
LIST OF TABLES	XXVI
ABBREVIATIONS.....	XXVII
AUTHOR CONTRIBUTIONS AND PUBLICATIONS	XXXI
<u>1 INTRODUCTION.....</u>	<u>1</u>
1.1 CHEMISTRY OF ROS AND ANTIOXIDANTS.....	3
1.1.1 REACTIVE OXYGEN SPECIES.....	3
1.1.2 LIPID PEROXIDATION	5
1.1.3 UBIQUINOL	9
1.1.4 VITAMIN E.....	15
1.1.5 MONITORING ROS, LIPID PEROXIDATION, AND REDOX REACTIONS	20
1.2 FLUORESCENCE	20
1.2.1 EXCITED STATE PROCESSES.....	21
1.2.2 FLUOROPHORE PROPERTIES.....	22
1.2.3 FLUORESCENCE QUENCHING.....	24
1.3 DESIGN OF FLUORESCENT PROBES.....	27
1.3.1 DESIGN OF PROBES RELYING ON PHOTOINDUCED ELECTRON TRANSFER	28
1.3.2 RATIOMETRIC PROBES	34
1.4 FLUORESCENT PROBES FOR REACTION SCREENING AND REDOX STATE	35
1.4.1 PROBES FOR DETECTION OF REACTIVE OXYGEN SPECIES AND LIPID PEROXIDATION.....	36
1.4.2 FLUOROGENIC PROBES FOR REDOX-REVERSIBLE REACTIONS.....	40
1.4.3 FLUOROGENIC PROBES FOR DETECTING NUCLEOPHILES AND MONITORING NUCLEOPHILIC REACTIONS.....	44
1.5 RESEARCH GOALS AND SCOPE OF THESIS	48
1.6 REFERENCES.....	51
<u>2 FLUROGENIC UBIQUINONE ANALOGUE FOR MONITORING CHEMICAL AND BIOLOGICAL REDOX PROCESSES.....</u>	<u>60</u>

2.1	PREFACE	61
2.2	ABSTRACT	61
2.3	INTRODUCTION	62
2.4	RESULTS AND DISCUSSION	64
2.4.1	DESIGN	64
2.4.2	SYNTHESIS	65
2.4.3	SPECTROSCOPIC PROPERTIES	66
2.4.4	ELECTROCHEMICAL PROPERTIES	68
2.4.5	REDOX REVERSIBILITY	69
2.4.6	ROS SCAVENGING AND SYNERGY WITH A-TOCOPHEROL.....	70
2.5	CONCLUSION	75
2.6	EXPERIMENTAL SECTION	76
2.6.1	MATERIALS.....	76
2.6.2	INSTRUMENTATION.....	76
2.6.3	COMPUTATIONAL METHODS	76
2.6.4	FLUORESCENCE QUANTUM YIELD.....	77
2.6.5	FLUORESCENCE LIFETIME STUDIES	77
2.6.6	ELECTROCHEMICAL STUDIES	77
2.6.7	KINETIC STUDIES IN THE PRESENCE OF ROS AND H ₂ B-PMHC.....	78
2.6.8	SYNTHESIS	78
2.7	SUPPORTING INFORMATION	81
2.7.1	DENSITY FUNCTIONAL THEORY TO CONFIRM AND VISUALIZE PET.....	81
2.7.2	ABSORPTION SPECTRA	83
2.7.3	ANALYSIS OF INTENSITY-TIME TRAJECTORY OF H ₂ B-PMHC WITH H ₂ B-QH ₂ WITH EQUATION 2.6	84
2.8	REFERENCES	85

3 TUNING PHOTOINDUCED ELECTRON TRANSFER EFFICIENCY ON FLUOROGENIC BODIPY-A-TOCOPHEROL ANALOGUES: A QUEST FOR DARKNESS..... 88

3.1	PREFACE	89
3.2	ABSTRACT	89
3.3	INTRODUCTION	90
3.4	RESULTS AND DISCUSSION	93
3.4.1	LIBRARY OF BODIPY CHROMANOL CONSTRUCTS.....	93
3.4.2	DFT STUDIES	95

3.4.3	EVALUATION OF $\Delta G^{\circ}_{\text{PET}}$ FROM ELECTROCHEMICAL AND PHOTOPHYSICAL DATA.....	97
3.4.4	EVALUATION OF THE RATE CONSTANT AND EFFICIENCY OF PET.....	98
3.4.5	MAXIMIZING K_{PET}	100
3.4.6	DISTANCE DEPENDENCE ON K_{PET}	103
3.5	CONCLUSION	104
3.6	EXPERIMENTAL	105
3.6.1	MATERIALS.....	105
3.6.2	INSTRUMENTATION.....	106
3.6.3	COMPUTATIONAL METHODS.....	106
3.6.4	ELECTROCHEMICAL STUDIES.....	106
3.6.5	OXIDATION OF PROBES WITH PEROXYL RADICALS.....	107
3.6.6	FLUORESCENCE QUANTUM YIELD	107
3.6.7	FLUORESCENCE LIFETIME STUDIES.....	108
3.6.8	SYNTHESIS.....	108
3.7	SUPPORTING INFORMATION	112
3.7.1	DFT TO CONFIRM AND VISUALIZE PHOTOINDUCED ELECTRON TRANSFER.....	113
3.7.2	CYCLIC VOLTAMMETRY	116
3.7.3	OPTIMIZED STRUCTURES OF H ₂ BPMHC AND H ₂ BTOH.....	117
3.8	REFERENCES.....	118

4 LIPID PEROXYL RADICALS PRODUCED DURING CELLULAR HOMEOSTASIS UNRAVELLED VIA FLUORESCENCE IMAGING..... 121

4.1	PREFACE.....	122
4.2	ABSTRACT.....	122
4.3	INTRODUCTION	123
4.4	RESULTS AND DISCUSSION	126
4.4.1	H ₄ BPMHC DESIGN AND SYNTHESIS.....	126
4.4.2	SPECTROSCOPIC PROPERTIES	129
4.4.3	REACTIVITY WITH AZO-INITIATORS.....	129
4.4.4	UNMASKING THE INFLUENCE OF SERUM ALBUMIN IN MONITORING CELL-MEMBRANE EMBEDDING PROBES.....	131
4.4.5	LIPID PEROXYL RADICALS GENERATED DURING CELLULAR HOMEOSTASIS AND UNDER FENTON CONDITIONS.....	134
4.5	CONCLUSION	140
4.6	EXPERIMENTAL	141

4.6.1	MATERIALS.....	141
4.6.2	INSTRUMENTATION.....	141
4.6.3	TIME-BASED FLUORESCENT ENHANCEMENTS WITH RADICAL INITIATOR.....	141
4.6.4	FLUORESCENCE QUANTUM YIELD.....	142
4.6.5	FLUORESCENCE LIFETIME STUDIES	143
4.6.6	MICROSCOPY.....	143
4.6.7	CELL CULTURE.....	143
4.6.8	CELL IMAGING OF H ₄ BCH ₃	144
4.6.9	CELL IMAGING OF H ₄ BPMHC OR H ₄ BCH ₃ IN HEALTHY AND STRESSED CELLS	144
4.6.10	IMAGE ANALYSIS.....	145
4.6.11	QUANTIFYING CONCENTRATION OF PROBE IN CELLS.....	145
4.6.12	SYNTHESIS.....	146
4.7	SUPPORTING INFORMATION	149
4.7.1	PARTITIONING OF H ₄ BCH ₃ INTO CELLS IN VARIOUS BUFFERS: INFLUENCE OF SERUM ALBUMINS	151
4.7.2	IMAGING STUDIES WITH H ₄ BPMHC.....	152
4.7.3	APPROXIMATION OF CONCENTRATION OF DYE IN CELLS	154
4.7.4	CONTROLS FOR DETERMINING QUANTUM YIELDS.....	154
4.8	REFERENCES.....	155

5 DEVELOPMENT OF A FLUOROGENIC REACTIVITY-PALETTE FOR THE STUDY OF NUCLEOPHILIC ADDITION REACTIONS BASED ON MESO-FORMYL BODIPY DYES ...158

5.1	PREFACE.....	159
5.2	ABSTRACT.....	160
5.3	INTRODUCTION	160
5.4	RESULTS AND DISCUSSION	162
5.4.1	RATIONALE	162
5.4.2	REACTIVITY.....	162
5.4.3	EQUILIBRIUM.....	168
5.4.4	PHOTOPHYSICS OF THE REACTION MIXTURES.....	169
5.5	CONCLUSION	172
5.6	EXPERIMENTAL SECTION.....	172
5.6.1	MATERIALS.....	172
5.6.2	INSTRUMENTATION.....	173
5.6.3	TIME BASED FLUORESCENT ENHANCEMENTS	173
5.6.4	FLUORESCENCE QUANTUM YIELD.....	173

5.6.5	FLUORESCENCE LIFETIME STUDIES	174
5.6.6	SYNTHESIS	174
5.7	SUPPORTING INFORMATION	175
5.8	REFERENCES.....	176
6	<u>CONCLUSIONS AND OUTLOOK.....</u>	<u>178</u>
6.1	CONCLUSIONS AND CONTRIBUTION TO ORIGINAL KNOWLEDGE	178
6.2	OUTLOOK AND FUTURE DIRECTIONS.....	180
6.2.1	IMPROVING H ₂ B-Q FOR TARGETING MITOCHONDRIA AND USE IN BIOLOGICAL APPLICATIONS... 181	181
6.2.2	TARGETING H ₄ BPMHC TO MITOCHONDRIA FOR STUDYING ROS ACCUMULATION AND PRODUCTION IN ALZHEIMER'S DISEASE..... 182	182
6.2.3	EXPANDING THE PALETTE TO FLUOROGENIC ANALOGUES OF BIOLOGICAL MOLECULES OF INTEREST..... 183	183
6.2.4	STATE-OF-THE-ART FLUORESCENCE IMAGING METHODS	184
6.3	REFERENCES.....	186
7	<u>APPENDIX</u>	<u>188</u>

List of Figures

Figure 1.1 A) Thermolysis of azo compounds and subsequent reaction with oxygen. B) Structures of lipophilic azo compounds used in this thesis and their decomposition activation energy (E_a), pre-exponential factor (A) and calculated rate constants (k_i) at 37 °C. ^{52,53}	8
Figure 1.2 The five complexes involved in the electron transport chain. Reprinted by permission from Macmillan Publishers Ltd: Nature Reviews: Molecular Cell Biology, Sazanov, L. A. Nature Publishing Group 2015, 16 (6), 375–388. Copyright (2015). ⁷⁶	12
Figure 1.3 The Q cycle of Complex III in the electron transport chain. Reprinted from BBA – Bioenergetics, 1807, Cramer, W. A.; Hasan, S. S.; Yamashita, E The Q cycle of cytochrome bc complexes: A structure perspective, 788-802, Copyright (2011), with permission from Elsevier. ⁷⁷	14
Figure 1.4 Structure of Vitamin E compounds.....	15
Figure 1.5 Effect of substitution of a phenol with either electron withdrawing groups (EWG) or electron donating groups (EDG), on the bond dissociation energy (BDE). ⁸¹	17
Figure 1.6 A) Stabilization of the phenoxyl radical by a <i>para</i> oxygen atom B) Schematic of the overlap and thus stabilization of the phenoxyl radical which is dependent on θ . ⁴²	18
Figure 1.7 Photophysical processes represented in a Jablonski Diagram. ¹⁰¹ VR denotes vibrational relaxation (VR), IC stands for internal conversion, and ISC stands for intersystem crossing.	21
Figure 1.8 Effect of substitution with heavy atoms on the fluorescence quantum yield (Φ_f) of BODIPY dyes. ¹⁰³	25
Figure 1.9 A) Structure of non-fluorescent <i>meso</i> -formyl BODIPY dye B) Calculated energy diagrams of <i>meso</i> -formyl dye in the ground and excited states. Adapted with permission from Lincoln, R.; Greene, L. E.; Bain, C.; Flores-Rizo, J. O.; Bohle, D. S.; Cosa, G. J. Phys. Chem. B 2015, 119 (13), 4758–4765. Copyright 2015 American Chemical Society.....	26
Figure 1.10: Comparison of electron affinity (EA) and ionization potential (IP) between a fluorophore in the ground state (F) and in the photo-excited state (F*) in the gas phase. ¹⁰¹	29

Figure 1.11: Two scenarios of PeT. 1) Where the photo-excited fluorophore (F^*) is the electron donor (D) and the quencher (Q) is the acceptor (A) and 2) Where the photo-excited fluorophore is the electron acceptor and the quencher is the donor.¹⁰¹30

Figure 1.12 The Marcus Inverted region shown experimentally for electron transfer between a biphenyl group and an electron acceptor A. hexahydronaphthoquinon-2-yl (at $\Delta G^\circ = -1.2 \text{ eV} = \lambda$) marks the onset of the inverted region (right).¹⁰⁹ Reprinted with permission from “Miller, J. R.; Calcaterra, L. T.; Closs, G. L. Journal of the American Chemical Society, 1984 106 (10), 3047-3049” Copyright 1984 American Chemical Society.32

Figure 1.13 Fluorescent enhancement observed after 10% of the probe has reacted (i.e. 10% reaction completion) vs the amount of contamination with already activated probe (i.e. a pristine sample has 0% contamination). Dye 1 (black) has a poor dynamic range due to its higher ‘off’ Φ_n than dye 2 (red).33

Figure 1.14 Structures of ROS probes based on fluorescein and the emission wavelength and dynamic range (DR) expected upon reaction with ROS.^{117,119}36

Figure 1.15 Fluorogenic probes for the detection of singlet oxygen based on DMA.^{115,125}37

Figure 1.16 Fluorescent probes for the detection of lipid peroxidation based on the structure of fatty acids.^{126,128}38

Figure 1.17 A) First generation fluorogenic tocopherol analogue, BTOH, and its reaction with lipophilic radicals.¹³⁰ B) Subsequent generations of fluorogenic tocopherol analogues prepared in the Cosa Laboratory and their dynamic range (DR).^{19,48}40

Figure 1.18 Thiol-reactive fluorogenic probes relying on chemistry with maleimide. A) CPM developed by Sippel and coworkers, and its reaction with thiols,¹⁵⁶ B) probe developed by Keillor and coworkers¹⁶⁰ and C) probe developed by Nagano and coworkers.¹⁵⁷45

Figure 2.1: Cyclic voltammogram of **H₂B-Q** (0.7 mM) dissolved in 10% v/v MeCN in toluene (0.1 M tetrabutylammonium hexafluorophosphate) under argon recorded at 100 mVs⁻¹. Potentials were normalized to the ferrocene oxidation in these conditions.69

Figure 2.2: Emission spectra of **H₂B-Q** (1.3 μ M in toluene) before the redox cycle (black), after reduction by sodium borohydride (red), and after subsequent TEMPO oxidation (blue).70

Figure 2.3: Fluorescence-time trajectories of 100 μ M **H₂B-PMHC** (black traces) or 100 μ M **H₂B-QH₂** (red traces) in the presence of 0.5 mM MeO-AMVN in dichloromethane. Dashed lines indicate the solution where **H₂B-PMHC** and **H₂B-QH₂** were mixed together. **H₂B-PMHC** was excited at 480 nm and emission was monitored at 520 nm. In turn **H₂B-QH₂** was excited at 550 nm and emission was monitored at 600 nm. τ indicates the time of consumption of antioxidant in solution. $\tau_a = 3670$ s (consumption of **H₂B-PMHC**), $\tau_b = 6290$ s (consumption of **H₂B-PMHC** in the presence of **H₂B-QH₂**), and $\tau_c = 1560$ s (consumption of **H₂B-QH₂**).71

Figure 2.4 Orbital energies calculated for **H₂B-QH₂** and **H₂B-Q**.82

Figure 2.5 Visualization of calculated orbitals for **H₂B-QH₂**.82

Figure 2.6 Normalized absorbance spectra of **H₂B-phenol** (black), **H₂B-QH₂** (red) and **H₂B-Q** (blue). Note the peak corresponding to the quinone moiety at 287 nm for **H₂B-Q** and the lack of this peak for **H₂B-QH₂**.83

Figure 2.7 Absorbance spectra of 1.3 μ M of **H₂B-Q** before reduction with NaBH₄ (black), after reduction with NaBH₄ (red), and after sequential re-oxidation with 1 mM TEMPO (green). Absorbance spectrum of 1 mM TEMPO (blue) shows negligible absorption at the absorbance maximum of **H₂B-Q**.83

Figure 2.8 Analysis of the intensity time trajectory of **H₂BPMHC** and **H₂B-QH₂** using Equation 2.6. Fluorescence of **H₂BPMHC** was followed, and the time was adjusted such that **H₂B-QH₂** was fully consumed at $t=0$ s.84

Figure 3.1 Fluorogenic α -tocopherol analogues discussed here. A) XBTOH series, B) XPMHC series. Numbering of the positions of the BODIPY core is shown in orange.93

Figure 3.2 Orbital energies of the individual chromanol and BODIPY dye moieties for the fluorogenic probes presented here calculated at the B3LYP 6-31G(d) level. Structures of moieties may be found in Figure 3.4. Dotted lines represent the HOMO orbital energy of the trolox ester or PMHC. A) Orbitals calculated for the XBTOH series: HOMO and LUMO

levels of trolox ester in both reduced and oxidized form are compared to those of *meso*-acetoxymethyl-BODIPY dyes. B) Orbitals calculated for the XBPMHC series: HOMO and LUMO levels of PMHC in both reduced and oxidized form are compared to those of the *meso*-methyl-BODIPY dyes96

Figure 3.3 A) Correlation of the reduced quantum yields (Φ_0) of the XBTOH series (black) and XBPMHC series (red) with calculated $\Delta G^\circ_{\text{PeT}}$. Data trends were fit with a quadratic function (dashed lines), and a quadratic function based on fixed coefficients (B=20 and C=7) obtained from Marcus theory with $\lambda=1.4$ eV (blue). B) Assuming samples in A had a fraction of pre-oxidized probe of 0.1% (open symbols). Here the Φ_f were re-calculated (‘pristine’) from the values experimentally obtained (off state, ‘meas’) considering the latter were tainted with 0.1% pre-oxidized compound: $\Phi_{\text{pristine}} = (\Phi_{\text{meas}} - \Phi_{\text{ox}} * 0.001) / 0.999$, where Φ_{ox} is the emission quantum yield of BODIPY-tocopherol constructs once oxidized (on state, ‘ox’). 102

Figure 3.4 BODIPY moieties used to predict PeT using DFT in Figure 3.2. 113

Figure 3.5 Typical orbitals calculated for BODIPY, PMHC, and oxidized PMHC.. 114

Figure 3.6 Visualization of calculated orbitals for H₂BPMHC in both reduced and oxidized states..... 114

Figure 3.7 Orbitals calculated for H₂BPMHC and oxidized H₂BPMHC (H₂BPMHC_{ox}). Dark and light green bars indicate orbitals corresponding to the HOMO and LUMO of the BODIPY moiety respectively. Red and pink bars indicate orbitals corresponding to the HOMO and LUMO of the chromanol moiety respectively. Orbitals were assigned based on orbitals typical of chromanol and BODIPY as is shown in Figure 3.5. 115

Figure 3.8 Cyclic voltammogram for H₄BCH₃ in acetonitrile with 0.1 M tetrabutylammonium hexafluorophosphate supplemented with 1 mM ferrocene. 116

Figure 3.9 Cyclic voltammogram for H₄MeBOAc (1 mM) in acetonitrile with 0.1 M tetrabutylammonium hexafluorophosphate supplemented with 1 mM ferrocene. 116

Figure 3.10 The sensitivity of the newly prepared probe, H₄BPMHC as illustrated by the emission spectra of H₄BPMHC and once oxidized by the addition of peroxy radicals (H₄BPMHC_{ox}). 117

Figure 3.11 Optimized structures of H₂BPMHC and H₂BTOH obtained from DFT. Both structures are folded at the linker between the chromanol and BODIPY moiety. Determining the centre of both the BODIPY moiety and chromanol moiety of each structure places the distance separating each moiety at 6.127 and 6.392 Å for H₂BPMHC and H₂BTOH respectively..... 117

Figure 4.1 A) Structure of α -tocopherol and previously reported fluorogenic tocopherol analogue, H₂BPMHC. B) Proposed off/on sensing mechanism of the new fluorogenic probe, **H₄BPMHC** relying on PeT..... 127

Figure 4.2 Fluorescence-time trajectories of **H₄BPMHC** (1 μ M or 10 μ M as indicated) in the presence of the radical initiator MeO-AMVN (200 μ M) and supplemented with and without antioxidants (PMHC and α -tocopherol, 9 μ M). Solutions were excited at 485 nm and emission was monitored at 520 nm. Fluorescence enhancement times, τ , were 2730 s, 2870 s, and 2460 s for **H₄BPMHC** and tocopherol, **H₄BPMHC** and PMHC, and 10 μ M **H₄BPMHC** respectively. 130

Figure 4.3 Images of HeLa cells acquired over 30 minutes upon the addition of 100 nM **H₄BCH₃** in LCS, DMEM or DMEM supplemented with 10% FBS. Images were acquired using widefield fluorescence microscopy. 132

Figure 4.4 Images of HeLa cells acquired over 30 minutes upon the replacement of 100 nM **H₄BCH₃** in LCS, with fresh media (LCS, DMEM or DMEM supplemented with 10% FBS). Images were acquired using widefield fluorescence microscopy..... 133

Figure 4.5 A) Images of HeLa cells in the presence of 100 nM **H₄BPMHC** (Probe) with/without PMHC acquired after 50 minutes of treatment with (stressed) or without (healthy) cumene hydroperoxide (100 μ M) and copper sulfate (10 μ M). Images were acquired using widefield microscopy. Inset shows compressed DIC images for the same region. B) Corrected total cell fluorescence vs time determined from images acquired over a 45 minute period with 100 nM **H₄BPMHC** in healthy cells and cells exposed to Fenton reagents.... 135

Figure 4.6 CTCF of **H₄BPMHC** (A) and **H₄BCH₃** (B) in HeLa cells. Intensities were determined after 50 minutes of treatment with/without stressor. Dye = 100 nM in either **H₄BPMHC** or **H₄BCH₃**, stressor = 100 μ M cumene hydroperoxide and 10 μ M copper

sulfate. Images were acquired using widefield microscopy. CTCF of B was corrected by the exposure time used to match that of A. 137

Figure 4.7 Absorption and emission spectra acquired in acetonitrile: A) H₄BPMHC, B) H₄BPMHC_{ox} C) H₄BCH₃. 150

Figure 4.8 Plot of the rate analysis of Figure 4.2 using Equation 4.1. The relative rates determined from the slopes of the above plot ($k_{H_4rBPMHC}/k_{Toc}$ and k_{H_4BPMHC}/k_{PMHC}) were both 0.9. 150

Figure 4.9 Normalized corrected total cell fluorescence (CTCF) of 100 nM H₄BCH₃ in HeLa cells. A) LCS, DMEM, and FBS intensities were determined from images acquired after 30 minutes of the dye partitioning in the respective buffers on a widefield microscopy setup. B) LCS, DMEM, and FBS intensities were determined after 30 minutes of the dye solution being removed and replaced with the respective buffer. 151

Figure 4.10 CTCF-time trajectories acquired during the partitioning of 100 nM H₄BCH₃ in HeLa cells. A) Trajectories acquired for the first 30 minutes of partitioning in the respective buffers. Curves were fit to an exponential growth curve according to Equation S4.1, where $k = 0.15, 0.16,$ and 0.18 for LCS, DMEM, and FBS respectively. B) Trajectories acquired for the first 30 minutes after buffer exchange. Curves were fit to an exponential decay curve according to Equation S4.2, where $k = 0.093, 0.086,$ and 0.35 for LCS, DMEM, and FBS respectively. 151

Figure 4.11 Relative fluorescence enhancement from time 0 of 100 nM H₄BPMHC in HeLa cells treated with/without PMHC and Fenton reagents after 50 minutes. 152

Figure 4.12 Images acquired with a TIRF setup of stressed (A) HeLa cells with 100 μM cumene hydroperoxide and 10 μM copper sulfate) and healthy (B) HeLa cells with 100 nM H₄BPMHC. The intensities of the healthy cells were increased 5-fold to better see the localization of the probe. 153

Figure 4.13 Corresponding DIC images to Figure 4.5A to show cell viability. 153

Figure 4.14 Structures of the dye standards used to determine fluorescence quantum yields. 154

Figure 5.1 Structure of the *meso*-formyl BODIPY dyes used in this work. Numbering of the BODIPY core is shown in green..... 162

Figure 5.2 A) Intensity-time trajectories following the reaction of **3** (4.5 μM) with increasing methanol concentration at 21 $^{\circ}\text{C}$. B) Correlation between the intensity at infinite time (I_{∞}) obtained from fitting the intensity-time trajectories in panel A using Equation 5.2 and methanol concentration. C) Relationship of initial rate determined from panel A and methanol concentration. Error bars in y were obtained from the error associated with performing a linear fit on the initial increase of fluorescence enhancements in panel A. D) Intensity time trajectories following the reaction of 4.5 μM of **3** with 1.09 M methanol in acetonitrile with varying concentrations of *p*-TsOH at 21 $^{\circ}\text{C}$. E) Correlation between the apparent rate constants for **3** obtained from fitting the trajectories displayed in panel D with Equation 5.2 and *p*-TsOH concentration. Error bars were obtained from the error of the fitting with Equation 5.2. F) Equilibrium of *meso*-formyl BODIPY in the presence of an alcohol and an acid catalyst. 164

Figure 5.3 A) Intensity-time trajectories following the reaction of compounds **1** to **5** with 1.09 M methanol in acetonitrile supplemented with 0.333 mM of *p*-TsOH at 21 $^{\circ}\text{C}$. Dye concentrations were prepared such that their respective absorbance was 0.1 at the excitation wavelength used (i.e. 16 μM , 20 μM , 4.5 μM , 16 μM and 3 μM for dyes **1-5** respectively) B) Correlation between the ratio of apparent rate constants (k_{app}) and the difference in oxidation potentials (to compound **1**) in acetonitrile for the BODIPY dyes **1-5** vs ferrocene.¹⁸ Compound **1** k_{app} and oxidation potentials were used as a reference. C) Correlation between the ratio of intensities at infinite time (I_{∞}) and the difference in reduction potentials in acetonitrile for dyes **1-5** (to compound **1**) measured vs ferrocene.¹⁸ Compound **1** I_{∞} and reduction potentials were used as a reference. 165

Figure 5.4 A) Intensity-time trajectories following the reaction of 4.5 μM of compound **3** and 1.09 M of methanol (MeOH), ethanol (EtOH), butanol (BuOH), ethylene glycol (EtyGly), water (H_2O) and ethanedithiol (EtSH₂) at 21 $^{\circ}\text{C}$ in acetonitrile supplemented with 0.333 mM of *p*-TsOH. B) Apparent rate constants for the various nucleophiles tested were

obtained from fitting the intensity-time trajectories in panel A with Equation 5.2. Error bars are from the fitting with Equation 5.2..... 167

Figure 5.5 A) Structure of compound **6** and proposed structure of the major product of **5** dissolved in ethylene glycol. B) Absorption and emission spectra of **5** and **6** dissolved in ethylene glycol. 168

List of Schemes

Scheme 1.1 Formation of ROS via energy transfer or redox processes. Potentials given are versus Standard Hydrogen Electrode (SHE). Reprinted with permission from reference 14. ¹⁴	4
Scheme 1.2 Reactions and their rate constants for the 4 steps of lipid peroxidation: Initiation, Propagation, Termination and Inhibition. LH represents a polyunsaturated fatty acid. (k_{ox} , ⁴¹ k_p , ⁴¹ k_t , ⁴¹ k_{inh} , ⁴² k_{coup} ⁴³)	6
Scheme 1.3 H-atom abstraction by a hydroxyl radical and resulting stabilization of a polyunsaturated fatty acid.	6
Scheme 1.4 Free radical attack and subsequent fragmentation of linoleic acid into 4-HNE via Hock fragmentation and reduction. ^{41,47}	7
Scheme 1.5 The structure of ubiquinol and its three redox states.	10
Scheme 1.6 The formation and fate of the ubisemiquinone radical (UQH•). ⁶⁶	10
Scheme 1.7 Reversible reaction of ubiquinone (UQ) and superoxide radical anion ($O_2^{\bullet-}$), and disproportionation of the ubisemiquinone radical. ⁶⁶	11
Scheme 1.8 Mechanism of regeneration of α -tocopherol by ubiquinol. ^{71,75}	12
Scheme 1.9 Sequence of redox reactions involved in Complex I. ^{65,76}	13
Scheme 1.10 Sequence of redox reactions involved in Complex II. ⁶⁵	13
Scheme 1.11 Comparison of Vitamin E supplementation in animals vs in humans. Supplementation in humans typically occurs in older patients once symptoms have been detected (red), rather than when oxidative stress sets in (black). ⁹⁴	19
Scheme 1.12 Redox reversibility and dynamic range (DR) of Redoxfluor-1. ¹³³	41
Scheme 1.13 Redox reversibility and fluorogenicity of quinone redox probe, BD-PQ. ¹³⁷	42
Scheme 1.14 Redox reversibility and dynamic range (DR) of a quinone-rhodamine redox probe. ¹³⁸	42
Scheme 1.15 Redox reversibility and fluorogenicity of tellurium redox probe, Cy-NTeO. ¹⁴¹	43

Scheme 1.16 Redox reversibility and dynamic range (DR) of flavin redox probe, NpFR1. ¹⁴⁴	44
Scheme 1.17 Reaction mechanism of a fluorogenic probe specific for glutathione developed by Akkaya and coworkers. ¹⁶²	46
Scheme 1.18 Fluorogenic probe for screening alkynes for Sonogashira coupling developed by Bergstrom and coworkers. ¹⁶³	47
Scheme 1.19 Cycle of fluorogenic probe development.	48
Scheme 2.1: A) Structure of Ubiquinone B) Proposed off/on sensing mechanism for H₂B-Q relying on PeT.....	65
Scheme 2.2: Synthesis of H₂B-phenol , H₂B-Q , and H₂B-QH₂	66
Scheme 2.3: One pot reduction and subsequent oxidation of H₂BQ	69
Scheme 2.4: Regeneration of α -tocopherol from the tocopheroxyl radical by H₂B-QH₂	73
Scheme 3.1 Schematic representation of the PeT mechanism operating in fluorogenic α -tocopherol analogues, where HOMO/LUMO levels of the BODIPY fluorophores presented here may be tuned as shown by the grey band (<i>vide infra</i>).	92
Scheme 3.2 General synthesis of the tocopherol-BODIPY constructs compared in this paper.....	95
Scheme 4.1 Synthesis of H₄BPMHC and H₄BCH₃	128
Scheme 4.2 Formation of cumoperoxyl and cumoxyl radicals from cumene hydroperoxide in the presence of copper.	136
Scheme 5.1 Expected products from the reaction of <i>meso</i> -formyl BODIPY and an alcohol (ROH).	161
Scheme 6.1 Synthesis of H ₄ -mito-BPMHC from H ₄ BPMHC.	183

List of Tables

Table 2.1: Spectroscopic properties of H₂B-phenol , H₂B-Q and H₂B-QH₂ in various solvents.	67
Table 3.1 Calculated $\Delta G^{\circ}_{\text{PET}}$, from measured EA/A- \bullet° and $\Delta E_{0,0}$	97
Table 3.2 Photophysical properties of fluorogenic BODIPY-chromanol constructs and of their oxidized counterparts produced following reaction with thermally generated peroxy radicals and their corresponding fluorescence enhancement (Fl. En).....	99
Table 3.3 HOMO, LUMO and $\Delta E_{0,0}$ values obtained from DFT and the difference in HOMO levels between the BODIPY moiety and the tocopherol analogue ($\Delta \text{HOMO}_{\text{Bodipy-Toc}}$).....	115
Table 4.1 Photophysical properties of the novel BODIPY dyes presented herein....	129
Table 5.1 Photophysical properties of reaction mixtures for dyes 1-5 with 1.09 M methanol in acetonitrile and 0.333 mM <i>p</i> -TsOH.....	170
Table 5.2 Photophysical properties of reaction mixtures of dye 3 in the presence of 1.09 M nucleophile (Nu) in acetonitrile and 0.333 mM <i>p</i> -TsOH.....	171
Table 5.3 Photophysical properties of dye 6	175

Abbreviations

4-HNE	4-Hydroxynonenal
α -TOH	α -Tocopherol
$\Delta E_{0,0}$	Vibrational Zero Electronic Energy
ΔG°_{eT}	Free energy of electron transfer
ϵ	Extinction Coefficient
ϵ_0	Permittivity of Vacuum
λ	Reorganization Energy; Wavelength
ω	Coulombic Correction Term
Φ_{fl}	Fluorescence Quantum Yield
τ_{def}	Fluorescent Decay Lifetime
A	Acceptor
\mathcal{A}	Absorbance
AcOH	Acetic Acid
AMBN	2,2'-Azobis-(2-methylbutyronitrile)
AOH	Chain-Breaking Antioxidant
AOTF	Acousto-optical Tunable Filter
APCI	Atmospheric Chemical Ionization
ATP	Adenosine Triphosphate
BDE	Bond Dissociation Energy
BODIPY	Boron-dipyrromethene (4,4-difluoro-4-bora-3a,4a-diaza-s-indacene)
BSA	Bovine Serum Albumin
BTOH	8-((\pm) 6-Hydroxy-2,5,7,8-tetramethylchromane-2-carbonyloxy)-methyl-2,6-diethyl-1,3,5,7-tetramethylpyrromethene fluoroborate
BuOH	Butanol
C	Concentration
CTCF	Corrected Total Cell Fluorescence
CV	Cyclic Voltammetry
D	Donor
DCFH	Dichlorodihydrofluorescein
DCM	Dichloromethane
DFT	Density Functional Theory
DIC	Differential Interference Contrast
DIPEA	Diisopropylethilamine
DMA	9,10-Dimethylantracene

DMAP	Dimethylaminopyridine
DMEM	Dulbecco's Modified Eagle Medium
DMF	Dimethylformamide
DMSO	Dimethylsulfoxide
DNA	Deoxyribonucleic acid
E°	Redox Potential
EA	Electron Affinity
EDG	Electron Donating Group
EM-CCD	Electron Multiplying Charge Coupled Device
ESI	Electron Spray Ionization
EtOH	Ethanol
EtyGly	Ethylene Glycol
Et(SH) ₂	Ethanedithiol
eV	Electronvolts
EWG	Electron Withdrawing Group
F*	Excited State Fluorophore
FAD	Flavin Adenine Dinucleotide
FBS	Fetal Bovine Serum
FLIM	Fluorescence Lifetime Imaging Microscopy
FMN	Flavin Mononucleotide
FMO	Frontier Molecular Orbital
H ₂ BPMHC	8-((6-hydroxy-2,5,7,8-tetramethylchroman-2-yl)-methyl)-1,3,5,7-tetramethyl Pyrromethene Fluoroborate
HOMO	Highest Occupied Molecular Orbital
HPLC	High Performance Liquid Chromatography
HRMS	High Resolution Mass Spectrometry
<i>I</i>	Fluorescence Intensity
IC	Internal Conversion
IP	Ionization Potential
ISC	Intersystem Crossing
k_B	Boltzmann Constant
k_{app}	Apparent Rate Constant
k_{dec}	Decay Rate Constant
k_i	Initiation Rate Constant
k_{IC}	Internal Conversion Rate Constant
k_{inb}	Inhibition Rate Constant
k_{ISC}	Intersystem Crossing Rate Constant
k_{PeT}	Photoinduced Electron Transfer Rate Constant

k_{nr}	Non-radiative Decay Rate Constant
k_q	Quenching Rate Constant
k_r	Radiative Rate Constant
K_{eq}	Equilibrium Constant
K_{sv}	Stern-Volmer Quenching Constant
l	Pathlength
LCS	Live Cell Imaging Solution
LDL	Low Density Lipoprotein
LFER	Linear Free Energy Relationship
LOO•	Lipid Peroxyl Radical
LUMO	Lowest Unoccupied Molecular Orbital
MeCN	Acetonitrile
MeO-AMVN	2,2'-Azobis(4-methoxy-2,4-dimethyl valeronitrile)
MeOH	Methanol
N_A	Avogadro's Constant
NA	Numerical Aperture
NADH	Nicotinamide Adenine Dinucleotide
NASCA	Nanometer Accuracy by Stochastic Chemical Reactions
nm	Nanometres
NMR	Nuclear Magnetic Resonance
Nu	Nucleophile
PALM	Photo-activated Localization Microscopy
PBS	Phosphate Buffer Saline
PeT	Photoinduced Electron Transfer
PFS	Perfect Focus System
PMHC	2,2,5,7,8-Pentamethyl-6-hydroxychromanol
<i>p</i> -TsOH	<i>p</i> -Toluenesulfonic Acid
Q	Quencher
rds	Rate Determining Step
R_g	Rate of Generation
ROH	Alcohol
ROS	Reactive Oxygen Species
RT	Room Temperature
S_n	Singlet Excited State
SDS PAGE	Sodium Dodecyl Sulfate Polyacrylamide Gel Electrophoresis
SHE	Standard Hydrogen Electrode
SMS	Single Molecule Spectroscopy
SOMO	Semi-Occupied Molecular Orbital

STED	Stimulated Emission Depletion Microscopy
STORM	Stochastic Optical Reconstruction Microscopy
t	Time
T_n	Triplet Excited State
TCSPC	Time Correlated Single Photon Counting
TEMPO	(2,2,6,6-Tetramethylpiperidin-1-yl)oxyl
THF	Tetrahydrofuran
TIRF	Total Internal Reflection Fluorescence
UQ	Ubiquinone
UV	Ultraviolet
ν_n	Nuclear Vibrational Frequency
VR	Vibrational Relaxation
WF	Widefield

Author Contributions and Publications

All publications (submitted and in preparation) were co-authored with Professor Gonzalo Cosa who jointly designed projects and directed this thesis.

- Chapter 2: Lana Greene; Robert Godin; Gonzalo Cosa, *J. Am. Chem. Soc.* **2016**, 138, 11327

Lana Greene contributed to project design, performed the synthesis and spectroscopic characterization of the compounds presented in the article, performed the DFT calculations, acquired the cyclic voltammograms, and performed the kinetics studies. Contributions also include analysis and interpretation of data, in addition to manuscript writing and editing

Robert Godin acquired the absorption and fluorescence spectra of the compounds in the presence of oxidizing and reducing agents, as well as contributed to data analysis and manuscript writing and editing.

- Chapter 3 Lana Greene, Gonzalo Cosa, *To be Submitted*

Lana Greene contributed to project design, performed the synthesis and spectroscopic characterization of the compounds presented in the article, also performed the DFT calculations, acquired the cyclic voltammograms, the kinetic experiments, and the fluorescence lifetimes and quantum yields. Contributions also include analysis and interpretation of the data, in addition to manuscript writing and editing.

- Chapter 4: Lana Greene, Richard Lincoln, Gonzalo Cosa, *To be Submitted*

Lana Greene contributed to project design, performed the synthesis and spectroscopic characterization of the compounds presented in the article, also performed the competitive kinetics studies, the cell culture, and the fluorescence microscopy. Contributions also include analysis and interpretation of the data, in addition to manuscript writing and editing.

Richard Lincoln contributed to project design and assisted with the fluorescence microscopy and analysis of the acquired images. Contributions also include manuscript editing.

- Chapter 5: Lana Greene, Richard Lincoln, Katerina Krumova, Gonzalo Cosa, *To be Submitted*

Lana Greene contributed to the project design, performed the kinetic experiments, the synthesis and characterization of the novel *meso*-acetal BODIPY compounds described, and acquired the quantum yields and fluorescence lifetimes. Contributions also include analysis and interpretation of the data, in addition to manuscript writing and editing.

Richard Lincoln assisted in preliminary studies and contributed to project design and manuscript editing.

Katerina Krumova performed preliminary studies and contributed to project design.

Additionally, the following articles were published during my doctoral work, but were not included as chapters in my thesis:

- Lincoln, R.; Greene, L.E.; Zhang, W.; Louisia, S.; Cosa, G. Alkylation and Trafficking Mapped at the Cellular Level with a Fluorogenic Nonenal Mimic. *Submitted*
- Wong, F.; AbuArish, A.; Matthes, E.; Greene, L.E.; Robert, R. Thomas, D.Y.; Cosa, G.; Cantin, A.; Hanrahan, J.W. Cigarette smoke activates CFTR in human bronchial epithelial cells, *Submitted*
- Lincoln, R.; Durantini, A.M.; Greene, L.E.; Martinez, S.R.; Knox, R.; Cosa, G. meso-Acetoxyethyl BODIPY Dyes for Photodynamic Therapy: Improved Photostability of Singlet Oxygen Photosensitizers, *Photochemical and Photobiological Sciences*, **2017**, *16*, 178-184.
- Durantini, A. M.; Greene, L. E.; Lincoln, R.; Martínez, S. R.; Cosa, G. Reactive Oxygen Species Mediated Activation of a Dormant Singlet Oxygen Photosensitizer: From Autocatalytic Singlet Oxygen Amplification to Chemically Controlled Photodynamic Therapy *J. Am. Chem. Soc.* **2016**, *138* (4), 1215.
- Lincoln, R.; Greene, L. E.; Bain, C.; Flores-Rizo, J. O.; Bohle, D. S.; Cosa, G. When Push Comes to Shove: Unravelling the Mechanism and Scope of

Nonemissive meso-Unsaturated BODIPY Dyes. *J. Phys. Chem. B* **2015**, *119* (13), 4758–4765.

- Lincoln, R.; Greene, L. E.; Krumova, K.; Ding, Z.; Cosa, G. Electronic Excited State Redox Properties for BODIPY Dyes Predicted from Hammett Constants: Estimating the Driving Force of Photoinduced Electron Transfer. *J. Phys. Chem. A* **2014**, *118* (45), 10622–10630.
- Krumova, K.; Greene, L. E.; Cosa, G. Fluorogenic α -Tocopherol Analogue for Monitoring the Antioxidant Status within the Inner Mitochondrial Membrane of Live Cells. *J. Am. Chem. Soc.* **2013**, *135* (45), 17135–17143.

1 Introduction

“It was certainly a curious sight to see the tube instantaneously lighted up when plunged into the invisible rays: it was literally darkness visible. Altogether the phenomenon had something of an unearthly appearance.”

–George Gabriel Stokes, On the Change of Refrangibility of Light¹

The use of fluorescence as an analytical technique dates back to the mid 1500s, when Spanish physician, Nicolás Monardes reported a bluish glow to the infusion of water and a wood sample from Mexico (*Eysenhardtia polystachya*) thought to cure urinary diseases.² This bluish glow was the fluorescence of matlaline, a natural product found in this wood. He suggested that only wood samples that render the water bluish were genuine while those that did not were false. While Monardes did not comprehend what this “glow” was, it allowed him to identify and distinguish samples of wood with curing properties.

Nearly 5 centuries later, in 2014, Eric Betzig, Stefan Hell, and William Moerner won the Nobel Prize in Chemistry for “the development of super-resolved fluorescence microscopy.”³ Their techniques have enabled the observation of single fluorescent molecules (fluorophores) which were previously impossible to resolve with conventional tools due to the diffraction limit. Their achievement has paved the road to study the dynamics of individual molecules, shedding light on numerous phenomena such as live cell dynamics,^{4,5} bacterial cell biology,⁶ DNA self assembly,⁷ electron transfer⁸ and protein dynamics and distribution,^{9,10} among others. While even the concept of molecules was unthinkable of in the 1500s, Monardes’ fundamental idea of using a fluorophore (or in his case, an ensemble of fluorophores) to study a system, remains much the same today.

The development of fluorescent molecules has become a central part under the umbrella of advances in fluorescence techniques, and one that rests upon the shoulders of chemists. These molecules may be used simply as reagents for labeling cell organelles or catalysts, or as probes to report on reactions of interest. Fluorescent dye photo-physical properties such as brightness and absorption/emission wavelength have been tailored to probe the questions

being asked. In parallel with the steady improvement and increased sophistication of fluorescence microscopy, is the ongoing quest for more sensitive fluorescent probes, undergoing reactions with specific analytes of interest, or mimicking biological molecules.¹¹⁻¹⁶

Fluorescence imaging is particularly suited to study chemical and biological processes in a non-invasive manner, both *in vitro* and *in vivo*.^{5,13,17,18} In conjunction with suitable fluorescent probes, it allows for the direct visualization of specific reactions of interest offering high sensitivity and spatio-temporal resolution.^{17,19}

From a chemical standpoint, our own interest lies in deciphering the complex relationship existing between antioxidant status, and physiological phenomena ultimately bridging/reconciling the chemistry with the biology of reactive oxygen species. The work described in this thesis highlights our progress in developing fluorescent probes, in combination with fluorescence spectroscopy, to monitor bio-redox reactions in real time. In particular, this thesis will discuss the development of highly sensitive probes based on Coenzyme Q10 to report on redox reactions of quinones (Chapter 2), based on α -tocopherol (a member of the vitamin E family) to report on basal levels of lipid peroxidation in cells (Chapters 3 and 4), and based on electrophiles to report on nucleophilic additions to aldehydes (Chapter 5).

The intent of this introduction is to give an overview of the core concepts and techniques involved in fluorogenic probe design, as well as the incentive to build fluorogenic probes to study bio-redox reactions and the antioxidant status in cells. First, an overview of reactive oxygen species (ROS), lipid peroxidation, and the various physiological roles of Vitamin E and Coenzyme Q10 will be given. Fluorescence and fluorescence quenching will then be summarised to provide the concepts needed to understand the design of fluorogenic probes in general. The details of designing fluorogenic probes will then be discussed, including an introduction of quenching pathways such as photo-induced electron transfer, that may be used as an off/on molecular switch and is used in many of the probes presented in this thesis. Lastly, a review of fluorogenic probes used for reaction screening will be presented.

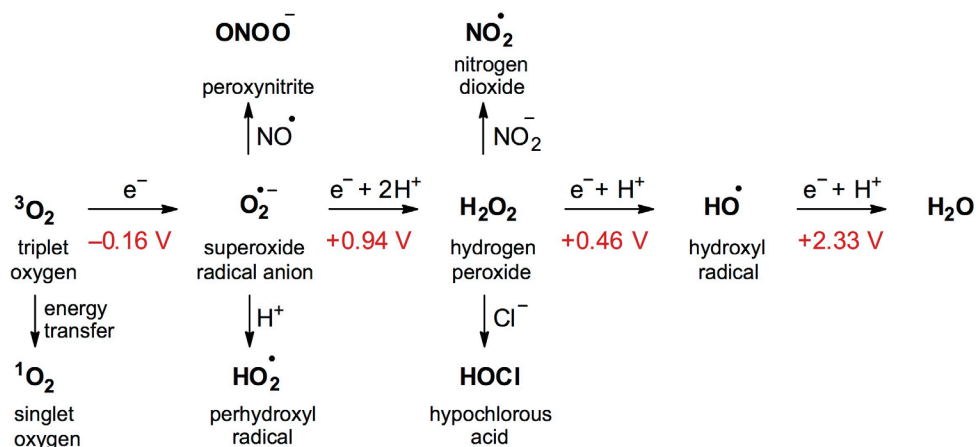
1.1 Chemistry of ROS and Antioxidants

Reactive oxygen species (ROS) are formed from the incomplete reduction of oxygen, as well as from the by-products of their reactions.²⁰ The implication of ROS to various physiologies and pathologies is a complex topic, and much remains to be understood of their role in life. Overproduction of ROS has been linked with several pathologies such as neurodegenerative diseases, and inflammation, while lower levels of ROS have been observed to be beneficial.²¹⁻²⁴ This section will discuss how ROS are produced and will give an overview of lipid peroxidation, how it is inhibited, and the influence of some vital small molecules, namely coenzyme Q10 and Vitamin E. By understanding the chemistry of these molecules, we can exploit them in the development of fluorogenic probes to detect ROS and report on the antioxidant status *in vitro* and *in vivo*.

1.1.1 Reactive oxygen species

Ground state molecular oxygen with a triplet multiplicity ($^3\text{O}_2$), while mostly unreactive to ground state organic molecules with paired electrons, is poised for single electron reduction by organic radicals or transition metals with unpaired electrons. This one electron reduction results in the formation of superoxide radical anion ($\text{O}_2^{\bullet-}$). While already a ROS itself, once formed, $\text{O}_2^{\bullet-}$ can continue to react to form other ROS. Further reduction of $\text{O}_2^{\bullet-}$ gives hydrogen peroxide (H_2O_2), which can be further reduced via Fenton chemistry to give the most reactive oxygen radical, hydroxyl radical (OH^{\bullet}) and water. These reductive products of oxygen are all more oxidizing than molecular oxygen as indicated by their redox properties (Scheme 1.1), and are therefore potentially more reactive towards bio-molecules.^{14,25}

Scheme 1.1 Formation of ROS via energy transfer or redox processes. Potentials given are versus Standard Hydrogen Electrode (SHE). Reprinted with permission from reference 14.¹⁴



Most endogenous ROS are produced in the mitochondrion as by-products of redox reactions occurring in the electron transport chain. Indeed, 0.1-2% of oxygen is converted to superoxide radical anion ($\text{O}_2^{\bullet-}$) during respiration *in vitro*. Significant $\text{O}_2^{\bullet-}$ production can occur when mitochondria are not making ATP (high proton motive force) and when the ratio of reduced:oxidized electron carriers is high (e.g. NADH:NAD⁺ and ubiquinol:ubiquinone).^{26,27}

ROS production can also stem from exogenous sources such as UV radiation, drug metabolism, and bio-redox reactions. The most prevalent ROS found in living systems are singlet oxygen (${}^1\text{O}_2$), superoxide radical anion ($\text{O}_2^{\bullet-}$), hydroxyl radical (OH^\bullet), hydrogen peroxide (H_2O_2), and lipid peroxyl radicals (LOO^\bullet).

Once formed, ROS may oxidize vital bio-molecules such as proteins, DNA, and lipids, effectively altering their structure and hence their function.^{20,28} Proteins, following attack by ROS, may undergo conformational changes affecting their activity. Oxidation of cysteine residues acting as redox-switches can result in structural associated activity changes due to formation of disulfide bonds.²⁹ In addition, oxidation of proteins may lead to formation of carbonyl derivatives along their backbone, whose formation is used as a maker of oxidative stress in general.³⁰

Given that most endogenous ROS are produced in the mitochondrion, mitochondrial DNA is prone to attack by ROS. Oxidation of mitochondrial DNA results in compromised

mitochondrial function which in turn can lead to further ROS production.^{28,30} In addition, ROS may damage nuclear DNA where aging cells have been observed to have increased levels of oxidized nuclear DNA.³⁰

Oxidation of lipids, termed “lipid peroxidation,” can result in a chain reaction of lipid autoxidation causing damage to the cell lipid milieu. This chain reaction and its implications will be discussed at length in the next section.

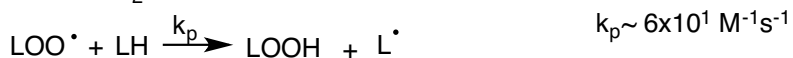
The role of ROS in biological systems is highly controversial. According to the “free radical theory of aging,” advanced by Denham Harman in 1956, ROS are deleterious molecules directly responsible for aging and disease.³¹ While once a long-held belief, this hypothesis is currently under revision.^{24,32} Indeed, overproduction of ROS is associated with many diseases and pathologies such as neurodegenerative diseases, inflammation and cancer.^{22,23,30,33} However, controlled production and release of ROS is critical for maintaining homeostasis, and enhancing the defence mechanisms of the cell.^{21,24} The development of probes to highlight the beneficial/deleterious effects of ROS would provide a step forward in understanding the complex physiological role they play in life.

1.1.2 Lipid peroxidation

Polyunsaturated fatty acids present in membranes are particularly susceptible to ROS elicited damage due to the relatively weak H-C bond adjacent to the unsaturation. Lipid peroxidation products can lead to the loss of fluidity and permeability of bio-membranes eventually compromising the cell.³⁴ In addition, by-products of lipid peroxidation include α,β -unsaturated aldehydes: highly electrophilic molecules capable of undergoing Michael addition with DNA bases, amino acids of proteins, and glutathione.³⁵⁻³⁷ It is therefore not surprising that lipid peroxidation and its reaction by-products are associated with both disease and signalling pathways.³⁷⁻⁴⁰

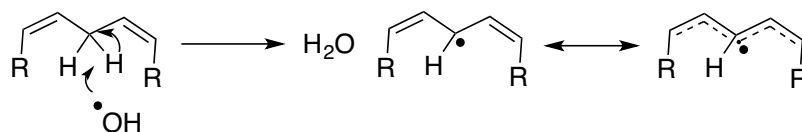
Lipid peroxidation takes place through a free radical chain reaction, and can be divided into 4 key steps: 1) initiation, 2) propagation, 3) termination, and 4) (in the presence of an inhibitor antioxidant) inhibition (Scheme 1.2).⁴¹

Scheme 1.2 Reactions and their rate constants for the 4 steps of lipid peroxidation: Initiation, Propagation, Termination and Inhibition. LH represents a polyunsaturated fatty acid. (k_{ox} ,⁴¹ k_p ,⁴¹ k_t ,⁴¹ k_{inh} ,⁴² k_{coup} ⁴³)

Initiation**Propagation****Termination****Inhibition**

Lipid peroxidation is initiated by an H-atom abstraction at the bis-allylic position of a polyunsaturated acid by a source of ROS (such as $\text{OH}\cdot$), to give a carbon centred radical $\text{L}\cdot$. The relatively weak bond dissociation energy (BDE) of the bis-allylic H-C bond (estimated at 80 kcal/mol)⁴⁴ makes it particularly vulnerable to abstraction compared to H-C bonds of saturated lipids (100 kcal/mol).⁴⁴ This low BDE is due to delocalization and thus stabilization of the resulting radical with the adjacent unsaturations (Scheme 1.3).

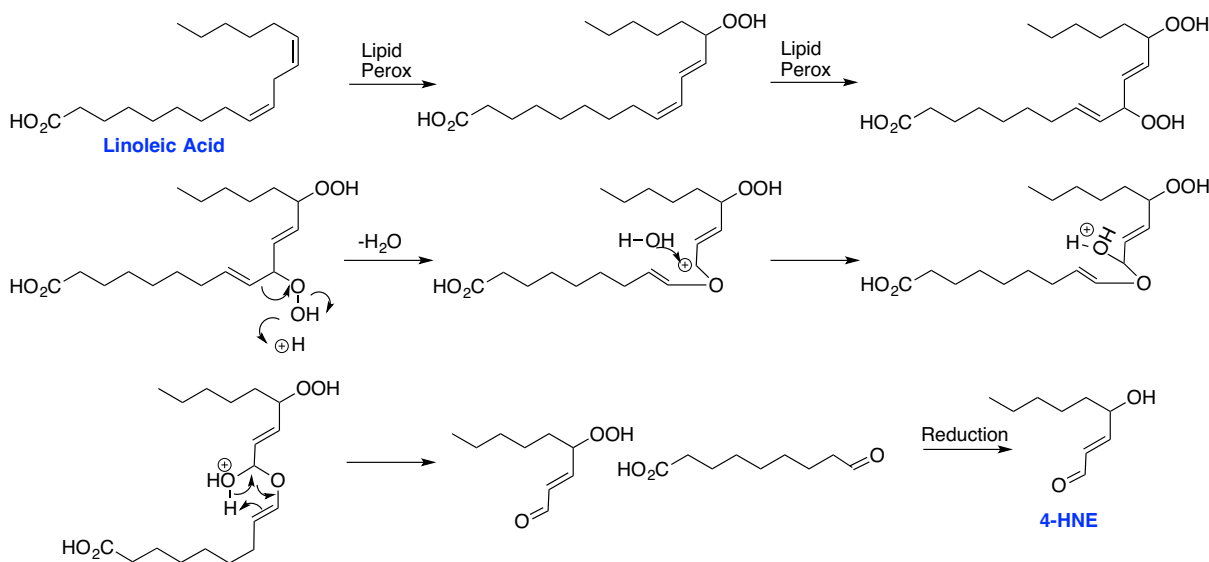
Scheme 1.3 H-atom abstraction by a hydroxyl radical and resulting stabilization of a polyunsaturated fatty acid.



Once formed, $\text{L}\cdot$ may propagate the free radical chain reaction. Molecular oxygen first reacts at diffusion controlled rates with $\text{L}\cdot$ to give a lipid peroxy radical, $\text{LOO}\cdot$.^{41,45} This newly formed lipid peroxy radical may abstract a hydrogen atom from another lipid, LH, to give $\text{L}\cdot$

and LOOH. Once formed, L^\bullet can continue the chain reaction. H-atom abstraction by LOO^\bullet is relatively slow and consequently the rate determining step of the chain reaction.⁴¹ LOOH may additionally decompose to generate new ROS further propagating the chain reaction (LO^\bullet and OH^\bullet). LOOH may also further oxidize and subsequently fragment to generate highly reactive aldehydes such as 4-hydroxy-2-nonenal (4-HNE, Scheme 1.4)⁴⁶

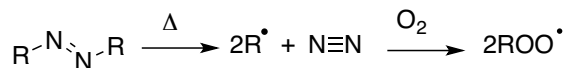
Scheme 1.4 Free radical attack and subsequent fragmentation of linoleic acid into 4-HNE via Hock fragmentation and reduction.^{41,47}



In a laboratory setting, lipid peroxidation can be initiated by use of a radical initiator to control the rate of ROS formation.^{48,49} The thermolysis of azo-compounds is one such method to generate peroxy radicals.⁴⁹⁻⁵¹ Azo-compounds thermally decompose by first order kinetics to give two carbon centred radicals (R^\bullet), releasing N_2 (Figure 1.1 A). Once formed, the carbon centred radicals rapidly react with oxygen to give peroxy radicals, ROO^\bullet .⁴⁵ The rate constant of initiation can be determined using the Arrhenius equation (Equation 1.1) at a given temperature, T , where k_i is the rate constant of initiation, E_a is the activation energy, and A is the pre-exponential factor. Lipophilic radical initiators used in the next chapters are given with their respective E_a , A and their calculated k_i determined at 37 °C (Figure 1.1 B).

$$k_i = Ae^{\frac{-E_a}{RT}} \quad \text{Equation 1.1}$$

A



B

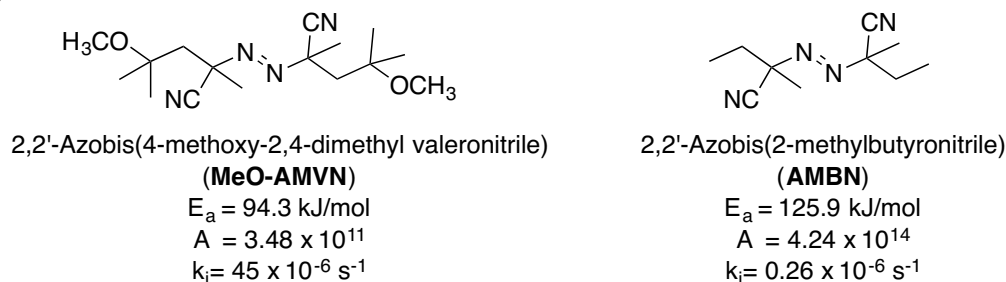


Figure 1.1 A) Thermolysis of azo compounds and subsequent reaction with oxygen. B) Structures of lipophilic azo compounds used in this thesis and their decomposition activation energy (E_a), pre-exponential factor (A) and calculated rate constants (k_i) at 37 °C.^{52,53}

Under steady state conditions, the rate of generation (R_g) can be determined from the calculated k_i with Equation 1.2, where e is the escape fraction of radicals which is dependent on the solvent used.^{54,55} Only radicals which escape the solvent cage may next react with oxygen and initiate peroxidation.

$$R_i = R_g = 2k_i e [\text{Azo compound}] \quad \text{Equation 1.2}$$

Termination of the chain reaction occurs when two LOO^\bullet couple or disproportionate to form non-radical species.⁴¹

Antioxidants prevent lipid peroxidation chain reactions from taking place in one of two ways: 1) via a reduction of the rate of initiation of lipid peroxidation (preventative antioxidants), and 2) via interference with the propagation steps of the chain reaction (chain-breaking antioxidants). Chain-breaking antioxidants (AOH) are only effective when the rate of lipid peroxy radical scavenging by AOH is significantly higher than the rate of H-atom abstraction from a polyunsaturated fatty acid of interest.⁵⁶ In addition, both the antioxidant

and its newly formed radical product must not be toxic and must not react with oxygen or lipids as they would otherwise further propagate the chain reaction.⁵⁷ Phenolic compounds are highly effective chain breaking antioxidants due to their large rate constants for H-atom transfer to lipid peroxy radicals (inhibition rate constant $k_{inh} \sim 0.1-10 \times 10^5 \text{ M}^{-1}\text{s}^{-1}$).⁵⁸

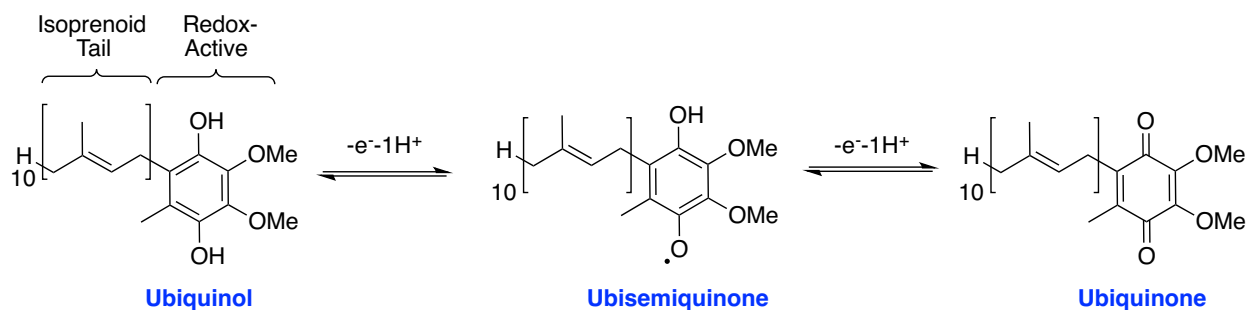
Phenolic compounds inhibit lipid peroxidation by scavenging peroxy radicals via H-atom abstraction of the phenolic group, resulting in a phenoxyl radical. This radical then may couple to a second peroxy radical to form a non-radical product. When the rate of initiation of lipid peroxidation (R_i) is constant, the consumption of AOH is zeroth order in antioxidant concentration and is dependent on R_i and the stoichiometric number of peroxy radicals scavenged by the antioxidant, n (Equation 1.3). In homogeneous non-polar solvents, phenolic antioxidants typically scavenge two peroxy radicals (i.e. $n=2$).⁴²

$$\frac{\delta[AOH]}{\delta t} = -\frac{R_i}{n} \quad \text{Equation 1.3}$$

1.1.3 Ubiquinol

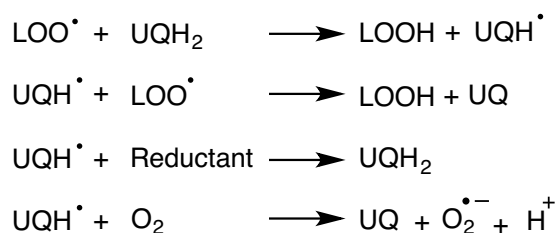
Due to the highly reductive nature of the mitochondrion, the mitochondrial membrane is particularly vulnerable to lipid peroxidation. Consequently, mitochondria dysfunction resulting from oxidative stress has been associated to several diseases.⁵⁹⁻⁶² Ubiquinol, (also known as ubiquinone in its oxidized form, or coenzyme Q10) can inhibit oxidative damage in mitochondrial membranes, and is the only endogenously synthesized lipophilic antioxidant in humans.^{63,64} Situated in the hydrophobic core of the inner mitochondrial membrane, ubiquinol is also involved in the electron transport chain as a mobile carrier of electrons.⁶⁵

Ubiquinol bears a quinoid head group which imparts its antioxidant ability, as well as a long hydrophobic group (isoprenoid chain), to impart lipophilicity (Scheme 1.5). It is found in all intracellular membranes, with especially high concentrations in mitochondria, golgi vesicles and lysosomes, as well as in plasma membranes and lipoproteins.⁶⁴ It can exist in three different redox states: ubiquinol (reduced), ubisemiquinone radical (1 electron oxidation from ubiquinol), and ubiquinone (2 electron oxidation from ubiquinol).

Scheme 1.5 The structure of ubiquinol and its three redox states.

1.1.3.1 Direct antioxidant action of ubiquinol

The antioxidant ability of ubiquinol is very complex and depends on all three redox forms. Ubiquinol may directly inhibit lipid peroxidation by intercepting chain carrying lipid peroxy radicals via H-atom abstraction of the quinolic hydrogen ($k_{inh} \sim 3 \times 10^5 \text{ M}^{-1} \text{ s}^{-1}$).⁶⁶ This reaction gives the ubisemiquinone radical. The fate of this newly formed radical is uncertain and depends highly on the local oxidative state (Scheme 1.6). The ubisemiquinone radical can react with a second lipid peroxy radical to give ubiquinone, or it can be recycled back to ubiquinol by a reducing agent present. Alternatively, it can react with oxygen to give superoxide radical anion and ubiquinone (Scheme 1.6). In short, the ubisemiquinone radical may act as an antioxidant by trapping lipid peroxy radicals, or act as a pro-oxidant by producing superoxide radical anion. Ubiquinone, bearing no phenolic hydrogen atoms, is not a chain breaking antioxidant.

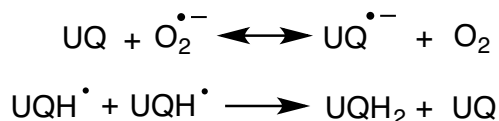
Scheme 1.6 The formation and fate of the ubisemiquinone radical (UQH^\bullet).⁶⁶

Given the high abundancy of ubiquinol present in mitochondria, its oxidized form, ubiquinone, can be effectively reduced back to ubiquinol by the electron transport chain (*vide*

infra). The redox-reversibility of ubiquinol/ubiquinone prolongs its ability to inhibit lipid peroxidation. However, there are also considerable concentrations of ubiquinol in other organelle membranes, as discussed above, where there are no electron transport chains to reduce ubiquinone. Endogenous concentrations of ubiquinol in these membranes would exert a small and even negligible effect on the oxidative status unless another source of reduction exists.

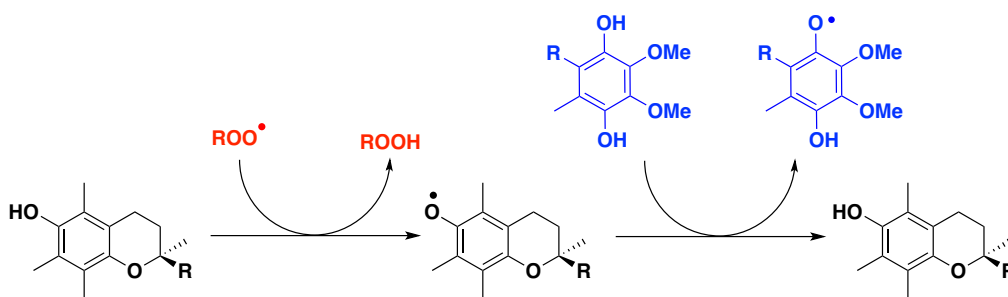
While the ubisemiquinone radical may react with oxygen to form superoxide radical anion ($O_2^{\bullet-}$) and ubiquinone, this reaction is reversible, partly owing to the similar reduction potentials (-230 mV vs -160 mV vs SHE for ubiquinone and oxygen respectively), where ubiquinone may directly react with $O_2^{\bullet-}$ to generate the semiquinone radical (Scheme 1.7).^{66,67} Two semiquinone radicals can then disproportionate to give one molecule of ubiquinone and one molecule of ubiquinol, thus providing a route of regeneration in non-mitochondrial membranes. The ability to scavenge $O_2^{\bullet-}$ may also play a pivotal role in the overall antioxidant ability of ubiquinol/ubiquinone *in vivo*.⁶⁸

Scheme 1.7 Reversible reaction of ubiquinone (UQ) and superoxide radical anion ($O_2^{\bullet-}$), and disproportionation of the ubisemiquinone radical.⁶⁶



1.1.3.2 Indirect antioxidant action: Synergy with Vitamin E

Ubiquinol can also prevent lipid peroxidation indirectly by regenerating α -tocopherol, the most active and abundant form of Vitamin E in human tissue (*vide infra*, Section 1.1.4). Ubiquinol reacts with peroxy radicals at about an order of magnitude slower than α -tocopherol in homogeneous solution, yet their efficacy *in vivo* are observed to be similar.^{69,70} This is likely due to cooperation between ubiquinol and α -tocopherol, where ubiquinol can reduce the tocopheroxyl radical back to its active, reduced form (Scheme 1.8).^{71,72} *In vivo*, this effect is observed through faster consumption of ubiquinol over α -tocopherol, creating a sparing effect on α -tocopherol.^{73,74}

Scheme 1.8 Mechanism of regeneration of α -tocopherol by ubiquinol.^{71,75}

1.1.3.3 Role of ubiquinol in the electron transport chain

Ubiquinol is also a cofactor involved in the electron transport chain (Figure 1.2). The lipophilicity and redox reversibility of the ubiquinol/ubiquinone redox couple makes it perfectly suited as a mobile transporter of electrons and protons through the mitochondrial membrane. Through a series of relay reactions, electrons are transferred to molecular oxygen, reducing it to water and releasing energy along the way. This energy is stored as a proton gradient between the mitochondrial matrix and the intermembrane space and ultimately in the form of adenosine triphosphate (ATP).⁶⁵

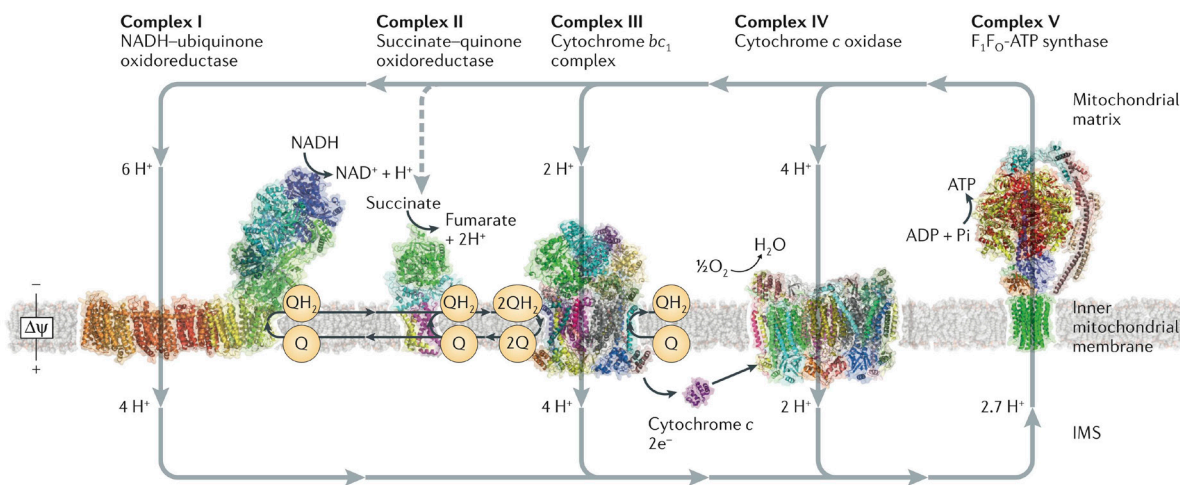
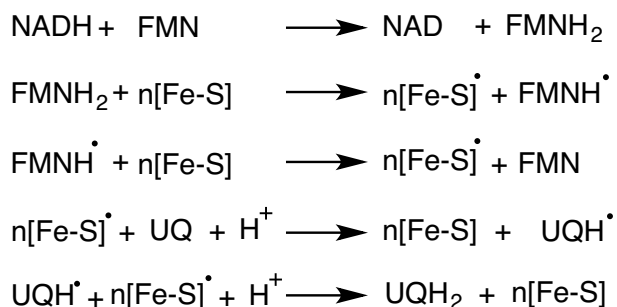


Figure 1.2 The five complexes involved in the electron transport chain. Reprinted by permission from Macmillan Publishers Ltd: Nature Reviews: Molecular Cell Biology, Sazanov, L. A. Nature Publishing Group 2015, 16 (6), 375–388. Copyright (2015).⁷⁶

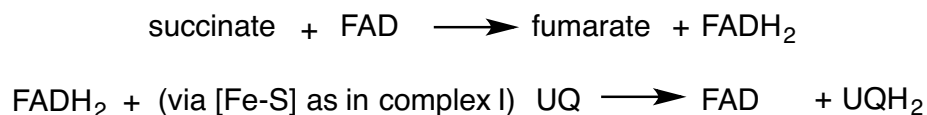
The electron transport chain consists of five complex domains, where ubiquinone plays an essential role in the first three. In Complex I (NADH-ubiquinone oxidoreductase) the overall redox reaction is the reduction of ubiquinone by NADH to give ubiquinol and is accompanied by the translocation of 4 protons producing a proton gradient (Scheme 1.9).^{65,76} Specifically, NADH is oxidized by flavin mononucleotide (FMN) to give FMNH₂ which then undergoes 2 one electron oxidations (via electron transfer) to a series of iron-sulfur clusters present in Complex I. The ‘electron wire’ iron clusters then reduce ubiquinone via two single electron reductions to first give ubisemiquinone and then ubiquinol which may freely diffuse through the membrane to Complex III.

Scheme 1.9 Sequence of redox reactions involved in Complex I.^{65,76}



Complex II (succinate dehydrogenase) also delivers electrons to the quinone pool, effectively reducing ubiquinone to ubiquinol (Scheme 1.10) to deliver electrons to Complex III, and couples the citric acid cycle to the electron transport chain.⁶⁵ Simplified, succinate is oxidized by flavin adenine dinucleotide (FAD) to give FADH₂ and fumarate. FADH₂ then transfers electrons via iron-sulfur clusters to ubiquinone to give ubiquinol. Unlike Complex I however, no protons are transported.

Scheme 1.10 Sequence of redox reactions involved in Complex II.⁶⁵



In Complex III, electrons from Complexes I and II are delivered by ubiquinol, where the reduction of cytochrome c and translocation of four protons occurs.⁶⁵ The reaction mechanism for the redox processes occurring in Complex III is known as the Q-cycle (Figure 1.3). Here ubiquinol binds to cytochrome b of Complex III and is oxidized to ubiquinone by both a Rieske iron-sulfur protein and heme (one electron each). The Rieske protein then diffuses to cytochrome c1 subunit where it reduces cytochrome c (which is re-oxidized in Complex IV upon the reduction of oxygen), and causes a release of a proton into the intermembrane space. The other reduced heme effectively reduces a bound molecule of ubiquinone to ubisemiquinone and causes a second proton to release. The Q-cycle then repeats to reduce the newly formed ubisemiquinone to ubiquinol. The overall reaction for Complex III is thus the oxidation of two equivalents of ubiquinol, the reduction of one equivalent of ubiquinone, the reduction of two equivalents of cytochrome c, and the translocation of four protons.

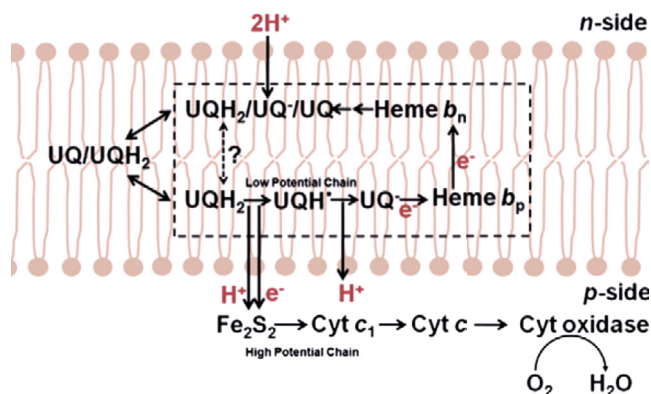


Figure 1.3 The Q cycle of Complex III in the electron transport chain. Reprinted from BBA – Bioenergetics, 1807, Cramer, W. A.; Hasan, S. S.; Yamashita, E The Q cycle of cytochrome bc complexes: A structure perspective, 788-802, Copyright (2011), with permission from Elsevier.⁷⁷

The triple role of ubiquinone as antioxidant, electron transporter and proton transporter makes it a complex molecule to study *in vivo*, thus much remains to be understood in its role in disease. Not surprisingly, mitochondrial deficiencies in ubiquinol are associated with pathologies linked with both mitochondrial dysfunction and oxidative stress such as Parkinson's Disease.⁷⁸ Indeed, research by Murphy and coworkers show promising

therapeutic results with a mitochondrion-targeting form of ubiquinone, Mito-Q,⁷⁹ for example in treating obesogenic rats⁸⁰ and renal ischemia–reperfusion in mice.⁶²

Tools to de-convolute the antioxidant activity from electron transport would have a constructive effect on the development of therapeutics for such diseases. In particular, the development of probes based on ubiquinone, and their subsequent imaging *in vitro*, would provide a real-time and non-invasive approach to elucidate the complex redox pathways of ubiquinone in biological systems.

1.1.4 Vitamin E

Lipid peroxidation and the resulting damage to organelle membranes is also inhibited by Vitamin E. Vitamin E represents two classes of fat soluble, chain-breaking antioxidants: tocopherols and tocotrienols that are both synthesised by plants (Figure 1.4). These classes of compounds are characterized by a chromanol head-group which is responsible for their high antioxidant activity, and a phytyl chain that brings about lipid membrane partitioning. Tocopherols and tocotrienols differ in their saturation of the phytyl tail which is responsible for the orientation of the molecule in membranes. The most active form of vitamin E is α -tocopherol ($k_{\text{inh}} \sim 3 \times 10^6 \text{ M}^{-1}\text{s}^{-1}$).⁴² It is the most common form found in human tissue.

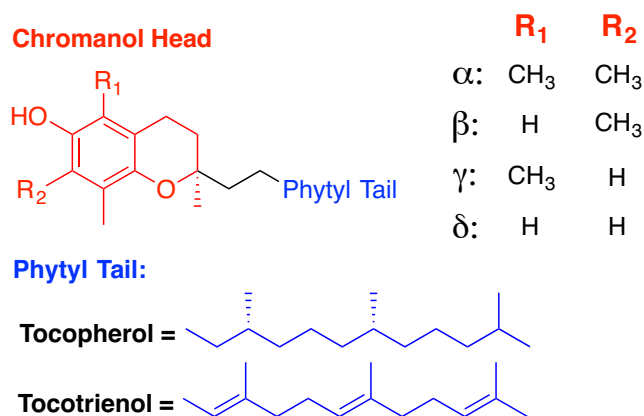


Figure 1.4 Structure of Vitamin E compounds.

1.1.4.1 Antioxidant action of Vitamin E

The high antioxidant activity of Vitamin E can be attributed to both substituent effects and stereoelectronic effects on the bond strength of the phenol. As described earlier, to be an effective chain-breaking antioxidant, a compound must competitively scavenge lipid peroxy radicals to form closed shell lipid hydroperoxides (LOOH) and a non-toxic phenoxyl radical. The rate constant for this scavenging must be greater than the rate of chain propagation (i.e. the rate of LOO^\bullet reacting with LH) where the rate depends on the O-H bond strength of the phenol.

The bond strength of the phenol is given by the difference in energy between the phenol and the resulting phenoxyl radical.⁸¹ Electron withdrawing substituents such as esters, CN, and NO_2 are stabilizing to the electron rich phenol, but upon H-atom abstraction, are destabilizing to the resulting electron deficient phenoxyl radical. This effect causes a higher BDE relative to unsubstituted phenol (Figure 1.5).⁸¹ Electron donating groups on the other hand, such as methoxy, destabilize the phenol, but stabilize the resulting phenoxyl radical, resulting in a lower BDE. The stabilization of the phenoxyl radical by electron donating groups can be attributed to hyperconjugation (as is the case for alkyl substituents), or via resonance (electron delocalization, as is the case for alkoxy substituents). The large density of alkyl groups and the *para*-alkoxy moiety on the chromanol head group of Vitamin E, thus lower the BDE compared to phenol (74.8 kcal/mol vs 86.7 kcal/mol calculated in gas phase),^{82,83} and enhance the antioxidant activity.

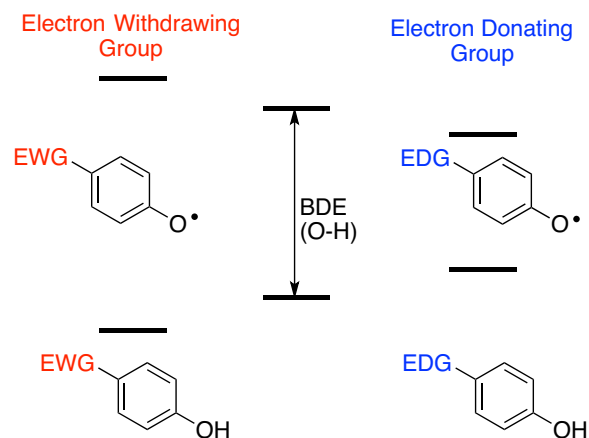


Figure 1.5 Effect of substitution of a phenol with either electron withdrawing groups (EWG) or electron donating groups (EDG), on the bond dissociation energy (BDE).⁸¹

Stereoelectronic effects of *para*-substituents also play a role in the BDE of the phenol antioxidant.⁴² Favourable overlap between the p-type lone pair of electrons on the *para*-heteroatom, and the semi-occupied molecular orbital (SOMO) of the phenoxyl radical affects the stability of the phenoxyl radical and thus the BDE. The extent of overlap between the orbitals depends on the orientation of the p-orbital of the *para*-heteroatom. The orientation can be characterized by the dihedral angle (θ) between the heteroatom p-orbital and a plane perpendicular to the aromatic plane and by the dihedral angle (θ') between the heteroatom-R bond and the aromatic plane (where $\theta = \theta'$, Figure 1.6). Overlap and thus stabilization is maximized when $\theta = 0^\circ$, and is at a minimum when $\theta = 90^\circ$. The chromanol structure of vitamin E, which locks the *para*-heteroatom in place through the 6-membered ring, gives a dihedral angle of 17° . When compared to a phenol with analogous substituents, but without the *para*-heteroatom locked in place as is the case for 4-methoxy-2,3,5,6-tetramethylphenol, the dihedral angle is 89° . Determined by Ingold and coworkers,⁵⁸ the BDE for these compounds were estimated at 80 and 83 kcal/mol respectively, based on a 10-fold reduction in reactivity of the latter.^{58,84}

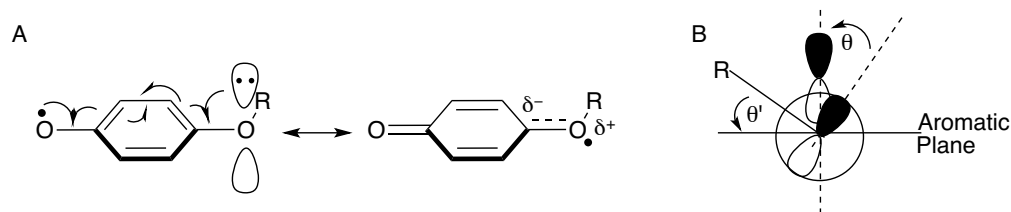


Figure 1.6 A) Stabilization of the phenoxyl radical by a *para* oxygen atom B) Schematic of the overlap and thus stabilization of the phenoxyl radical which is dependent on θ .⁴²

1.1.4.2 Role of the phytyl tail on antioxidant activity

While the chromanol head group is responsible for reaction with ROS, the phytyl tail of Vitamin E is responsible for partitioning into lipid membranes. Localization of Vitamin E in membranes and its mobility are also factors which determine its radical scavenging activity. The lipophilic phytyl tail of Vitamin E allows for preferential partitioning into membranes to access lipophilic peroxy radicals formed as a result of lipid peroxidation, which would otherwise be inaccessible by water soluble antioxidants. The more polar chromanol head group can allow access to the more polar regions of the membrane (closer to the phosphoesters and lipid-water interface) where it may interact with aqueous reductants such as ascorbic acid prolonging the life of Vitamin E (via reduction of the chromanoxyl radical by ascorbate).^{85,86}

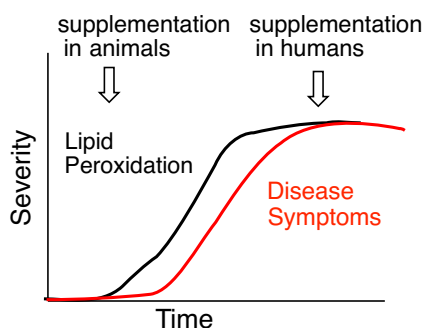
The phytyl tail of Vitamin E is also responsible for its decreased reactivity in membranes when compared to the single carbon chain analogue, 2,2,5,7,8-pentamethyl-6-hydroxychromanol (PMHC). While in homogeneous solution their reactivity is similar, in membranes, PMHC is more effective in scavenging hydrophilic (about 8-fold more effective) and lipophilic radicals (about 4-fold).⁴⁸ Thus, the phytyl tail reduces the overall mobility in membranes.^{48,87}

1.1.4.3 Vitamin E as a therapeutic

The antioxidant properties of Vitamin E make it a promising candidate as a therapeutic agent for treatment of disorders associated with oxidative stress.^{88,89} Animal models of disease have shown encouraging results when supplemented with Vitamin E,⁹⁰ while human models

have often been disappointing and even conflicting.^{24,91} Nevertheless, there are a couple of examples where treatment with Vitamin E has shown to be beneficial, such as for non-alcoholic fatty liver disease and for Alzheimer's disease.^{91,92} One speculation into the disappointing effect of Vitamin E on disease in humans is the delay of treatment in humans vs in animals (as described in Scheme 1.11).²⁴ Perhaps oxidative stress is important in the early onset of disease, but alleviation at later stages is futile. On the other hand, oxidative stress may be correlative with disease rather than causative. In these cases, treatment with Vitamin E may alleviate oxidative stress, but not alleviate the disease. Finally, supplementation with Vitamin E will evenly distribute through cells and tissues, yet oxidative damage may be localized to particular tissues, cells or organelles. Thus, while the antioxidant load may be sufficient, the local concentration of Vitamin E may be inadequate to quench oxidative stress 'hot spots'.⁹³

Scheme 1.11 Comparison of Vitamin E supplementation in animals vs in humans. Supplementation in humans typically occurs in older patients once symptoms have been detected (red), rather than when oxidative stress sets in (black).⁹⁴



Due to the conflicting and disappointing evidence of amelioration of oxidative stress by Vitamin E, controversy exists as to the molecular action of Vitamin E in humans. Vitamin E is a critical small molecule for human health. However, whether it is truly an antioxidant *in vivo* or rather a ligand for certain receptors and transcription factors is debated.^{95,96} For example, it has been reported that α -tocopherol is an inhibitor of protein kinase C, a signalling molecule involved in the regulation of cell growth and differentiation, suggesting a non-antioxidant and perhaps ligand role. However, protein kinase C regulation is also affected by oxidative stress

and instead of observing a specific signaling interaction between protein kinase C and α -tocopherol, perhaps an antioxidant phenomenon is observed.

The apparent contrasting roles of Vitamin E make it an interesting molecule of study. While there is a wealth of information on its properties in homogeneous solution, its role in heterogeneous solution and *in vivo* remains very much unclear. The development of tools to study these molecules and their mechanism of action is therefore of critical need.

1.1.5 Monitoring ROS, lipid peroxidation, and redox reactions

There are several methods available to study lipid peroxidation, its effects, and antioxidant activity. These techniques include product studies aided by high performance liquid chromatography (HPLC) and mass spectrometry,^{46,97,98} reactivity studies with laser flash photolysis (LFP)^{99,100}, and characterization of product radicals by electron paramagnetic resonance (EPR).⁷⁵ These methods, while having provided valuable information on the mechanisms of lipid peroxidation and reactivity of antioxidants, are destructive. Furthermore, they are limited in providing information on the rate of ROS production (temporal resolution) and location of ROS production (spatial resolution). Fluorescence imaging, in combination with suitable fluorescent probes, overcomes some of these challenges. Furthermore, fluorescence imaging is compatible with studying processes *in vivo*, as it provides a non-invasive yet highly sensitive approach to detect bio-redox reactions.

The next sections will provide an overview of fluorescence and the techniques and concepts used to design fluorescent probes.

1.2 Fluorescence

Key to the development of fluorescent probes for reaction screening, is the ability to manipulate the photochemical and photophysical properties of a fluorophore such that it undergoes a detectable change upon reaction. These changes include an increase in fluorescence intensity (quenched to fluorescent: fluorogenic probes), a decrease in intensity (fluorescent to quenched), a shift in emission wavelength (ratiometric probes), or a change in fluorescence lifetime (also ratiometric). To understand the processes which may modulate

fluorescence intensity, lifetime, and wavelength to give the desirable properties of our probes, the fundamental photophysics must first be explained.

1.2.1 Excited state processes

Electromagnetic radiation (light) of sufficient energy is absorbed by a molecule, promoting an electron from the highest occupied molecular orbital (HOMO) to the lowest unoccupied molecular orbital (LUMO). During this process, transition rules indicate the spin multiplicity of the electron remains unchanged. Thus, excitation of molecules in their singlet ground state yields molecules with the excited electron residing in the LUMO antiparallel with respect to the electron remaining in the HOMO (S_n , Figure 1.7).

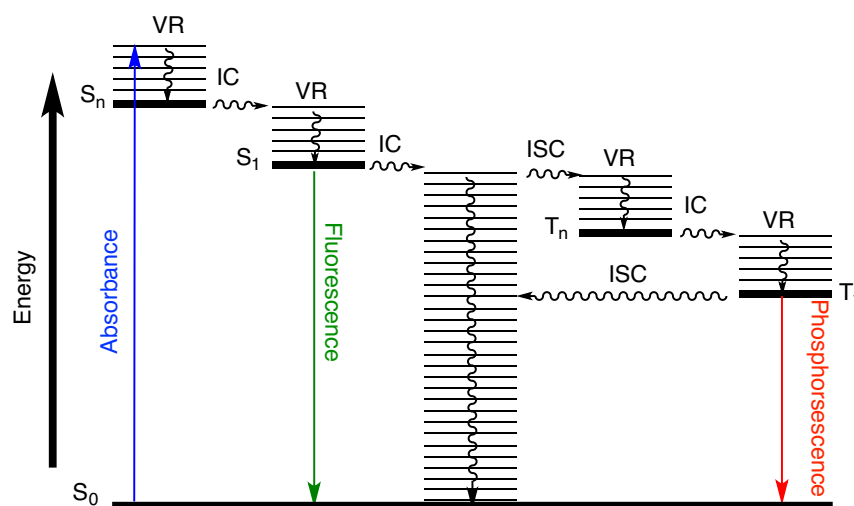


Figure 1.7 Photophysical processes represented in a Jablonski Diagram.¹⁰¹ VR denotes vibrational relaxation (VR), IC stands for internal conversion, and ISC stands for intersystem crossing.

Following excitation, energy dissipation must then follow and can occur via several mechanisms as outlined in the Jablonski diagram.¹⁰¹ Through internal conversion (IC, the relaxation between electronic states), and vibrational relaxation (VR, the vibrational relaxation within each electronic state), the molecule reaches the fundamental vibrational level of the lowest singlet excited state S_1 in an average time scale of a few picoseconds.

From S_1 , there are three main mechanisms for energy dissipation to the singlet ground state, S_0 : Internal conversion followed by vibrational relaxation, intersystem-crossing (ISC), or fluorescence.^{101,102} The rate constants of these processes will determine which mechanism the molecule will undergo to reach S_0 .

Intersystem-crossing occurs when a molecule undergoes a change in spin-multiplicity to give a triplet excited state (T_n). This process can result from overlapping triplet and singlet vibrational levels, or via spin-orbit coupling where the change in spin angular momentum of the electron is coupled to the change in orbital angular momentum (El Sayed's rule) and is often catalyzed by the presence of heavy atoms.¹⁰² This long lived process (nanoseconds to milliseconds timescale), due to the relaxation process being spin forbidden, may result in a radiative decay from T_1 to S_0 called phosphorescence (milliseconds to seconds time scale).

Fluorescence occurs when the molecule dissipates energy from S_1 to reach S_0 via the emission of a photon (typically nanoseconds timescale).¹⁰¹ The rate constant of fluorescence (k_{rad}), in combination with tuning the rate constants of all other energy dissipation pathways, is fundamental to the design and optimization of fluorogenic probes and will be discussed in the next section.

1.2.2 Fluorophore properties

The ability to tune the photo-physical properties of a fluorophore is of paramount importance in the design of fluorescent probes. For example, with this ability, we may modulate the fluorescence intensity of an 'off-on' probe which will ultimately determine the sensitivity of the probe.

The fluorescence intensity of a molecule is dictated by two photophysical properties: the extinction coefficient (ϵ) and the radiative rate constant (k_r). The extinction coefficient is an intrinsic property of a fluorophore that is dictated by its electronic structure. Its value is rendered by measuring the ability of a molecule to absorb a photon as given by Beer's Law (Equation 1.4) where A is the absorbance of the molecule, l is the pathlength of the light, and C is the concentration of the molecule.¹⁰²

$$A = \epsilon l C \quad \text{Equation 1.4}$$

The radiative rate constant, and its competition with all deactivation processes (k_{dec}) impacts the observed fluorescence intensity of a molecule. The probability of a molecule to undergo fluorescence is given by the fluorescence quantum yield (ϕ_f) which is defined as the ratio of photons emitted to photons absorbed. This value can also be determined from a ratio of the radiative rate constant and all deactivation rate constants (Equations 1.5-1.7).

$$\phi = \frac{k_r}{k_{dec}} \quad \text{Equation 1.5}$$

$$k_{dec} = k_r + k_{nr} \quad \text{Equation 1.6}$$

$$k_{nr} = k_{ISC} + k_{IC} + k_q[Q] \quad \text{Equation 1.7}$$

The average lifetime a molecule spends in the excited state before emitting a photon is a measurable quantity and is defined as the inverse of k_{dec} . Non-radiative decay processes (whose rate constant is defined as k_{nr}) include decay through internal conversion (k_{IC}), decay through intersystem crossing (k_{ISC}), or decay through reaction with a quencher ($k_q[Q]$).

The fluorescence quantum yield depends on the competition between a series of parallel decay processes as shown above. From Equations 1.5-1.7 we note that the fluorescence quantum yield becomes close to unity when $k_r \gg k_{nr}$ (i.e. fluorescence effectively outcompetes all other decay processes).

If the size of k_{dec} is mostly impacted by k_{nr} , however, most excited state fluorophores will decay without having emitted a photon. It is this photophysical/photochemical associated parameter, k_{nr} , that can provide the fluorescence modulation we require in designing fluorogenic ('off-on') probes. In the 'off' state, fluorescence will be quenched due to

competing decay pathways occurring ($k_{rad} \ll k_{nr}$) and in the 'on' state fluorescence will be restored, effectively out-competing non-radiative decay pathways ($k_{rad} \gg k_{nr}$).

1.2.3 Fluorescence quenching

The ability to tune non-radiative decay processes of a fluorophore is one of the key facets of designing fluorogenic probes. There are three main rate constants we can affect to out-compete, or under-compete with the rate of fluorescence. These are k_{ISC} , k_{IC} , and $k_q[Q]$.

1.2.3.1 Fluorescence quenching via intersystem crossing

To outcompete fluorescence, we may promote intersystem crossing. As mentioned in Section 1.2.1, intersystem-crossing involves the change in spin-multiplicity of the singlet excited state to generate a triplet excited state (T_n). While theoretically a spin-forbidden process, this process can be aided by heavy atoms (such as bromine or iodine) via spin-orbit coupling.¹⁰² Here, the spin angular momentum of the excited electron of the fluorophore couples with the orbital angular momentum of the heavy atom. The strong positive charge of the heavy atom nucleus can accelerate the approaching excited electron, thereby creating a strong magnetic moment as the result of the orbital motion. This strong magnetic moment accompanying an orbital jump favours the likelihood of spin-orbit coupling, and thus intersystem-crossing.

By increasing the likelihood of intersystem-crossing, the opportunity for the fluorophore to emit a photon will be decreased, and fluorescence will be quenched. This phenomenon may be observed upon the substitution of a boron-dipyrromethene (BODIPY) dye with heavy atoms.¹⁰³ Decoration of the BODIPY core with bromine and iodine decreases ϕ_f significantly for an otherwise fluorescent molecule (Figure 1.9). The issue with this quenching method is that the molecule, while no longer in S_1 , is still in an excited state. This excited triplet molecule may undergo phosphorescence, another form of radiative decay characterized by its longer wavelength and lifetime than that of fluorescence. Alternatively, it may sensitize molecular oxygen to form the highly reactive and oxidizing, singlet oxygen.^{103,104} It is for this reason,

that fluorophores decorated with heavy atoms such as bromine are often developed as photodynamic therapy agents to generate singlet oxygen at a wound site in the presence of light.

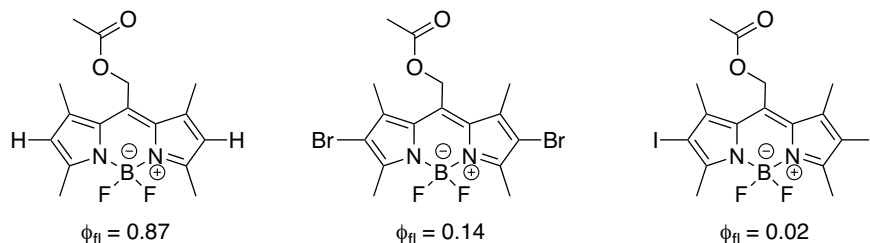


Figure 1.8 Effect of substitution with heavy atoms on the fluorescence quantum yield (ϕ_{fl}) of BODIPY dyes.¹⁰³

1.2.3.2 Fluorescence quenching via internal conversion

Deactivation of fluorescence may also occur through internal conversion. Encouraging deactivation via internal conversion typically requires modification of the dye backbone to promote a vibronic interaction such as the “loose bolt” effect (e.g. C-C bond stretching) and “free rotor” effect (e.g. C=C bond twisting).¹⁰² These effects are usually caused by stretching or twisting motions of substituents of an excited state molecule to dissipate the excess energy. Bending of the molecule in the excited state may also promote conjugation, resulting in a lower energy excited state configuration. Internal conversion to an energetically-hot ground state species may then proceed, which can outcompete with fluorescence. For example, in the case of *meso*-formyl BODIPY dyes, bending of the molecule takes place in the excited state to promote conjugation of the *meso*-formyl to one pyrrole moiety causing the other pyrrole moiety to shift out of the plane. Internal conversion to an energetically-hot ground state species then proceeds, which efficiently outcompetes emission (Figure 1.9).¹⁰⁵

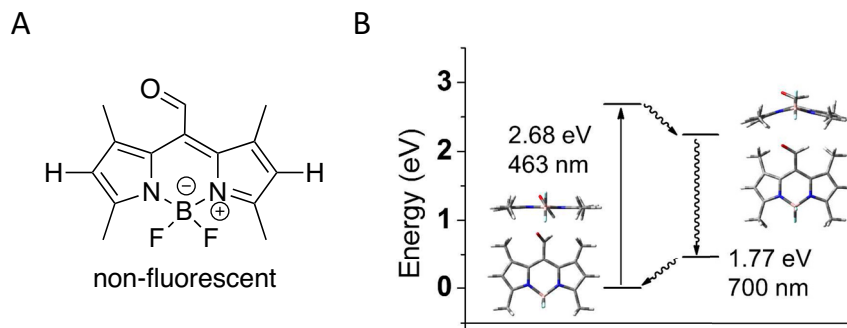


Figure 1.9 A) Structure of non-fluorescent *meso*-formyl BODIPY dye B) Calculated energy diagrams of *meso*-formyl dye in the ground and excited states. Adapted with permission from Lincoln, R.; Greene, L. E.; Bain, C.; Flores-Rizo, J. O.; Bohle, D. S.; Cosa, G. J. *Phys. Chem. B* 2015, 119 (13), 4758–4765. Copyright 2015 American Chemical Society.

1.2.3.3 Intermolecular fluorescence quenching, $k_q[Q]$

The addition of a known fluorescence quencher may outcompete fluorescence via, for example, electron transfer (discussed at length in Section 1.2.1). The ability of a molecule to quench the fluorescence of a fluorophore depends on the bimolecular quenching constant, k_q and the concentration of the quencher $[Q]$. One may determine the efficiency of a quencher by studying the intermolecular kinetics of the fluorophore and the quencher. This is performed by measuring the fluorescence lifetime (τ) of the fluorophore in the absence of a quencher and measuring the fluorescence intensity in the absence (I_0) and presence (I) of the quencher as given by the Stern-Volmer equation (Equation 1.8) where K_{sv} is known as the Stern-Volmer quenching constant.

$$\frac{I_0}{I} = 1 + k_q\tau[Q] = 1 + K_{sv}[Q] \quad \text{Equation 1.8}$$

Intuitively, this equation may be obtained by understanding the kinetics of the processes happening. During continuous illumination, the concentration of excited fluorophores reaches a steady state as given by:

$$\frac{\partial[F^*]}{\partial t} = f(t) - k_{dec}[F^*] = 0 \quad \text{Equation 1.9}$$

where $f(t)$ is the continuous illumination function. Equating Equation 1.9 for both the presence and absence (denoted by ‘0’) of a quencher (Equation 1.10), followed by rearrangement and substitution of intensity for $[F^*]$, we get the Stern Volmer Equation (Equation 1.11).¹⁰¹

$$f(t) - (k_r + k_{ISC} + k_{IC})[F_0^*] = f(t) - (k_r + k_{ISC} + k_{IC} + k_q[Q])[F^*] = 0 \quad \text{Equation 1.10}$$

$$\frac{I_0}{I} = \frac{k_r + k_{ISC} + k_{IC} + k_q[Q]}{k_r + k_{ISC} + k_{IC}} = 1 + \frac{k_q}{k_r + k_{ISC} + k_{IC}} [Q] = 1 + k_q \tau [Q] \quad \text{Equation 1.11}$$

While this section is related to intermolecular quenching, we may utilize a Stern Volmer analysis as a strategy for the design of fluorogenic probes where a quencher is covalently linked to a fluorophore. This analysis can provide experimental evidence to aid in the judicious choice of a quencher-fluorophore pair with optimized sensitivity thereby justifying the synthesis of a fluorogenic probe. To maximize sensitivity, we must outcompete fluorescence in one state such that $k_q[Q] \gg k_r$ and have fluorescence outcompete all other decay processes in the other state ($k_{nr} + k_q \ll k_r$). The next section will discuss the importance of maximizing the rate constant of quenching as well as the ways we can tune this parameter.

1.3 Design of Fluorescent Probes

Fluorescent probes often bear two segments: a reporter fluorophore and a receptor that undergoes a change or reaction of interest (i.e. the question you are studying). In their design, we must consider whether the receptor will act as a quencher (to modulate the fluorescence intensity) or whether the receptor is to be conjugated to the fluorophore (to modulate the emission wavelength). These two strategies of fluorescent probe design will be discussed in this section, as well as the mechanisms exploited to achieve the desired response.

1.3.1 Design of probes relying on photoinduced electron transfer

An effective quenching mechanism to consider in the design of fluorescent probes is photoinduced electron transfer (PeT). This mechanism is particularly effective when an ‘off’ or quenched state is desired prior to the reaction of interest, and an ‘on’ or fluorescent state is desired following the reaction. Molecules that behave according to this off/on scheme are referred to as “fluorogenic probes”. In essence, this process involves the transfer of an electron from an electron donor (D) to an electron acceptor (A) generating a geminate radical pair. The respective role (donor or acceptor) of the photo-excited fluorophore and the receptor is dependent on the reduction/oxidation potentials of both the fluorophore and the receptor.

When a fluorophore is photo-excited it becomes both a better electron acceptor and electron donor. While seemingly contradictory, this statement becomes obvious when considering the actual processes at play. Consider a photo-excited molecule in the gas phase as in Figure 1.10. An electron once residing in the HOMO is now promoted to the LUMO leaving a hole in the HOMO, and a higher energy electron in the LUMO. The partially empty HOMO causes the molecule to be a stronger oxidant (better electron acceptor), and the partially filled LUMO causes the molecule to be a stronger reductant (better electron donor) than the ground state molecule. Thus, the electron affinity (EA) is larger for the photo-excited molecule than the ground state (more energy released from accepting an electron), and the ionization potential (IP) is smaller for the photo-excited molecule than the ground state (less energy required to remove an electron):

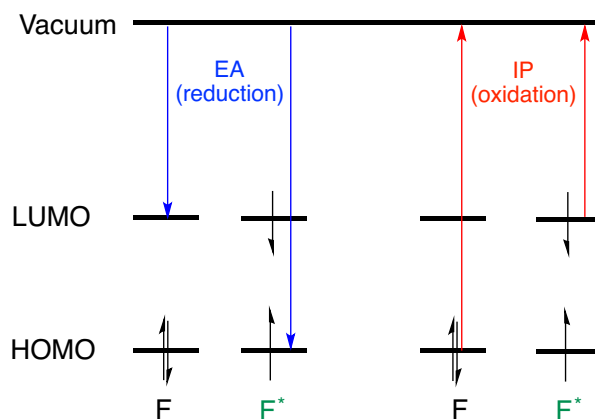


Figure 1.10: Comparison of electron affinity (EA) and ionization potential (IP) between a fluorophore in the ground state (F) and in the photo-excited state (F*) in the gas phase.¹⁰¹

1.3.1.1 Thermodynamics of PeT

For PeT to occur, electron transfer from the donor to the acceptor must be exergonic (i.e. the free energy of electron transfer, $\Delta G^{\circ}_{eT} < 0$). To determine which role (donor or acceptor) the fluorophore and quencher each play, the orbital energies of both molecules must be compared. Consider two scenarios: 1) Where the fluorophore is the donor and 2) where the fluorophore is the acceptor (Figure 1.11). In order for the excited fluorophore to transfer an electron to the quencher, the electron must come from the LUMO of the fluorophore. Because electron transfer must be thermodynamically favourable, the LUMO of the acceptor quencher must be lower in energy than that of the fluorophore. Conversely, in scenario 2, the excited fluorophore must accept an electron in the HOMO. For this process to be thermodynamically favourable, the HOMO of the quencher donor must be higher in energy than that of the fluorophore.

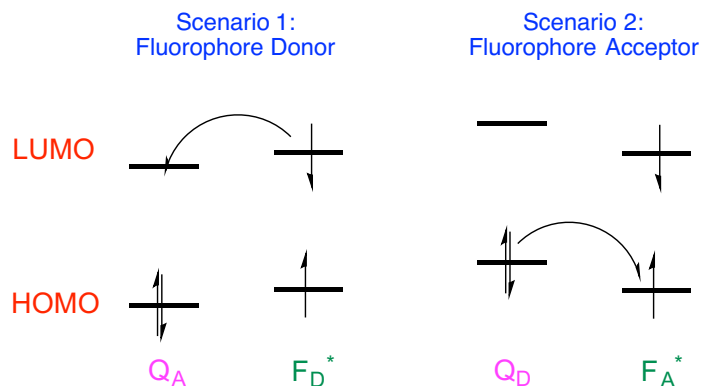


Figure 1.11: Two scenarios of PeT. 1) Where the photo-excited fluorophore (F^*) is the electron donor (D) and the quencher (Q) is the acceptor (A) and 2) Where the photo-excited fluorophore is the electron acceptor and the quencher is the donor.¹⁰¹

To predict the direction of electron transfer in the gas phase, ΔG_{eT}° can be calculated from Equation 1.12.

$$\Delta G_{eT}^\circ = IP_D - EA_A - \Delta E_{0,0} + \omega \quad \text{Equation 1.12}$$

where $\Delta E_{0,0}$ is the vibrational zero electronic energy of the excited fluorophore and ω is the coulombic correction term. The coulombic correction term, ω , is given by Equation 1.13 where N_A is Avogadro's constant ($6.022 \times 10^{23} \text{ mol}^{-1}$), e is the elementary charge of the electron ($1.60 \times 10^{-19} \text{ C}$), ϵ_0 is the permittivity of a vacuum ($8.854 \times 10^{-12} \text{ CV}^{-1}\text{m}^{-1}$), ϵ is the dielectric constant and r is the distance between the two charges.

$$\omega = -N_A \frac{e^2}{4\pi\epsilon_0\epsilon r} \quad \text{Equation 1.13}$$

In solution, the solvent changes the energetics of the process due to the solvation of the charged species and the redox potentials of the donor and acceptor are used instead of IP and EA. Thus the equation for free energy of photo-induced electron transfer in solution is given by Equation 1.14 below, where $E_{D^+/D}$ and E_{A/A^*} are the one electron standard redox potentials of the donor and acceptor respectively.^{102,106}:

$$\Delta G_{eT}^{\circ} = [(E_{D^{+\bullet}/D}^{\circ} - E_{A/A^{-\bullet}}^{\circ}) - \Delta E_{0,0} + \omega] \quad \text{Equation 1.14}$$

One can appreciate the importance solvent may play in the thermodynamics of electron transfer from Equations 1.13 and 1.14. In very polar solvents, where ϵ is large, the resulting low magnitude of ω causes little effect on ΔG_{eT}° . However, in non-polar solvents the effect of ω can become quite large potentially favouring ionic association instead of ion dissociation.¹⁰¹

1.3.1.2 Kinetics of PeT

The rate constant of photoinduced electron transfer (k_{peT}) must be significantly larger than the radiative rate constant (k_r) to effectively quench fluorescence. There is an interesting relationship between the thermodynamics (*vide supra*) and kinetics (*vide infra*) of electron transfer that was discovered by Rudolph Marcus, and is known as Marcus Theory of electron transfer.^{107,108}

According to Marcus Theory,^{107,108} the free energy required to reach the transition state for electron transfer to occur (ΔG_{eT}^{\ddagger}) is a function of both the free energy of electron transfer (ΔG_{eT}°) and the inner and outer shell reorganization energy (λ) as shown in Equation 1.15. From transition state theory, the rate constant for electron transfer is given by Equation 1.16 which relates the rate constant of electron transfer (k_{eT}) with the thermodynamics (ΔG_{eT}°) where ν_n is the nuclear vibrational frequency, κ is the transmission coefficient (probability that reactants in the transition state will proceed to products), and k_B is the Boltzmann constant.¹⁰² Interestingly, the smallest barrier of activation (i.e. $\Delta G_{eT}^{\ddagger} = 0$), arises when $\Delta G_{eT}^{\circ} = -\lambda$. Due to the quadratic dependence of ΔG_{eT}^{\ddagger} on ΔG_{eT}° , a quadratic dependence of $-\ln(k_{eT})$ on ΔG_{eT}° is observed, where k_{eT} is maximum when $\Delta G_{eT}^{\circ} = -\lambda$ (Figure 1.12). Hence, reactions with very large driving forces (i.e. $\Delta G_{eT}^{\circ} < -\lambda$) decrease k_{eT} and are said to occur in the Marcus Inverted Region.

$$\Delta G_{eT}^{\ddagger} = \frac{(\Delta G_{eT}^{\circ} + \lambda)^2}{4\lambda} \quad \text{Equation 1.15}$$

$$k_{eT} = \nu_n \kappa e^{-\frac{\Delta G_{eT}^{\ddagger}}{k_B T}} \quad \text{Equation 1.16}$$

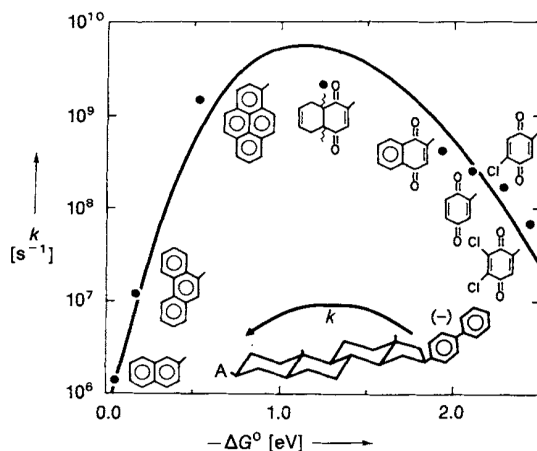


Figure 1.12 The Marcus Inverted region shown experimentally for electron transfer between a biphenyl group and an electron acceptor A. hexahydronaphthoquinon-2-yl (at $\Delta G^{\circ} = -1.2 \text{ eV} = \lambda$) marks the onset of the inverted region (right).¹⁰⁹ Reprinted with permission from “Miller, J. R.; Calcaterra, L. T.; Closs, G. L. *Journal of the American Chemical Society*, 1984 106 (10), 3047-3049” Copyright 1984 American Chemical Society.

Equations 1.14, 1.15 and 1.16 thus provide a means to predict the rate constant of electron transfer (or in our case the rate constant of quenching via PeT) from the redox potentials of a fluorophore and a quencher.

1.3.1.3 Maximizing the dynamic range

Our work seeks to design fluorogenic probes based on PeT such that ΔG°_{eT} is very negative (without entering the Marcus Inverted Region) to maximize k_{eT} . Practically speaking, this means that in the ‘off’ state, the quantum yield of the fluorogenic probe will be close to zero. Additionally, a fluorophore should be chosen where the quantum yield of the ‘on’ state is close to 1, thus providing a maximal dynamic range. While not important for absolute, 100% conversion “black and white situations,” a large dynamic range is key in distinguishing small differences in reagent consumption (fluorescence activation).

The significance of a large dynamic range is illustrated in Figure 1.13. Here we have 2 fluorogenic probes (dye 1 and dye 2), with different initial quantum yields (i.e. different k_{PeT}). Upon a reaction, the fluorescence is restored in both dyes giving the same final quantum yield of 1. After 10% reaction completion, the expected fluorescence enhancement is displayed for the 2 dyes based on how much they may have pre-activated (i.e. the ratio of fluorescence intensity initially vs. after 10 % reaction completion). For Dye 1, we have a poor dynamic range due to the moderately low initial quantum yield ($\phi_{fl} = 0.02$). Small differences are not easily detected. Even with an initially pristine sample, only a 5-fold fluorescence enhancement would be observed. However, for Dye 2, the dynamic range is excellent due to a larger k_{PeT} and hence very low initial quantum yield ($\phi_{fl} = 0.001$). Very small differences can be detected, and as much as a 50-fold enhancement would be observed from a pristine sample upon 10% conversion. Thus, the key to designing fluorogenic probes relying on PeT is maximizing k_{PeT} in the ‘off’ state, and minimizing k_{eT} in the ‘on’ state.

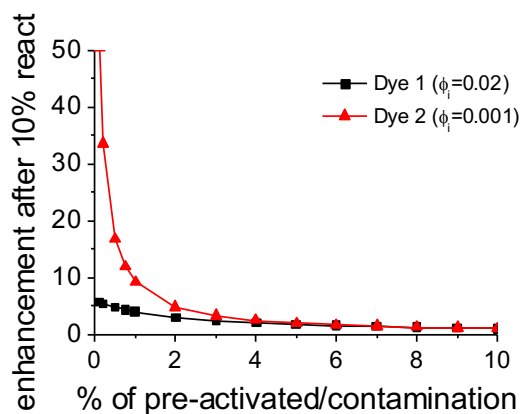


Figure 1.13 Fluorescent enhancement observed after 10% of the probe has reacted (i.e. 10% reaction completion) vs the amount of contamination with already activated probe (i.e. a pristine sample has 0% contamination). Dye 1 (black) has a poor dynamic range due to its higher ‘off’ ϕ_{fl} than dye 2 (red).

1.3.1.4 Predicting thermodynamics of PeT

To aid in the design of fluorogenic probes, we may estimate the thermodynamics of PeT by measuring the redox potentials of a series of fluorophores and potential quenchers. We may also explore the rates of PeT by performing a Stern-Volmer analysis (Section 1.2.3.3)

While both methods are effective, they are time consuming and expensive, especially when compounds must first be synthesised or bought. Alternatively, or in addition to these methods, we can employ prediction methods which can aid in the choice of a fluorophore-quencher pair.

Density functional theory (DFT) is a very valuable tool to predict and visualize PeT between a fluorophore and quencher. Calculated energies of the HOMO and LUMO of each molecule can be compared quantitatively showcasing whether PeT is feasible. If PeT is desired from the LUMO of the fluorophore to the LUMO of the quencher (scenario 1, Figure 1.11), one would compute the difference in the orbital energies of quencher and fluorophore donor to predict if PeT is exergonic (i.e. LUMO of fluorophore is higher in energy than LUMO of quencher). Several fluorophores can be compared in this way to facilitate choosing an appropriate fluorophore for a desired quencher.

Recognizing that redox potentials are typically influenced by the types of substituents on fluorophores,¹¹⁰ Fahrni and coworkers developed a series of linear free energy relationships (LFER) based on Hammett parameters to predict the thermodynamics of PeT in 1,3,5-triarylpyrazolines.¹¹¹ This method can be extended to other fluorophore systems, such as in BODIPY fluorophores,¹¹² where Hammett parameters of a subset of BODIPY dyes were related to DFT, preventing the need to compute every fluorophore-substituent option.

1.3.2 Ratiometric probes

Fluorescent probes relying on a change or shift in emission wavelength are known as ratiometric probes. Ratiometric probes often rely on a change in the conjugation of the fluorophore upon reaction of interest. Such a change may be as simple as reduction of a double bond to a single bond resulting in a blue shift of the emission. Quantification may be performed by taking a ratio of the red emission to the blue emission. Essentially, ratiometric probes have a built-in internal standard.

Conceptually, the simplicity of designing ratiometric probes is a big advantage over the complexity of designing probes relying on PeT. While an ‘off’ to ‘on’ fluorescence change is easily detectable, designing probes based on PeT requires extensive prior design research to

optimize the redox potentials between quencher and reporter, and may be quite challenging. Furthermore, quantification of reactions/products becomes difficult if no standard or control is available bearing similar photo-physical properties. This becomes especially important if partitioning/solubility is a problem.

The obvious drawback of ratiometric probes, however, is the need for dual excitation sources and/or dual emission detectors. While most fluorimeters are equipped to measure multiple emission spectra, the drawback becomes more important with a microscopy setup, where multiple lasers and filters may be needed to prevent any cross-talk. Additionally, the use of a ratiometric probe may inhibit the use of additional dyes in the study, such as commercial organelle targeting dyes to show localization, since two laser lines and/or emission filters are already occupied. Finding a commercial dye with no overlapping spectra of both states of the ratiometric probe may also be difficult.

The next section will provide examples of fluorescent probes in the literature taking advantage of some of the design mechanisms discussed in this section.

1.4 Fluorescent Probes for Reaction Screening and Redox State

Recently, fluorescent probes have garnered much attention jointly with advances in the microscopy field. This attention has unsurprisingly brought about a tremendous number of fluorescent probes designed to answer various chemical and biological questions.^{13-15,113,114} The underlying similarity of these fluorescent probes is their ability to monitor a reaction. These include sensing an analyte of interest as it is produced in a system, or reporting on the movement of electrons in a redox reaction. Their utility relies on both their sensitivity (large dynamic range, see discussion in Section 1.3.1) and their specificity to the reaction they are monitoring.

This section is aimed at showcasing a few examples of fluorescent probes, highlighting their mechanism of action for insight into the design of future fluorescent probes. Primarily probes for the detection of reactive oxygen species and the overall redox state of a system will be discussed. The design of the probes discussed in this section takes advantage of some of

the strategies discussed in Section 1.3 as well as exploits the endogenous chemistry of the reaction of interest.

1.4.1 Probes for detection of reactive oxygen species and lipid peroxidation

Fluorogenic probes, when combined with microscopy, can give information on the localization, quantification and build-up of ROS in specific organelles and in real-time. The probes thus have the potential to help elucidate the complex role of ROS *in vivo*. To date, a number of fluorogenic probes to detect ROS and their by-products have been developed.^{14,115,116}

One of the first fluorogenic ROS sensors developed was dichlorodihydrofluorescein (DCFH, Figure 1.14).¹¹⁷ DCFH is based on fluorescein (a commonly used fluorophore) and is initially non-fluorescent due to the lack of conjugation. Upon oxidation by ROS to a fully conjugated system, the fluorophore becomes emissive ($\lambda_{em} = 522$ nm). DCFH however has serious drawbacks, as it auto-oxidizes upon light irradiation and is not specific to any type of ROS.¹¹⁸

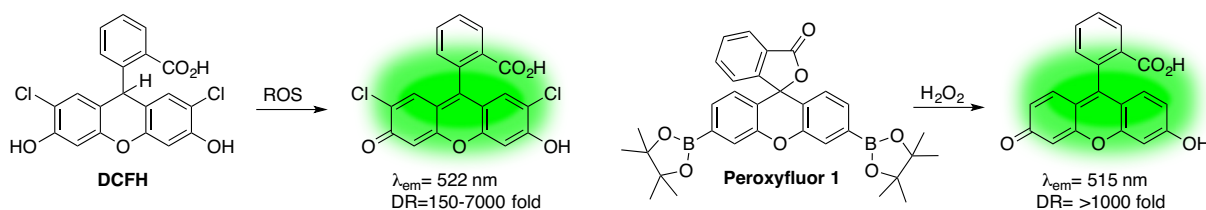


Figure 1.14 Structures of ROS probes based on fluorescein and the emission wavelength and dynamic range (DR) expected upon reaction with ROS.^{117,119}

Building upon the concept of DCFH, Chang and co-workers, developed Peroxyfluor 1 (Figure 1.14),¹¹⁹ a boronate protected fluorescein. The protecting boronate groups on the phenol prevented the auto-oxidation and sensitivity problems associated with DCFH. Upon treatment of Peroxyfluor 1 with hydrogen peroxide, the boronate esters are cleaved, leaving the oxidized, conjugated fluorescent form of fluorescein. Their work with boronate protected fluorescein derivatives and subsequent, improved generations has allowed the Chang group to study oxidation in live cells, and in specific organelles.^{17,120-122}

Singlet oxygen ($^1\text{O}_2$) is an excited state of molecular oxygen and is highly reactive. Its high reactivity and ability to oxidize DNA, proteins, and lipids makes it an important toxic species to study. Because of its high reactivity, and short lifetime ($2 \mu\text{s}$ in water)¹²³ it is difficult to detect, and availability of probes is limited. 9-10-Dimethylantracene (DMA) is a fluorescent molecule which undergoes reaction with $^1\text{O}_2$ selectively and with a high rate constant ($\sim 10^8 \text{ M}^{-1}\text{s}^{-1}$ in micelles) to form a non-fluorescent endoperoxide (Figure 1.15).^{123,124} Although its excitation is very blue shifted (375 nm), precluding its use in cell studies, its chemistry is exploited in the design of more practical probes. Nagano and co-workers developed one such probe, DMAX (Figure 1.15).¹²⁵ DMAX consists of a fluorescein fluorophore reporter and a DMA trap. Relying on PeT, the DMA trap acts as an electron donor to the photo-excited fluorescein to render the probe initially non-fluorescent. Upon reaction with $^1\text{O}_2$ the anthracene moiety is oxidized to an endoperoxide, lowering the HOMO, deactivating PeT and rendering the probe highly emissive. This probe is currently the most effective $^1\text{O}_2$ probe available due to its fast kinetics on parallel to that of DMA, as well as its large dynamic range between ‘off’ and ‘on’ (about 50-fold).

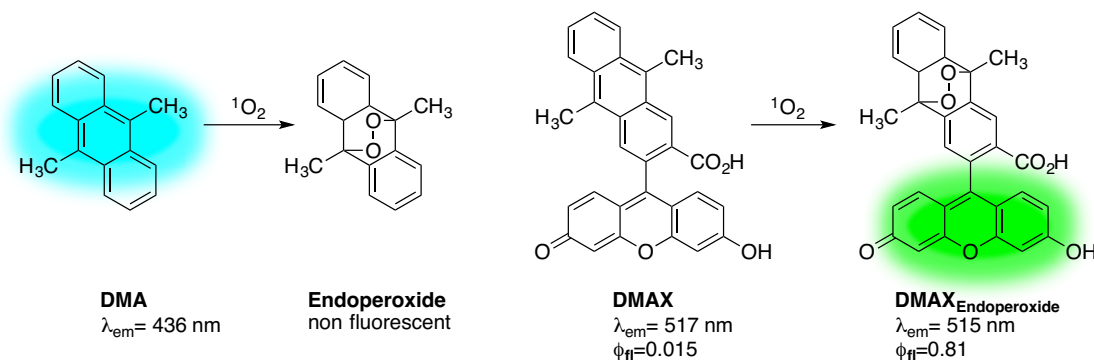


Figure 1.15 Fluorogenic probes for the detection of singlet oxygen based on DMA.^{115,125}

As discussed earlier in Section 1.1, polyunsaturated fatty acids of lipid membranes are particularly vulnerable to ROS elicited damage. Due to their high reactivity with ROS, oxidation of lipids provides a sensitive marker to the oxidative state of the cell, and thus a unique opportunity to exploit in the design of fluorogenic probes for lipophilic ROS.

Initially, lipophilic probes for ROS were designed after polyunsaturated fatty acids, bearing a tail of poly-unsaturation. The first lipophilic ROS probe was developed in the 1970s

by Hudson and coworkers: *cis*-parinaric acid (Figure 1.16).¹²⁶ This ‘on/off’ probe relies on the destruction of the double bonds by ROS. The resulting de-conjugation causes a decrease in fluorescence. This probe was validated by Post and coworkers where they found the use of the probe gave sensitive and reproducible results in model systems and myocytes.¹²⁷ The structure of *cis*-parinaric acid makes the probe an attractive candidate for detecting lipophilic radicals as the structure closely resembles endogenous fatty acid moieties. Mobility of the probe is likely comparable to endogenous phospholipids, and partitioning into membranes would not perturb the lipid bilayer. However, the utility of this probe is limited due to its absorption in the UV (320 nm) precluding its use in real-time live cell studies, in addition to its instability in air, and photolability.

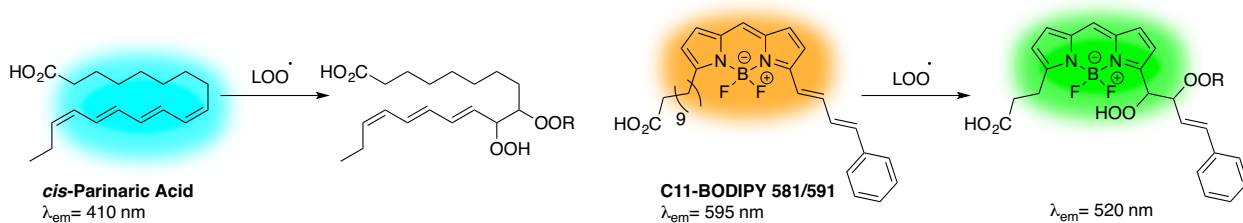


Figure 1.16 Fluorescent probes for the detection of lipid peroxidation based on the structure of fatty acids.^{126,128}

The simplicity of *cis*-parinaric in design is very appealing, which prompted the design of new and improved probes for lipid peroxidation. The new designs improve the photostability of the fluorophore, emit in the visible range making them well suited to detect lipid peroxidation in cells, and have comparable reactivity to peroxidation as endogenous fatty acids. One such probe is C11-BODIPY 581/591 (Figure 1.16).¹²⁸ The highly conjugated structure of the fluorophore gives a relatively red emission. Upon oxidation by ROS, and subsequent de-conjugation, the emission becomes blue-shifted. This probe is thus a ratiometric probe (Section 1.3.2). This probe has been further adapted by Murphy and coworkers to target mitochondria,¹²⁹ a major source of lipid peroxidation due to the electron transport chain.

Probes modelled after polyunsaturated lipids provide detection of ROS once they have become the chain carriers (i.e. the antioxidant load is completely compromised). Thus, they can only indicate the depletion of an antioxidant load in membranes and cells rather than the onset of antioxidant consumption.

Our laboratory has attempted to fill this niche by designing fluorogenic analogues of α -tocopherol, (the most biologically active form of Vitamin E) which become emissive upon scavenging lipid peroxy radicals.^{19,48,100,130} These probes report the point in time when the antioxidant load is changing.

The first generation fluorogenic analogue of α -tocopherol reported by our laboratory was BTOH (Figure 1.18A).¹³⁰ BTOH is a reporter-trap based probe relying on PeT. The BODIPY reporter ensures emission in the visible range, while the chromanol trap possesses the radical-scavenging reactivity of α -tocopherol (discussed in detail in Section 1.1.4). The HOMO of the chromanol is high enough in energy to donate an electron to the photo-excited BODIPY moiety quenching the fluorescence. Upon oxidation by two equivalents of ROS, the HOMO of the newly formed chromanone (Figure 1.18A) is very low-lying, preventing PeT, thus restoring the fluorescence of the molecule.

The subsequent generations of probes developed in our laboratory follow the same conceptual design as BTOH, but have a larger dynamic range (Figure 1.18B).^{48,100} The redox potentials of the BODIPY moiety of these later generations were tuned to facilitate more exergonic PeT in the reduced, chromanol forms, and allow for a larger dynamic range. In addition, we have pursued the development of mitochondria targeting fluorogenic probes based on α -tocopherol.¹⁹ The development and improvement of fluorogenic analogues of α -tocopherol will be main points of discussion in Chapters 3 and 4.

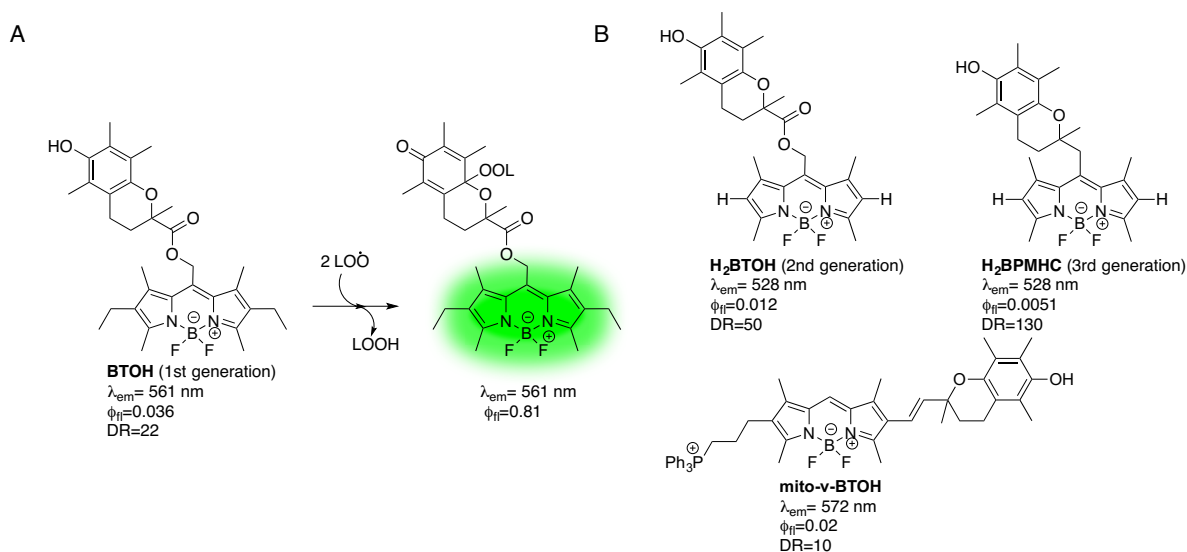


Figure 1.17 A) First generation fluorogenic tocopherol analogue, BTOH, and its reaction with lipophilic radicals.¹³⁰ B) Subsequent generations of fluorogenic tocopherol analogues prepared in the Cosa Laboratory and their dynamic range (DR).^{19,48}

1.4.2 Fluorogenic probes for redox-reversible reactions

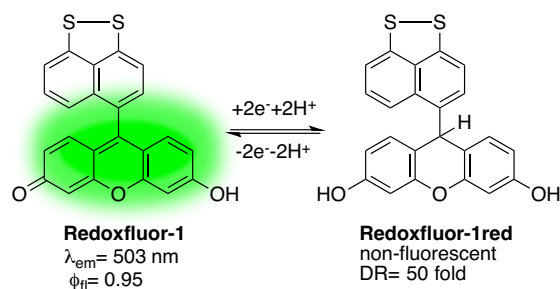
As discussed in the previous sections, the ability to detect ROS is of great importance to understand the onset of various pathologies associated with oxidative stress, as well as distinguishing between excess ROS (oxidative stress), and healthy oxidation (cell signalling and cellular defence mechanisms). Many of the probes used to detect ROS, including most of the examples discussed in the previous section, take advantage of an irreversible chemical reaction, whether it being the removal of a boronate protecting group as in Peroxyfluor 1, or the irreversible oxidation of the chromanol ring as in BTOH. These probes, while having much use in the biological community, are unable to distinguish between chronically elevated ROS levels (e.g. disease) and temporary bursts in ROS levels (e.g. homeostasis), due to their irreversibility. Probes capable of cycling between redox states (redox-reversible) and reporting time-resolved changes are required to make this important distinction.¹¹

Several genetically encoded fluorescent proteins, both reversible and redox-sensitive, are capable of reporting dynamic changes in redox state.^{12,131,132} This class of probes has some obvious advantages such as biocompatibility and ease of cellular targeting. However, use of these probes often require invasive genetic modification of the system under study, which

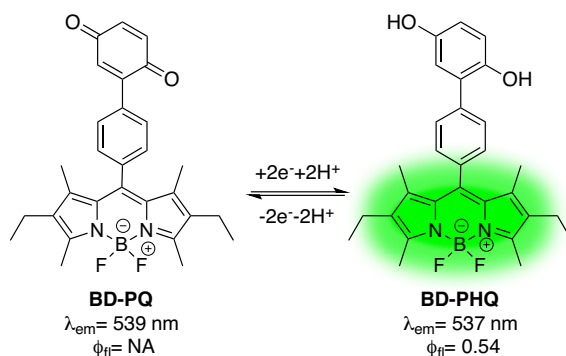
precludes potential applications in both non-biological and clinical settings. Small-molecule fluorescent probes are therefore promising candidates for the design and application of reversible-redox fluorescent probes and have been recently reviewed by New and coworkers.¹¹

The first redox-reversible, small molecule fluorogenic probe for monitoring redox events in live cells was based on the chemistry of DCFH and was reported by Chang and coworkers.¹³³ Like DCFH, their probe, Redoxfluor-1, consists of an unconjugated, reduced form of fluorescein, which upon oxidation, conjugates and fluoresces (Scheme 1.12). Unlike DCFH, Redoxfluor-1 is reversible due to a disulfide which facilitates the reduction of the probe once oxidized.

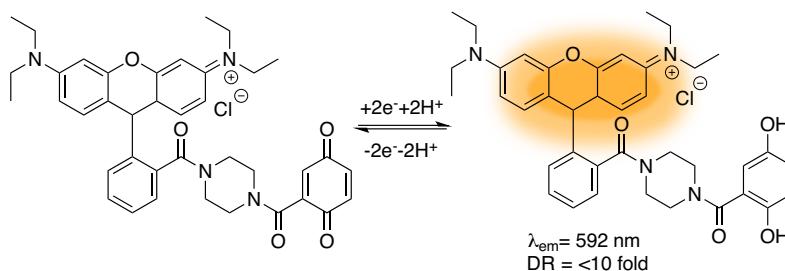
Scheme 1.12 Redox reversibility and dynamic range (DR) of Redoxfluor-1.¹³³



Due to their redox reversible couple, quinones/quinols are obvious candidates as traps for redox-sensitive fluorescent probes.^{134,135} In addition, the high electron accepting ability of the quinone, or the high electron donation ability of the quinol may enable the design of redox-reversible-fluorogenic probes relying on PeT.¹³⁶ Clegg and coworkers developed one such probe, BD-PQ (Scheme 1.13).¹³⁷ BD-PQ combines a BODIPY reporter, and a quinol/quinone trap. In the oxidized state, BD-PQ is non fluorescent due to PeT from the LUMO of the photo-excited BODIPY to the low lying LUMO of the quinone moiety (Scenario 1, Figure 1.11). Upon reduction to the quinol, PeT is deactivated and fluorescence is restored. The redox-reversibility was demonstrated in the sequential treatment of hydrogen peroxide to oxidize the quinol moiety, and ascorbate to reduce back to the quinone.

Scheme 1.13 Redox reversibility and fluorogenicity of quinone redox probe, BD-PQ.¹³⁷

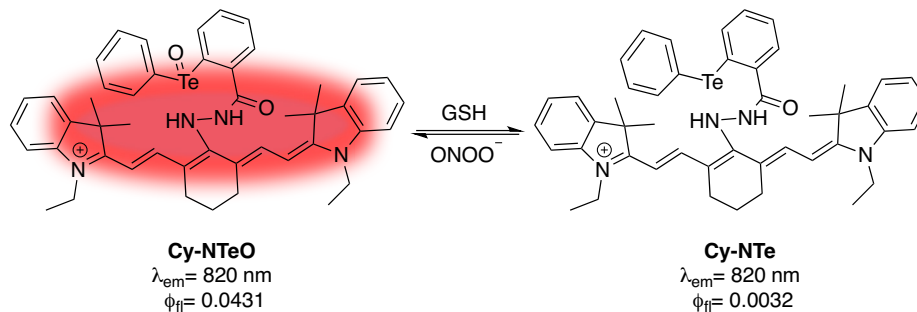
Building upon the proof of concept provided by Clegg and coworkers, Krämer and coworkers developed a fluorogenic reversible, redox sensitive probe for imaging the oxidation state in live cells,¹³⁸ and monitoring quinone redox cycles at the single molecule level.¹³⁹ Their probe combines a quinol/quinone trap moiety and a rhodamine fluorophore (Scheme 1.14). Like BD-PQ, their probe is weakly fluorescent in the oxidized, quinone form due to PeT, and fluorescent upon reduction. While difficult to oxidize in cells (likely due to the presence of glutathione effectively keeping the dye pool reduced), Krämer and coworkers showed redox reversibility at the single molecule level in the presence of Cu^{2+} to oxidize, and cysteine to reduce.

Scheme 1.14 Redox reversibility and dynamic range (DR) of a quinone-rhodamine redox probe.¹³⁸

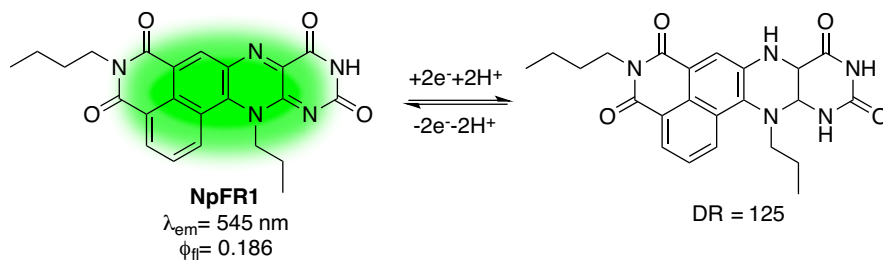
A common group of redox-reversible fluorescent probes, known as chalcogen-based probes, involve oxidation of sulfur, selenium, and tellurium. These probes monitor redox

processes through either direct oxidation of the chalcogen itself to form the oxide, or through the formation of bridged chalcogens (e.g. disulfides).^{11,140} Han and coworkers recently reported a tellurium based fluorogenic chalcogen probe, Cy-NTe (Scheme 1.15)¹⁴¹ Interestingly, this probe undergoes selective oxidation by peroxyxynitrite and is reversibly reduced by cellular thiols such as glutathione. Cy-NTe consists of a near IR fluorophore, heptamethine cyanine (Cy7) to optimize detection *in vivo*, and 2-(phenyltellanyl)benzohydrazide which in its reduced state quenches the Cy7 dye via PeT. Oxidation of the tellurium to telluroxide deactivates PeT and renders Cy7 emissive.

Scheme 1.15 Redox reversibility and fluorogenicity of tellurium redox probe, Cy-NTeO.¹⁴¹



Redox regulation in biological systems often rely on derivatives of flavins and nicotinamides. As redox-cofactors and coenzymes in cellular redox reactions, they are inherently biocompatible with redox properties tuned to cellular reactions. Thus, they are an attractive class of molecules for the design of redox-reversible fluorogenic probes for biological applications.^{142,143} New and coworkers recently reported a flavin based redox sensor NpFR1, and mitochondria targeting analogue NpFR2 (Scheme 1.16).^{144,145} These probes rely on the inherent fluorogenic properties of flavins which are fluorescent in the oxidized form (conjugated) and non fluorescent once reduced (non-conjugated system). To distinguish from the autofluorescence associated with endogenous flavins, NpFR1 consists of a flavin backbone, whose conjugation is extended by a naphthalimide fluorophore, causing a redshift in the emission. The NpFR fluorophores were both redox reversible in the presence of hydrogen peroxide/glutathione among other oxidants/reductants.

Scheme 1.16 Redox reversibility and dynamic range (DR) of flavin redox probe, NpFR1.¹⁴⁴

1.4.3 Fluorogenic probes for detecting nucleophiles and monitoring nucleophilic reactions

The ubiquity of nucleophilic reactions both in a biological context and in an organic synthesis context, make the study of nucleophilic reactions an important and vast area of research. Fluorescent probes allow the detection of biological nucleophiles such as amino acids enabling the visualization of nucleophilic reactions *in vivo*.^{18,146,147} Similar probes also enable high-throughput screening of reaction conditions, nucleophiles, and catalysts allowing a rapid method for a synthetic chemist to optimize a reaction.¹⁴⁸⁻¹⁵⁰ While these two applications appear significantly different, they both require use of a fluorescent probe which undergoes a reaction with a nucleophile.

1.4.3.1 Fluorescent probes to detect biological nucleophiles

Nucleophiles and nucleophilic reactions and their regulation in biological systems have been linked to many diseases, toxicity, and allergic reactions.^{38,151-153} Therefore, study and detection of biological nucleophiles and pollutants is very important. Several examples of fluorescent probes for nucleophiles such as those developed for the detection of cyanide ions^{154,155} and thiols^{113,146,156,157} have been developed over the last decade. One of the main challenges associated with the development of nucleophile probes is designing a probe specific for the nucleophile of interest.

Thiols are soft nucleophiles. Therefore, they undergo nucleophilic addition to the corresponding soft electrophilic carbon of α,β -unsaturated carbonyls (Michael addition). One

of the first examples of a fluorescent probe for thiols was developed by Sippel and coworkers. They exploited this chemistry with the use of a maleimide moiety (Figure 1.18 A).¹⁵⁶ The probe, CPM, relies on the coupling of a coumarin fluorophore and a maleimide trap. Initially, the probe is quenched and upon reaction of a thiol with the electrophilic maleimide moiety, becomes highly fluorescent. The mechanism of quenching was later explored by Keillor and coworkers and was rationalized as PeT from the photo-excited coumarin moiety, to the electron deficient maleimide.^{158,159} While CPM reacts effectively with thiols, it absorbs in the UV region, and thus is not suitable for use in live biological samples. However, this probe was later modified by Keillor and coworkers to discern substituent effects on the reactivity of thiol addition to maleimides (Figure 1.19B).

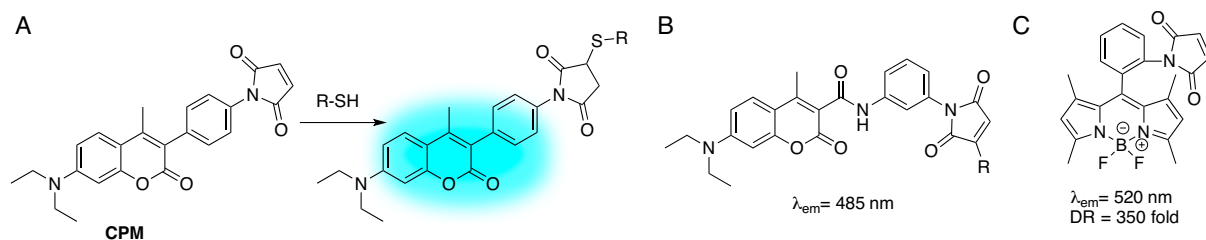


Figure 1.18 Thiol-reactive fluorogenic probes relying on chemistry with maleimide. A) CPM developed by Sippel and coworkers, and its reaction with thiols,¹⁵⁶ B) probe developed by Keillor and coworkers¹⁶⁰ and C) probe developed by Nagano and coworkers.¹⁵⁷

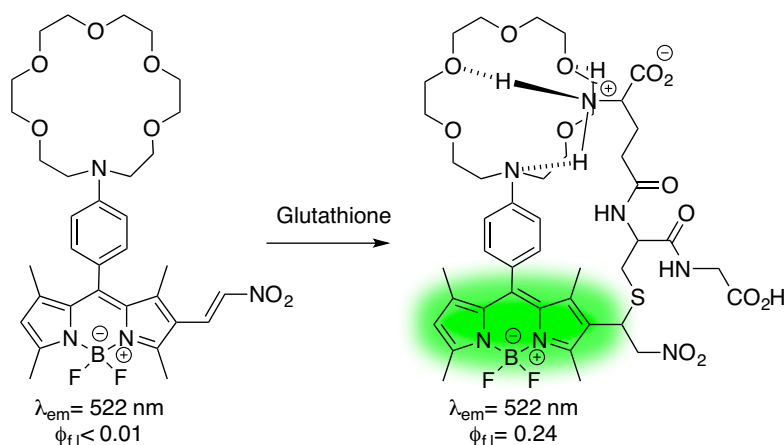
Nagano and coworkers built upon the concept developed by Sippel and designed a BODIPY-maleimide based probe for the detection of thiols excitable in the visible region (Figure 1.18 C).¹⁵⁷ Similar to CPM, their probe is initially non-fluorescent due to PeT, and upon reaction with thiols becomes highly fluorescent. They exemplified their sensitivity with the detection of very low concentrations of bovine serum albumin (5 $\mu\text{g}/\text{mL}$) in SDS PAGE.

The probes developed by Sippel, Keillor and Nagano detect thiols in general, whether free thiols, or those making up a protein. Cysteine, homocysteine, and glutathione, are important small molecule thiols *in vivo* and their regulation is associated with different physiologies and pathologies. For example, cysteine concentration is associated with myocardial and cerebral infarctions,¹⁶¹ while glutathione levels are associated with the

oxidative state of a cell. Detection of specific thiols is therefore important, and thiol chemistry alone cannot be exploited in the development of such specific probes.

Akkaya and coworkers recently developed a fluorogenic probe specific for the detection of glutathione (Scheme 1.17).¹⁶² Their probe combines two reaction sites to garner glutathione selectivity: 1) an activated unsaturated carbon which undergoes reaction with thiols, and 2) a distance dependent recognition site for ammonium groups. Like the previous thiol-probes discussed, this probe also undergoes reaction with thiols at the unsaturated carbon. However, this initial reaction does not deactivate the fluorescence quenching. The probe also bears an *N*-phenylazacrown moiety which effectively quenches the BODIPY fluorophore via PeT. This quenching is deactivated upon hydrogen bonding of the ammonium of glutathione to the *N*-phenyl moiety and crown ether. This hydrogen bonding prevents electron donation from the *N*-phenyl moiety into the photo-excited BODIPY and effectively deactivates PeT. Cysteine, and homocysteine are too short to reach the *N*-phenylazacrown, and are thus unable to modulate PeT. The differences in structure of thiols is thus a useful way of designing thiol-specific probes.¹⁴⁶

Scheme 1.17 Reaction mechanism of a fluorogenic probe specific for glutathione developed by Akkaya and coworkers.¹⁶²



1.4.3.2 Fluorescent probes for reaction screening

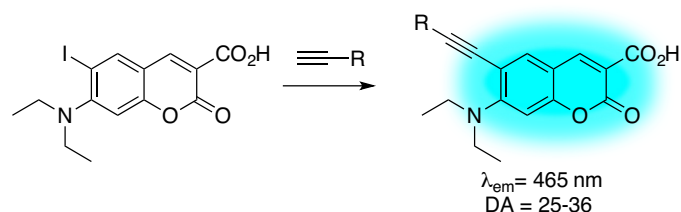
Significant effort has been devoted this century to the development of techniques for rapid reaction screening.¹⁶ Screening nucleophiles, catalysts, and reaction conditions are often

requirements to optimize yields, or to improve the environmental footprint of a chemical transformation. Fluorescent probes and fluorescence based assays are thus particularly suited to facilitate this process.

Fluorescence based assays for high-throughput reaction screening was pioneered by Hartwig and coworkers.¹⁴⁸ Their assay relied on a coumarin tagged acrylate to undergo a Heck reaction with a solid-support tagged aryl halide. Fluorescence detection of the solid support allowed them to screen 40 phosphine ligands. This assay, however, suffers from the drawback that both reactant and reagent must be modified to tag to a fluorophore and to a solid support respectively. This requires the synthesis of multiple reactants and reagents which may not be of later use.

Fluorescence based assays using fluorogenic probes are more convenient than Hartwig's method for reaction screening since reagent modification is not required. Bergstrom and coworkers developed a fluorogenic coumarin which becomes fluorescent upon reaction with an alkyne via a Sonogashira coupling (Scheme 1.18).¹⁶³ The coumarin, bearing an iodine atom is quenched due to the heavy atom effect (discussed in Section 1.2.3.1). Upon substitution of the iodine atom with the alkyne in the presence of palladium, the emission of the coumarin is restored. Bergstrom and coworkers tested this probe in the presence of various alkynes and conducted kinetic studies via fluorescence enhancement to determine alkyne reactivity. Many other groups have developed fluorescent based assays to monitor bond formation in aldol reactions,¹⁶⁴ Mannich type reactions,¹⁶⁵ Michael additions¹⁶⁶ and palladium catalyzed reactions.^{167,168} These assays provide a rapid and *in situ* approach for the optimization of reaction conditions, and screening catalysts and reactivity of nucleophiles.

Scheme 1.18 Fluorogenic probe for screening alkynes for Sonogashira coupling developed by Bergstrom and coworkers.¹⁶³

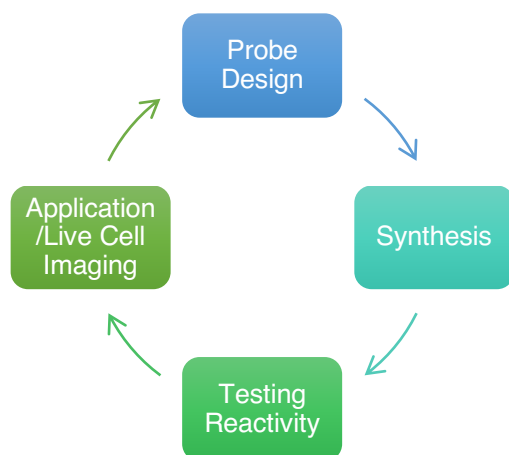


1.5 Research goals and scope of thesis

Fluorescence spectroscopy and microscopy have emerged as powerful tools that provide high sensitivity as well as spatial and temporal resolution. In particular, fluorescence may be useful in the study of reactions occurring in biological milieu and on the benchtop to provide insight into their mechanism and kinetics. Critical to the exploration of reactions using fluorescence is the availability of sensitive and specific fluorescent probes as well as protocols in which to use them. The overarching goal of this thesis is thus two pronged: 1) the development of highly sensitive fluorogenic probes to reconcile the chemistry and the biology of lipid peroxidation, and 2) insight into the rational design of fluorogenic probes and fluorescence based assays in general.

The development of fluorogenic probes is cyclical with 4 distinct stages: probe design, probe synthesis, testing reactivity and sensitivity, and application (e.g. live cell imaging) (Scheme 1.19). The cycle then continues with the improvement of probes building on the knowledge gleaned from previous cycles. The following chapters discuss the challenges and potential solutions associated with each stage in probe development, while also addressing the goals of the thesis discussed above.

Scheme 1.19 Cycle of fluorogenic probe development.



As discussed in Section 1.1, the multiple roles of ubiquinone, as both a cofactor of the electron transport chain and an important inhibitor of lipid peroxidation, make it a complex molecule to study *in vivo*. In Chapter 2, we propose the development of a reversible,

fluorogenic analogue of ubiquinone to monitor its complex redox pathways. The design of an ubiquinone-BODIPY probe relying on PeT, is first presented. This probe, H₂B-Q, is fluorescent in the reduced state, and upon oxidation, is quenched via PeT from the photoexcited BODIPY to the electron poor quinone. The synthesis is then discussed as well as the challenges overcome in the synthesis of a quinone-BODIPY construct. Reversible reduction/oxidation of H₂B-Q is then shown, as well as its antioxidant behaviour and cooperativity with a Vitamin E analogue. Such a tool shows promise in understanding quinone-quinol redox chemistry.

On our quest to reconcile the chemistry and the biology of lipid peroxidation *in vivo*, we realized our lack of sensitivity to distinguish subtle levels of ROS with our current fluorogenic probes based on tocopherol.^{19,48,100,169} With the ultimate goal of determining the sensitivity ceiling in our probes, we explored the effect of redox potential and distance between fluorophore and quencher on the efficiency of PeT in Chapter 3. Using DFT and electrochemistry in tandem with the photophysical properties of a series of BODIPY-tocopherol compounds, PeT efficiency was rationalized within the context of Marcus theory providing us with more understanding for the design of future probes relying on PeT. This work thus led to the development of a new generation fluorogenic tocopherol, H₄BPMHC, characterized by a 3 orders of magnitude dynamic range.

Armed with a highly sensitive probe showcased in Chapter 3, in Chapter 4 we image lipid peroxidation in HeLa cells. In order to preserve the optimum sensitivity of the probe in cells, the challenges associated with staining cells with BODIPY dyes are discussed as well as potential solutions. Due to the large dynamic range of H₄BPMHC, we were able to monitor basal levels of lipid peroxidation in live cells. We believe this probe shows potential to investigate the physiological relevance of lipid peroxy radical production during cell homeostasis and disease.

In Chapter 5 we turn towards developing fluorogenic electrophiles. As discussed in Section 1.1, aldehydes (such as 4-hydroxynonenal) are potent by-products of lipid peroxidation which undergo addition by biological nucleophiles. Here we present our initial steps to ultimately develop a fluorogenic lipophilic electrophile. A reactivity palette is assembled based

on non-emissive *meso*-formyl BODIPY dyes previously synthesised in the Cosa group¹⁷⁰ which become fluorescent upon reaction with alcohols. In addition to exploring the sensitivity and reactivity of these dyes towards nucleophilic attack, this chapter discusses the valuable and often overlooked information a fluorescence based assay can provide, such as yield of reaction intermediates otherwise insensitive to isolation techniques.

1.6 References

- (1) Stokes, G. G. On the Change of Refrangibility of Light *Phil. Trans. R. Soc of London* **1852**, *142*, 463-562.
- (2) Safford, W. E. *Ann. Rep. Smithsonian Inst.* **1915**, 271-298.
- (3) The Nobel Prize in Chemistry 2014 *NobelPrize.org Media* **2014**, accessed 7 Feb 2017.
- (4) Calver, C. F.; Liu, H.-W.; Cosa, G. Exploiting Conjugated Polyelectrolyte Photophysics toward Monitoring Real-Time Lipid Membrane-Surface Interaction Dynamics at the Single-Particle Level *Langmuir* **2015**, *31*, 11842-11850.
- (5) Liu, Z.; Lavis, L. D.; Betzig, E. Imaging Live-Cell Dynamics and Structure at the Single-Molecule Level *Mol. Cell* **2015**, *58*, 644-659.
- (6) Gahlmann, A.; Moerner, W. E. Exploring bacterial cell biology with single-molecule tracking and super-resolution imaging *Nat Rev Micro* **2014**, *12*, 9-22.
- (7) Hariri, A. A.; Hamblin, G. D.; Gidi, Y.; Sleiman, H. F.; Cosa, G. Stepwise growth of surface-grafted DNA nanotubes visualized at the single-molecule level *Nat Chem* **2015**, *7*, 295-300.
- (8) Tachikawa, T.; Yonezawa, T.; Majima, T. Super-Resolution Mapping of Reactive Sites on Titania-Based Nanoparticles with Water-Soluble Fluorogenic Probes *ACS Nano* **2013**, *7*, 263-275.
- (9) Betzig, E.; Patterson, G. H.; Sougrat, R.; Lindwasser, O. W.; Olenych, S.; Bonifacino, J. S.; Davidson, M. W.; Lippincott-Schwartz, J.; Hess, H. F. Imaging intracellular fluorescent proteins at nanometer resolution *Science* **2006**, *313*, 1642-1645.
- (10) Barlag, B.; Beutel, O.; Janning, D.; Czarniak, F.; Richter, C. P.; Kommnick, C.; Göser, V.; Kurre, R.; Fabiani, F.; Erhardt, M.; Piehler, J.; Hensel, M. Single molecule super-resolution imaging of proteins in living *Salmonella enterica* using self-labelling enzymes *Sci. Rep.* **2016**, *6*, 31601.
- (11) Kaur, A.; Kolanowski, J. L.; New, E. J. Reversible Fluorescent Probes for Biological Redox States *Angew. Chem. Int. Ed.* **2016**, *55*, 1602-1613.
- (12) Lukyanov, K. A.; Belousov, V. V. Genetically encoded fluorescent redox sensors *Biochim. Biophys. Acta* **2014**, *1840*, 745-756.
- (13) Kowada, T.; Maeda, H.; Kikuchi, K. BODIPY-based probes for the fluorescence imaging of biomolecules in living cells *Chem. Soc. Rev.* **2015**, *44*, 4953-4972.
- (14) Krumova, K.; Cosa, G. Fluorogenic probes for imaging reactive oxygen species *Photochemistry* **2013**, *41*, 279-301.
- (15) Boens, N.; Leen, V.; Dehaen, W. Fluorescent indicators based on BODIPY *Chem. Soc. Rev.* **2012**, *41*, 1130-1172.
- (16) Collins, K. D.; Gensch, T.; Glorius, F. Contemporary screening approaches to reaction discovery and development *Nat Chem* **2014**, *6*, 859-871.
- (17) Dickinson, B. C.; Huynh, C.; Chang, C. J. A Palette of Fluorescent Probes with Varying Emission Colors for Imaging Hydrogen Peroxide Signaling in Living Cells *J. Am. Chem. Soc.* **2010**, *132*, 5906-5915.
- (18) Umezawa, K.; Yoshida, M.; Kamiya, M.; Yamasoba, T.; Urano, Y. Rational design of reversible fluorescent probes for live-cell imaging and quantification of fast glutathione dynamics *Nat Chem* **2017**, *9*, 279-286.
- (19) Krumova, K.; Greene, L. E.; Cosa, G. Fluorogenic α -Tocopherol Analogue for Monitoring the Antioxidant Status within the Inner Mitochondrial Membrane of Live Cells. *J. Am. Chem. Soc.* **2013**, *135*, 17135-17143.
- (20) Krumova, K.; Cosa, G. In *Singlet Oxygen: Applications in Biosciences and Nanosciences, Volume 1*; The Royal Society of Chemistry: 2016; Vol. 1, p 1-21.

- (21) D'Autreaux, B.; Toledano, M. B. ROS as signalling molecules: mechanisms that generate specificity in ROS homeostasis *Nat Rev Mol Cell Biol* **2007**, *8*, 813-824.
- (22) Barnham, K. J.; Masters, C. L.; Bush, A. I. Neurodegenerative diseases and oxidative stress *Nat Rev Drug Discov* **2004**, *3*, 205-214.
- (23) Mittal, M.; Siddiqui, M. R.; Tran, K.; Reddy, S. P.; Malik, A. B. Reactive Oxygen Species in Inflammation and Tissue Injury *Antioxid. Redox Signal.* **2014**, *20*, 1126-1167.
- (24) Niki, E. Oxidative stress and antioxidants: Distress or eustress? *Arch. Biochem. Biophys.* **2016**, *595*, 19-24.
- (25) Imlay, J. A. Pathways of Oxidative Damage *Annu Rev Microbiol.* **2003**, *57*, 395-418.
- (26) Murphy, M. P. How mitochondria produce reactive oxygen species *Biochem. J* **2009**, *417*, 1-13.
- (27) Turrens, J. F. Mitochondrial formation of reactive oxygen species *J. Physiol* **2003**, *552*, 335-344.
- (28) Nathan, C.; Cunningham-Bussel, A. Beyond oxidative stress: an immunologist's guide to reactive oxygen species *Nature reviews. Immunology* **2013**, *13*, 349-361.
- (29) Antelmann, H.; Helmann, J. D. Thiol-Based Redox Switches and Gene Regulation *Antioxidants & Redox Signaling* **2011**, *14*, 1049-1063.
- (30) Finkel, T.; Holbrook, N. J. Oxidants, oxidative stress and the biology of ageing *Nature* **2000**, *408*, 239-247.
- (31) Harman, D. Aging: A Theory Based on Free Radical and Radiation Chemistry *J Gerontol* **1956**, *11*, 298-300.
- (32) Lapointe, J.; Hekimi, S. When a theory of aging ages badly *Cell. Mol. Life Sci.* **2009**, *67*, 1-8.
- (33) Wu, R. P.; Hayashi, T.; Cottam, H. B.; Jin, G.; Yao, S.; Wu, C. C.; Rosenbach, M. D.; Corr, M.; Schwab, R. B.; Carson, D. A. Nrf2 responses and the therapeutic selectivity of electrophilic compounds in chronic lymphocytic leukemia *Proc. Natl. Acad. Sci. U.S.A.* **2010**, *107*, 7479-7484.
- (34) Borst, J. W.; Visser, N. V.; Kouptsova, O.; Visser, A. J. W. G. Oxidation of unsaturated phospholipids in membrane bilayer mixtures is accompanied by membrane fluidity changes *BBA- Mol Cell Biol L* **2000**, *1487*, 61-73.
- (35) Uchida, K.; Shiraishi, M.; Naito, Y.; Torii, Y.; Nakamura, Y.; Osawa, T. Activation of stress signaling pathways by the end product of lipid peroxidation. 4-hydroxy-2-nonenal is a potential inducer of intracellular peroxide production *J. Biol. Chem.* **1999**, *274*, 2234-2242.
- (36) Uchida, K. 4-Hydroxy-2-nonenal: a product and mediator of oxidative stress *Prog. Lipid Res.* **2003**, *42*, 318-343.
- (37) Poli, G.; Biasi, F.; Leonarduzzi, G. 4-Hydroxynonenal-protein adducts: A reliable biomarker of lipid oxidation in liver diseases *Mol. Aspects Med.* **2008**, *29*, 67-71.
- (38) Sultana, R.; Perluigi, M.; Butterfield, D. A. Lipid peroxidation triggers neurodegeneration: A redox proteomics view into the Alzheimer disease brain *Free Radical Biol. Med.* **2013**, *62*, 157-169.
- (39) Perluigi, M.; Coccia, R.; Butterfield, D. A. 4-Hydroxy-2-Nonenal, a Reactive Product of Lipid Peroxidation, and Neurodegenerative Diseases: A Toxic Combination Illuminated by Redox Proteomics Studies *Antioxid. Redox Signal.* **2012**, *17*, 1590-1609.
- (40) Valko, M.; Leibfritz, D.; Moncol, J.; Cronin, M. T. D.; Mazur, M.; Telser, J. Free radicals and antioxidants in normal physiological functions and human disease *Int. J. Biochem. Cell Biol.* **2007**, *39*, 44-84.
- (41) Yin, H.; Xu, L.; Porter, N. A. Free Radical Lipid Peroxidation: Mechanisms and Analysis *Chem. Rev.* **2011**, *111*, 5944-5972.
- (42) Burton, G. W.; Ingold, K. U. Vitamin E: application of the principles of physical organic chemistry to the exploration of its structure and function *Acc. Chem. Res.* **1986**, *19*, 194-201.
- (43) Jonsson, M.; Lind, J.; Reitberger, T.; Eriksen, T. E.; Merenyi, G. Free radical combination reactions involving phenoxy radicals *J. Phys. Chem.* **1993**, *97*, 8229-8233.

- (44) Blanksby, S. J.; Ellison, G. B. Bond Dissociation Energies of Organic Molecules *Acc. Chem. Res.* **2003**, *36*, 255-263.
- (45) Maillard, B.; Ingold, K. U.; Scaiano, J. C. Rate constants for the reactions of free radicals with oxygen in solution *J. Am. Chem. Soc.* **1983**, *105*, 5095-5099.
- (46) Liu, W.; Porter, N. A.; Schneider, C.; Brash, A. R.; Yin, H. Formation of 4-hydroxynonenal from cardiolipin oxidation: Intramolecular peroxy radical addition and decomposition *Free Radical Biol. Med.* **2011**, *50*, 166-178.
- (47) Wang, Z. In *Comprehensive Organic Name Reactions and Reagents*; John Wiley & Sons, Inc.: 2010.
- (48) Krumova, K.; Friedland, S.; Cosa, G. How Lipid Unsaturation, Peroxyl Radical Partitioning, and Chromanol Lipophilic Tail Affect the Antioxidant Activity of α -Tocopherol: Direct Visualization via High-Throughput Fluorescence Studies Conducted with Fluorogenic α -Tocopherol Analogues *J. Am. Chem. Soc.* **2012**, *134*, 10102-10113.
- (49) Noguchi, N.; Yamashita, H.; Gotoh, N.; Yamamoto, Y.; Numano, R.; Niki, E. 2,2'-Azobis (4-Methoxy-2,4-Dimethylvaleronitrile), a New Lipid-Soluble Azo Initiator: Application to Oxidations of Lipids and Low-Density Lipoprotein in Solution and in Aqueous Dispersions *Free Radical Biol. Med.* **1998**, *24*, 259-268.
- (50) Barclay, L. R. C.; Locke, S. J.; MacNeil, J. M.; VanKessel, J.; Burton, G. W.; Ingold, K. U. Autoxidation of micelles and model membranes. Quantitative kinetic measurements can be made by using either water-soluble or lipid-soluble initiators with water-soluble or lipid-soluble chain-breaking antioxidants *J. Am. Chem. Soc.* **1984**, *106*, 2479-2481.
- (51) Bedard, L.; Young, M. J.; Hall, D.; Paul, T.; Ingold, K. U. Quantitative Studies on the Peroxidation of Human Low-Density Lipoprotein Initiated by Superoxide and by Charged and Neutral Alkylperoxyl Radicals *J. Am. Chem. Soc.* **2001**, *123*, 12439-12448.
- (52) http://www.wako-chem.co.jp/kaseihin_en/oilazo/V-59.htm; Wako Pure Chemical Industries: accessed 23 Feb 2017.
- (53) http://www.wako-chem.co.jp/kaseihin_en/oilazo/V-70.htm; Wako Pure Chemical Industries: accessed 23 Feb 2017.
- (54) Barclay, L. R. C.; Ingold, K. U. Autoxidation of biological molecules. 2. Autoxidation of a model membrane. Comparison of the autoxidation of egg lecithin phosphatidylcholine in water and in chlorobenzene *J. Am. Chem. Soc.* **1981**, *103*, 6478-6485.
- (55) Boozer, C. E.; Hammond, G. S.; Hamilton, C. E.; Sen, J. N. Air oxidation of hydrocarbons. II. The stoichiometry and fate of inhibitors in benzene and chlorobenzene *J. Am. Chem. Soc.* **1955**, *77*, 3233-3237.
- (56) Mulder, P.; Korth, H.-G.; Ingold, K. U. Why Quantum-Thermochemical Calculations Must Be Used with Caution to Indicate 'a Promising Lead Antioxidant' *Helv. Chim. Acta* **2005**, *88*, 370-374.
- (57) Zhang, H.-Y.; Sun, Y.-M.; Wang, X.-L. Substituent Effects on O-H Bond Dissociation Enthalpies and Ionization Potentials of Catechols: A DFT Study and Its Implications in the Rational Design of Phenolic Antioxidants and Elucidation of Structure-Activity Relationships for Flavonoid Antioxidants *Chem. Eur. J.* **2003**, *9*, 502-508.
- (58) Burton, G. W.; Doba, T.; Gabe, E.; Hughes, L.; Lee, F. L.; Prasad, L.; Ingold, K. U. Autoxidation of biological molecules. 4. Maximizing the antioxidant activity of phenols *J. Am. Chem. Soc.* **1985**, *107*, 7053-7065.
- (59) Schapira, A. H. V. Mitochondria in the aetiology and pathogenesis of Parkinson's disease *Lancet Neurology* **2008**, *7*, 97-109.
- (60) Abou-Sleiman, P. M.; Muqit, M. M. K.; Wood, N. W. Expanding insights of mitochondrial dysfunction in Parkinson's disease *Nat Rev Neurosci* **2006**, *7*, 207-219.

- (61) Beal, M. F. Mitochondria take center stage in aging and neurodegeneration *Annals of Neurology* **2005**, *58*, 495-505.
- (62) Dare, A. J.; Bolton, E. A.; Pettigrew, G. J.; Bradley, J. A.; Saeb-Parsy, K.; Murphy, M. P. Protection against renal ischemia-reperfusion injury in vivo by the mitochondria targeted antioxidant MitoQ *Redox Biology* **2015**, *5*, 163-168.
- (63) Mellors, A.; Tappel, A. L. The inhibition of mitochondrial peroxidation by ubiquinone and ubiquinol *J. Biol. Chem.* **1966**, *241*, 4353-4356.
- (64) Bentinger, M.; Brismar, K.; Dallner, G. The antioxidant role of coenzyme Q *Mitochondrion* **2007**, *7*, S41-S50.
- (65) Scheffler, I. E. In *Mitochondria*; John Wiley & Sons, Inc.: 2002, p 141-245.
- (66) James, A. M.; Smith, R. A. J.; Murphy, M. P. Antioxidant and prooxidant properties of mitochondrial Coenzyme Q *Arch. Biochem. Biophys.* **2004**, *423*, 47-56.
- (67) Kagan, V. E.; Tyurina, Y. Y.; Witt, E. In *Fat-Soluble Vitamins*; Quinn, P. J., Kagan, V. E., Eds.; Springer US: Boston, MA, 1998, p 491-507.
- (68) Maroz, A.; Anderson, R. F.; Smith, R. A. J.; Murphy, M. P. Reactivity of ubiquinone and ubiquinol with superoxide and the hydroperoxyl radical: implications for in vivo antioxidant activity *Free Radical Biol. Med.* **2009**, *46*, 105-109.
- (69) Frei, B.; Kim, M. C.; Ames, B. N. Ubiquinol-10 is an effective lipid-soluble antioxidant at physiological concentrations. *Proc. Natl. Acad. Sci. U.S.A.* **1990**, *87*, 4879-4883.
- (70) Ingold, K. U.; Bowry, V. W.; Stocker, R.; Walling, C. Autoxidation of lipids and antioxidation by alpha-tocopherol and ubiquinol in homogeneous solution and in aqueous dispersions of lipids: unrecognized consequences of lipid particle size as exemplified by oxidation of human low density lipoprotein *Proc. Natl. Acad. Sci. USA* **1993**, *90*, 45-49.
- (71) Mukai, K.; Kikuchi, S.; Urano, S. Stopped-flow kinetic study of the regeneration reaction of tocopheroxyl radical by reduced ubiquinone-10 in solution *BBA - General Subjects* **1990**, *1035*, 77-82.
- (72) Kagan, V.; Serbinova, E.; Packer, L. Antioxidant effects of ubiquinones in microsomes and mitochondria are mediated by tocopherol recycling *Biochem. Biophys. Res. Commun.* **1990**, *169*, 851-857.
- (73) Lass, A.; Forster, M. J.; Sohal, R. S. Effects of coenzyme Q10 and α -tocopherol administration on their tissue levels in the mouse: elevation of mitochondrial α -tocopherol by coenzyme Q10 *Free Radical Biol. Med.* **1999**, *26*, 1375-1382.
- (74) Lass, A.; Sohal, R. S. Effect of coenzyme Q10 and α -tocopherol content of mitochondria on the production of superoxide anion radicals *The FASEB Journal* **2000**, *14*, 87-94.
- (75) Shi, H.; Noguchi, N.; Niki, E. Comparative study on dynamics of antioxidative action of alpha-tocopheryl hydroquinone, ubiquinol, and alpha-tocopherol against lipid peroxidation. *Free Radic. Biol. Med.* **1999**, *27*, 334-346.
- (76) Sazanov, L. A. A giant molecular proton pump: structure and mechanism of respiratory complex I *Nat. Rev. Mol. Cell Biol* **2015**, *16*, 375-388.
- (77) Cramer, W. A.; Hasan, S. S.; Yamashita, E. The Q cycle of cytochrome bc complexes: A structure perspective *BBA - Bioenergetics* **2011**, *1807*, 788-802.
- (78) Shults, C. W. Therapeutic role of coenzyme Q10 in Parkinson's disease *Pharmacol. Ther* **2005**, *107*, 120-130.
- (79) Kelso, G. F.; Porteous, C. M.; Coulter, C. V.; Hughes, G.; Porteous, W. K.; Ledgerwood, E. C.; Smith, R. A.; Murphy, M. P. Selective targeting of a redox-active ubiquinone to mitochondria within cells: antioxidant and antiapoptotic properties. *J. Biol. Chem.* **2001**, *276*, 4588-4596.
- (80) Coudray, C.; Fouret, G.; Lambert, K.; Ferreri, C.; Rieusset, J.; Blachnio-Zabielska, A.; Lecomte, J.; Ebabe Elle, R.; Badia, E.; Murphy, M. P.; Feillet-Coudray, C. A mitochondrial-targeted ubiquinone modulates muscle lipid profile and improves mitochondrial respiration in obesogenic diet-fed rats. *Br. J. Nutr.* **2016**, *115*, 1155-1166.

- (81) Brigati, G.; Lucarini, M.; Mugnaini, V.; Pedulli, G. F. Determination of the Substituent Effect on the O–H Bond Dissociation Enthalpies of Phenolic Antioxidants by the EPR Radical Equilibration Technique *J. Org. Chem.* **2002**, *67*, 4828-4832.
- (82) Wijtmans, M.; Pratt, D. A.; Valgimigli, L.; DiLabio, G. A.; Pedulli, G. F.; Porter, N. A. 6-Amino-3-Pyridinols: Towards Diffusion-Controlled Chain-Breaking Antioxidants *Angew. Chem. Int. Ed.* **2003**, *42*, 4370-4373.
- (83) Mulder, P.; Korth, H.-G.; Pratt, D. A.; DiLabio, G. A.; Valgimigli, L.; Pedulli, G. F.; Ingold, K. U. Critical Re-evaluation of the O–H Bond Dissociation Enthalpy in Phenol *J. Phys. Chem. A* **2005**, *109*, 2647-2655.
- (84) Kamal-Eldin, A.; Appelqvist, L.-Å. The chemistry and antioxidant properties of tocopherols and tocotrienols *Lipids* **1996**, *31*, 671-701.
- (85) Barclay, L. R. C.; Locke, S. J.; MacNeil, J. M. Autoxidation in micelles. Synergism of vitamin C with lipid-soluble vitamin E and water-soluble Trolox *Can. J. Chem.* **1985**, *63*, 366-374.
- (86) Niki, E.; Saito, T.; Kawakami, A.; Kamiya, Y. Inhibition of oxidation of methyl linoleate in solution by vitamin E and vitamin C *J. Biol. Chem.* **1984**, *259*, 4177-4182.
- (87) Niki, E.; Noguchi, N. Dynamics of Antioxidant Action of Vitamin E *Acc. Chem. Res.* **2004**, *37*, 45-51.
- (88) Murphy, M. P. Development of lipophilic cations as therapies for disorders due to mitochondrial dysfunction *Expert Opin. Biol. Ther* **2001**, *1*, 753-764.
- (89) Murphy, M. P.; Smith, R. A. J. Targeting Antioxidants to Mitochondria by Conjugation to Lipophilic Cations *Annu. Rev. Pharmacol. Toxicol.* **2007**, *47*, 629-656.
- (90) Sokol, R. J.; McKim Jr, J. M.; Goff, M. C.; Ruyle, S. Z.; Devereaux, M. W.; Han, D.; Packer, L.; Everson, G. Vitamin E reduces oxidant injury to mitochondria and the hepatotoxicity of taurochenodeoxycholic acid in the rat *Gastroenterol.* **1998**, *114*, 164-174.
- (91) Galli, F.; Azzi, A.; Birringer, M.; Cook-Mills, J. M.; Eggersdorfer, M.; Frank, J.; Cruciani, G.; Lorkowski, S.; Ozer, N. K. Vitamin E: Emerging aspects and new directions *Free Radic Biol Med* **2017**, *102*, 16-36.
- (92) Dysken, M. W.; Sano, M.; Asthana, S.; Vertrees, J. E.; Pallaki, M.; Llorente, M.; Love, S.; Schellenberg, G. D.; McCarten, J. R.; Malphurs, J.; Prieto, S.; Chen, P.; Loreck, D. J.; Trapp, G.; Bakshi, R. S.; Mintzer, J. E.; Heidebrink, J. L.; Vidal-Cardona, A.; Arroyo, L. M.; Cruz, A. R.; Zachariah, S.; Kowall, N. W.; Chopra, M. P.; Craft, S.; Thielke, S.; Turvey, C. L.; Woodman, C.; Monnell, K. A.; Gordon, K.; Tomaska, J.; Segal, Y.; Peduzzi, P. N.; Guarino, P. D. Effect of vitamin E and memantine on functional decline in Alzheimer disease: the TEAM-AD VA cooperative randomized trial *JAMA* **2014**, *311*, 33-44.
- (93) Murphy, M. P. Antioxidants as therapies: can we improve on nature? *Free Radical Biol. Med.* **2014**, *66*, 20-23.
- (94) Niki, E. Evidence for beneficial effects of vitamin E *Korean J Intern Med* **2015**, *30*, 571-579.
- (95) Azzi, A. Molecular mechanism of alpha-tocopherol action *Free Radic Biol Med* **2007**, *43*, 16-21.
- (96) Traber, M. G.; Atkinson, J. Vitamin E, antioxidant and nothing more *Free Radic. Biol. Med.* **2007**, *43*, 4-15.
- (97) Leichert, L. I.; Gehrke, F.; Gudiseva, H. V.; Blackwell, T.; Ilbert, M.; Walker, A. K.; Strahler, J. R.; Andrews, P. C.; Jakob, U. Quantifying changes in the thiol redox proteome upon oxidative stress in vivo *Proceedings of the National Academy of Sciences of the United States of America* **2008**, *105*, 8197-8202.
- (98) Cadet, J.; Delatour, T.; Douki, T.; Gasparutto, D.; Pouget, J.-P.; Ravanat, J.-L.; Sauvaigo, S. Hydroxyl radicals and DNA base damage *Mutation Research/Fundamental and Molecular Mechanisms of Mutagenesis* **1999**, *424*, 9-21.

- (99) Evans, C.; Scaiano, J. C.; Ingold, K. U. Absolute Kinetics of Hydrogen Abstraction from Alpha-Tocopherol by Several Reactive Species Including an Alkyl Radical *J. Am. Chem. Soc.* **1992**, *114*, 4589-4593.
- (100) Krumova, K.; Oleynik, P.; Karam, P.; Cosa, G. Phenol-Based Lipophilic Fluorescent Antioxidant Indicators: A Rational Approach *J. Org. Chem.* **2009**, *74*, 3641-3651.
- (101) Lakowicz, J. R. In *Principles of Fluorescence Spectroscopy*; Lakowicz, J. R., Ed.; Springer US: 2006, p 1-26.
- (102) Turro, N. J.; Ramamurthy, V.; Scaiano, J. C. *Principles of Molecular Photochemistry: An Introduction*; University Science Books: Sausalito, CA, 2009.
- (103) Durantini, A. M.; Greene, L. E.; Lincoln, R.; Martínez, S. R.; Cosa, G. Reactive Oxygen Species Mediated Activation of a Dormant Singlet Oxygen Photosensitizer: From Autocatalytic Singlet Oxygen Amplification to Chemically Controlled Photodynamic Therapy *J. Am. Chem. Soc.* **2016**, *138*, 1215-1225.
- (104) Lincoln, R.; Durantini, A. M.; Greene, L. E.; Martinez, S. R.; Knox, R.; Becerra, M. C.; Cosa, G. meso-Acetoxyethyl BODIPY dyes for photodynamic therapy: improved photostability of singlet oxygen photosensitizers *Photochem. Photobiol. Sci.* **2017**, *16*, 178-184.
- (105) Lincoln, R.; Greene, L. E.; Bain, C.; Flores-Rizo, J. O.; Bohle, D. S.; Cosa, G. When Push Comes to Shove: Unravelling the Mechanism and Scope of Nonemissive meso-Unsaturated BODIPY Dyes. *J. Phys. Chem. B* **2015**, *119*, 4758-4765.
- (106) Rehm, D.; Weller, A. Kinetics of Fluorescence Quenching by Electron and H-Atom Transfer *Isr. J. Chem.* **1970**, *8*, 259-&.
- (107) Marcus, R. A. On the theory of oxidation—reduction reactions involving electron transfer. V. comparison and properties of electrochemical and chemical rate constants *J. Phys. Chem.* **1963**, *67*, 853-857.
- (108) Marcus, R. A. Electron Transfer Reactions in Chemistry: Theory and Experiment (Nobel Lecture) *Angew. Chem. Int. Ed. (English)* **1993**, *32*, 1111-1121.
- (109) Miller, J. R.; Calcaterra, L. T.; Closs, G. L. Intramolecular long-distance electron transfer in radical anions. The effects of free energy and solvent on the reaction rates *J. Am. Chem. Soc.* **1984**, *106*, 3047-3049.
- (110) Cody, J.; Mandal, S.; Yang, L.; Fahrni, C. J. Differential Tuning of the Electron Transfer Parameters in 1,3,5-Triarylpyrazolines: A Rational Design Approach for Optimizing the Contrast Ratio of Fluorescent Probes *J. Am. Chem. Soc.* **2008**, *130*, 13023-13032.
- (111) Verma, M.; Chaudhry, A. F.; Fahrni, C. J. Predicting the photoinduced electron transfer thermodynamics in polyfluorinated 1,3,5-triarylpyrazolines based on multiple linear free energy relationships *Org. Biomol. Chem.* **2009**, *7*, 1536-1546.
- (112) Lincoln, R.; Greene, L. E.; Krumova, K.; Ding, Z.; Cosa, G. Electronic excited state redox properties for BODIPY dyes predicted from Hammett constants: estimating the driving force of photoinduced electron transfer *J. Phys. Chem. A* **2014**, *118*, 10622-10630.
- (113) Chen, X.; Zhou, Y.; Peng, X.; Yoon, J. Fluorescent and colorimetric probes for detection of thiols *Chem. Soc. Rev.* **2010**, *39*, 2120-2135.
- (114) Chan, J.; Dodani, S. C.; Chang, C. J. Reaction-based small-molecule fluorescent probes for chemoselective bioimaging *Nat Chem* **2012**, *4*, 973-984.
- (115) Gomes, A.; Fernandes, E.; Lima, J. L. F. C. Fluorescence probes used for detection of reactive oxygen species *J. Biochem. Biophys. Methods* **2005**, *65*, 45-80.
- (116) Nagano, T. Bioimaging Probes for Reactive Oxygen Species and Reactive Nitrogen Species *Journal of clinical biochemistry and nutrition* **2009**, *45*, 111-124.
- (117) Keston, A. S.; Brandt, R. The fluorometric analysis of ultramicro quantities of hydrogen peroxide *Anal. Biochem.* **1965**, *11*, 1-5.

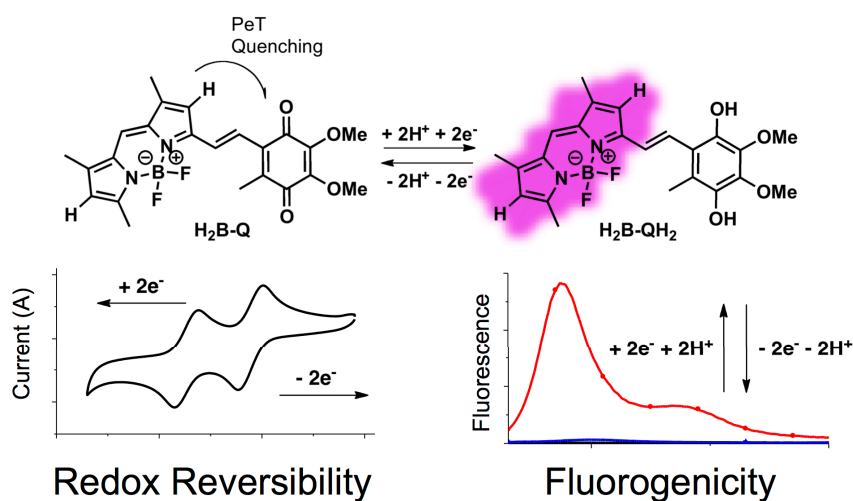
- (118) Winterbourn, C. C. The challenges of using fluorescent probes to detect and quantify specific reactive oxygen species in living cells *Biochim. Biophys. Acta* **2014**, *1840*, 730-738.
- (119) Miller, E. W.; Albers, A. E.; Pralle, A.; Isacoff, E. Y.; Chang, C. J. Boronate-Based Fluorescent Probes for Imaging Cellular Hydrogen Peroxide *J. Am. Chem. Soc.* **2005**, *127*, 16652-16659.
- (120) Dickinson, B. C.; Chang, C. J. A Targetable Fluorescent Probe for Imaging Hydrogen Peroxide in the Mitochondria of Living Cells *J. Am. Chem. Soc.* **2008**, *130*, 9638-9639.
- (121) Lippert, A. R.; Van de Bittner, G. C.; Chang, C. J. Boronate oxidation as a bioorthogonal reaction approach for studying the chemistry of hydrogen peroxide in living systems *Acc. Chem. Res.* **2011**, *44*, 793-804.
- (122) Miller, E. W.; Tulyathan, O.; Isacoff, E. Y.; Chang, C. J. Molecular imaging of hydrogen peroxide produced for cell signaling *Nat Chem Biol* **2007**, *3*, 263-267.
- (123) Wilkinson, F.; Helman, W. P.; Ross, A. B. Rate Constants for the Decay and Reactions of the Lowest Electronically Excited Singlet-State of Molecular-Oxygen in Solution - an Expanded and Revised Compilation *J. Phys. Chem. Ref. Data* **1995**, *24*, 663-1021.
- (124) Corey, E. J.; Taylor, W. C. A Study of the Peroxidation of Organic Compounds by Externally Generated Singlet Oxygen Molecules *J. Am. Chem. Soc.* **1964**, *86*, 3881-3882.
- (125) Tanaka, K.; Miura, T.; Umezawa, N.; Urano, Y.; Kikuchi, K.; Higuchi, T.; Nagano, T. Rational Design of Fluorescein-Based Fluorescence Probes. Mechanism-Based Design of a Maximum Fluorescence Probe for Singlet Oxygen *J. Am. Chem. Soc.* **2001**, *123*, 2530-2536.
- (126) Sklar, L. A.; Hudson, B. S.; Simoni, R. D. Conjugated polyene fatty acids as membrane probes: preliminary characterization *P. Natl. Acad. Sci. USA* **1975**, *72*, 1649-1653.
- (127) Steenbergen, R. H. G.; Drummen, G. P. C.; Op den Kamp, J. A. F.; Post, J. A. The use of cis-parinaric acid to measure lipid peroxidation in cardiomyocytes during ischemia and reperfusion *BBA - Biomembranes* **1997**, *1330*, 127-137.
- (128) Drummen, G. P. C.; van Liebergen, L. C. M.; Op den Kamp, J. A. F.; Post, J. A. C11-BODIPY581/591, an oxidation-sensitive fluorescent lipid peroxidation probe: (micro)spectroscopic characterization and validation of methodology *Free Radic. Biol. Med.* **2002**, *33*, 473-490.
- (129) Prime, T. A.; Forkink, M.; Logan, A.; Finichiu, P. G.; McLachlan, J.; Li Pun, P. B.; Koopman, W. J. H.; Larsen, L.; Latter, M. J.; Smith, R. A. J.; Murphy, M. P. A ratiometric fluorescent probe for assessing mitochondrial phospholipid peroxidation within living cells *Free Radic Biol Med* **2012**, *53*, 544-553.
- (130) Oleynik, P.; Ishihara, Y.; Cosa, G. Design and Synthesis of a BODIPY- α -Tocopherol Adduct for Use as an Off/On Fluorescent Antioxidant Indicator *J. Am. Chem. Soc.* **2007**, *129*, 1842-1843.
- (131) Dooley, C. T.; Dore, T. M.; Hanson, G. T.; Jackson, W. C.; Remington, S. J.; Tsien, R. Y. Imaging Dynamic Redox Changes in Mammalian Cells with Green Fluorescent Protein Indicators *J. Biol. Chem.* **2004**, *279*, 22284-22293.
- (132) Fan, Y.; Ai, H.-w. Development of redox-sensitive red fluorescent proteins for imaging redox dynamics in cellular compartments *Anal. Bioanal. Chem* **2016**, *408*, 2901-2911.
- (133) Miller, E. W.; Bian, S. X.; Chang, C. J. A Fluorescent Sensor for Imaging Reversible Redox Cycles in Living Cells *J. Am. Chem. Soc.* **2007**, *129*, 3458-3459.
- (134) Komatsu, H.; Shindo, Y.; Oka, K.; Hill, J. P.; Ariga, K. Ubiquinone-Rhodol (UQ-Rh) for Fluorescence Imaging of NAD(P)H through Intracellular Activation *Angew. Chem. Int. Ed.* **2014**, *53*, 3993-3995.
- (135) Ma, W.; Qin, L.-X.; Liu, F.-T.; Gu, Z.; Wang, J.; Pan, Z. G.; James, T. D.; Long, Y.-T. Ubiquinone-quantum dot bioconjugates for in vitro and intracellular complex I sensing *Sci. Rep.* **2013**, *3*, 1537.
- (136) Liu, X.-Y.; Long, Y.-T.; Tian, H. New insight into photo-induced electron transfer with a simple ubiquinone-based triphenylamine model *RSC Adv.* **2015**, *5*, 57263-57266.

- (137) Benniston, A. C.; Copley, G.; Elliott, K. J.; Harrington, R. W.; Clegg, W. Redox-Controlled Fluorescence Modulation in a BODIPY-Quinone Dyad *Eur. J. Org. Chem.* **2008**, *2008*, 2705-2713.
- (138) Kierat, R. M.; Thaler, B. M. B.; Krämer, R. A fluorescent redox sensor with tuneable oxidation potential *Bioorg. Med. Chem. Lett.* **2010**, *20*, 1457-1459.
- (139) Rybina, A.; Thaler, B.; Kramer, R.; Herten, D. P. Monitoring hydroquinone-quinone redox cycling by single molecule fluorescence spectroscopy *PCCP* **2014**, *16*, 19550-19555.
- (140) Lou, Z.; Li, P.; Han, K. Redox-Responsive Fluorescent Probes with Different Design Strategies *Acc. Chem. Res.* **2015**, *48*, 1358-1368.
- (141) Yu, F.; Li, P.; Wang, B.; Han, K. Reversible Near-Infrared Fluorescent Probe Introducing Tellurium to Mimetic Glutathione Peroxidase for Monitoring the Redox Cycles between Peroxynitrite and Glutathione in Vivo *J. Am. Chem. Soc.* **2013**, *135*, 7674-7680.
- (142) Yamada, Y.; Tomiyama, Y.; Morita, A.; Ikekita, M.; Aoki, S. BODIPY-Based Fluorescent Redox Potential Sensors that Utilize Reversible Redox Properties of Flavin *ChemBioChem* **2008**, *9*, 853-856.
- (143) Yan, P.; Holman, M. W.; Robustelli, P.; Chowdhury, A.; Ishak, F. I.; Adams, D. M. Molecular Switch Based on a Biologically Important Redox Reaction *J. Phys. Chem. B* **2005**, *109*, 130-137.
- (144) Yeow, J.; Kaur, A.; Anscumb, M. D.; New, E. J. A novel flavin derivative reveals the impact of glucose on oxidative stress in adipocytes *Chem. Commun.* **2014**, *50*, 8181-8184.
- (145) Kaur, A.; Brigden, K. W. L.; Cashman, T. F.; Fraser, S. T.; New, E. J. Mitochondrially targeted redox probe reveals the variations in oxidative capacity of the haematopoietic cells *Org. Biomol. Chem.* **2015**, *13*, 6686-6689.
- (146) Madhu, S.; Gonnade, R.; Ravikanth, M. Synthesis of 3,5-Bis(acrylaldehyde) Boron-dipyrromethene and Application in Detection of Cysteine and Homocysteine in Living Cells *J. Org. Chem.* **2013**, *78*, 5056-5060.
- (147) Yue, Y.; Guo, Y.; Xu, J.; Shao, S. A Bodipy-based derivative for selective fluorescence sensing of homocysteine and cysteine *New J. Chem.* **2011**, *35*, 61.
- (148) Shaughnessy, K. H.; Kim, P.; Hartwig, J. F. A Fluorescence-Based Assay for High-Throughput Screening of Coupling Reactions. Application to Heck Chemistry *J. Am. Chem. Soc.* **1999**, *121*, 2123-2132.
- (149) Matsumoto, T.; Urano, Y.; Takahashi, Y.; Mori, Y.; Terai, T.; Nagano, T. In Situ Evaluation of Kinetic Resolution Catalysts for Nitroaldol by Rationally Designed Fluorescence Probe *J. Org. Chem.* **2011**, *76*, 3616-3625.
- (150) Xia, B.; Gerard, B.; Solano, D. M.; Wan, J.; Jones II, G.; Porco Jr, J. A. ESIPT-Mediated Photocycloadditions of 3-Hydroxyquinolinones: Development of a Fluorescence Quenching Assay for Reaction Screening *Org. Lett.* **2011**, *13*, 1346-1349.
- (151) Hauser, D. N.; Dukes, A. A.; Mortimer, A. D.; Hastings, T. G. Dopamine quinone modifies and decreases the abundance of the mitochondrial selenoprotein glutathione peroxidase 4 *Free Radic. Biol. Med.* **2013**, 1-9.
- (152) Vayalil, P. K.; Oh, J.-Y.; Zhou, F.; Diers, A. R.; Smith, M. R.; Golzarian, H.; Oliver, P. G.; Smith, R. A. J.; Murphy, M. P.; Velu, S. E.; Landar, A. A Novel Class of Mitochondria-Targeted Soft Electrophiles Modifies Mitochondrial Proteins and Inhibits Mitochondrial Metabolism in Breast Cancer Cells through Redox Mechanisms *PLoS ONE* **2015**, *10*, e0120460.
- (153) Aptula, A. O.; Patlewicz, G.; Roberts, D. W. Skin Sensitization: Reaction Mechanistic Applicability Domains for Structure–Activity Relationships *Chem. Res. Toxicol.* **2005**, *18*, 1420-1426.
- (154) Kwon, S. K.; Kou, S.; Kim, H. N.; Chen, X.; Hwang, H.; Nam, S.-W.; Kim, S. H.; Swamy, K. M. K.; Park, S.; Yoon, J. Sensing cyanide ion via fluorescent change and its application to the microfluidic system *Tetrahedron Lett.* **2008**, *49*, 4102-4105.

- (155) Madhu, S.; Basu, S. K.; Jadhav, S.; Ravikanth, M. 3,5-Diformyl-borondipyrromethene for selective detection of cyanide anion *Analyst* **2012**, *138*, 299.
- (156) Sippel, T. O. New fluorochromes for thiols: maleimide and iodoacetamide derivatives of a 3-phenylcoumarin fluorophore *J. Histochem. Cytochem.* **1981**, *29*, 314-316.
- (157) Matsumoto, T.; Urano, Y.; Shoda, T.; Kojima, H.; Nagano, T. A Thiol-Reactive Fluorescence Probe Based on Donor-Excited Photoinduced Electron Transfer: Key Role of Ortho Substitution *Org. Lett.* **2007**, *9*, 3375-3377.
- (158) Caron, K.; Lachapelle, V.; Keillor, J. W. Dramatic increase of quench efficiency in "spacerless" dimaleimide fluorogens *Org. Biomol. Chem* **2011**, *9*, 185-197.
- (159) Guy, J.; Caron, K.; Dufresne, S.; Michnick, S. W.; Skene; Keillor, J. W. Convergent Preparation and Photophysical Characterization of Dimaleimide Dansyl Fluorogens: Elucidation of the Maleimide Fluorescence Quenching Mechanism *J. Am. Chem. Soc.* **2007**, *129*, 11969-11977.
- (160) Chen, Y.; Tsao, K.; De Francesco, É.; Keillor, J. W. Ring Substituent Effects on the Thiol Addition and Hydrolysis Reactions of N-Arylmaleimides *J. Org. Chem* **2015**, *80*, 12182-12192.
- (161) Page, J. H.; Ma, J.; Chiuve, S. E.; Stampfer, M. J.; Selhub, J.; Manson, J. E.; Rimm, E. B. Plasma total cysteine and total homocysteine and risk of myocardial infarction in women: A prospective study *Am Heart J* **2010**, *159*, 599-604.
- (162) Işık, M.; Guliyev, R.; Kolemen, S.; Altay, Y.; Senturk, B.; Tekinay, T.; Akkaya, E. U. Designing an Intracellular Fluorescent Probe for Glutathione: Two Modulation Sites for Selective Signal Transduction *Org. Lett.* **2014**, *16*, 3260-3263.
- (163) Rozhkov, R. V.; Davisson, V. J.; Bergstrom, D. E. Fluorogenic Transformations Based on Formation of C-C Bonds Catalyzed by Palladium: An Efficient Approach for High Throughput Optimizations and Kinetic Studies *Adv. Synth. Catal.* **2008**, *350*, 71-75.
- (164) Guo, H.-M.; Tanaka, F. A Fluorogenic Aldehyde Bearing a 1,2,3-Triazole Moiety for Monitoring the Progress of Aldol Reactions *J. Org. Chem.* **2009**, *74*, 2417-2424.
- (165) Guo, H.-M.; Minakawa, M.; Tanaka, F. Fluorogenic Imines for Fluorescent Detection of Mannich-Type Reactions of Phenols in Water *J. Org. Chem.* **2008**, *73*, 3964-3966.
- (166) Tanaka, F.; Thayumanavan, R.; Barbas, C. F. Fluorescent Detection of Carbon–Carbon Bond Formation *J. Am. Chem. Soc.* **2003**, *125*, 8523-8528.
- (167) Song, F.; Garner, A. L.; Koide, K. A Highly Sensitive Fluorescent Sensor for Palladium Based on the Allylic Oxidative Insertion Mechanism *J. Am. Chem. Soc.* **2007**, *129*, 12354-12355.
- (168) Stauffer, S. R.; Hartwig, J. F. Fluorescence Resonance Energy Transfer (FRET) as a High-Throughput Assay for Coupling Reactions. Arylation of Amines as a Case Study *J. Am. Chem. Soc.* **2003**, *125*, 6977-6985.
- (169) Khatchadourian, A.; Krumova, K.; Boridy, S.; Ngo, A. T.; Maysinger, D.; Cosa, G. Molecular imaging of lipid peroxy radicals in living cells with a BODIPY-alpha-tocopherol adduct. *Biochemistry* **2009**, *48*, 5658-5668.
- (170) Krumova, K.; Cosa, G. Bodipy Dyes with Tunable Redox Potentials and Functional Groups for Further Tethering: Preparation, Electrochemical, and Spectroscopic Characterization *J. Am. Chem. Soc.* **2010**, *132*, 17560-17569.

2 Fluorogenic Ubiquinone Analogue for Monitoring Chemical and Biological Redox Processes

"Reprinted with permission from Greene, L. E.; Godin, R.; Cosa, G. J. Am. Chem. Soc. 2016, 138, 11327. Copyright 2016 American Chemical Society."



2.1 Preface

“So we beat on, boats against the current, borne back ceaselessly into the past.”

-F. Scott Fitzgerald, *The Great Gatsby*

The complex roles of ubiquinone (Coenzyme Q10) as an electron transporter, a proton transporter, and an antioxidant were described in Chapter 1. Critical to elucidating these roles in biological systems, and their association with disease, is the development of non-invasive techniques to monitor the complex redox pathways of quinones in real time. This chapter describes the design and synthesis of a fluorogenic ubiquinone analogue which reversibly reports on the redox state of the quinone moiety utilizing key concepts described in Chapter 1 for the design of fluorescent probes.

To gain sensitivity for an off/on probe, photoinduced electron transfer (PeT) was exploited through a comparably electron rich BODIPY core and the electron poor quinone moiety of ubiquinone. Upon reduction of the quinone moiety to a quinol, PeT may no longer operate and a 200-fold fluorescence enhancement was recorded in non-polar solvents. The reversible nature of the quinone/quinol couple, conserved in the BODIPY-quinone construct, positions the new probe as a unique candidate to report on quinone redox reactions with high fluorescence sensitivity. In addition, the antioxidant behavior of the new probe was shown, as well as its synergistic activity with chromanol (the active segment of Vitamin E) towards peroxy radical scavenging. As described in Chapter 1, these are all well-established behaviors for ubiquinone which further validates the new probe as a suitable fluorogenic analogue of ubiquinone.

2.2 Abstract

We report herein the synthesis and characterization of a fluorogenic analogue of ubiquinone designed to reversibly report on redox reactions in biological systems. The analogue, **H₂B-Q**, consists of the redox-active quinone segment found in ubiquinone -2,3-dimethoxy-1,4-benzoquinone-, coupled to a boron-dipyrromethene (BODIPY) fluorophore

segment that both imparts lipophilicity in lieu of the isoprenyl tail of ubiquinone, and reports on redox changes at the quinone/quinol segment. Redox sensing is mediated by a photoinduced electron transfer intramolecular switch. In its reduced dihydroquinone form, **H₂B-QH₂** is highly emissive in non-polar media (quantum yields 55-66%), while once oxidized, the resulting quinone **H₂B-Q** emission is suppressed. Cyclic voltammetry of **H₂B-Q** shows two reversible, 1-electron reduction peaks at -1.05 V and -1.37 V (vs ferrocene) on par with those of ubiquinone. Chemical reduction of **H₂B-Q** by NaBH₄ resulted in >200-fold emission enhancement. **H₂B-QH₂** is shown to react with peroxy radicals, a form of reactive oxygen species (ROS) as well as to cooperatively interact with chromanol (the active segment of α -tocopherol). Kinetic analysis further shows the antioxidant reactivity of the non-fluorescent intermediate semiquinone. We anticipate that the **H₂B-Q/H₂B-QH₂** off/on reversible couple may serve as a tool to monitor chemical redox processes in real-time, and in a non-invasive manner.

2.3 Introduction

The mitochondrion is the major production site of cellular energy during aerobic respiration. Following electron transport in the electron transport chain of the inner mitochondrial membrane, through a series of relay systems, electrons from e.g. NADH, and succinate are transferred to oxygen, reducing it to water, and releasing energy. This energy is next stored as a proton gradient and ultimately in the form of adenosine triphosphate (ATP).¹

The essential co-factor ubiquinone (coenzyme Q10), situated in the hydrophobic core of the inner mitochondrial membrane lipid bilayer is actively involved in the transport of the electrons through the membrane. Due to its lipophilicity and its redox reversibility, ubiquinone may serve as both a mobile transporter of electrons in the redox reactions of the electron transport chain, and as a hydrogen carrier to create a proton gradient between the mitochondrial matrix and the mitochondrial intermembrane space.²⁻⁴ Importantly, ubiquinone has three redox states: ubiquinone (oxidized), ubisemiquinone (1 electron reduction from ubiquinone to yield a semiquinone radical), and ubiquinol (2 electron reduced form). Various protonation states are also possible for the reduced species, leading to complex proton-

coupled electron transfer processes.^{5,6} Besides acting as a transporter of electrons and protons in the electron transport chain, ubiquinol is also involved in preventing lipid peroxidation within the mitochondrial membrane via trapping peroxy radicals either by itself or via regenerating other antioxidants such as α -tocopherol (Vitamin E).^{7,8} The intermediate ubisemiquinone radical formed in these processes is however considered to promote oxidation through direct reaction with molecular oxygen to generate superoxide radical anion.⁹

Regular cell homeostasis is intrinsically associated with the chemical activity of ubiquinone in its triple role as an electron and proton couple transporter, and as an antioxidant. Not surprisingly, a number of pathologies are associated with ubiquinone deficiency.^{8,10-14} Key to understanding the complex role of ubiquinone and its relationship with disease, as well as the palliative effect of new drugs, is the availability of probes with the proper chemical selectivity and enhanced sensitivity toward monitoring the complex redox pathways of quinones in biological systems in real-time, in situ, and in a non-perturbing manner.¹⁵⁻¹⁷

Here we describe the design, preparation, and characterization of a two-segment - receptor-reporter-¹⁸ fluorogenic analogue of ubiquinone, conceived to report on the redox status of cellular environments. The new probe was obtained upon covalently binding 2,3-dimethoxy-1,4-benzoquinone, the redox-active quinone segment found in ubiquinone (receptor segment), to a lipophilic boron-dipyrromethene (BODIPY) fluorophore (reporter segment). The new compound exploits activation/deactivation of photoinduced electron transfer (PeT)¹⁹ between the trap and reporter segments to switch off/on the emission from the BODIPY core yielding a highly sensitive probe of redox status. Cyclic voltammogram experiments conducted in organic solutions confirmed that the redox potentials for the quinone segment of the new probe are on par with those reported for ubiquinone. Redox chemical reactions conducted in bulk, in the presence of reducing and oxidizing agents, validated the fluorogenic character of the probe, its sensitivity to redox processes, and its reversible nature. Experiments with both peroxy radicals and a fluorogenic analogue of α -tocopherol previously reported by us (**H₂B-PMHC**)²⁰ confirmed that the quinol segment regenerates chromanol as well as competitively scavenges free radicals. The new probe, for which we have coined the name **H₂B-Q**, appropriately emulates the reactivity of ubiquinone

and displays desirable fluorescence sensitivity. We anticipate that **H₂B-Q** may serve as a tool to image redox processes, potentially including at the cellular level, in real-time and in a non-invasive manner.

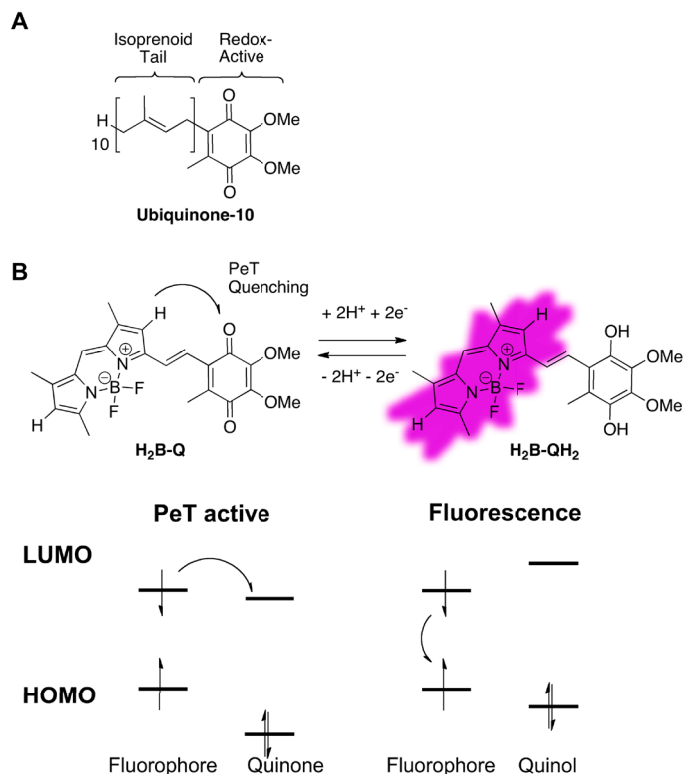
2.4 Results and Discussion

2.4.1 Design

Our design incorporated 2,3-dimethoxy-1,4-benzoquinone, the active part of ubiquinone, as the redox-sensitive receptor segment to emulate both the redox properties and the antioxidant activity of the ubiquinone/ubiquinol redox couple. Our design further envisioned a BODIPY lipophilic fluorophore as a reporter segment in lieu of the isoprenoid tail of ubiquinone, to preserve the preferential partitioning of ubiquinone within lipid membranes in the new probe.^{20,21} In addition to the desirable lipophilic character, BODIPY fluorophores have optimal spectroscopic properties and are easily modified synthetically to accommodate groups of interest.²²⁻²⁴ Furthermore, the redox properties of BODIPY dyes can be tuned to facilitate exergonic PeT in order to impart a fluorescence ‘off-on’ switching mechanism in the redox probe and ensure a high contrast between off (oxidized) and on (reduced) states.^{20,25}

To calculate and visualize the HOMO, LUMO, HOMO-1 and LUMO+1 of the optimized geometries of **H₂B-Q** (oxidized) and **H₂B-QH₂** (reduced), and to predict the potential for PeT, we employed density functional theory (DFT) calculations at the B3LYP 6-31G(d) level²⁶ (Supplementary Information, Figure 2.4, Figure 2.5). Our results suggest an operating PeT mechanism for **H₂B-Q** but not for **H₂B-QH₂** and was experimentally validated (see Spectroscopic Properties). Here the oxidized form (**H₂B-Q**) is quenched due to PeT from the photoexcited BODIPY to the LUMO of the quinone moiety (BODIPY photoinduced oxidation, Scheme 2.1). Reduction of the quinone to the dihydroquinone (**H₂B-QH₂**) deactivates PeT and restores emission by raising the HOMO and LUMO of the ubiquinol segment preventing efficient electron transfer from the BODIPY dye.

Scheme 2.1: A) Structure of Ubiquinone B) Proposed off/on sensing mechanism for **H₂B-Q** relying on PeT.



2.4.2 Synthesis

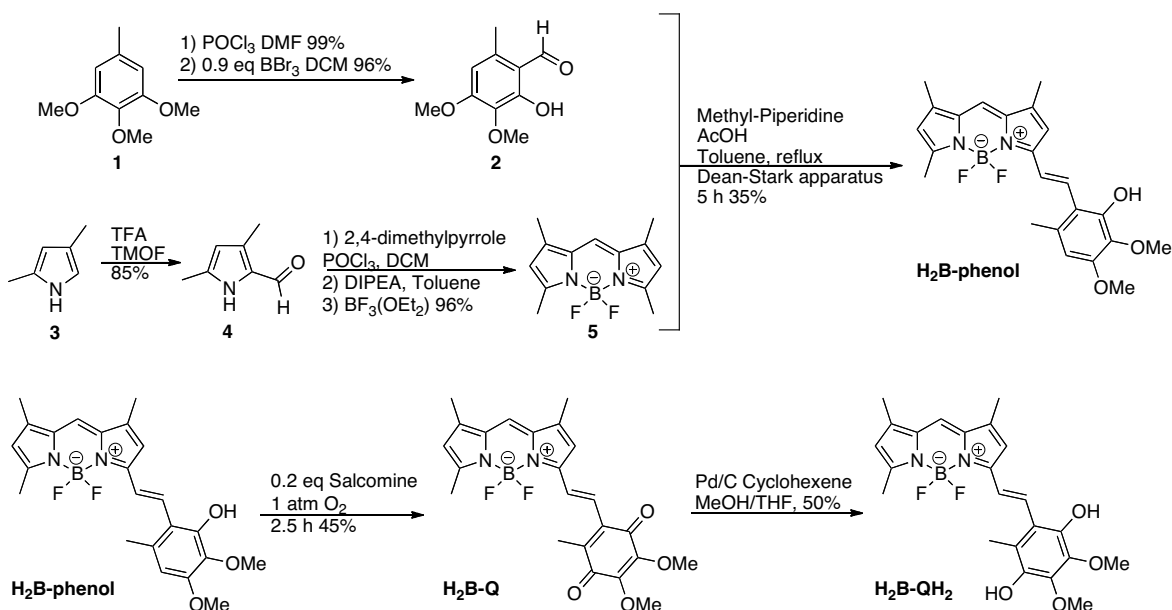
Our preparation involved a convergent synthesis where the BODIPY dye and a precursor of the redox active quinone segment were prepared separately and next coupled via Knoevenagel condensation. A BODIPY-phenol conjugate (**H₂B-phenol**) was thus initially prepared where the phenol segment carried a free *para* position that would next be oxidized to the desired quinone. This strategy circumvented the challenges associated with the synthesis and purification of dihydroquinones (prone to auto-oxidation) and quinones (Michael acceptors prone to nucleophilic attack).

Compound **1** was chosen as our starting material for the synthesis of the precursor of the redox active quinone segment, where a formyl moiety was installed using the Vilsmeier-Haack reaction according to literature procedures (Scheme 2.2).²⁷ The methoxy group *ortho* to the formyl moiety was selectively de-methylated using boron tribromide.^{28,29} Removal of this methoxy group yielded compound **2** with the desired free phenol bearing a formyl moiety

needed for coupling to BODIPY **5** via Knoevenagel condensation (*vide infra*). The BODIPY dye **5** was synthesised from **3** and **4** following a previously established protocol.³⁰

In order to couple phenol **2** and BODIPY **5**, we employed a Knoevenagel condensation³¹ in the presence of 4-methylpiperidine and glacial acetic acid to give **H₂B-phenol** as a fluorescent dye. Subsequent oxidation of **H₂B-phenol** to give the corresponding non-fluorescent quinone (**H₂B-Q**) was performed using catalytic amounts of the cobalt catalyst salcomine. **H₂B-Q** was finally reduced to the corresponding dihydroquinone, **H₂B-QH₂**, through *in situ* production of hydrogen gas from cyclohexene in the presence of palladium catalyst.

Scheme 2.2: Synthesis of **H₂B-phenol**, **H₂B-Q**, and **H₂B-QH₂**.



2.4.3 Spectroscopic properties

The absorption and fluorescence maxima, fluorescence quantum yields (Φ_f), absorption extinction coefficients and fluorescence decay lifetimes (τ_{dec}) of **H₂B-phenol**, **H₂B-Q**, and **H₂B-QH₂** are listed in Table 2.1. The dyes prepared here are characterized by red shifted absorption (ca. 580 nm) compared to precursor **5**³⁰ (505 nm) due to the extended conjugation of the BODIPY resulting upon the Knoevenagel condensation which installs an arylvinyl

moiety bond. **H₂B-phenol** and **H₂B-QH₂** both exhibit a weak absorption band around 330 nm corresponding to the aryl group, while **H₂B-Q** exhibits a strong absorption band at 287 nm corresponding to the quinone moiety (Supplementary Information, Figure 2.6), in line with previous optical investigations of ubiquinones.³²

As predicted by the DFT calculations (where PeT may operate for **H₂B-Q**), **H₂B-Q** is non-emissive in polar (acetonitrile) and non-polar (dichloromethane) solvents. **H₂B-phenol** is very fluorescent in all solvents studied, and **H₂B-QH₂** is highly fluorescent in non-polar solvents, with quantum yields ranging from 55%-66%. In polar solvents such as acetonitrile however, the emission of **H₂B-QH₂** is reduced (quantum yield \sim 1%). We postulate that PeT from the HOMO of the dihydroquinone moiety to the photo-excited BODIPY segment (BODIPY photoinduced reduction) readily occurs in polar solvents where charge transfer and formation of radical ions is stabilized. In summary, the oxidized form, **H₂B-Q** is non emissive while, as per design, the reduced form, **H₂B-QH₂** displays desirable emission. The sought after redox-mediated off/on fluorescence switching is observed in dichloromethane and toluene solvents. Modifications of the BODIPY backbone to prevent PeT from the dihydroquinone moiety will be required however to provide optimum sensitivity in polar solvents.

Table 2.1: Spectroscopic properties of **H₂B-phenol**, **H₂B-Q** and **H₂B-QH₂** in various solvents.

Dye	Solvent	Abs λ_{\max} (nm)	Em λ_{\max} (nm)	$\epsilon \times 10^3$ (M ⁻¹ cm ⁻¹)	ϕ_f	τ_{dec} (ns) ^b
H₂B-phenol	MeCN	574	602	91	0.65	3.84
	Toluene	584	597	95	0.88	3.67
	DCM	582	595	89	0.80	3.83
H₂B-Q	MeCN	573	N/A	35	<0.01	N/A
	Toluene	583	740 ^a	37	0.02	0.37
	DCM	582	N/A	34	< 0.01	N/A
H₂B-QH₂	MeCN	572	592	45	0.01	N/A
	Toluene	582	595	51	0.66	3.62
	DCM	579	595	41	0.55	3.16

^aThe significant differences in emission properties in toluene, namely a large Stokes shift, short lifetime, and solvent dependence, indicate a probable change in emission mechanism which we tentatively propose to be intramolecular charge transfer emission.³³ ^bLifetimes too short to accurately measure are indicated by 'N/A'

2.4.4 Electrochemical properties

In order to verify the electrochemical reversibility of **H₂B-Q**, cyclic voltammetry was employed to measure the redox characteristics of **H₂B-Q**. **H₂B-Q** (0.7 mM) was dissolved in argon-sparged acetonitrile (10% v/v) in toluene with 0.1 M tetrabutylammonium hexafluorophosphate as the supporting electrolyte. The ferrocenium/ferrocene (Fc⁺/Fc) redox couple was used to calibrate the silver/silver chloride reference electrode used. The cyclic voltammogram of **H₂B-Q** over 6 scans is shown in Figure 2.1. Two separate and reversible one electron redox processes were observed, in line with the electrochemical behavior of quinones in aprotic media.³⁴ The first redox process corresponds to the reduction of **H₂B-Q** to its semiquinone radical form and occurs at -1.05 V (vs. ferrocene), in accordance with reported values for ubiquinone (-1.1 V vs. ferrocene in DMF).³⁵ The second process is the subsequent reduction of the semiquinone radical to **H₂B-Q²⁻** (deprotonated **H₂B-QH₂**) at -1.37 V (vs. ferrocene), at more positive bias than what has been reported for ubiquinone (-1.8 V vs. ferrocene in DMF, no isoprenoid tail).³⁵ We attribute an easier (less negative) second reduction to the conjugation of the quinone moiety to the BODIPY core. The radical di-anion formed after two subsequent reductions is stabilized via resonance through the BODIPY core, effectively facilitating the second reduction of the quinone moiety. The peak current ratios (i_{pa}/i_{pc}) were estimated to be around 0.93 each, approximately unity, indicating that the radical anion and di-anion were stable and that no additional reactions took place. Sequential reduction/oxidation over 6 scans were performed to show the high electrochemical reversibility of **H₂B-Q** and hence its potential utility as a redox-reversible probe.

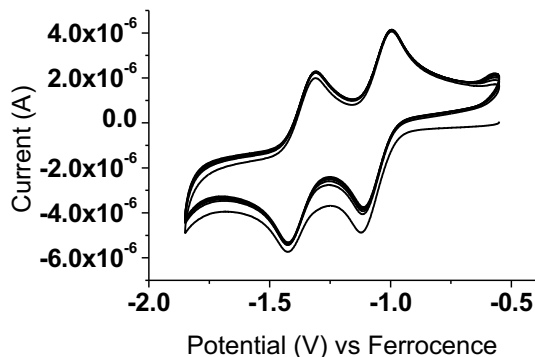
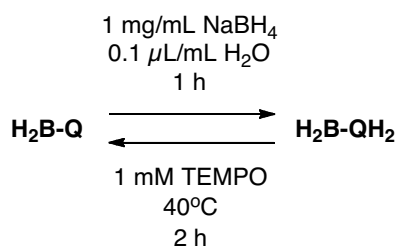


Figure 2.1: Cyclic voltammogram of **H₂B-Q** (0.7 mM) dissolved in 10% v/v MeCN in toluene (0.1 M tetrabutylammonium hexafluorophosphate) under argon recorded at 100 mVs⁻¹. Potentials were normalized to the ferrocene oxidation in these conditions.

2.4.5 Redox reversibility

After demonstrating the electrochemical reversibility of **H₂B-Q**, we next sought to test the chemical reversibility of the **H₂B-Q/H₂B-QH₂** redox couple by taking advantage of the differential fluorescence of the two redox states. The chemical reversibility of the redox couple was evaluated by the one pot sequential reduction of **H₂B-Q** by sodium borohydride (NaBH₄), followed by oxidation of the resulting **H₂B-QH₂** by the stable free radical, TEMPO (Scheme 2.3).

Scheme 2.3: One pot reduction and subsequent oxidation of **H₂BQ**.



The fluorescence spectra of the starting solution of **H₂B-Q**, (1.3 μM in toluene), and those following chemical reduction and oxidation are shown in Figure 2.2. In a cuvette, **H₂B-Q** was reduced at room temperature over NaBH₄ (1 mg/mL) with the addition of a small amount of water (1 μL/mL), acting as a source of protons, to accelerate the reaction. The increasing fluorescence intensity was periodically monitored to determine reaction completion. Maximal fluorescence was observed after 80 minutes (Figure 2.2, red trace), at

which point the insoluble NaBH_4 was filtered out. The spectroscopic properties of the reduction product matched those of isolated $\text{H}_2\text{B-QH}_2$, confirming the product of hydride reduction. Significantly, a 200-fold fluorescence enhancement was measured following completion of the reduction reaction, demonstrating the remarkable off/on fluorescence ratio of the probe.

Following confirmation of the reduction product, the resulting $\text{H}_2\text{B-QH}_2$ was next oxidized by adding 1 mM TEMPO to the same cuvette. TEMPO aerobic oxidation³⁶ was used to revert $\text{H}_2\text{B-QH}_2$ to the initial dark $\text{H}_2\text{B-Q}$ state. The minimum fluorescence intensity was observed after 2.5 hours at 40 °C. The absorption of the solution at this point matched that of pristine $\text{H}_2\text{B-Q}$ confirming the success of the oxidation. We estimate an overall yield of 52% for the full chemical reduction/oxidation cycle by comparing the initial and final absorbances at 640 nm, where the contribution of $\text{H}_2\text{B-QH}_2$ and TEMPO is negligible (Supplementary Information, Figure 2.7). At the end of the oxidation, a residual fluorescence was observed with a peak at 606 nm (opposed to 595 nm for $\text{H}_2\text{B-QH}_2$), which we attribute to side products from the TEMPO oxidation reaction.

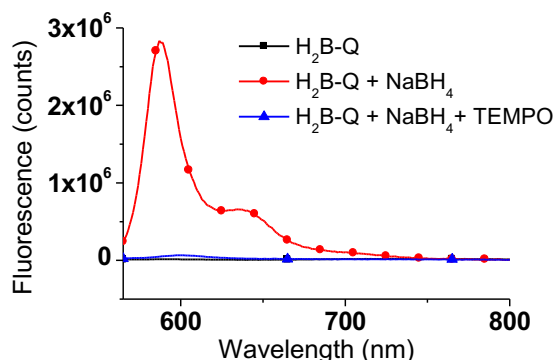


Figure 2.2: Emission spectra of $\text{H}_2\text{B-Q}$ (1.3 μM in toluene) before the redox cycle (black), after reduction by sodium borohydride (red), and after subsequent TEMPO oxidation (blue).

2.4.6 ROS scavenging and synergy with α -tocopherol

To investigate the antioxidant activity of $\text{H}_2\text{B-QH}_2$, we next determined the stoichiometric coefficient “ n ” for peroxy radical scavenging by $\text{H}_2\text{B-QH}_2$, that is the number of equivalents of ROS each equivalent of antioxidant may react with. Lipophilic peroxy

radicals were generated via thermolysis of the azo initiator, 2,2'-azobis(4-methoxy-2,4-dimethyl valeronitrile) (MeO-AMVN), in air-equilibrated dichloromethane (Equation 2.1). Intensity-time trajectories were recorded and showed the oxidation of $\mathbf{H}_2\mathbf{B-QH}_2$ (as indicated by a drop in fluorescence) over time via reaction with radicals produced upon MeO-AMVN thermolysis (Figure 2.3, solid red trace). The fluorescence quenching observed is consistent with the activation of the intramolecular PeT process upon the scavenging of peroxy radicals and concomitant oxidation of the dihydroquinone moiety ($\mathbf{H}_2\mathbf{B-QH}_2$) to the quinone form ($\mathbf{H}_2\mathbf{B-Q}$) (Equations 2.2 and 2.3). We also note that partial oxidation to the semiquinone radical (Equation 2.2) would lead to the formation of a non-emissive product due to paramagnetic quenching by the unpaired electron.³⁷

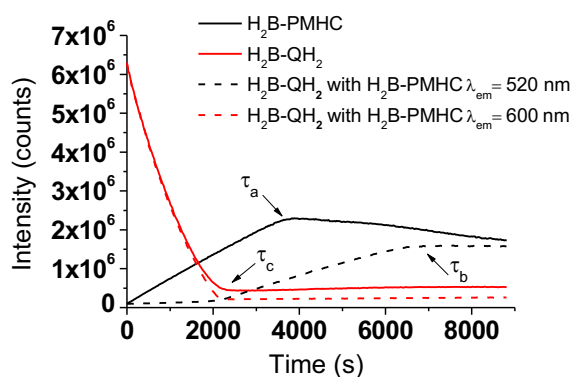
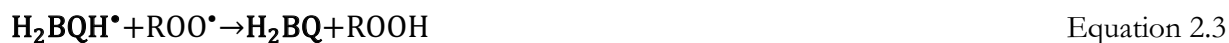


Figure 2.3: Fluorescence-time trajectories of 100 μM $\mathbf{H}_2\mathbf{B-PMHC}$ (black traces) or 100 μM $\mathbf{H}_2\mathbf{B-QH}_2$ (red traces) in the presence of 0.5 mM MeO-AMVN in dichloromethane. Dashed lines indicate the solution where $\mathbf{H}_2\mathbf{B-PMHC}$ and $\mathbf{H}_2\mathbf{B-QH}_2$ were mixed together. $\mathbf{H}_2\mathbf{B-PMHC}$ was excited at 480 nm and emission was monitored at 520 nm. In turn $\mathbf{H}_2\mathbf{B-QH}_2$ was excited at 550 nm and emission was monitored at 600 nm. τ indicates the time of consumption of antioxidant in solution. $\tau_a = 3670$ s (consumption of $\mathbf{H}_2\mathbf{B-PMHC}$), $\tau_b = 6290$ s (consumption of $\mathbf{H}_2\mathbf{B-PMHC}$ in the presence of $\mathbf{H}_2\mathbf{B-QH}_2$), and $\tau_c = 1560$ s (consumption of $\mathbf{H}_2\mathbf{B-QH}_2$).

The value of n was estimated from the consumption time (or inhibition time, τ) observed for **H₂B-QH₂** and from the rate of generation of radicals (R_g) upon rearrangement of Equation 2.4. Inhibition times (τ , Figure 2.3) were determined from the intercept of tangential lines from the decrease (or increase) in fluorescence intensity and the subsequent linear change arising from BODIPY degradation.²⁰ The rate of generation of free radicals (R_g) was in turn estimated from the thermolysis rate constant of the radical initiator (k_i) and the escape fraction (e) from geminate recombination (Equation 2.5).³⁸ Under the conditions used herein, 0.5 mM MeO-AMVN at 37 °C in air, peroxy radicals were generated at a constant rate of $R_g = 4.3 \times 10^{-8} \text{ Ms}^{-1}$ assuming $e = 0.8$ as reported in chloroform.^{39,40}

H₂B-QH₂ may react with at most 2 equivalents of ROS as shown in Equations 2.2 and 2.3, however hydroquinones may have n values ranging from 0 to 2 depending on the reaction conditions, due to their susceptibility to auto-oxidation. Under the conditions we used, we estimated n for **H₂B-QH₂** to be 0.7 based on τ_c of 1560 s. Since **H₂B-QH₂** requires only 1 reaction with ROS before becoming non-fluorescent the value of $n = 0.7$ obtained thus corresponds to the first oxidation process (formation of the quenched semiquinone, Equation 2.2). This value thus reports partial oxidation and does not reflect the potential reactivity of the semiquinone product or **H₂B-QH₂** as a whole.

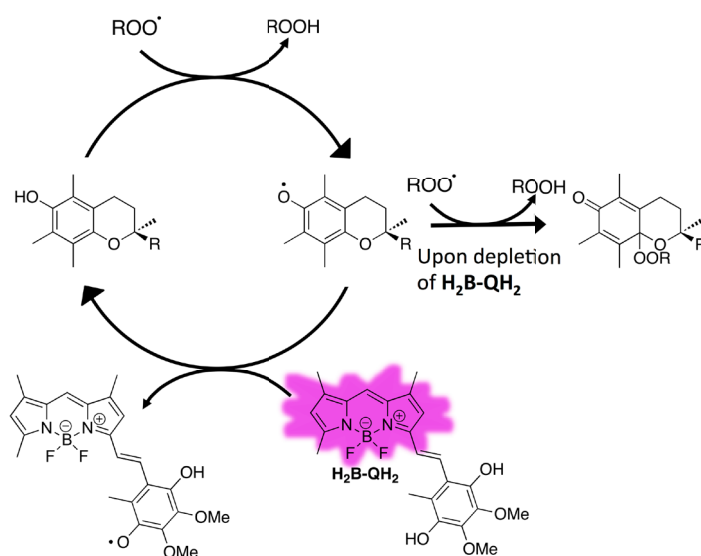
$$\tau = \frac{n [\text{Antioxidant}]}{R_g} \quad \text{Equation 2.4}$$

$$R_g = 2ek_i[\text{azo initiaor}] \quad \text{Equation 2.5}$$

Ubiquinone has been noted to participate synergistically with α -tocopherol in the inhibition of lipid peroxidation.^{7,41} Specifically it has been shown that upon the scavenging of ROS in lipid membranes by α -tocopherol to yield tocopheroxyl radical, ubiquinol can (in addition to directly scavenging ROS) regenerate α -tocopherol thus prolonging the life of α -tocopherol to act as an antioxidant (Scheme 2.4). Indeed, in organic solution, ubiquinol reacts

with tocopheroxyl radicals very efficiently with a rate constant of about $10^6 \text{ M}^{-1}\text{s}^{-1}$, while reaction with peroxy radicals proceeds with a rate constant of about $10^5 \text{ M}^{-1}\text{s}^{-1}$ (about one order of magnitude slower than that reported for α -tocopherol scavenging of peroxy radicals).⁴² The synergistic regeneration of α -tocopherol by ubiquinol may be understood thermodynamically since the one-electron redox potential of the semiquinone radical/ubiquinol couple is 0.200 V (vs. SHE) while that of tocopheroxyl radical/ α -tocopherol couple is more positive at 0.50 V (vs. SHE), suggesting that ubiquinol will spontaneously reduce the tocopheroxyl radical.⁴³ Moreover, α -tocopherol has been shown to suppress the rate of auto-oxidation of ubiquinol.⁷

Scheme 2.4: Regeneration of α -tocopherol from the tocopheroxyl radical by $\text{H}_2\text{B-QH}_2$.



To test the cooperative relationship of $\text{H}_2\text{B-QH}_2$ and α -tocopherol, we determined the inhibition time for the oxidation of an α -tocopherol analogue in the presence of $\text{H}_2\text{B-QH}_2$. Specifically, we measured how the presence $\text{H}_2\text{B-QH}_2$ delays the formation of chromanone following reaction of two peroxy radicals with the chromanol moiety. To that effect we utilized $\text{H}_2\text{B-PMHC}$, a fluorogenic α -tocopherol analogue previously reported by us.²⁰ $\text{H}_2\text{B-PMHC}$ bears a BODIPY reporter segment and a chromanol (the active part of α -tocopherol) trap segment. In its reduced form, $\text{H}_2\text{B-PMHC}$ is quenched through intramolecular PeT.

Oxidation of the non-emissive chromanol by 2 equivalents of ROS, via the also non-emissive chromanoxyl radical intermediate yields an emissive chromanone with a distinct spectral window compared to **H₂B-QH₂**. By following the onset of enhancement of oxidized **H₂B-PMHC** (establish the inhibition time) in the absence and presence of **H₂B-QH₂**, we were able to confirm the regeneration of the chromanol form from the chromanoxyl radical by **H₂B-QH₂**.

Consistent with a cooperative behaviour between **H₂B-QH₂** and α -tocopherol, addition of **H₂B-QH₂** lead to an induction in the onset of emission from oxidized **H₂B-PMHC** (compare solid vs. dashed black traces in Figure 2.3). Only after full consumption of **H₂B-QH₂** (loss of emission from this substrate) did the onset of emission from oxidized **H₂B-PMHC** take place (compare red and black dashed traces in Figure 2.3). The rate of consumption of **H₂B-QH₂** in turn was not affected by the presence of the α -tocopherol analogue. Altogether these results are in accordance with the regeneration of the non-emissive **H₂B-PMHC** from the non-emissive tocopheroxyl radical by **H₂B-QH₂**, on par with the reported synergy between α -tocopherol and ubiquinol.^{44,45}

Importantly, evaluation of the initial rates of intensity enhancement for **H₂B-PMHC** recorded without vs with **H₂B-QH₂** in otherwise identical conditions enabled determining the effect of **H₂B-QH₂** on the rate of consumption of **H₂B-PMHC**. Based on initial slopes, the rate of consumption of **H₂B-PMHC** (formation of chromanone) was 14-fold slower in the presence of **H₂B-QH₂**. Close inspection of Figure 2.3 further reveals that upon consumption of **H₂B-QH₂**, the rate of intensity enhancement upon formation of oxidized **H₂B-PMHC** is half that recorded when no **H₂B-QH₂** is present in solution. This would be consistent with the newly generated ubiquinol semiquinone radical, **H₂B-QH[•]** from **H₂B-QH₂**, effectively competing with the α -tocopherol analogue for peroxy radicals (compare τ_a vs the time span between τ_c and τ_b). A kinetic analysis based on Equation 2.6 where I_∞ , I_t , and I_0 are the intensity of **H₂B-PMHC** at the maximum, time t , and at $t=0$ s, respectively²⁰ provides the relative peroxy radical scavenging activity of **H₂B-QH[•]** to **H₂B-PMHC**. We obtained a relative rate constant for reaction with peroxy radicals of 1 for **H₂B-QH[•]** compared to **H₂B-PMHC** (Supplementary Information, Figure 2.8)

$$-\ln\left(\frac{I_{\infty}-I_t}{I_{\infty}-I_0}\right) = -\frac{k_{inh}^{H_2B-PMHC}}{k_{inh}^{unk}} \ln\left(1 - \frac{t}{\tau}\right) \quad \text{Equation 2.6}$$

Taken together, **H₂B-QH₂** reactivity towards α -tocopheroxyl radical is analogous to that reported in the literature for ubiquinol.⁷ **H₂B-QH₂** can scavenge ROS, as well as inhibit the oxidation of and regenerate α -tocopherol from the tocopheroxyl radical. We have shown this behaviour via a drop in fluorescence of **H₂B-QH₂** in the presence of **H₂B-PMHC**, as well as via a delayed fluorescence enhancement of **H₂B-PMHC**.

2.5 Conclusion

Here we provide guiding rules for the synthesis of a fluorogenic ubiquinone analogue which may provide useful in preparing related analogues in the future. Upon exploiting PeT from BODIPY to the quinone moiety (BODIPY photoinduced oxidation), we have successfully achieved a sensitive probe that is non-emissive when in its oxidized form, yet emissive once the quinone moiety becomes a dihydroquinone. While a current limitation of our newly prepared compound lies in its lower fluorescence sensitivity in high polarity solvents, an outcome that is related to the extent that PeT may occur from the ubiquinol moiety to the BODIPY dye, we anticipate that future evolutions may drastically enhance the sensitivity at this end of the solvent spectrum. In this regard, we further note that a judicious choice of the BODIPY dye utilized may render the oxidized form emissive while the reduced form may in turn be rendered non-emissive.

Important to our work is the preparation route for the ubiquinone analogue that circumvents the synthetic challenges of working with either dihydroquinone or quinone moieties by introducing this functionality through a selective oxidation of a phenol precursor in the last reaction step. Such a protocol should become important in planning related probes with sensitive receptor segments in the future.

The newly developed probe exhibits both chemical and electrochemical reversibility, crucial for monitoring both reduction and oxidation reactions. In addition, we show the

antioxidant behaviour of **H₂B-QH₂**, as well as its synergistic activity with chromanol (the active segment of Vitamin E) towards peroxy radical scavenging. These are well-established behaviours for ubiquinone which further validates **H₂B-Q** as a suitable fluorogenic analogue of ubiquinone. The newly prepared fluorogenic ubiquinone analogue, **H₂B-Q**, should provide a crucial tool towards understanding the complex role of ubiquinone in its triple character as an electron and proton couple transporter, and as an antioxidant. We anticipate that **H₂B-Q/H₂B-QH₂** may serve as a candidate for understanding complex redox reactions in non-polar media, and as a model for developing second generation probes with the required sensitivity to monitor electron transfer processes in mitochondria.

2.6 Experimental Section

2.6.1 Materials

8-Acetoxyethyl-2,6-diethyl-1,3,5,7-tetramethyl-pyrromethene fluoroborate (PM605) was purchased from Exciton, Inc. (Dayton, OH). HPLC grade solvents for spectroscopy and column chromatography were purchased through Fisher Scientific. All other chemicals were supplied by Sigma-Aldrich, Co. and used without further purification

2.6.2 Instrumentation

Absorption spectra were recorded using a Hitachi U-2800 UV-Vis-NIR spectrophotometer. Luminescence spectra were recorded using a PTI QuantaMaster spectrofluorimeter using 1 cm × 1 cm quartz cuvettes. Spectra were corrected for detector sensitivity. ¹H NMR and ¹³C NMR spectra were recorded on a Varian VNMRS 500 instrument at 500 and 125 MHz, respectively. Electrospray ionization (ESI) mass spectra were measured on a Bruker maXis impact. Voltammetry experiments were conducted with a computer-controlled CHI760C potentiostat.

2.6.3 Computational methods

Quantum mechanical calculations were performed using the Gaussian 09M package.²⁶ HOMO and LUMO orbital energies were determined from molecular geometries optimized

at the B3LYP 6-31G(d) level with an applied polarizable continuum model solvation of toluene. Orbitals were visualized using the GaussView 5 package.

2.6.4 Fluorescence quantum yield

Fluorescence quantum yields were measured using PM605 in acetonitrile as a reference ($\Phi = 0.72$). Absorption and emission spectra of PM605 and the dye of interest were measured -at the same wavelength in each case- in acetonitrile at five different concentrations. The integrated intensity versus absorbance were then plotted and fitted linearly. Relative quantum yields of fluorescence for the unknown with respect to the standard were obtained from Equation 2.7, where Φ , Δ , and η refer, respectively, to the fluorescence quantum yield, the slope obtained from the above-mentioned plot, and the solvent refractive index for the unknown (x) or standard (st).

$$\phi_x = \phi_{st} \left(\frac{\Delta_x}{\Delta_{st}} \right) \times \left(\frac{\eta_x^2}{\eta_{st}^2} \right) \quad \text{Equation 2.7}$$

2.6.5 Fluorescence lifetime studies

The fluorescence lifetime measurements were carried out using a Picoquant Fluotime 200 Time Correlated Single Photon Counting (TCSPC) setup employing an LDH 470 diode laser from Picoquant as the excitation source. The laser output was 466 nm. The excitation rate was 10 MHz, and the laser power was adjusted to ensure that the detection frequency was less than 100 kHz. The laser was controlled by a PDL 800 B picosecond laser driver from Picoquant. Photons were collected at the magic angle to mitigate polarization effects.

2.6.6 Electrochemical studies

Electrochemical measurements were performed using a three-electrode system. The working electrode was a Pt wire. A twisted Pt wire was used as the counter electrode, and a Ag/AgCl electrode (solution of 1 M KCl in a separate fritted compartment) was used as the reference. A 0.1 M solution of tetrabutylammonium hexafluorophosphate in dry

acetonitrile/toluene was used as the electrolyte solvent in which 0.7 mM **H₂B-Q** was dissolved. **H₂B-Q** concentration was determined from the absorption and calculated extinction coefficient. The solution also contained 1 mM ferrocene as an internal standard. The solution was equilibrated with argon, and measured under inert atmosphere, with a minimum scan rate of 0.1 V s⁻¹. Formal redox potentials were calculated as the average of the cathodic and anodic peak potentials observed in the cyclic voltammograms. All values were reported vs. ferrocene.

2.6.7 Kinetic studies in the presence of ROS and H₂B-PMHC

Oxidation of **H₂B-QH₂** (100 μM) and/or **H₂B-PMHC** (100 μM) in the presence of peroxy radicals generated upon MeO-AMVN (0.5 mM) thermolysis was monitored via fluorescence at 37 °C in dichloromethane. Intensity-time trajectories were recorded using a PTI QuantaMaster spectrofluorimeter equipped with a four-position Peltier with motorized turret. Three samples in total were measured: 1) **H₂B-QH₂** (100 μM), 2) **H₂B-PMHC** (100 μM), and 3) **H₂B-QH₂** (100 μM) in the presence of **H₂B-PMHC** (100 μM). Samples (1.5 mL) were measured in triangular quartz cuvettes (1cm x 1cm) with Teflon stoppers. Each sample was excited at 480 nm (**H₂B-PMHC**) and 550 nm (**H₂B-QH₂**), and emission was collected at 520 nm, and 600 nm respectively over 8000 s. Slits were set to 1 nm spectral resolution.

2.6.8 Synthesis

6-Methyl-2,3,4-trimethoxy-benzaldehyde²⁷ and 1,3,5,7-tetramethyl-8-H-pyromethene fluoroborate (5)³⁰ were prepared according to literature procedures where spectroscopic data matched that of the reported material.

3,4-Dimethoxy-2-hydroxy-6-methylbenzaldehyde (2). 6-Methyl-2,3,4-trimethoxy-benzaldehyde (1.15 g, 5.5 mmol, 1 equiv) was dissolved in dry dichloromethane (36 mL) under argon and cooled to -78 °C using a dry ice-acetone bath. Borontribromide 1 M in dichloromethane solution (4.7 mL, 4.7 mmol, 0.85 equiv) was added dropwise to the reaction mixture. The reaction mixture was gradually warmed up to room temperature. The reaction

was monitored by TLC, and it was complete after 2 h. The reaction was quenched with water (30 mL) and extracted 3 times with dichloromethane. The organic phase was washed with brine and dried over anhydrous MgSO_4 . The solvent was removed under reduced pressure leaving a pale brown solid. The solid residue was loaded onto a silica gel flash column and eluted with hexanes/ethyl acetate 4:1 to give the product as a pale yellow solid (1.02 g, 5.2 mmol, 96%). $^1\text{H-NMR}$ (300 MHz; CDCl_3): δ 12.14 (s, 1H), 10.03 (s, 1H), 6.25 (s, 1H), 3.86 (s, 3H), 3.79 (s, 3H), 2.48 (s, 3H). $^{13}\text{C-NMR}$ (75 MHz, CDCl_3): δ 193.7, 159.0, 157.5, 139.0, 134.4, 114.1, 106.1, 60.7, 56.1, 18.2. HRMS (APCI) for $\text{C}_{10}\text{H}_{11}\text{O}_4$ (M-H) calculated: 195.06628, found 195.06583.

3-(2-(E)-Vinyl-5,6-dimethoxy-3-methylphenol)-1,5,7-tetramethyl-8-H-pyrromethene fluoroborate ($\text{H}_2\text{B-phenol}$). 5 (1,3,5,7-Tetramethyl-8-H-pyrromethene fluoroborate) (390 mg, 16 mmol, 1 equiv) and **2** (280 mg, 14 mmol, 0.9 equiv) were dissolved in 15 mL of toluene under argon. 4-methylpiperidine (0.8 mL) and glacial acetic acid (0.8 mL) were added dropwise to the solution at room temperature. The reaction mixture was stirred for 5 hours at 110 °C using a Dean-Stark trap. The reaction mixture was diluted with ethyl acetate, washed once with saturated aqueous NaHCO_3 , once with saturated aqueous NH_4Cl , and the organic layer was dried over anhydrous MgSO_4 . The solvent was removed under reduced pressure leaving a dark purple residue. The crude product was loaded onto a silica gel flash column and eluted with hexanes/ethyl acetate 3:2 affording the product as a purple solid (165 mg, 24%). $^1\text{H-NMR}$ (500 MHz; CDCl_3): δ 7.94 (d, $J = 16.5$ Hz, 1H), 7.43 (d, $J = 16.4$ Hz, 1H), 6.99 (s, 1H), 6.69 (s, 1H), 6.54 (s, 1H), 6.34 (s, 1H), 6.04 (s, 1H), 3.88 (s, 3H), 3.88 (s, 3H), 2.56 (s, 3H), 2.44 (s, 3H), 2.29 (s, 3H), 2.25 (s, 3H). $^{13}\text{C-NMR}$ (126 MHz, CDCl_3): δ 156.1, 155.4, 151.7, 149.2, 140.6, 139.7, 135.1, 133.9, 133.6, 133.4, 131.0, 121.6, 118.6, 118.0, 115.7, 115.0, 106.2, 61.1, 55.7, 21.3, 14.8, 11.4, 11.3. HRMS (ESI) for $\text{C}_{23}\text{H}_{24}\text{N}_2\text{O}_3\text{BF}_2$ (M-H) calculated: 425.18535, found: 425.18524.

3-(2-(E)-Vinyl-5,6-dimethoxy-3-methyl-1,4-quinone)-1,5,7-tetramethyl-8-H-pyrromethene fluoroborate (H₂B-Q). H₂B-phenol (48 mg, 0.11 mmol, 1 equiv) was dissolved in dry acetonitrile (8 mL). Salcomine (7 mg, 0.02 mmol, 0.2 equiv) was added and the reaction mixture was stirred under an oxygen atmosphere for 3 h. The reaction mixture was filtered through celite, and the solvent was removed under reduced pressure. The resulting dark purple residue was loaded onto a silica gel flash column and eluted with hexanes/ethyl acetate 3:2 to afford the product as a dark purple residue (22 mg, 45%). ¹H-NMR (500 MHz; CDCl₃): δ 7.69 (d, *J* = 16.8 Hz, 1H), 7.24 (d, *J* = 16.8 Hz, 1H), 7.07 (s, 1H), 6.71 (s, 1H), 6.12 (s, 1H), 4.03 (s, 3H), 4.01 (s, 3H), 2.57 (s, 3H), 2.30 (s, 3H), 2.28 (s, 3H), 2.28 (s, 3H). ¹³C NMR (126 MHz; CDCl₃): δ 184.0, 183.6, 160.2, 151.3, 145.1, 144.0, 143.1, 139.4, 138.4, 136.4, 135.3, 134.8, 129.9, 125.6, 120.4, 119.6, 115.6, 61.3, 61.1, 15.1, 13.4, 11.40, 11.30. HRMS (ESI) for C₂₃H₂₄N₂O₄BF₂ (M+H) calculated: 441.17917, found: 441.17960.

3-(2-(E)-Vinyl-5,6-dimethoxy-3-methyl-1,4-quinol)-1,5,7-tetramethyl-8-H-pyrromethene fluoroborate (H₂B-QH₂). H₂B-Q (22 mg, 0.05 mmol, 1 equiv) was dissolved in tetrahydrofuran (1 mL) and methanol (2 mL) under argon. Palladium on carbon (2 mg, 10% by weight) was added followed by the addition of cyclohexene (1 mL). The reaction mixture was heated to 45 °C and stirred for 18 h. The mixture was subsequently filtered through celite and the solvent was removed under reduced pressure. The resulting crude purple residue was loaded on to a short silica gel flash column and eluted with hexanes/ethyl acetate 3:2 to afford the product as a purple residue. (11 mg, 50% yield) ¹H-NMR (500 MHz; CDCl₃ degassed): δ 7.94 (d, *J* = 16.5 Hz, 1H), 7.41 (d, *J* = 16.5 Hz, 1H), 7.01 (s, 1H), 6.70 (s, 1H), 6.05 (s, 1H), 6.03 (s, 1H), 5.40 (s, 1H), 3.95 (s, 3H), 3.89 (s, 3H), 2.55 (s, 3H), 2.33 (s, 3H), 2.30 (s, 3H), 2.25 (s, 3H). ¹³C NMR (126 MHz; CDCl₃): δ 156.0, 155.4, 142.3, 140.5, 140.2, 140.1, 139.2, 136.8, 135.0, 133.6, 130.6, 123.4, 118.8, 118.4, 118.2, 117.9, 115.1, 60.9, 60.8, 14.8, 12.1, 11.4, 11.3. HRMS (ESI) for C₂₃H₂₄N₂O₄BF₂ (M-H) calculated: 441.18027, found: 441.18103.

2.7 Supporting Information

The Supporting Information contains a detailed explanation of the calculated energies of orbitals for **H₂B-Q** and **H₂B-QH₂** as well as the visualization of the calculated orbitals for **H₂B-Q** and **H₂B-QH₂**, absorption spectra of **H₂B-Q** before reduction, after reduction, and after-re-oxidation and absorption spectra for compounds **H₂B-phenol**, **H₂B-Q**, and **H₂B-QH₂**.

¹H NMR and ¹³C NMR spectra for compounds **2**, **H₂B-phenol**, **H₂B-Q**, and **H₂B-QH₂** may be found in the Appendix at the end of the thesis.

2.7.1 Density functional theory to confirm and visualize PeT

We employed density functional theory (DFT) to calculate and visualize the HOMO, LUMO, HOMO-1 and LUMO+1 of both **H₂B-QH₂** and **H₂B-Q** in toluene. The energies in electron volts for the respective orbitals are illustrated in Figure 2.4. There is a significant drop observed in these orbitals upon oxidation of the quinone moiety.

We sought to visualize the orbitals using GaussView to assign each orbital and provide reasonable evidence to support a photoinduced electron transfer mechanism in our probes. The orbitals are shown in Figure 2.5. The HOMO and LUMO orbitals visualized for **H₂B-QH₂** are representative of typical HOMO/LUMO orbitals for BODIPYs²⁵ suggesting **H₂B-QH₂** to be a fluorescent molecule. The HOMO orbital visualized for **H₂B-Q** is representative of typical BODIPYs, however, the LUMO is not, with most electron density localized on the quinone moiety. The LUMO+1 on the other hand is representative of a typical LUMO of a BODIPY and is similar in energy to the LUMO of **H₂B-QH₂**. Taken together we may interpret these results to support an operating PeT mechanism in **H₂B-Q** as the LUMO of the molecule is centered on the quinone moiety and is lower in energy than that of the BODIPY moiety.

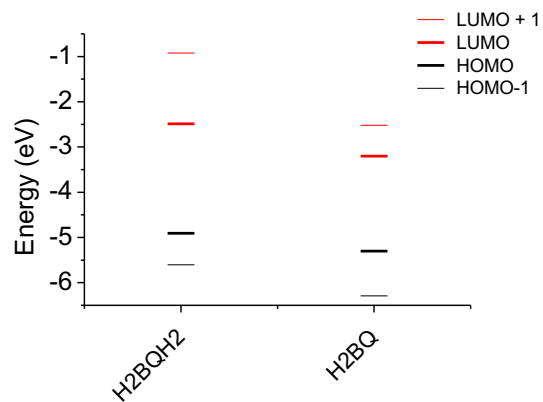


Figure 2.4 Orbital energies calculated for $\text{H}_2\text{B-QH}_2$ and $\text{H}_2\text{B-Q}$.

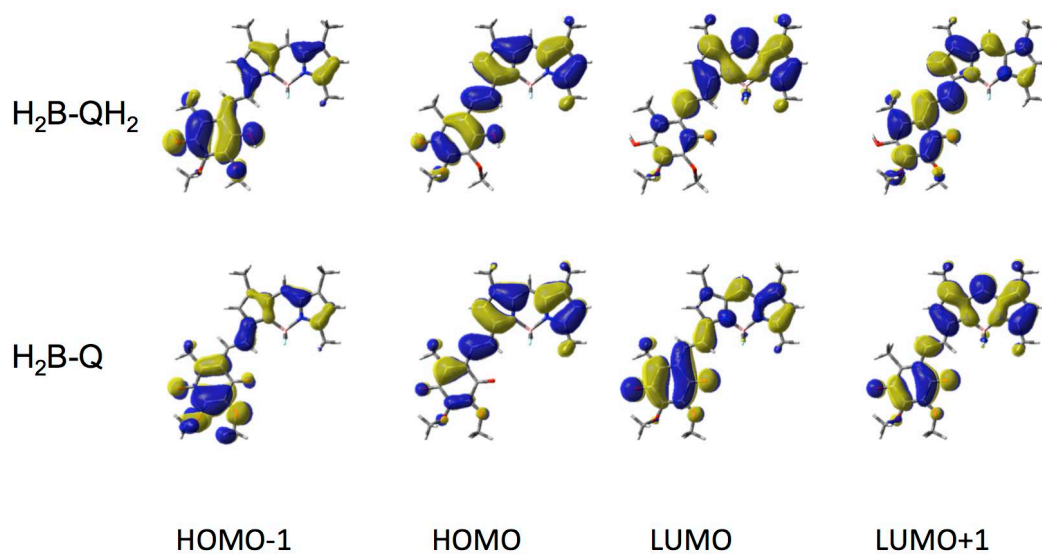


Figure 2.5 Visualization of calculated orbitals for $\text{H}_2\text{B-QH}_2$.

2.7.2 Absorption spectra

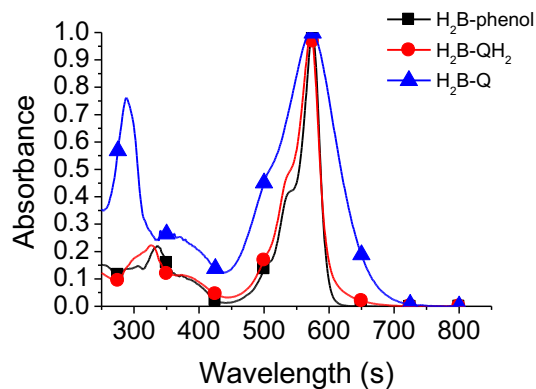


Figure 2.6 Normalized absorbance spectra of **H₂B-phenol** (black), **H₂B-QH₂** (red) and **H₂B-Q** (blue). Note the peak corresponding to the quinone moiety at 287 nm for **H₂B-Q** and the lack of this peak for **H₂B-QH₂**.

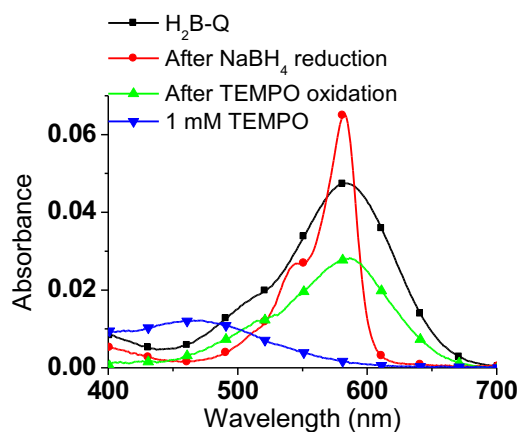


Figure 2.7 Absorbance spectra of 1.3 μM of **H₂B-Q** before reduction with NaBH₄ (black), after reduction with NaBH₄ (red), and after sequential re-oxidation with 1 mM TEMPO (green). Absorbance spectrum of 1 mM TEMPO (blue) shows negligible absorption at the absorbance maximum of **H₂B-Q**.

2.7.3 Analysis of intensity-time trajectory of **H₂B-PMHC** with **H₂B-QH₂** with

Equation 2.6

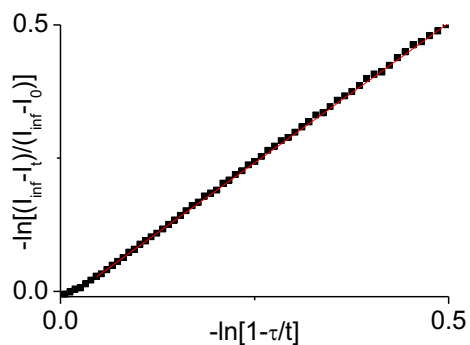


Figure 2.8 Analysis of the intensity time trajectory of **H₂BPMHC** and **H₂B-QH₂** using Equation 2.6. Fluorescence of **H₂BPMHC** was followed, and the time was adjusted such that **H₂B-QH₂** was fully consumed at $t=0$ s.

2.8 References

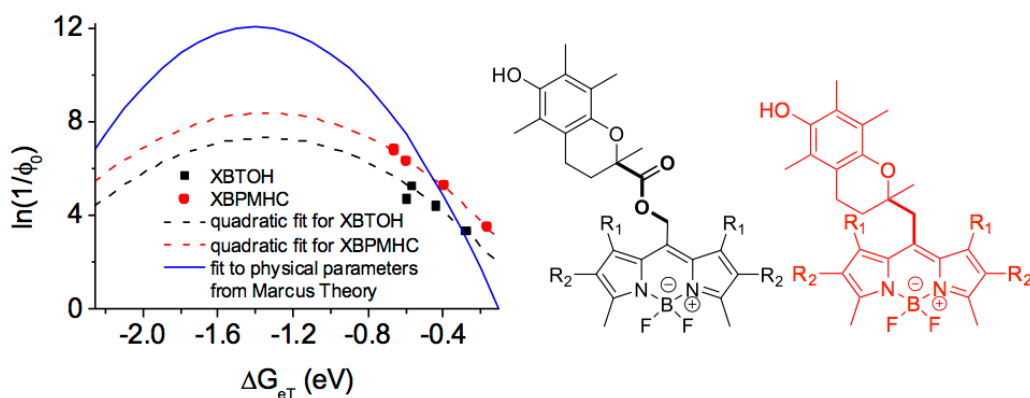
- (1) Scheffler, I. E. In *Mitochondria*; John Wiley & Sons, Inc.: 2002, p 141-245.
- (2) Trumpower, B. New concepts on the role of ubiquinone in the mitochondrial respiratory chain *J Bioenerg Biomembr* **1981**, *13*, 1-24.
- (3) Echtay, K. S.; Winkler, E.; Klingenberg, M. Coenzyme Q is an obligatory cofactor for uncoupling protein function *Nature* **2000**, *408*, 609-613.
- (4) Rokitskaya, T. I.; Murphy, M. P.; Skulachev, V. P.; Antonenko, Y. N. Ubiquinol and plastoquinol triphenylphosphonium conjugates can carry electrons through phospholipid membranes *Bioelectrochemistry* **2016**, *111*, 23-30.
- (5) Tessensohn, M. E.; Hirao, H.; Webster, R. D. Electrochemical Properties of Phenols and Quinones in Organic Solvents are Strongly Influenced by Hydrogen-Bonding with Water *J. Phys. Chem. C* **2013**, *117*, 1081-1090.
- (6) Bonin, J.; Robert, M. Photoinduced Proton-Coupled Electron Transfers in Biorelevant Phenolic Systems *Photochem. Photobiol.* **2011**, *87*, 1190-1203.
- (7) Shi, H.; Noguchi, N.; Niki, E. Comparative study on dynamics of antioxidative action of alpha-tocopheryl hydroquinone, ubiquinol, and alpha-tocopherol against lipid peroxidation. *Free Radic. Biol. Med.* **1999**, *27*, 334-346.
- (8) Kelso, G. F.; Porteous, C. M.; Coulter, C. V.; Hughes, G.; Porteous, W. K.; Ledgerwood, E. C.; Smith, R. A.; Murphy, M. P. Selective targeting of a redox-active ubiquinone to mitochondria within cells: antioxidant and antiapoptotic properties. *J. Biol. Chem.* **2001**, *276*, 4588-4596.
- (9) Schnurr, K.; Hellwing, M.; Seidemann, B.; Jungblut, P.; Kühn, H.; Rapoport, S. M.; Schewe, T. Oxygenation of biomembranes by mammalian lipoxigenases: The role of ubiquinone *Free Radical Biol. Med.* **1996**, *20*, 11-21.
- (10) Desbats, M. A.; Vetro, A.; Limongelli, I.; Lunardi, G.; Casarin, A.; Doimo, M.; Spinazzi, M.; Angelini, C.; Cenacchi, G.; Burlina, A.; Rodriguez Hernandez, M. A.; Chiandetti, L.; Clementi, M.; Trevisson, E.; Navas, P.; Zuffardi, O.; Salviati, L. Primary coenzyme Q10 deficiency presenting as fatal neonatal multiorgan failure *Eur J Hum Genet* **2015**, *23*, 1254-1258.
- (11) Wang, Y.; Oxeer, D.; Hekimi, S. Mitochondrial function and lifespan of mice with controlled ubiquinone biosynthesis *Nat Commun* **2015**, *6*.
- (12) Ogasahara, S.; Engel, A. G.; Frens, D.; Mack, D. Muscle coenzyme Q deficiency in familial mitochondrial encephalomyopathy *Proc. Natl. Acad. Sci. U.S.A.* **1989**, *86*, 2379-2382.
- (13) Dare, A. J.; Bolton, E. A.; Pettigrew, G. J.; Bradley, J. A.; Saeb-Parsy, K.; Murphy, M. P. Protection against renal ischemia-reperfusion injury in vivo by the mitochondria targeted antioxidant MitoQ *Redox Biology* **2015**, *5*, 163-168.
- (14) Coudray, C.; Fouret, G.; Lambert, K.; Ferreri, C.; Rieusset, J.; Blachnio-Zabielska, A.; Lecomte, J.; Ebabe Elle, R.; Badia, E.; Murphy, M. P.; Feillet-Coudray, C. A mitochondrial-targeted ubiquinone modulates muscle lipid profile and improves mitochondrial respiration in obesogenic diet-fed rats. *Br. J. Nutr.* **2016**, *115*, 1155-1166.
- (15) Komatsu, H.; Shindo, Y.; Oka, K.; Hill, J. P.; Ariga, K. Ubiquinone-Rhodol (UQ-Rh) for Fluorescence Imaging of NAD(P)H through Intracellular Activation *Angew. Chem. Int. Ed.* **2014**, *53*, 3993-3995.
- (16) Ma, W.; Qin, L.-X.; Liu, F.-T.; Gu, Z.; Wang, J.; Pan, Z. G.; James, T. D.; Long, Y.-T. Ubiquinone-quantum dot bioconjugates for in vitro and intracellular complex I sensing *Sci. Rep.* **2013**, *3*, 1537.

- (17) Silvers, W. C.; Prasai, B.; Burk, D. H.; Brown, M. L.; McCarley, R. L. Profluorogenic Reductase Substrate for Rapid, Selective, and Sensitive Visualization and Detection of Human Cancer Cells that Overexpress NQO1 *J. Am. Chem. Soc.* **2013**, *135*, 309-314.
- (18) Oleynik, P.; Ishihara, Y.; Cosa, G. Design and Synthesis of a BODIPY- α -Tocopherol Adduct for Use as an Off/On Fluorescent Antioxidant Indicator *J. Am. Chem. Soc.* **2007**, *129*, 1842-1843.
- (19) Liu, X.-Y.; Long, Y.-T.; Tian, H. New insight into photo-induced electron transfer with a simple ubiquinone-based triphenylamine model *RSC Adv.* **2015**, *5*, 57263-57266.
- (20) Krumova, K.; Friedland, S.; Cosa, G. How Lipid Unsaturation, Peroxyl Radical Partitioning, and Chromanol Lipophilic Tail Affect the Antioxidant Activity of α -Tocopherol: Direct Visualization via High-Throughput Fluorescence Studies Conducted with Fluorogenic α -Tocopherol Analogues *J. Am. Chem. Soc.* **2012**, *134*, 10102-10113.
- (21) Godin, R.; Liu, H.-W.; Smith, L.; Cosa, G. Dye Lipophilicity and Retention in Lipid Membranes: Implications for Single-Molecule Spectroscopy *Langmuir* **2014**, *30*, 11138-11146.
- (22) Kowada, T.; Maeda, H.; Kikuchi, K. BODIPY-based probes for the fluorescence imaging of biomolecules in living cells *Chem. Soc. Rev.* **2015**, *44*, 4953-4972.
- (23) Loudet, A.; Burgess, K. BODIPY Dyes and Their Derivatives: Syntheses and Spectroscopic Properties *Chem. Rev.* **2007**, *107*, 4891-4932.
- (24) Wood, T. E.; Thompson, A. Advances in the Chemistry of Dipyrins and Their Complexes *Chem. Rev.* **2007**, *107*, 1831-1861.
- (25) Lincoln, R.; Greene, L. E.; Krumova, K.; Ding, Z.; Cosa, G. Electronic excited state redox properties for BODIPY dyes predicted from Hammett constants: estimating the driving force of photoinduced electron transfer *J. Phys. Chem. A* **2014**, *118*, 10622-10630.
- (26) Frisch, M. J.; Trucks, G. W.; Schlegel, H. B.; Scuseria, G. E.; Robb, M. A.; Cheeseman, J. R.; Scalmani, G.; Barone, V.; Mennucci, B.; Petersson, G. A.; Nakatsuji, H.; Caricato, M.; Li, X.; Hratchian, H. P.; Izmaylov, A. F.; Bloino, J.; Zheng, G.; Sonnenberg, J. L.; Hada, M.; Ehara, M.; Toyota, K.; Fukuda, R.; Hasegawa, J.; Ishida, M.; Nakajima, T.; Honda, Y.; Kitao, O.; Nakai, H.; Vreven, T.; Montgomery Jr., J. A.; Peralta, J. E.; Ogliaro, F.; Bearpark, M. J.; Heyd, J.; Brothers, E. N.; Kudin, K. N.; Staroverov, V. N.; Kobayashi, R.; Normand, J.; Raghavachari, K.; Rendell, A. P.; Burant, J. C.; Iyengar, S. S.; Tomasi, J.; Cossi, M.; Rega, N.; Millam, N. J.; Klene, M.; Knox, J. E.; Cross, J. B.; Bakken, V.; Adamo, C.; Jaramillo, J.; Gomperts, R.; Stratmann, R. E.; Yazyev, O.; Austin, A. J.; Cammi, R.; Pomelli, C.; Ochterski, J. W.; Martin, R. L.; Morokuma, K.; Zakrzewski, V. G.; Voth, G. A.; Salvador, P.; Dannenberg, J. J.; Dapprich, S.; Daniels, A. D.; Farkas, Ö.; Foresman, J. B.; Ortiz, J. V.; Cioslowski, J.; Fox, D. J.; Gaussian, Inc.: Wallingford, CT, USA, 2009.
- (27) Lipshutz, B. H.; Lower, A.; Berl, V.; Schein, K.; Wetterich, F. An Improved Synthesis of the "Miracle Nutrient" Coenzyme Q 10 *Org. Lett.* **2005**, *7*, 4095-4097.
- (28) Schäfer, W. Selektive Ätherspaltung von 4-Hydroxy-methoxy-chinolincarbonsäureestern *Chem. Ber.* **1966**, 160-164.
- (29) Mcomie, J. F. W.; Watts, M. L.; West, D. E. Demethylation of Aryl Methyl Ethers by Boron Tribromide *Tetrahedron* **1968**, *24*, 2289-2292.
- (30) Wu, L.; Burgess, K. A new synthesis of symmetric boraindacene (BODIPY) dyes *Chem. Commun.* **2008**, 4933.
- (31) Zhang, X.; Xiao, Y.; Qi, J.; Qu, J.; Kim, B.; Yue, X.; Belfield, K. D. Long-Wavelength, Photostable, Two-Photon Excitable BODIPY Fluorophores Readily Modifiable for Molecular Probes *J. Org. Chem.* **2013**, *78*, 9153-9160.
- (32) Ma, W.; Zhou, H.; Ying, Y.-L.; Li, D.-W.; Chen, G.-R.; Long, Y.-T.; Chen, H.-Y. In situ spectroelectrochemistry and cytotoxic activities of natural ubiquinone analogues *Tetrahedron* **2011**, *67*, 5990-6000.

- (33) Hu, R.; Lager, E.; Aguilar-Aguilar, A.; Liu, J.; Lam, J. W. Y.; Sung, H. H. Y.; Williams, I. D.; Zhong, Y.; Wong, K. S.; Peña-Cabrera, E.; Tang, B. Z. Twisted Intramolecular Charge Transfer and Aggregation-Induced Emission of BODIPY Derivatives *J. Phys. Chem. C* **2009**, *113*, 15845-15853.
- (34) Costentin, C.; Robert, M.; Savéant, J.-M. Update 1 of: Electrochemical Approach to the Mechanistic Study of Proton-Coupled Electron Transfer *Chem. Rev.* **2010**, *110*, PR1-PR40.
- (35) Dutton, P. L.; Bruce, J. M. Electrochemistry of ubiquinones: Menaquinones and plastoquinones in aprotic solvents *FEBS Lett.* **1983**, 273-276.
- (36) Studer, A.; Vogler, T. Applications of TEMPO in Synthesis *Synthesis* **2008**, *2008*, 1979-1993.
- (37) Turro, N. J.; Ramamurthy, V.; Scaiano, J. C. *Principles of Molecular Photochemistry: An Introduction*; University Science Books: Sausalito, CA, 2009.
- (38) Barclay, L. R. C.; Locke, S. J.; MacNeil, J. M.; VanKessel, J.; Burton, G. W.; Ingold, K. U. Autoxidation of micelles and model membranes. Quantitative kinetic measurements can be made by using either water-soluble or lipid-soluble initiators with water-soluble or lipid-soluble chain-breaking antioxidants *J. Am. Chem. Soc.* **1984**, *106*, 2479-2481.
- (39) Noguchi, N.; Yamashita, H.; Gotoh, N.; Yamamoto, Y.; Numano, R.; Niki, E. 2,2'-Azobis (4-Methoxy-2,4-Dimethylvaleronitrile), a New Lipid-Soluble Azo Initiator: Application to Oxidations of Lipids and Low-Density Lipoprotein in Solution and in Aqueous Dispersions *Free Radical Biol. Med.* **1998**, *24*, 259-268.
- (40) We anticipate that a value of $e = 0.8$ is an underestimate, since this value was determined in chloroform, and our experiments are carried out in dichloromethane. Since geminate recombination is more likely in more viscous solvents, we expect $e > 0.8$ in the dichloromethane (less viscous).
- (41) Gille, L.; Rosenau, T.; Kozlov, A. V.; Gregor, W. Ubiquinone and tocopherol: Dissimilar siblings *Biochem. Pharmacol.* **2008**, *76*, 289-302.
- (42) Kagan, V. E.; Tyurina, Y. Y.; Witt, E. In *Fat-Soluble Vitamins*; Quinn, P. J., Kagan, V. E., Eds.; Springer US: Boston, MA, 1998, p 491-507.
- (43) Buettner, G. R. The pecking order of free radicals and antioxidants: lipid peroxidation, alpha-tocopherol, and ascorbate. *Arch. Biochem. Biophys.* **1993**, *300*, 535-543.
- (44) Frei, B.; Kim, M. C.; Ames, B. N. Ubiquinol-10 is an effective lipid-soluble antioxidant at physiological concentrations. *Proc. Natl. Acad. Sci. U.S.A.* **1990**, *87*, 4879-4883.
- (45) Ouchi, A.; Nagaoka, S.-i.; Mukai, K. Tunneling Effect in Regeneration Reaction of Vitamin E by Ubiquinol *J. Phys. Chem. B* **2010**, *114*, 6601-6607.

3 Tuning Photoinduced Electron Transfer Efficiency on Fluorogenic BODIPY- α -Tocopherol Analogues: A Quest for Darkness

Lana Greene and Gonzalo Cosa, *To be Submitted*



3.1 Preface

“In order for the light to shine so brightly, the darkness must be present.”

-Francis Bacon

Discussed in Chapter 1, reactive oxygen species (ROS) play both vital and deleterious roles in the biology of a cell. Critical for deciphering how their chemistry impacts various cell pathologies and physiologies are sensitive fluorogenic probes, that in combination with microscopy, enable real-time exploration of the spatiotemporal evolution of ROS in a non-invasive manner. Fluorogenic analogues of Vitamin E developed by our group have, in this regard, been instrumental in monitoring lipid peroxidation. Prepared as two-segment trap-reporter (chromanol-BODIPY) probes, photoinduced electron transfer (PeT) has been essential in providing these probes with an off/on switch mechanism warranting the necessary sensitivity.

Chapter 3 explores PeT efficiency of these probes to rationalize the preparation of more sensitive probes required to report on small changes in antioxidant status *in vivo*. We rationalize, within the context of Marcus theory of electron transfer, how substituents on the BODIPY core and linker length joining the trap and reporter segments tune PeT efficiency. Our results show that upon effectively competing with radiative rate, we may increase our dynamic range from 20 to 1,000, leading us to develop a new generation BODIPY-tocopherol probe, H₄BPMHC which will be discussed at length in Chapter 4.

3.2 Abstract

Fluorogenic analogues of Vitamin E developed by our group have been instrumental in monitoring reactive oxygen species (ROS) within lipid membranes. Prepared as two-segment trap-reporter (chromanol-BODIPY) probes, photoinduced electron transfer (PeT) was utilized to provide these probes with an off/on switch mechanism warranting the necessary sensitivity. Herein we rationalize within the context of Marcus theory of electron transfer how substituents on the BODIPY core and linker length joining the trap and reporter segments,

tune PeT efficiency. DFT and electrochemical studies were used to estimate the thermodynamic driving force of PeT in our constructs. By tuning the redox potential over a 400 mV range, we observed over an order of magnitude increase in PeT efficiency. Increasing the linker length between the chromanol and BODIPY by 2.8 angstroms in turn decreased PeT efficiency 2.7-fold. Our results illustrate how substituent and linker choice enable “darkening” the off state of fluorogenic probes based on BODIPY fluorophores, by favoring PeT over radiative emission from the singlet excited state manifold. Ultimately, our quest for BODIPY darkness brings light to the sensitivity ceiling one may achieve.

3.3 Introduction

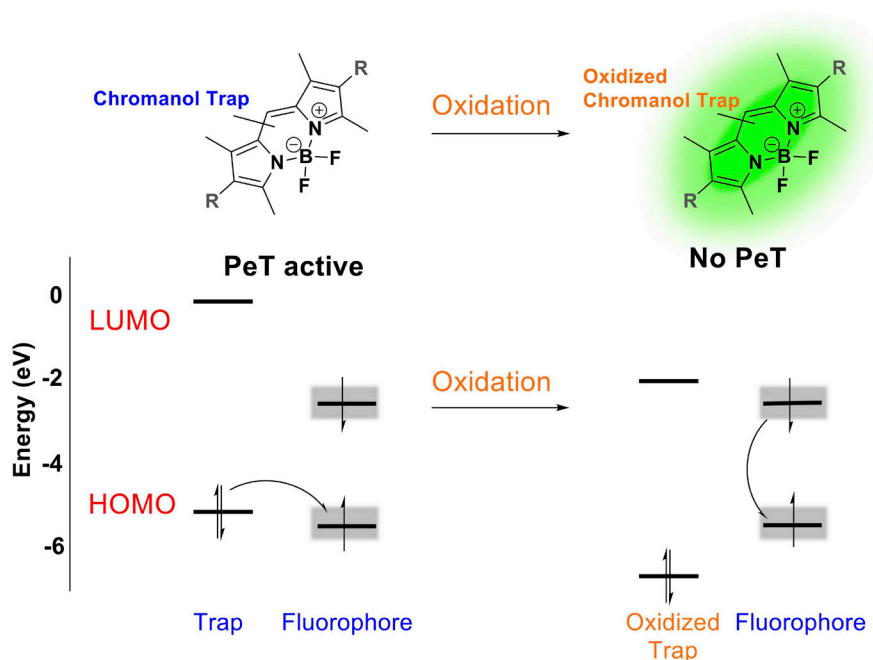
Reactive oxygen species (ROS) and their detrimental/beneficial effects have been greatly debated recently.¹ Crucial to unravelling the specific roles and implications of ROS in various pathologies^{2,3} and physiologies⁴ are tools that may report the evolution of ROS concentration in both time and space coordinates in live cells and in a non-invasive manner. Sensitive and chemoselective fluorogenic probes, when combined with fluorescence microscopy, have emerged as a solution to this challenge, yielding fundamental information of relevance to cell physiology.⁵⁻⁷

Over the past decade, we have reported a number of ROS sensors designed as fluorogenic analogues of α -tocopherol,⁸⁻¹¹ the most active lipid soluble antioxidant.¹² These are two-segment trap-reporter (chromanol-BODIPY) probes that become fluorescent upon trapping lipid peroxy radicals. The new probes have been instrumental in monitoring ROS within lipid membranes in high throughput, within single cells and in single molecule studies.^{10,11,13-15} The preserved chromanol head group in the probes has warranted for highly efficient trapping of lipid peroxy radicals, the chain carriers in lipid chain auto-oxidation (rate constants of $3 \times 10^6 \text{ M}^{-1}\text{s}^{-1}$, and $6 \times 10^3 \text{ M}^{-1}\text{s}^{-1}$ have been reported for α -tocopherol in homogeneous solution and lipid bilayers, respectively^{12,16}). In the new probes, the phytyl tail of α -tocopherol was replaced with a BODIPY lipophilic fluorophore to provide a reporting moiety while ensuring partitioning into lipid membranes, the site of peroxy radical mediated lipid chain auto-oxidation.

Our probes rely on intramolecular photoinduced electron transfer (PeT) to switch emission from the reduced (off/chromanol) to the oxidized (on/chromanone) state upon trapping lipid peroxy radicals (Scheme 3.1). Here the chromanol moiety, but not its oxidized chromanone form, is able to reduce the photo-excited BODIPY segment, providing an alternative decay pathway from the singlet excited state manifold, effectively quenching the fluorescence. Oxidation of the chromanol moiety with two equivalents of alkoxy or peroxy radicals next restores the emission.

Our quest to improve the sensitivity of our probes to detect trace levels of ROS, has led us to study the effect of substituents on the BODIPY core, and of the linker length between the chromanol and BODIPY segments, on the rate constant for intramolecular PeT (k_{PeT}). In order to maximize sensitivity, we need to ensure that the probe emission is at a minimum, ideally zero, when in the reduced form. Upon oxidation of the trap segment in the probe, the BODIPY emission quantum yield should be fully restored. The onus thus relies on maximizing the rate constant of PeT in the reduced state to effectively compete with the rate constant for radiative process (*i.e.* $k_{PeT} \gg k_{rad}$). Preventing any PeT from taking place in the oxidized form of the probe is also critical to ensure the maximum emission quantum yield may be obtained from the BODIPY core once trapping of peroxy radicals took place.

Scheme 3.1 Schematic representation of the PeT mechanism operating in fluorogenic α -tocopherol analogues, where HOMO/LUMO levels of the BODIPY fluorophores presented here may be tuned as shown by the grey band (*vide infra*).



Armed with a number of previously reported fluorogenic probes and a number of newly prepared compounds to cover a broad range of redox potentials and linker lengths, here we compare and discuss how these factors affect PeT efficiency, within the framework of Marcus Theory of Electron Transfer. Our results were recorded in two different scaffolds bearing either an ester linkage (XBTOH scaffold)⁸⁻¹⁰ or an alkyl linkage (XBPMHC scaffold)¹⁰ between the trap-reporter segments at the *meso* position of the BODIPY core (Figure 3.1). Substitution with either ethyl groups, hydrogen, or chlorines at the 2 and 6 positions of the BODIPY core and alkyl vs hydrogen at positions 1 and 7 provided a series to study how changes in redox potentials of the BODPY core translate to enhanced PeT in the reduced state of the probes, for each of the two scaffolds. Here the sensitivity dynamic range was increased by 1.5 orders of magnitude by tuning the redox potentials within a ca 400 mV window.

Our study reveals the importance of substituent choice and linker length in designing BODIPY-based lipophilic fluorogenic probes.

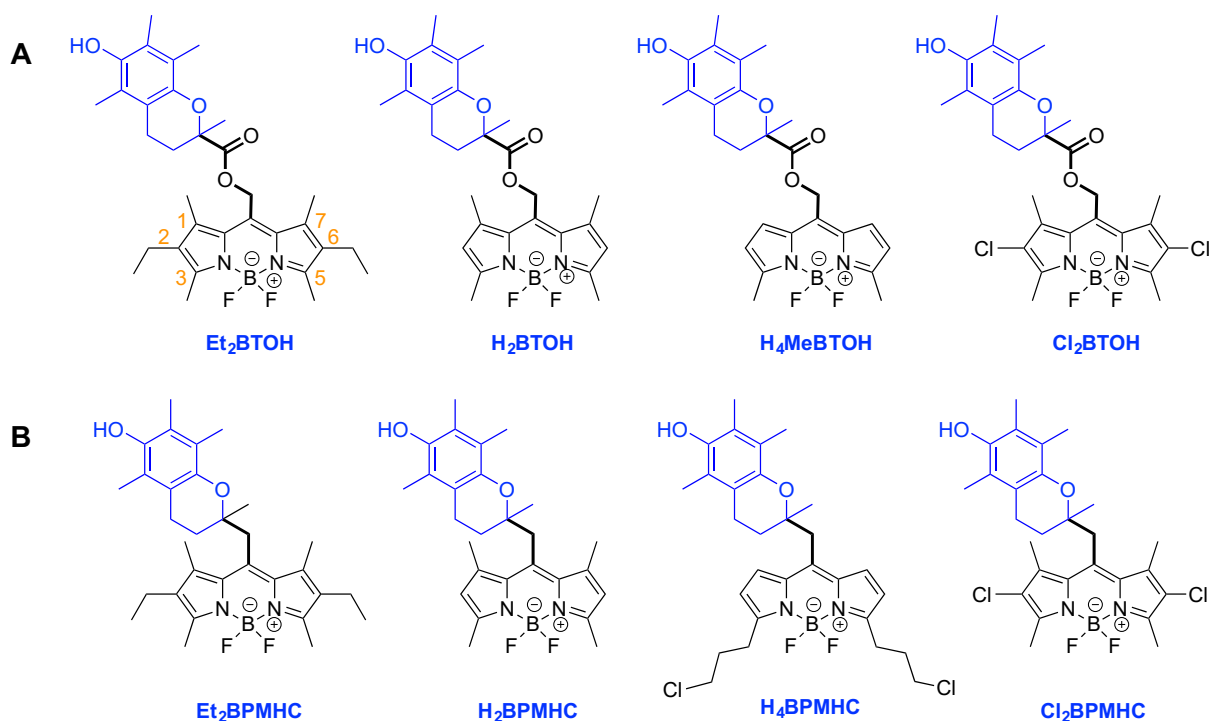


Figure 3.1 Fluorogenic α -tocopherol analogues discussed here. A) XBTOH series, B) XPMHC series. Numbering of the positions of the BODIPY core is shown in orange.

3.4 Results and Discussion

3.4.1 Library of BODIPY chromanol constructs

We reasoned that in our quest for darkness in the off state, we must maximize k_{peT} for the BODIPY-chromanol scaffolds, as the radiative rate (k_{rad}) remains fairly constant in as far as there is no electronic coupling between chromophore and trap.¹⁷ Based on Marcus theory of electron transfer,¹⁸⁻²⁰ k_{eT} is given by Equation 3.1 where the activation free energy, ΔG^{\ddagger}_{eT} , is related to the free energy of electron transfer ΔG°_{eT} (Equation 3.2, where λ is the reorganization energy) and thus with the one electron standard redox potentials of the electron donor and acceptor ($E_{D^{+}/D}$ and $E_{A/A^{\cdot}}$, respectively), see Equation 3.3.^{20,21} In Equation 3.3, $\Delta E_{0,0}$ is the vibrational zero electronic energy of the excited BODIPY, and ω is the coulombic attraction of the contact ion pair (values of -0.1 eV are typically used in the case of acetonitrile which corresponds to a separation of about 6 Å, *vide infra*).²² Marcus theory additionally shows that the pre-exponential factor, A , in Equation 3.1 is associated to electronic coupling, and depends exponentially on the distance between the donor and acceptor segments (chromanol

and photoexcited BODIPY) as described in Equation 3.4.²⁰ Here, k_0 is the rate constant of electron transfer when the donor and acceptor are in Van der Waals contact (R_{DA}^0), R_{DA} is the distance between the donor and acceptor, and β is the sensitivity parameter of k_{eT} to distance.

$$k_{eT} = A e^{\frac{-\Delta G_{eT}^\ddagger}{RT}} \quad \text{Equation 3.1}$$

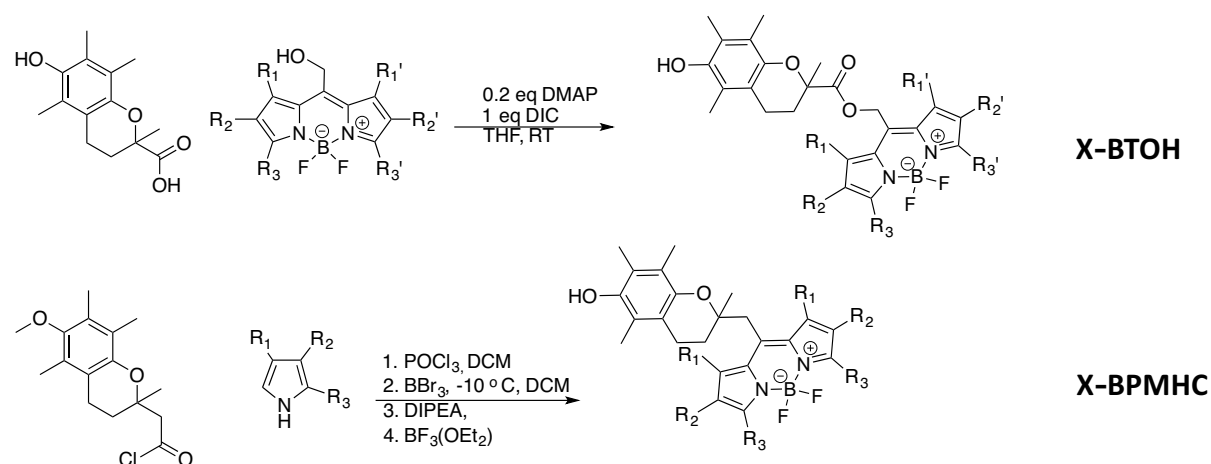
$$\Delta G_{eT}^\ddagger = \frac{(\Delta G_{eT}^\circ + \lambda)^2}{4\lambda} \quad \text{Equation 3.2}$$

$$\Delta G_{eT}^\circ = [(E_{D^{+\bullet}/D}^\circ - E_{A/A^{-\bullet}}^\circ) - \Delta E_{0,0} + \omega] \quad \text{Equation 3.3}$$

$$k_{eT} = k_0 e^{[-\beta(R_{DA} - R_{DA}^0)]} \quad \text{Equation 3.4}$$

To explore the role that varying the linker and varying the substituents/redox potential play on PeT, we collected photophysical and electrochemical parameters for newly prepared trap-reporter chromanol-BODIPY compounds and compared these to existing data from previously published probes.

BODIPY-chromanol compounds new to this work were synthesised via 2 general routes; a coupling reaction to obtain the XBPMHC series¹⁰ and a condensation reaction to obtain the XBTOH series (Scheme 3.2).⁸⁻¹⁰ In the latter case, synthesis relied on coupling the corresponding *meso*-hydroxymethyl BODIPY with the commercially available trolox compound facilitated by diisopropylcarbodiimide and catalytic dimethylaminopyridine. Here the *meso*-hydroxymethyl BODIPY dyes were prepared according to literature procedures involving the condensation of acetoxy-acetyl chloride with 2 equivalents of pyrrole followed by deprotonation and chelation with boron, followed by hydrolysis of the resulting ester to an alcohol.^{17,23}

Scheme 3.2 General synthesis of the tocopherol-BODIPY constructs compared in this paper

The synthesis of the XBPMHC series involved, in turn, building the BODIPY moiety directly onto the chromanol moiety through a condensation reaction between 2 pyrroles, and a methoxy-protected chromanol bearing an acid chloride.¹⁰ Subsequent deprotection of the chromanol, deprotonation of the dipyrin and chelation with boron yielded the final probe. Addition of chlorines was obtained through reaction with *N*-chlorosuccinimide.¹⁷

3.4.2 DFT studies

In order to predict and visualize PeT between the chromanol and BODIPY moieties, we conducted calculations via density functional theory (DFT) at the B3LYP 6-31G(d) level.²⁴ The calculated energies of the HOMO and LUMO for each chromanol moiety and BODIPY moiety are shown in Figure 3.2 (See Supplementary Information for structures of BODIPY moieties and visualized orbitals, Figures 3.4-3.7). Our results suggest an operating PeT mechanism for all the dyes presented herein, where the chromanol ring (either trolox methyl ester or 2,2,5,7,8-pentamethyl-6-chromanol (PMHC)) acts as the electron donor (higher HOMO energy) and the photoexcited BODIPY moiety as the electron acceptor. Importantly, in all cases, LUMO levels of the BODIPY dyes are lower in energy than the chromanone (oxidized chromanol) LUMO, preventing reverse PeT (i.e. one electron reduction of chromanone from photoexcited BODIPY), from taking place. DFT results thus predict our probes to be intramolecularly quenched (off) in the reduced state, and fluorescent (on) in the

withdrawing nature of the ester linkage of XBTOH (when compared to the alkyl linkage of XBPMHC) making the BODIPY core a better electron acceptor overall.

3.4.3 Evaluation of $\Delta G^\circ_{\text{PeT}}$ from electrochemical and photophysical data

To calculate $\Delta G^\circ_{\text{PeT}}$ for the XBTOH and XBPMHC series, we used the oxidation potential of trolox (0.6 V) and PMHC (0.5V), respectively, recorded in acetonitrile versus ferrocene.²⁵ Utilizing Equation 3.3, in conjunction with the one electron reduction potentials recorded herein (see Supplementary Information for cyclic voltammograms obtained in acetonitrile, Figures 3.8 and 3.9), or previously reported in acetonitrile,^{17,26,27} we estimated $\Delta G^\circ_{\text{PeT}}$ for each BODIPY-chromanol construct (Table 3.1). Cathodic peak potentials were used in lieu of redox potentials when reversible reduction potentials were not available for the BODIPY dyes. For the XBTOH and XBPMHC series, the redox potentials of the BODIPY moieties studied were tuned over a 300 mV or 460 mV window, respectively, upon changing the substitution from ethyl to chlorine.

Table 3.1 Calculated $\Delta G^\circ_{\text{PeT}}$, from measured $E^\circ_{A/A^{\cdot-}}$ and $\Delta E_{0,0}$.

Dye	$E^\circ_{A/A^{\cdot-}}$ (V) ^a	$E^\circ_{A^{\cdot+}/A}$ (V) ^a	$\Delta E_{0,0}$ (eV) ^b	$\Delta G^\circ_{\text{PeT}}$ (eV)
Et ₂ BOAc	-1.48 ^{c,d}	0.70 ^d	2.26 ^d	-0.28
H ₂ BOAc	-1.44 ^{c,d}	0.75 ^d	2.38 ^d	-0.44
H ₄ MeBOAc	-1.29	1.06 ^e	2.39	-0.60
Cl ₂ BOAc	-1.18 ^d	0.99 ^d	2.25 ^d	-0.57
Et ₂ BCH ₃	-1.84 ^d	0.60 ^d	2.41 ^d	-0.17
H ₂ BCH ₃	-1.73 ^d	0.77 ^d	2.53 ^d	-0.40
H ₄ BCH ₃	-1.41	0.90 ^f	2.47	-0.67
Cl ₂ BCH ₃	-1.38 ^d	0.90 ^d	2.38 ^d	-0.60

^aPotentials are reported vs ferrocene and were measured in acetonitrile. ^bThe vibrational zero electronic energy of the excited BODIPY ($\Delta E_{0,0}$) was determined from the intercept of the normalized absorption and emission spectrum of the BODIPY dye of interest. ^cCathodic peak potential. ^dPreviously reported by us. ²⁶ ^eAnodic peak potential. ^fAcquired at 500 mVs⁻¹.

Consistent with our DFT calculations, PeT from the trolox ester or PMHC, to the BODIPY dyes, was determined to be exergonic for all the dyes presented in Figure 3.1. Furthermore, given that values of $\Delta E_{0,0}$ remained fairly constant within either the XBTOH or

XBPMHC series, changes in $\Delta G^\circ_{\text{PeT}}$ followed the redox potentials of the BODIPY core. Thus, Et_2BCH_3 , having the most negative reduction potential, corresponded with the least exergonic $\Delta G^\circ_{\text{PeT}}$. The $\Delta E_{0,0}$ value became an important factor when comparing dyes with relatively similar reduction potentials as is the case between Cl_2BCH_3 and H_4BCH_3 . The larger $\Delta E_{0,0}$ of H_4BCH_3 allowed for more exergonic PeT by ~ 0.1 eV despite having a marginally lower redox potential. The chlorine groups of Cl_2BCH_3 lead to a bathochromic shift in the absorption and emission of the BODIPY chromophore,^{23,28} reducing the exergonic nature of PeT. Our DFT calculations did not predict more exergonic PeT for H_4BCH_3 . However, calculations were performed for closed shell ground state, rather than excited state molecules, likely causing the discrepancy between $\Delta G^\circ_{\text{PeT}}$ predicted by DFT and calculated from redox potentials.

3.4.4 Evaluation of the rate constant and efficiency of PeT

To evaluate how PeT outcompetes other processes once the molecule is in its first excited singlet state (PeT efficiency, ϕ_{PeT}), and the rate constant for PeT, we next compared the experimentally determined fluorescence quantum yields (ϕ_f , Equation 3.5) and fluorescence decay lifetimes (τ_{dec} , equation 3.6) of our BODIPY-chromanol constructs in the reduced state (off) and once oxidized to restore their emission (Table 3.2). Fluorescence quantum yields and decay lifetimes provides an estimate of the PeT rate constant as $k_{\text{PeT}} \approx k_{\text{rad}}/\phi_f$ in our BODIPY-chromanol constructs, under the assumption that $k_{\text{rad}} > k_{\text{ISC}}, k_{\text{IC}}$, and that $k_{\text{PeT}} \gg k_{\text{rad}}$. Fluorescence quantum yields for the isolated BODIPY constructs utilized herein are typically larger than 0.8, satisfying the first condition.^{17,26} Furthermore, lifetimes measured for our oxidized probes, on par with BODIPY fluorophores with analogous substituents,^{17,26} indicate that emission is fully restored upon oxidation. While the quantum yields of our oxidized compounds are slightly smaller (by 10-30%) than those expected for BODIPY, the discrepancy likely reflects a lack of full conversion to oxidized product and/or degradation of the BODIPY under the oxidation conditions used. In turn, fluorescence quantum yields and lifetimes measured for our reduced probes show that $k_{\text{PeT}} \gg k_{\text{rad}}$, ranging from 20-1,000 times larger, satisfying the second condition. Under the above conditions, the

rate constant for PeT is thus proportional to the inverse of the measured fluorescence quantum yield ($k_{PeT} = k_{rad}/\phi_f$), and PeT efficiency may be considered equal to $1-\phi_f$.

$$\phi_f = \frac{k_{rad}}{k_{rad}+k_{nr}+k_{PeT}} \quad \text{Equation 3.5}$$

$$\tau_{dec} = \frac{1}{k_{dec}} = \frac{1}{k_{rad}+k_{nr}+k_{PeT}} \quad \text{Equation 3.6}$$

$$k_{nr} = k_{IC} + k_{ISC} \quad \text{Equation 3.7}$$

Table 3.2 Photophysical properties of fluorogenic BODIPY-chromanol constructs and of their oxidized counterparts produced following reaction with thermally generated peroxy radicals and their corresponding fluorescence enhancement (Fl. En).

Compound	abs. λ_{max} (nm)	em. λ_{max} (nm)	ϕ_f^a	τ_{dec} (+/- 0.01 ns) ^b	k_{rad} (10^8 s^{-1}) ^b	$k_{nr} + k_{PeT}$ (10^8 s^{-1}) ^b	Fl. En ^c
Et ₂ BTOH	544	561	0.036 +/- 0.001	0.74	0.48	13	22
Et ₂ BTOH _{ox}			0.810	6.83	1.20	0.26	
H ₂ BTOH	517	528	0.012 +/- 0.001	0.251	0.48	40	51
H ₂ BTOH _{ox}			0.760	5.69	1.40	0.37	
Cl ₂ BTOH	545	562	0.0052 +/- 0.0004	0.15	0.35	66	102
Cl ₂ BTOH _{ox}			0.510	6.38	0.80	0.77	
H ₄ MeBTOH	520	529	0.0099 +/- 0.0004	0.10	0.99	99	71
H ₄ MeBTOH _{ox}			0.700	7.10	0.99	0.42	
Et ₂ BPMHC	530	558	0.030 +/- 0.001	0.21	1.40	45	42
Et ₂ BPMHC _{ox}			0.500	5.03	0.99	1.0	
H ₂ BPMHC	507	528	0.0051 +/- 0.0004	0.10	0.5	100	131
H ₂ BPMHC _{ox}			0.540	5.67	0.95	0.81	
Cl ₂ BPMHC	531	558	0.0018 +/- 0.0001	0.04	0.5	250	274
Cl ₂ BPMHC _{ox}			0.480	5.71	0.86	0.89	
H ₄ BPMHC	509	520	0.0011 +/- 0.0001	0.02	0.5	500	636
H ₄ BPMHC _{ox}			0.700	5.68	1.2	0.53	

^aErrors were obtained from linear fittings of absorbance vs emission. ^bValues in bold indicate estimations, where fluorescent lifetimes were too short to measure accurately. ^cFluorescent

enhancements were calculated as the ratio between the fluorescence quantum yields of the oxidized and reduced BODIPY-chromanol constructs.

As predicted by our estimations of $\Delta G^\circ_{\text{PeT}}$ (*vide supra*), the ϕ_f measured for completely alkylated reduced probes, Et₂BTOH and Et₂BPMHC were the highest (0.03), indicating modest PeT efficiency. Accordingly, the smallest fluorescence enhancements were observed, in the range of 20 to 40-fold. Likewise, reduced probes alkylated exclusively at positions 3 and 5 had extremely low ϕ_f (0.001 for H₄BPMHC) indicating excellent PeT efficiency and superior sensitivity (>600-fold fluorescence enhancement, sensitivity is illustrated in Figure 3.10) consistent with the trend of $\Delta G^\circ_{\text{PeT}}$ calculated from electrochemical measurements. Fluorescence lifetimes of dyes with quantum yields <1% were too short to accurately measure. Based on the assumption that $k_{\text{rad}} = 0.5 \times 10^8 \text{ s}^{-1}$, lifetimes for these highly quenched compounds were estimated from their fluorescence quantum yields and are shown in bold in Table 3.2. The k_{PeT} determined increase with increasing BODIPY redox potentials as expected, indicating the role substituents on the BODIPY core play in the PeT quenching pathway and thus observed fluorescence enhancement. Here, judicious choice in the substituent pattern of the BODIPY core may increase our dynamic range from ~20-fold to ~1,000-fold.

3.4.5 Maximizing k_{PeT}

Armed with the two series of compounds and their k_{PeT} estimates, we next determined the potential for further improvements to sensitivity by correlating $\ln(k_{\text{PeT}})$ with $\Delta G^\circ_{\text{PeT}}$ determined from the electrochemical measurements, within the framework of Marcus Theory of Electron Transfer, see Equations 3.1-3.3. By fitting the experimental data according to the model, we retrieved parameters for the reorganizational energy, λ , and thus the Gibbs free energy of PeT that corresponds to when k_{PeT} is maximum, that is, when $\Delta G^\circ_{\text{eT}} = -\lambda$. This point corresponds to the smallest barrier of activation (i.e. $\Delta G^\ddagger_{\text{eT}} = 0$). Beyond this point, the large thermodynamic driving force (i.e. $\Delta G^\circ_{\text{eT}} < -\lambda$) results in a decrease of k_{eT} signifying the onset of the Marcus Inverted region.

The correlation between $\ln(\kappa_{PeT})$ and ΔG°_{PeT} is illustrated in Figure 3.3 for both the XBTOH series and the XBPMHC series. A correlation was obtained where the largest κ_{PeT} (lowest Φ_f) corresponded to the most exergonic ΔG°_{PeT} , indicative of our series having a relatively narrow range of ΔG°_{PeT} within the normal Marcus region. A maximum at $\Delta G^\circ_{PeT} = -1.4$ eV was retrieved from fitting the correlation with a quadratic function (Equation 3.8, Figure 3.3A). Significantly more electron withdrawing groups would be required on the BODIPY core to shift the ΔG°_{PeT} from the current most exergonic value of 0.67 eV, estimated for H₄BPMHC, to -1.4 eV toward achieving maximum sensitivity.

Based on the solvent used, and radii of the BODIPY moiety and tocopherol moiety determined from DFT, the outer shell contribution to λ (λ_o , Equation 3.9) was approximated at 0.9 eV, determined from Equation 3.10 where e is the charge of an electron, r_a and r_b are the radii of BODIPY and tocopherol (4.3 Å and 4.4 Å, respectively), ϵ_s is the relative permittivity of the solvent (37.5 for acetonitrile), ϵ_{op} is the square of the refractive index of the solvent (1.344²), and ϵ_0 is the permittivity of space. With λ_o and using Equation 3.9, this approximation gives an inner shell reorganization energy of $\lambda_i = 0.5$ eV, in good agreement with electron transfer processes between other organic small molecules.^{29,30}

$$y = A + Bx + Cx^2 \quad \text{Equation 3.8}$$

$$\lambda = \lambda_o + \lambda_i \quad \text{Equation 3.9}$$

$$\lambda_o = e^2 \frac{[(2*r_a)^{-1} + (2*r_b)^{-1} - (r_a + r_b)^{-1}](\epsilon_s^{-1} + \epsilon_{op}^{-1})}{4\pi\epsilon_0} \quad \text{Equation 3.10}$$

We may also estimate λ_i using DFT. Nelsen's four point method may be used to calculate λ_i by treating the tocopherol donor (D) and BODIPY acceptor (A) separately, as is expressed in Equation 3.11.^{31,32} Here, $E(a|b)$ represents the energy of state 'a' calculated at the equilibrium structure of state 'b' and the superscript '*' denotes the BODIPY acceptor in the excited state. The enthalpic portion of λ_i is thus the sum of the relaxation energy between

the cation obtained from a vertical transition from the neutral donor species and the relaxed cation, and that for the anion obtained from a vertical transition from the neutral acceptor species and the relaxed anion. While this estimation does not provide entropic considerations, it still provides us with a good estimation and is one of the most prevalent methods used to calculate λ_i .^{31,32} These calculations are thus underway to provide us with a more rigorous estimation of λ_i .

$$\lambda_i = [E(D^+|D) - E(D^+|D^*)] + [E(A^{*-}|A) - E(A^{*-}|A^*)] \quad \text{Equation 1.11}$$

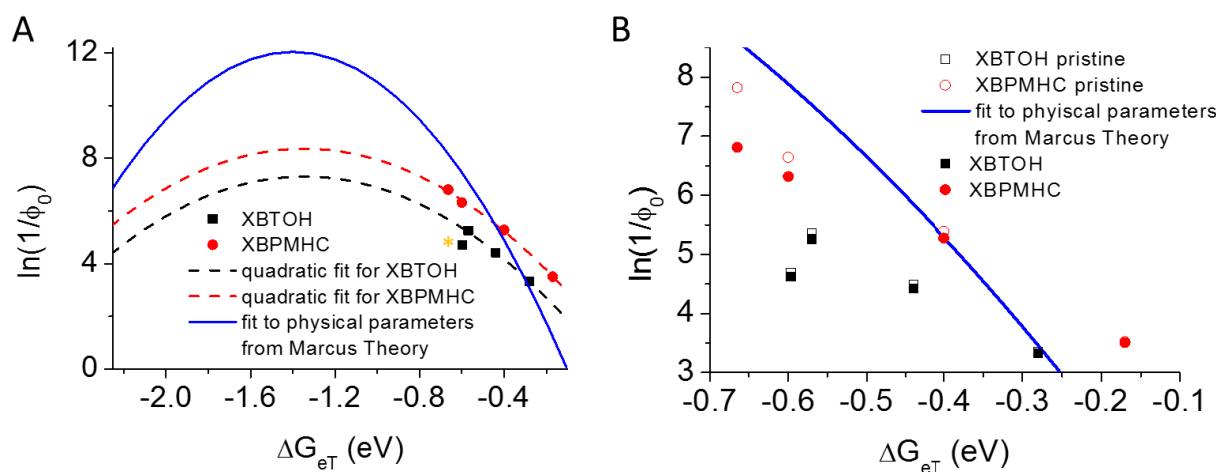


Figure 3.3 A) Correlation of the reduced quantum yields (ϕ_0) of the XBTOH series (black) and XBPMHC series (red) with calculated ΔG_{eT}° . Data trends were fit with a quadratic function (dashed lines), and a quadratic function based on fixed coefficients ($B=20$ and $C=7$) obtained from Marcus theory with $\lambda=1.4$ eV (blue). B) Assuming samples in A had a fraction of pre-oxidized probe of 0.1% (open symbols). Here the ϕ_f were re-calculated ('pristine') from the values experimentally obtained (off state, 'meas') considering the latter were tainted with 0.1% pre-oxidized compound: $\phi_{\text{pristine}} = (\phi_{\text{meas}} - \phi_{\text{ox}} * 0.001) / 0.999$, where ϕ_{ox} is the emission quantum yield of BODIPY-tocopherol constructs once oxidized (on state, 'ox').

Closer inspection of the quadratic function obtained from fitting the correlation in Figure 3.3 showed that the quadratic coefficients (B and C in Equation 3.8) were too low, by a factor of two, when compared to their physical magnitudes based on Marcus equations (i.e. $B = -1/(2k_B T)$, $C = -1/(4\lambda k_B T)$). The discrepancy would indicate that the fitting function is

too shallow and the free energy relationship we retrieved is thus less steep than predicted by Marcus Theory (Figure 3.3, blue trace). We argue that the disagreement is due in part to the reactivity of our BODIPY tocopherol constructs. Here, traces of impurities in the solvent may oxidize the antioxidant segment of the probes, deactivating PeT and thus giving an artificially high quantum yield for the reduced species. This effect becomes more pronounced for darker (initially more quenched) probes, and leads to a less steep quadratic function. Indeed, if we assume the BODIPY-tocopherol constructs had oxidized by 0.1% before their quantum yields were measured, our observations fit closer to that expected from Marcus Theory (Figure 3.3B). Related to this discussion, we note that the point marked by an asterisk in Figure 3.3, and corresponding to data from H₄BTOH, may be affected by systematic errors. An accurate quantum yield was especially difficult to measure for this compound as it was susceptible to hydrolysis/decomposition owing to the less sterically hindered ester where methyls at positions 1 and 7 in the BODIPY core are missing. Consistent with the above, hydrolysis was observed in running 2D TLC experiments. This experimental point may thus be artificially low.

3.4.6 Distance dependence on k_{PeT}

In our quest to maximize k_{PeT} , we next explored the role that varying the linker, and thus the distance between donor and acceptor dyes, plays on PeT. We compared rate constants of PeT measured for the XBTOH series with those of the XPMHC series. We posit that reorganization energies are similar for both series, and as such the bell-shaped curves fitting both sets of data within the Marcus Theory framework should be equal (Equations 3.1 and 3.2), yet offset from one another by a magnitude related to the larger distance expected *a priori* for PeT in the XBTOH series, as determined from Equation 3.4. The clearly observed offset in Figure 3.3 would thus point to the difference in the linker length of the two scaffolds. The offset value ($\Delta \ln(1/\phi) = 1$) for similar ΔG°_{PeT} indicates k_{PeT} is approximately 2.7-fold larger for XBPMHC than XBTOH. Determined from DFT, the ester linkage between the chromanol donor and BODIPY acceptor for H₂BTOH is 5.9 Å, compared to 3.1 Å for H₂BPMHC. If our BODIPY-chromanol constructs were linear structures, this difference in

distance (2.8 Å) would translate to a ratio of k_{PeT} rate constants ~ 16 (according to Equation 3.4, assuming $\beta = 1$ Å), significantly larger than the observed 2.7-fold. DFT calculations performed on both H₂BTOH and H₂BPMHC, however, support non-linear structures (see Supplementary Info, Figure 3.11) that are relatively folded with the donor and acceptor within close proximity (~ 6 Å). Determining the centre coordinates of both the chromanol and BODIPY moiety for each of these structures and calculating the distance between these points, reveals that the two moieties are closer in H₂BPMHC by 0.26 Å. Assuming the sensitivity parameter, β , is around 1 Å^{-1} ,¹⁹ k_{PeT} for H₂BPMHC would be approximately 1.3-fold larger than that of H₂BTOH. The offset in y between the two traces recorded in Figure 3.3 would ultimately translate to a ~ 1 Å difference in distance. Therefore, the correlations illustrated in Figure 3.3 imply neither completely folded structures (corresponding to a difference of 0.26 Å), nor elongated linkers (corresponding to a difference of 2.8 Å). Ultimately our results suggest that the offset between the two correlations in Figure 3.3, while arising from differences in distance between donor and acceptor in each structure, is less significant than the linker lengths would imply due to their folded conformation, in addition to sampling many conformations. Overall, distance would not be nearly as convenient a knob to tune in the quest for enhanced sensitivity, as it is fairly optimized.

3.5 Conclusion

One of the key components of fluorogenic probe design is optimizing PeT to increase the off/on dynamic range. Armed with a library of BODIPY-chromanol analogues whose redox potentials are tuned over a ~ 400 mV window, we studied the role substituent decoration pattern on the BODIPY core plays on PeT efficiency within the context of Marcus Theory. Our results show fluorescent enhancements ranging from 20 to 1,000 fold within this redox window. The effect of the length of the linkage connecting our BODIPY electron acceptor segment to our chromanol electron donor segment was also explored. Given that our BODIPY-chromanol constructs may adopt a folded conformation, an increase in the linker length by 2 carbon-carbon bonds led only to a 2.7-fold reduction in PeT efficiency.

Detection of subtle changes in ROS levels in cells, in particular at basal levels, requires very sensitive probes in order to shed light on the relevance of ROS to cell physiology. Given that λ is approximately 1.4 eV in our study, our free energy relationship relating quantum yield and $\Delta G^\circ_{\text{PeT}}$ suggests there is room for improvement, as the library of dyes presented here provides for $\Delta G^\circ_{\text{PeT}} \sim -0.7$ eV. BODIPY chromophores characterized by redox potentials 0.7 eV more positive than the best acceptor reported herein would satisfy maximum sensitivity, i.e. $\Delta G^\circ_{\text{PeT}} = -\lambda$. Based on our recent work on estimating redox potentials for BODIPY cores,²⁶ we propose a compound bearing CN at the 2 and 6 positions and no methyl groups at the 1 and 7 position as the ideal candidate.

While the enhanced sensitivity reported for H₄BPMHC (1,000-fold) may fulfil the needs to detect subtle changes in ROS, the search for red-emissive probes, well suited for live cell imaging, will create new challenges. Here redox potentials will have to be further tuned to account for the change in $\Delta E_{0,0}$ that translates in a drop of 0.57 eV in PeT exergonic character in going from a 500 nm to 650 nm emitting dye, in order to yield the excellent sensitivity showcased here.

In search for maximum sensitivity in fluorogenic analogues of Vitamin E to monitor ROS, our quest for darkness has led us to introduce a molecular switch based on PeT that effectively competes with emission from the singlet excited state manifold. Our results, presented here, while conforming to long standing theories of electron transfer, indicate the sensitivity ceiling one may achieve based on redox potentials of a BODIPY electron acceptor segment, and its distance from the chromanol electron donor.

3.6 Experimental

3.6.1 Materials

8-Acetoxyethyl-2,6-diethyl-1,3,5,7-tetramethyl-pyrromethene fluoroborate (PM605) was purchased from Exciton, Inc. (Dayton, OH). HPLC grade solvents for spectroscopy and column chromatography were purchased through Fisher Scientific. All other chemicals were supplied by Sigma-Aldrich, Co. and used without further purification.

3.6.2 Instrumentation

Absorption spectra were recorded using a Hitachi U-2800 UV–vis–NIR spectrophotometer. Luminescence spectra were recorded using a PTI QuantaMaster spectrofluorimeter using 1 cm × 1 cm quartz cuvettes. Spectra were corrected for detector sensitivity. ¹H NMR and ¹³C NMR spectra were recorded on a Varian VNMRS 500 or a Bruker AVIIIHD 500 instrument at 500 and 125 MHz, respectively. Electrospray ionization (ESI) and atmospheric chemical ionization (APCI) mass spectra were measured on a Bruker maXis impact. Voltammetry experiments were conducted with a computer-controlled CHI760C potentiostat.

3.6.3 Computational Methods

Quantum mechanical calculations were performed using the Gaussian 09 M package. HOMO and LUMO orbital energies and radii were determined from molecular geometries optimized at the B3LYP 6-31G(d) level. Orbitals were visualized using the GaussView 5 package.

3.6.4 Electrochemical Studies

Electrochemical measurements of H₄MeBOAc and H₄BCH₃ were performed using a three-electrode system. The working electrode was a Pt wire. A Pt wire mesh electrode was used as the counter electrode, and a Ag/AgNO₃ non-aqueous electrode was used as the reference. A 0.1 M solution of tetrabutylammonium hexafluorophosphate in dry acetonitrile was used as the electrolyte solvent in which 1 mM of the dye of interest was dissolved. Concentrations were determined from the absorption and calculated extinction coefficient (32,700 cm⁻¹M⁻¹ and 78,700 cm⁻¹M⁻¹ for H₄MeBOAc and H₄BCH₃ respectively). The solutions also contained 1 mM ferrocene as an internal standard. The solutions were equilibrated with nitrogen, and measured under inert atmosphere, with a minimum scan rate of 0.2 V s⁻¹. Formal redox potentials were calculated as the average of the cathodic and anodic peak potentials observed in the cyclic voltammograms. All values were reported vs. ferrocene.

3.6.5 Oxidation of Probes with Peroxyl Radicals

1 μM solutions of tocopherol analogue in acetonitrile supplemented with 5 μM PMHC were prepared. PMHC was added to quench any radicals initially present in the solvent. Initial fluorescence of the samples was measured, upon which solutions were spiked with radical initiator, V59 (2,2'-Azobis(2-methylbutyronitrile)) (84.5 mM). Oxidation was then monitored over time until the fluorescence intensity of the sample reached a maximum plateau. Time based fluorescent measurements were recorded on a PTI QuantaMaster spectrofluorimeter equipped with a four-position Peltier with motorized turret. 3 mL glass fluorimetry cells with 1 cm path lengths were used as sample cells. The excitation and emissions slits were set to 1.2 nm. The temperature control was set to 37°C. H₂BTOH, H₄BPMHC, and H₂BPMHC were excited at 485 nm and emission was collected at 520 nm, H₄MeBTOH and Et₂BPMHC were excited at 500 nm and emission was collected at 520 nm and 545 nm respectively, Cl₂BPMHC and Cl₂BTOH were excited at 510 nm and emission was collected at 550 nm, and Et₂BTOH was excited at 515 nm and emission collected at 570 nm. Once a plateau was reached, lifetimes and single point quantum yields were measured as described below.

3.6.6 Fluorescence Quantum Yield

Acetonitrile solutions of 8-phenyl pyrromethene fluoroborate ($\Phi_f=0.013$) and *meso*-acetoxymethyl-BODIPY dyes,¹⁷ H₂BOAc or PM605, were used as standards to calculate the quantum yields of solutions of the reduced and oxidized tocopherol analogues respectively in acetonitrile supplemented with 5 μM PMHC. Absorption and emission spectra of the dye standards and the reduced tocopherol analogues were measured at five different concentrations. A radical initiator was then added to each tocopherol analogue sample (*vide supra*) and absorption and emission spectra were then measured once the maximum fluorescence intensity was reached. The integrated intensity versus absorbance were then plotted and fitted linearly. Quantum yields for the tocopherol analogues with respect to the standard were obtained from Equation 3.12, where Φ_x , Δ , and η refer, respectively, to the fluorescence quantum yield, the slope obtained from the above-mentioned plot, and the solvent refractive index for the unknown (x) or standard (st) sample. Emission spectra were

recorded for solutions containing reduced species and 8-phenyl pyrromethene fluoroborate using excitation and emission slits of 4 nm and for solutions containing oxidized species, H₂BOAc and PM605 using excitation and emission slits of 1.2 nm.

$$\phi_x = \phi_{st} \left(\frac{\Delta_x}{\Delta_{st}} \right) \times \left(\frac{\eta_x^2}{\eta_{st}^2} \right) \quad \text{Equation 3.12}$$

3.6.7 Fluorescence Lifetime Studies

The fluorescence lifetime measurements were carried out using a Picoquant Fluotime 200 Time Correlated Single Photon Counting setup employing a supercontinuum laser (WhiteLase SC-400-4, Fianium, Beverly, MA). Excitation wavelengths were spectrally separated from broadband emission by a computer controlled acousto-optical tunable filter (AOTF, Fianium). H₂BTOH, H₄BPMHC, and H₂BPMHC were excited at 485 nm, H₄MeBTOH and Et₂BPMHC were excited at 500 nm, Cl₂BPMHC and Cl₂BTOH were excited at 510 nm, and Et₂BTOH was excited at 515 nm. Photons were collected at the emission maximum of each dye. The excitation rate was 10 MHz, and the detection frequency was less than 100 kHz. Photons were collected at the magic angle.

3.6.8 Synthesis

8-Phenyl Pyrromethene Fluoroborate, 8-Hydroxymethyl-2,6-dichloro-1,3,5,7-tetramethyl Pyrromethene Fluoroborate (Cl₂BOH), 2-(6-Methoxy-2,5,7,8-tetramethylchroman-2-yl)acetic acid, and H₂BPMHC, were prepared according to literature procedures^{10,17,33} where spectroscopic data matched those of the reported materials. Synthetic details for 2-(3-Chloropropyl)-1H-pyrrole, H₄BPMHC and H₄BCH₃ can be found in Chapter 4.

8-Acetoxyethyl-3,5-dimethyl Pyrromethene Fluoroborate (H₄Me-BOAc). 2-Methyl-pyrrole (0.24 g, 3 mmol, 2 eq) was dissolved in dry dichloromethane (4 mL) under argon. Acetoxy-acetyl chloride (0.16 mL, 1.5 mmol, 1 eq) was added dropwise to the solution

and was refluxed for 6 hours, and then stirred at room temperature for 16 h. The solution was then diluted with dichloromethane and washed with brine. The organic fraction was dried over sodium sulfate and solvent was removed under reduced pressure. The resulting residue was dissolved in dichloromethane (5 mL) and toluene (10 mL) at room temperature under argon. Diisopropylethylamine (1 mL, 4 eq) was added dropwise and the solution was stirred for 15 minutes. Boron trifluoride diethyl etherate (1.5 mL, 8 eq) was added dropwise and the solution was stirred for 1 h at room temperature. The solution was then diluted with ethyl acetate and washed with brine. The organic fraction was dried over anhydrous sodium sulfate and solvent was removed under reduced pressure. The resulting residue was purified using flash chromatography and eluted with hexanes/ethyl acetate (3:2) affording an orange solid (47 mg, 11%). ¹H-NMR (500 MHz; CDCl₃): δ 7.18 (d, *J* = 4.2 Hz, 2H), 6.30 (d, *J* = 4.2 Hz, 2H), 5.22 (s, 2H), 2.62 (s, 6H), 2.09 (s, 3H). ¹³C NMR (126 MHz; CDCl₃): δ 170.2, 159.0, 134.6, 134.0, 128.0, 119.8, 59.1, 20.8, 15.0 HRMS (ESI⁺) for C₁₄H₁₅N₂O₂BF₂Na (M+Na) calculated 315.10978, found 315.11009

8-Hydroxymethyl-3,5-dimethyl Pyrromethene Fluoroborate (H₄Me-BOH). H₄Me-BOAc (0.047 g, 0.16 mmol, 1 eq) was dissolved in a methanol/dichloromethane solution (2:1, 4.5 mL) under argon. 0.1 M NaOH (1 mL) was added dropwise. The solution was stirred for 5.5 h and was then diluted with dichloromethane and washed with saturated aqueous ammonium chloride. The organic fraction was dried over sodium sulfate and solvent was removed under pressure. The resulting residue was purified using flash column chromatography and eluted with hexanes/ethyl acetate (3:2) affording an orange solid (18 mg, 45%), ¹H-NMR (500 MHz; CDCl₃): δ 7.26 (d, *J* = 4.1 Hz, 2H), 6.32 (d, *J* = 4.2 Hz, 2H), 4.84 (s, 2H), 2.64 (s, 6H). ¹³C NMR (126 MHz; CDCl₃): δ 158.5, 139.2, 134.0, 127.6, 119.6, 59.5, 15.0 HRMS (ESI⁻) for C₁₂H₁₂N₂OBF₂ (M+Na) calculated 249.10162, found 249.10216.

8-((±)-6-Hydroxy-2,5,7,8-tetramethylchromane-2-carboxyloxy)-methyl-3,5-dimethyl Pyrromethene Fluoroborate (H₄Me-BTOH). Trolox (0.026 g, 0.1 mmol, 1 eq) and H₄Me-BOH (0.018 g, 0.07 mmol, 0.7 eq) were dissolved in dry THF (1 mL) under argon.

Dimethylaminopyridine (0.0024 g, 0.02 mmol, 0.2 eq) and *N,N'*-Diisopropylcarbodiimide (0.016 mL, 0.1 mmol, 1 eq) were then added. The solution was stirred for 1 h at room temperature after which the solvent was removed under reduced pressure. The resulting residue was purified using flash column chromatography and eluted with hexanes/ethyl acetate (3:2) affording a pink solid (8 mg, 24%) ¹H-NMR (500 MHz; CDCl₃): δ 7.00 (d, *J* = 4.2 Hz, 2H), 6.24 (d, *J* = 4.2 Hz, 2H), 5.47 (d, *J* = 12.1 Hz, 1H), 4.86 (d, *J* = 12.1 Hz, 1H), 4.40 (s, 1H), 2.63 (s, 6H), 2.52-2.44 (m, 2H), 2.35-2.32 (m, 1H), 2.02 (s, 3H), 2.01 (s, 3H), 1.88-1.82 (m, 4H), 1.63 (s, 3H). ¹³C NMR (126 MHz; CDCl₃): δ 174.0, 158.9, 146.0, 145.3, 134.6, 133.0, 127.9, 122.5, 122.4, 119.8, 119.6, 116.6, 77.4, 58.8, 31.3, 25.5, 21.0, 15.0, 12.2, 11.7, 11.1 HRMS (ESI⁻) for C₂₆H₂₈N₂O₄BF₂ (M-H) calculated 481.21157, found 481.21178.

8-((±)-6-Hydroxy-2,5,7,8-tetramethylchromane-2-carboxyloxy)-methyl-2,6-dichloro-1,3,5,7-tetramethyl Pyrromethene Fluoroborate (Cl₂B-TOH). Trolox (0.024 g, 0.1 mmol, 1 eq) and Cl₂BOH (0.018 g, 0.08 mmol, 0.8 eq) were dissolved in dry THF (1 mL) under argon. Dimethylaminopyridine (0.002 g, 0.02 mmol, 0.2 eq) and *N,N'*-Diisopropylcarbodiimide (0.015 mL, 0.1 mmol, 1 eq) were then added. The solution was stirred for 1.5 h at room temperature after which the solvent was removed under reduced pressure. The resulting residue was purified using flash column chromatography and eluted with hexanes/ethyl acetate (3:2) affording a pink solid (36.5 mg, 81%) ¹H-NMR (500 MHz; CDCl₃): δ 5.38 (d, *J* = 12.3 Hz, 1H), 5.11 (d, *J* = 12.3 Hz, 1H), 4.29 (s, 1H), 2.65-2.61 (m, 1H), 2.58 (s, 6H), 2.53-2.45 (m, 2H), 2.13 (s, 6H), 2.02 (s, 3H), 1.97 (s, 3H), 1.93 (s, 3H), 1.90-1.87 (m, 1H), 1.66 (s, 3H). ¹³C NMR (126 MHz; CDCl₃): δ 173.9, 153.5, 145.8, 145.6, 136.1, 133.5, 130.6, 123.3, 122.9, 121.7, 119.0, 116.8, 77.5, 57.5, 30.9, 25.7, 21.0, 12.61, 12.50, 11.9, 11.5, 11.0 HRMS (ESI⁻) for C₂₈H₃₀N₂O₄BCl₂F₂ (M-H) calculated 577.16554, found 577.16492.

8-((6-Hydroxy-2,5,7,8-tetramethylchroman-2-yl)-methyl)-2,6-diethyl-1,3,5,7-tetramethyl Pyrromethene Fluoroborate (Et₂B-PMHC). 2-(6-Methoxy-2,5,7,8-tetramethylchroman-2-yl)acetic acid (0.3 g, 0.0009 mol) was dissolved in thionyl chloride (2 mL) under argon and stirred at 50 °C for 1 h. The thionyl chloride was then removed by co-

evaporation with toluene (15 mL, 5 times) and the flask was left on a vacuum pump overnight. The resulting acid chloride was then dissolved in 10 mL of dichloromethane under argon. Phosphorus oxychloride (0.47 mL, 0.005 mol) was added dropwise followed by 2-4-dimethyl-3-ethylpyrrole (0.25g, 0.0021 mol). The reaction mixture was stirred for 24 h at 35°C. The mixture was then diluted with dichloromethane, washed with brine, and dried over sodium sulfate. Solvent was removed under reduced pressure. The resulting red oil was dissolved in dichloromethane (5 mL) under argon and cooled to -10 °C. Borontribromide (5 mL, 1 M in dichloromethane, 0.005 mol) was added dropwise. The reaction mixture was allowed to slowly warm to room temperature over the course of 1.5 h when the reaction was quenched carefully with water. The solution was extracted with ethyl acetate and the organic fractions were washed with brine and dried over sodium sulfate. Solvent was removed under reduced pressure. The resulting red oil was dissolved in 8 mL of dichloromethane and 12 mL of toluene under argon at 0 °C. Diisopropylethylamine (0.69 mL, 0.004 mol) was added dropwise. After 10 minutes, boron trifluoride diethyl etherate (0.99 mL, 0.008 mol) was added dropwise and stirred for 1 h. The mixture was then quenched with water and extracted with ethyl acetate. The organic fractions were washed with brine and dried over sodium sulfate. Solvent was removed under reduced pressure. The resulting red solid was purified by flash column chromatography (30% ethyl acetate in hexanes) followed by further purification by a preparatory silica plate eluted in dichloromethane giving a pink film (3 mg, ~1% yield). (We attribute the extremely low yield to considerable oxidation of the chromanol moiety of the product to give the chromo-quinone-BODIPY.) ¹H-NMR (500 MHz; CDCl₃): δ 4.16 (s, 1H), 3.62-3.55 (m, 2H), 2.68-2.63 (m, 2H), 2.51 (s, 3H), 2.49 (s, 3H), 2.42 (s, 3H), 2.38 (t, *J* = 7.3 Hz, 4H), 2.34 (s, 3H), 2.09 (s, 3H), 2.08 (s, 3H), 1.94-1.91 (m, 2H), 1.75 (s, 3H), 1.17 (s, 3H), 1.03 (t, *J* = 7.6 Hz, 6H). ¹³C NMR (126 MHz; CDCl₃): δ 152.3, 151.4, 148.6, 144.9, 139.7, 137.6, 135.6, 134.1, 133.3, 132.8, 128.8, 123.3, 121.2, 118.3, 116.8, 75.8, 38.6, 33.2, 29.7, 21.0, 20.8, 17.23, 17.18, 14.9, 14.8, 14.6, 14.5, 12.5, 12.1, 11.6, 11.2 HRMS (ESI⁺) for C₃₁H₄₁N₂O₂BF₂Na (M+Na) calculated 545.31214, found 545.31240.

¹ We attribute the extremely low yield to a considerable conversion of product to the oxidized-ring-opened product.

8-((6-Hydroxy-2,5,7,8-tetramethylchroman-2-yl)-methyl)-2,6-dichloro-1,3,5,7-tetramethyl Pyrromethene Fluoroborate (Cl₂B-PMHC). H₂B-PMHC (17 mg, 0.036 mmol, 1 eq) was dissolved in THF (2 mL) at room temperature under argon. *N*-Chlorosuccinimide (10 mg, 0.073 mmol, 2 eq) was added in one portion. The reaction was left to stir for 22 h, after which solvent was removed under reduced pressure. The resulting pink residue was purified using a glass prep plate (thin layer chromatography) and eluted with 40% ethyl acetate in hexanes yielding a pink residue (8 mg, 41%). ¹H-NMR (500 MHz; CDCl₃): δ 4.20 (s, 1H), 3.60-3.53 (m, 2H), 2.72-2.63 (m, 2H), 2.57 (s, 3H), 2.55 (s, 3H), 2.52 (s, 3H), 2.42 (s, 3H), 2.09 (s, 3H), 2.09 (s, 3H), 1.95-1.91 (m, 2H), 1.70 (s, 3H), 1.17 (s, 3H). ¹³C NMR (126 MHz; CDCl₃): δ 150.9, 150.2, 145.1, 144.5, 142.3, 137.5, 135.1, 134.3, 132.9, 132.1, 123.2, 123.1, 121.4, 118.4, 116.7, 75.5, 39.1, 33.5, 29.7, 21.0, 20.8, 14.93, 14.88, 12.4, 12.1, 11.22, 11.16 HRMS (ESI⁻) for C₂₇H₃₀N₂O₂BCl₂F₂ (M-H) calculated 533.17509, found 533.17732.

3.7 Supporting Information

The Supporting Information contains a detailed explanation of the calculated energies of orbitals for the BODIPY and chromanol constructs as well as the visualization of the calculated orbitals for H₂BPMHC and H₂BPMHC_{ox}. In addition, the cyclic voltammograms for H₄BCH₃ and H₄MeBOAc can be found here.

¹H NMR and ¹³C NMR spectra for H₄BOAc, H₄BOH, H₄BTOH, Cl₂BTOH, Et₂BPMHC, and Cl₂BPMHC may be found in the Appendix at the end of the thesis.

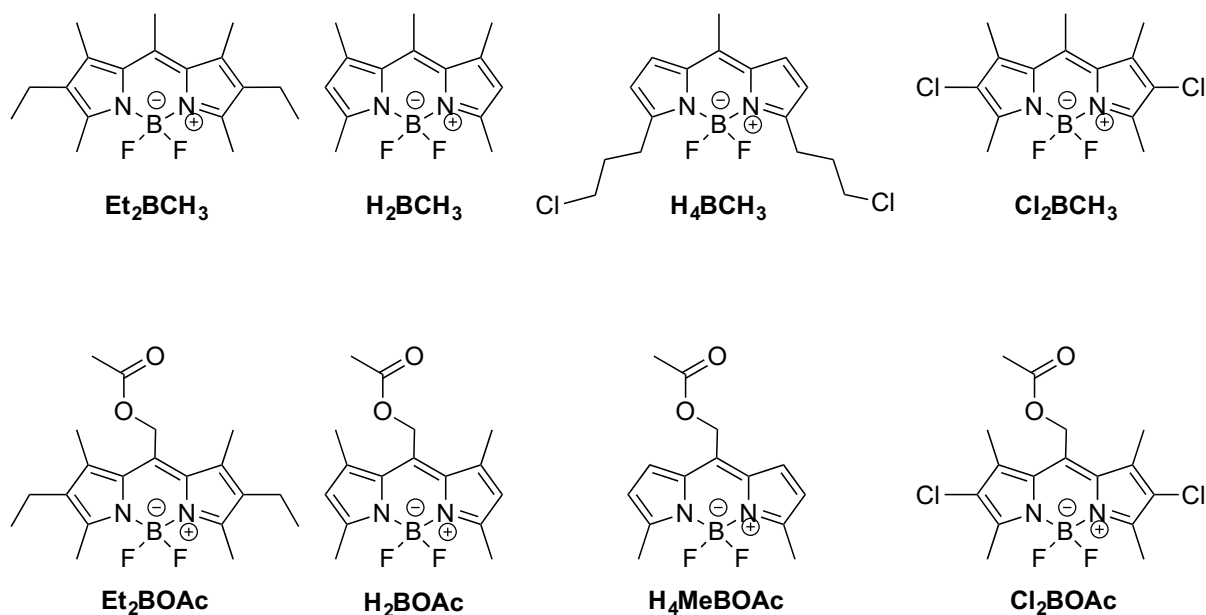


Figure 3.4 BODIPY moieties used to predict PeT using DFT in Figure 3.2.

3.7.1 DFT to confirm and visualize photoinduced electron transfer

We employed density functional theory (DFT) to calculate and visualize the HOMO, LUMO, HOMO-1 and LUMO+1 of the dyes studied in the paper. We sought to visualize the orbitals using GaussView to assign each orbital and provide reasonable evidence to support a photoinduced electron transfer mechanism in our probes. Example HOMO and LUMO orbitals of the chromanol moiety and BODIPY moiety are shown in Figure 3.5. The HOMO and LUMO orbitals visualized for BODIPY are representative of typical HOMO/LUMO orbitals for BODIPY.²⁶

The HOMO-1 orbitals visualized for reduced fluorogenic probes are representative of typical BODIPYs, with the HOMO of the reduced probe sitting on the chromanol moiety suggesting photoinduced electron transfer. The HOMO for the oxidized fluorogenic probes on the other hand is representative of a typical HOMO of a BODIPY and is similar in energy to the HOMO-1 of the reduced probes suggesting a fluorescent molecule. Taken together we may interpret these results to support an operating PeT mechanism as the HOMO of the reduced probe is centered on the chromanol moiety and is higher in energy than that of the BODIPY moiety.

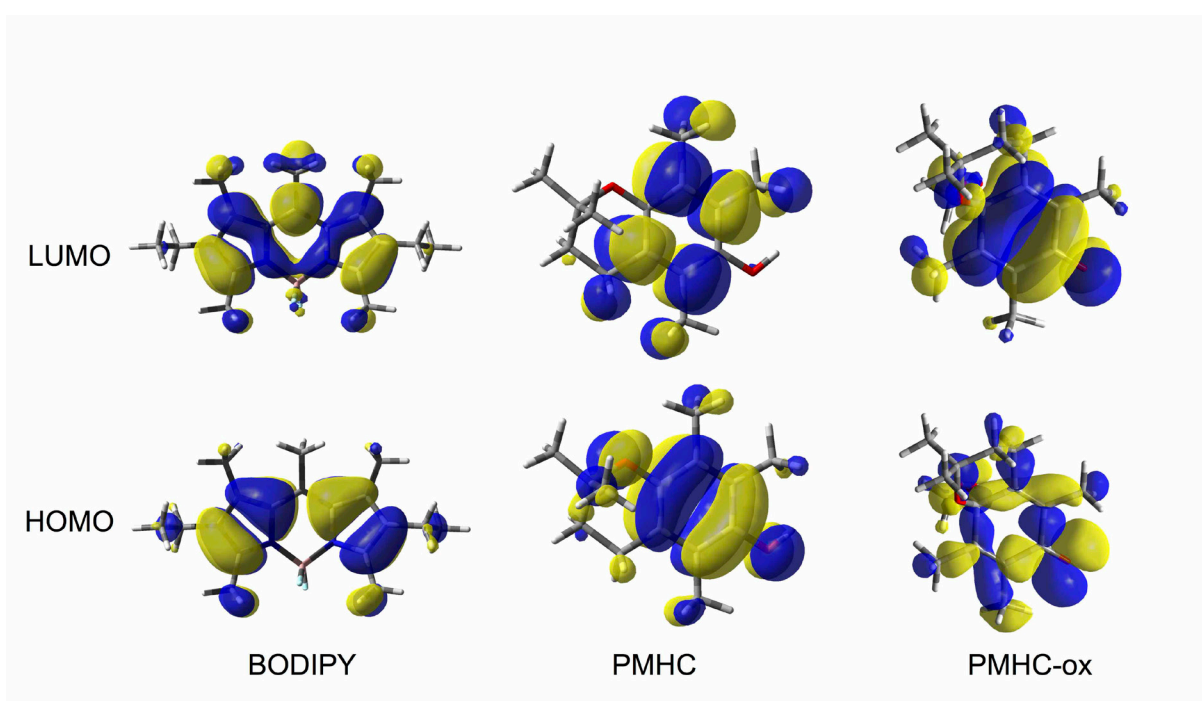


Figure 3.5 Typical orbitals calculated for BODIPY, PMHC, and oxidized PMHC.

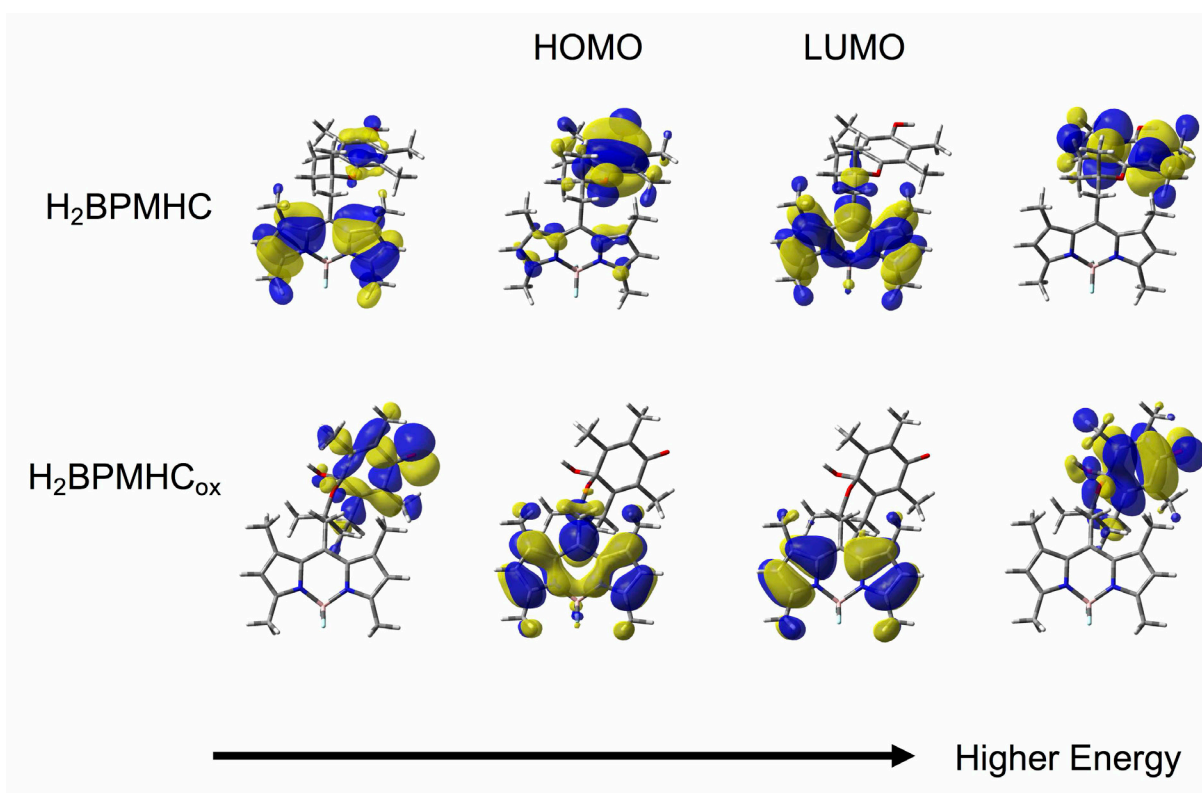


Figure 3.6 Visualization of calculated orbitals for H₂BPMHC in both reduced and oxidized states.

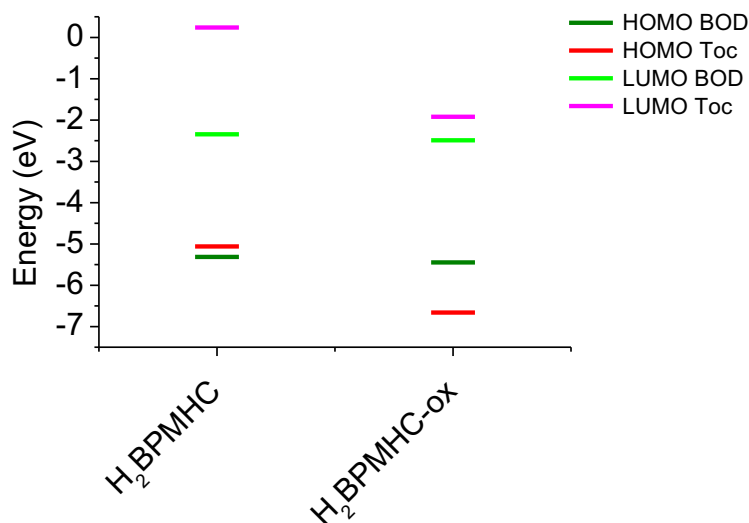


Figure 3.7 Orbitals calculated for H₂BPMHC and oxidized H₂BPMHC (H₂BPMHC_{ox}). Dark and light green bars indicate orbitals corresponding to the HOMO and LUMO of the BODIPY moiety respectively. Red and pink bars indicate orbitals corresponding to the HOMO and LUMO of the chromanol moiety respectively. Orbitals were assigned based on orbitals typical of chromanol and BODIPY as is shown in Figure 3.5.

Table 3.3 HOMO, LUMO and $\Delta E_{0,0}$ values obtained from DFT and the difference in HOMO levels between the BODIPY moiety and the tocopherol analogue ($\Delta\text{HOMO}_{\text{Bodipy-Toc}}$)

Dye	HOMO (eV)	LUMO (eV)	$\Delta E_{0,0}$	$\Delta\text{HOMO}_{\text{Bodipy-Toc}}$
Et ₂ BOAc	-5.31	-2.51	2.80	-0.21
H ₂ BOAc	-5.49	-2.61	2.88	-0.39
H ₄ MeBOAc	-5.67	-2.78	2.90	-0.57
Cl ₂ BOAc	-5.80	-3.01	2.79	-0.70
Et ₂ BCH ₃	-5.20	-2.24	2.96	-0.14
H ₂ BCH ₃	-5.36	-2.31	3.05	-0.31
H ₄ BCH ₃	-5.53	-2.51	3.03	-0.48
Cl ₂ BCH ₃	-5.69	-2.74	2.95	-0.64
Trolox ester	-5.10	-0.37	5.06	
PMHC	-5.06	0.17	5.22	

3.7.2 Cyclic voltammetry

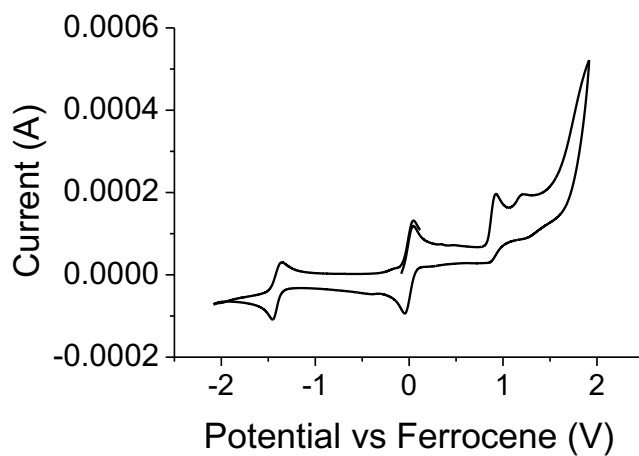


Figure 3.8 Cyclic voltammogram for H_4BCH_3 in acetonitrile with 0.1 M tetrabutylammonium hexafluorophosphate supplemented with 1 mM ferrocene.

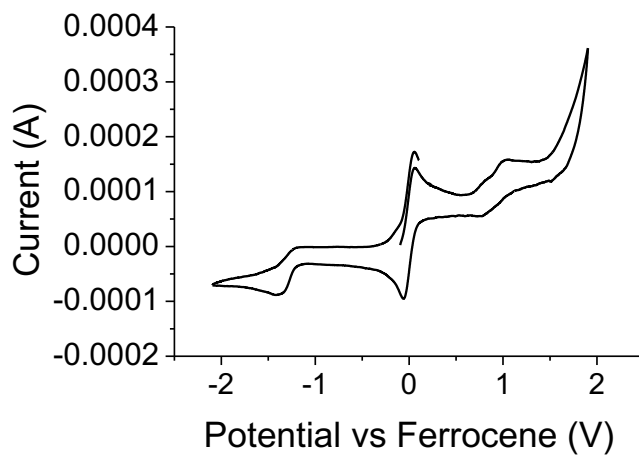


Figure 3.9 Cyclic voltammogram for H_4MeBOAc (1 mM) in acetonitrile with 0.1 M tetrabutylammonium hexafluorophosphate supplemented with 1 mM ferrocene.

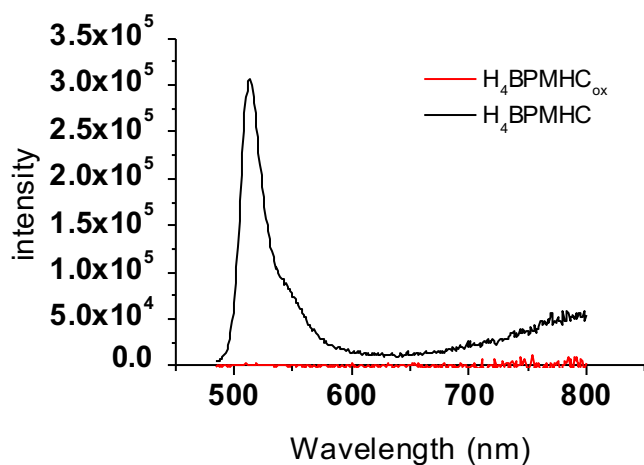


Figure 3.10 The sensitivity of the newly prepared probe, H_4BPMHC as illustrated by the emission spectra of H_4BPMHC and once oxidized by the addition of peroxy radicals (H_4BPMHC_{ox}).

3.7.3 Optimized structures of H_2BPMHC and H_2BTOH

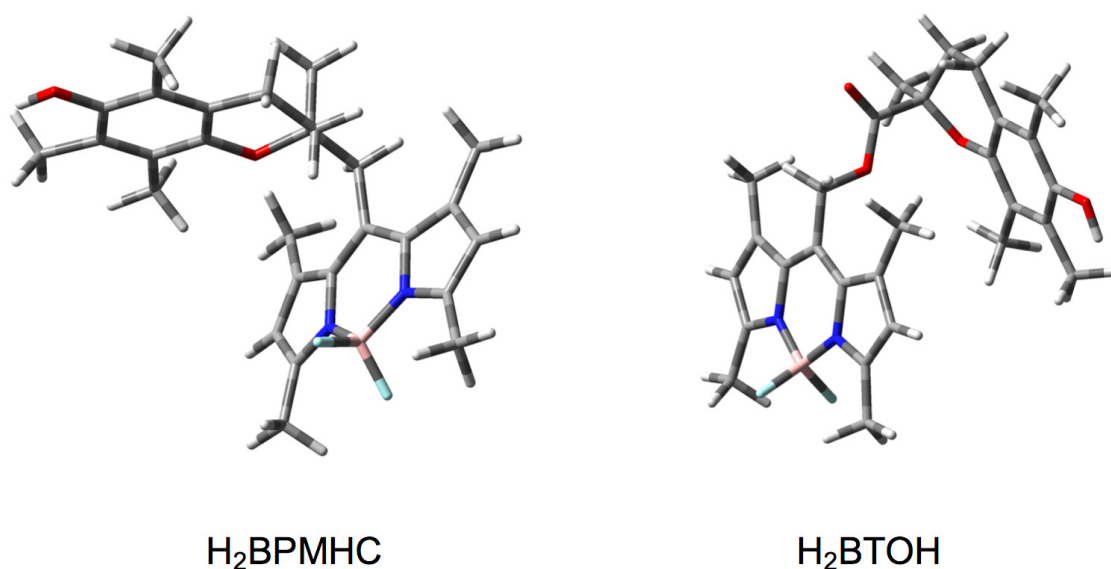


Figure 3.11 Optimized structures of H_2BPMHC and H_2BTOH obtained from DFT. Both structures are folded at the linker between the chromanol and BODIPY moiety. Determining the centre of both the BODIPY moiety and chromanol moiety of each structure places the distance separating each moiety at 6.127 and 6.392 Å for H_2BPMHC and H_2BTOH respectively.

3.8 References

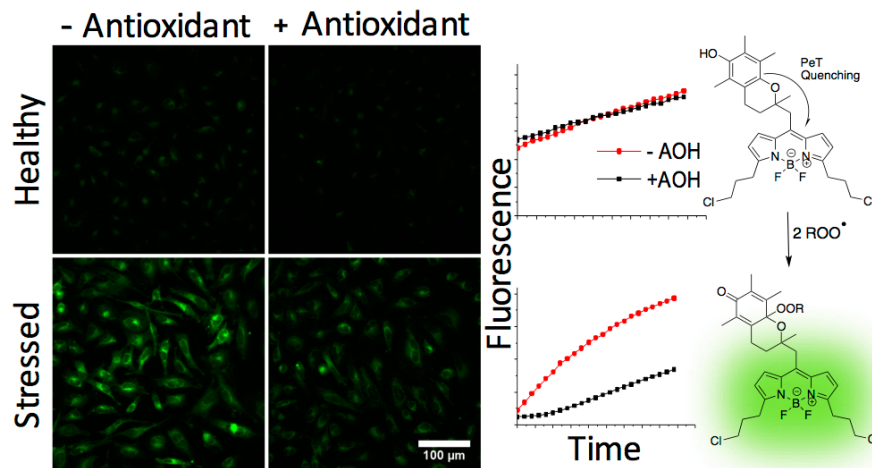
- (1) Niki, E. Oxidative stress and antioxidants: Distress or eustress? *Arch. Biochem. Biophys.* **2016**, *595*, 19-24.
- (2) Barnham, K. J.; Masters, C. L.; Bush, A. I. Neurodegenerative diseases and oxidative stress *Nat Rev Drug Discov* **2004**, *3*, 205-214.
- (3) Mittal, M.; Siddiqui, M. R.; Tran, K.; Reddy, S. P.; Malik, A. B. Reactive Oxygen Species in Inflammation and Tissue Injury *Antioxid. Redox Signal.* **2014**, *20*, 1126-1167.
- (4) D'Autreaux, B.; Toledano, M. B. ROS as signalling molecules: mechanisms that generate specificity in ROS homeostasis *Nat Rev Mol Cell Biol* **2007**, *8*, 813-824.
- (5) Krumova, K.; Cosa, G. Fluorogenic probes for imaging reactive oxygen species *Photochemistry* **2013**, *41*, 279-301.
- (6) Nagano, T. Development of fluorescent probes for bioimaging applications *Proc. Jpn. Acad., Ser. B, Phys. Biol. Sci.* **2010**, *86*, 837-847.
- (7) Chan, J.; Dodani, S. C.; Chang, C. J. Reaction-based small-molecule fluorescent probes for chemoselective bioimaging *Nat Chem* **2012**, *4*, 973-984.
- (8) Oleynik, P.; Ishihara, Y.; Cosa, G. Design and Synthesis of a BODIPY- α -Tocopherol Adduct for Use as an Off/On Fluorescent Antioxidant Indicator *J. Am. Chem. Soc.* **2007**, *129*, 1842-1843.
- (9) Krumova, K.; Oleynik, P.; Karam, P.; Cosa, G. Phenol-Based Lipophilic Fluorescent Antioxidant Indicators: A Rational Approach *J. Org. Chem.* **2009**, *74*, 3641-3651.
- (10) Krumova, K.; Friedland, S.; Cosa, G. How Lipid Unsaturation, Peroxyl Radical Partitioning, and Chromanol Lipophilic Tail Affect the Antioxidant Activity of α -Tocopherol: Direct Visualization via High-Throughput Fluorescence Studies Conducted with Fluorogenic α -Tocopherol Analogues *J. Am. Chem. Soc.* **2012**, *134*, 10102-10113.
- (11) Krumova, K.; Greene, L. E.; Cosa, G. Fluorogenic α -Tocopherol Analogue for Monitoring the Antioxidant Status within the Inner Mitochondrial Membrane of Live Cells. *J. Am. Chem. Soc.* **2013**, *135*, 17135-17143.
- (12) Burton, G. W.; Ingold, K. U. Vitamin E: application of the principles of physical organic chemistry to the exploration of its structure and function *Acc. Chem. Res.* **1986**, *19*, 194-201.
- (13) Khatchadourian, A.; Krumova, K.; Boridy, S.; Ngo, A. T.; Maysinger, D.; Cosa, G. Molecular imaging of lipid peroxyl radicals in living cells with a BODIPY- α -tocopherol adduct. *Biochemistry* **2009**, *48*, 5658-5668.
- (14) Li, B.; Harjani, J. R.; Cormier, N. S.; Madarati, H.; Atkinson, J.; Cosa, G.; Pratt, D. A. Besting Vitamin E: Sidechain Substitution is Key to the Reactivity of Naphthyridinol Antioxidants in Lipid Bilayers *J. Am. Chem. Soc.* **2012**, *135*, 1394-1405.
- (15) Godin, R.; Cosa, G. Counting Single Redox Turnovers: Fluorogenic Antioxidant Conversion and Mass Transport Visualization via Single Molecule Spectroelectrochemistry *J. Phys. Chem. C* **2016**, *120*, 15349-15353.
- (16) Barclay, L. R. C.; Baskin, K. A.; Dakin, K. A.; Locke, S. J.; Vinqvist, M. R. The antioxidant activities of phenolic antioxidants in free radical peroxidation of phospholipid membranes *Can. J. Chem.* **1990**, *68*, 2258-2269.
- (17) Krumova, K.; Cosa, G. Bodipy Dyes with Tunable Redox Potentials and Functional Groups for Further Tethering: Preparation, Electrochemical, and Spectroscopic Characterization *J. Am. Chem. Soc.* **2010**, *132*, 17560-17569.
- (18) Marcus, R. A. Electron Transfer Reactions in Chemistry: Theory and Experiment (Nobel Lecture) *Angew. Chem. Int. Ed. (English)* **1993**, *32*, 1111-1121.

- (19) Closs, G. L.; Miller, J. R. Intramolecular Long-Distance Electron Transfer in Organic Molecules *Science* **1988**, *240*, 440.
- (20) Turro, N. J.; Ramamurthy, V.; Scaiano, J. C. *Principles of Molecular Photochemistry: An Introduction*; University Science Books: Sausalito, CA, 2009.
- (21) Rehm, D.; Weller, A. Kinetics of Fluorescence Quenching by Electron and H-Atom Transfer *Isr. J. Chem.* **1970**, *8*, 259-&.
- (22) Tachiya, M. Energetics of Electron-Transfer Reactions in Polar-Solvents *Chem. Phys. Lett.* **1994**, *230*, 491-494.
- (23) Loudet, A.; Burgess, K. BODIPY Dyes and Their Derivatives: Syntheses and Spectroscopic Properties *Chem. Rev.* **2007**, *107*, 4891-4932.
- (24) Frisch, M. J. T., G. W.; Schlegel, H. B.; Scuseria, G. E.; Robb, M. A.; Cheeseman, J. R.; Montgomery, Jr., J. A.; Vreven, T.; Kudin, K. N.; Burant, J. C.; Millam, J. M.; Iyengar, S. S.; Tomasi, J.; Barone, V.; Mennucci, B.; Cossi, M.; Scalmani, G.; Rega, N.; Petersson, G. A.; Nakatsuji, H.; Hada, M.; Ehara, M.; Toyota, K.; Fukuda, R.; Hasegawa, J.; Ishida, M.; Nakajima, T.; Honda, Y.; Kitao, O.; Nakai, H.; Klene, M.; Li, X.; Knox, J. E.; Hratchian, H. P.; Cross, J. B.; Bakken, V.; Adamo, C.; Jaramillo, J.; Gomperts, R.; Stratmann, R. E.; Yazyev, O.; Austin, A. J.; Cammi, R.; Pomelli, C.; Ochterski, J. W.; Ayala, P. Y.; Morokuma, K.; Voth, G. A.; Salvador, P.; Dannenberg, J. J.; Zakrzewski, V. G.; Dapprich, S.; Daniels, A. D.; Strain, M. C.; Farkas, O.; Malick, D. K.; Rabuck, A. D.; Raghavachari, K.; Foresman, J. B.; Ortiz, J. V.; Cui, Q.; Baboul, A. G.; Clifford, S.; Cioslowski, J.; Stefanov, B. B.; Liu, G.; Liashenko, A.; Piskorz, P.; Komaromi, I.; Martin, R. L.; Fox, D. J.; Keith, T.; Al-Laham, M. A.; Peng, C. Y.; Nanayakkara, A.; Challacombe, M.; Gill, P. M. W.; Johnson, B.; Chen, W.; Wong, M. W.; Gonzalez, C.; and Pople, J. A.; . *Gaussian 03, Revision C.02, Gaussian, Inc., Wallingford CT, 2004*.
- (25) Peng, H. M.; Webster, R. D. Investigation into phenoxonium cations produced during the electrochemical oxidation of chroman-6-ol and dihydrobenzofuran-5-ol substituted compounds *J. Org. Chem.* **2008**, *73*, 2169-2175.
- (26) Lincoln, R.; Greene, L. E.; Krumova, K.; Ding, Z.; Cosa, G. Electronic excited state redox properties for BODIPY dyes predicted from Hammett constants: estimating the driving force of photoinduced electron transfer *J. Phys. Chem. A* **2014**, *118*, 10622-10630.
- (27) Durantini, A. M.; Greene, L. E.; Lincoln, R.; Martínez, S. R.; Cosa, G. Reactive Oxygen Species Mediated Activation of a Dormant Singlet Oxygen Photosensitizer: From Autocatalytic Singlet Oxygen Amplification to Chemically Controlled Photodynamic Therapy *J. Am. Chem. Soc.* **2016**, *138*, 1215-1225.
- (28) Duran-Sampedro, G.; Agarrabeitia, A. R.; Garcia-Moreno, I.; Costela, A.; Bañuelos, J.; Arbeloa, T.; López Arbeloa, I.; Chiara, J. L.; Ortiz, M. J. Chlorinated BODIPYs: Surprisingly Efficient and Highly Photostable Laser Dyes *Eur. J. Org. Chem.* **2012**, *2012*, 6335-6350.
- (29) Oevering, H.; Paddon-Row, M. N.; Heppener, M. Long-range photoinduced through-bond electron transfer and radiative recombination via rigid nonconjugated bridges: distance and solvent dependence *J. Am. Chem. Soc.* **1987**.
- (30) Miller, J. R.; Calcaterra, L. T.; Closs, G. L. Intramolecular long-distance electron transfer in radical anions. The effects of free energy and solvent on the reaction rates *J. Am. Chem. Soc.* **1984**, *106*, 3047-3049.
- (31) Nelsen, S. F.; Blackstock, S. C.; Kim, Y. Estimation of inner shell Marcus terms for amino nitrogen compounds by molecular orbital calculations *J. Am. Chem. Soc.* **1987**, *109*, 677-682.
- (32) Kazemiabnavi, S.; Dutta, P.; Banerjee, S. A density functional theory based study of the electron transfer reaction at the cathode-electrolyte interface in lithium-air batteries *PCCP* **2015**, *17*, 11740-11751.

(33) Kee, H. L.; Kirmaier, C.; Yu, L.; Thamyongkit, P.; Youngblood, W. J.; Calder, M. E.; Ramos, L.; Noll, B. C.; Bocian, D. F.; Scheidt, W. R.; Birge, R. R.; Lindsey, J. S.; Holten, D. Structural Control of the Photodynamics of Boron–Dipyrrin Complexes *J. Phys. Chem. B* **2005**, *109*, 20433-20443.

4 Lipid Peroxyl Radicals Produced During Cellular Homeostasis Unravalled Via Fluorescence Imaging

Lana E. Greene, Richard Lincoln, and Gonzalo Cosa, *To be Submitted*



4.1 Preface

“Look at how a single candle can both defy and define the darkness.”

-Anne Frank

Alluded to in Chapter 1, the role of Vitamin E *in vivo* is complex, interweaving its clear chemical antioxidant role with a less understood cell signalling role. Equally as intricate is the beneficial and injurious dichotomy of ROS *in vivo*. In order to reconcile the chemistry with the biology of both ROS and antioxidants *in vivo*, we required to detect subtle changes in antioxidant status to unmask low levels of lipid peroxidation and inhibition in cells under both normal and pathological conditions. Fundamental to detecting subtle changes, is a large dynamic range and thus sensitivity of the technique.

In Chapter 3, we explored PeT in the design of fluorogenic analogues of tocopherol based on BODIPY and showcased a novel probe with enhanced sensitivity: H₄BPMHC. H₄BPMHC, which undergoes 1,000-fold fluorescence enhancement upon reaction with peroxy radicals is poised to meet our needs to tackle our problem of sensitivity.

With the new probe in hand, in Chapter 4 we illustrate its high sensitivity through the detection of lipid peroxidation at basal levels and in the presence of supplemented Vitamin E surrogate, PMHC. Upon measuring the fluorescence intensity observed in cells, we quantified the amount of oxidized probe, and hence estimated the rate of lipid peroxidation.

Ultimately this chapter shows the progress that can be attained through improving fluorogenic probes in the context of the cycle of fluorogenic probe development. Our design, while not fundamentally different from previous generations, improved our sensitivity immensely, allowing us to distinguish minute concentrations of ROS in cells.

4.2 Abstract

Reactive oxygen species (ROS) and their associated byproducts have been traditionally associated with a range of pathologies. It is now believed however that at basal levels these molecules also play a beneficial cellular function in the form of cell signalling and redox

regulation. Critical to elucidating their physiological role is the opportunity to visualize and quantify the production of ROS with spatiotemporal accuracy. Armed with a newly developed, extremely sensitive fluorogenic α -tocopherol analogue (H₄BPMHC), we report herein the observation of steady concentrations of lipid peroxy radicals produced during cellular homeostasis. Imaging studies with H₄BPMHC indicate that the rate of production of lipid peroxy radicals in HeLa cells under basal conditions is 33 nM/h within the cell. Our work further provides undisputable evidence on the antioxidant role of Vitamin E, as lipid peroxidation was suppressed in HeLa cells both under basal conditions and in the presence of Fenton chemistry -generated by the presence of cumyl hydroperoxide and Cu²⁺ in solution-when supplemented with the α -tocopherol surrogate, PMHC (2,2,5,7,8-pentamethyl-6-hydroxy-chromanol, an α -tocopherol analogue lacking the phytyl tail). Overall, a major milestone has been achieved: the sensitivity needed to detect trace changes in oxidative status within the lipid membrane, underscoring the opportunity to illuminate the physiological relevance of lipid peroxy radical production during cell homeostasis and disease.

4.3 Introduction

It is almost 100 years since Vitamin E was first discovered by Evans and Bishop, who reported its role as a necessary dietary factor.¹ The antioxidant properties of Vitamin E were recognized shortly after.^{2,3} Mechanistic studies in homogeneous solution and model lipid membranes pioneered by Ingold and coworkers over 35 years ago showed that Vitamin E molecules, and in particular α -tocopherol, act as scavengers of lipid peroxy radicals effectively terminating lipid chain autoxidation.^{4,6} Notwithstanding its clear chemical antioxidant role, the biological action of α -tocopherol *in vitro* and *in vivo* has proven to be complex and at times, disputed, interweaving the antioxidant role with a cell signalling role.⁷

α -Tocopherol is a chain-breaking antioxidant with beneficial roles in treating diseases associated with oxidative stress such as non-alcoholic fatty liver diseases⁸, atherosclerosis,⁹ ataxia and other neurodegenerative diseases.^{10,11} There is however a significant body of work supporting non-antioxidant roles for α -tocopherol *in vivo* such as its role in cell signalling and gene regulation.¹²⁻¹⁴ Whether these roles are truly non-antioxidant is up for debate, as oxidative

stress and formation of lipid peroxy radicals might also account for the so called “non antioxidant roles”.^{7,15} Further complexities arise when considering the potentially detrimental or pro-oxidant effects of α -tocopherol.¹⁶

The deleterious-beneficial duality of reactive oxygen species (ROS) is an equally intricate emerging hypothesis. Indeed, overproduction of ROS has been linked to several pathologies such as neurodegenerative disease, inflammation and cancer.^{10,17,18} While it is evident that ROS can damage lipids and compromise membrane integrity leading to disease, low levels of ROS have been shown to be beneficial by enhancing the defence mechanism of cells, promoting the expression of antioxidants, proteins, and enzymes.¹⁹⁻²¹

We postulate that as part of cellular homeostasis, a steady state concentration of lipid peroxy radicals is produced. In this regard, the ability to observe lipid peroxy radical formation under standard physiological conditions would enable exploring the spatiotemporal nature and quantity of ROS production, and its physiological -potentially beneficial- role. It would further enable visualizing the failure in keeping ROS homeostasis in disease and under cellular pathological conditions. Monitoring the generation of lipid peroxy radicals in both healthy and pathological conditions would ultimately provide a way to underpin the biological mechanisms in the generation and elimination of lipid peroxy radicals and the associated physiological implications.

The study of both ROS and α -tocopherol *in vivo* is a difficult pursuit. While metabolite and product studies may be useful for studying many biological phenomena, they may not provide information on the kinetics of lipid peroxidation and its inhibition by α -tocopherol (temporal resolution), nor do they provide information on the location of ROS formation and build-up (spatial resolution). In particular, the regeneration of α -tocopherol from the tocopheroxyl radical by water soluble antioxidants (a key characteristic of its potent antioxidant power),²² further complicates the utility of product studies, and has in part imperilled the acceptance that α -tocopherol mechanism of action *in vivo* rests on its lipid soluble antioxidant properties.

In order to monitor the production of lipid peroxy radicals within lipid membranes in real-time and in a non-disruptive manner, we have developed fluorogenic α -tocopherol

analogues.²³⁻²⁷ These sensitive probes preserve the chromanol moiety of α -tocopherol, and bear a BODIPY lipophilic tail, mimicking the reactivity of α -tocopherol while undergoing emission enhancement upon reaction. The probes provide a sensitive marker of lipid peroxyl radical production under chemical stress, amenable to fluorescence high throughput and imaging studies.²⁵⁻²⁷

Currently lacking is the necessary sensitivity to monitor the production of lipid peroxyl radicals in live cells under basal conditions, devoid of chemical stressors such as methyl viologen, Fe^{3+} or other sources of ROS. Fundamentally, the problem at stake is detecting a highly reactive species produced in trace amounts. This brings a conundrum in the experimental design: a large amount of ROS scavenger is needed to efficiently trap the short-lived ROS, yet the scavenger concentration has to be really small to reliably detect relative changes in consumed scavenger over time, significant enough that the ensuing signal may be decoupled from background.

Armed with a newly developed, extremely sensitive, fluorogenic α -tocopherol analogue, we report herein the observation of steady concentrations of lipid peroxyl radical produced during cellular homeostasis. Our work relies on a fluorogenic α -tocopherol analogue that undergoes a $\sim 1,000$ -fold fluorescence enhancement upon scavenging peroxyl radicals. Our work also addresses the influence of serum albumins. These proteins may mask subtle changes in ROS production by transporting α -tocopherol and its oxidized product (and the fluorogenic α -tocopherol analogue) in and out of the cell, smearing the trapping of lipid peroxyl radicals by α -tocopherol analogues.

Our results indicate that the rate of production of lipid peroxyl radicals under basal conditions is at an upper estimate of 33 nM/h within the cell. Our work further provides indisputable evidence on the antioxidant role of Vitamin E, as lipid peroxidation was suppressed in cells both under basal conditions and in the presence of Fenton chemistry -generated by the presence of cumyl hydroperoxide and Cu^{2+} in solution- when supplemented with the α -tocopherol surrogate PMHC (2,2,5,7,8-pentamethyl-6-hydroxy-chromanol, an α -tocopherol analogue lacking the phytyl tail).

Overall, a major milestone has been achieved -the sensitivity needed to detect very small changes in oxidative status within the lipid membrane- underscoring the opportunity to illuminate the physiological relevance of lipid peroxy radical production during cell homeostasis and disease.

4.4 Results and Discussion

4.4.1 *H₄BPMHC design and synthesis*

To tackle the challenge of rapidly trapping peroxy radicals with minimum amounts of a chemoselective fluorogenic probe under conditions that trace amounts of reaction could be detected from the background, both the kinetics of peroxy radical trapping and the sensitivity of the probe had to be optimum.

Kinetics were optimized by choosing the chromanol moiety of α -tocopherol as a trap segment, as with our previously designed fluorogenic probes. α -Tocopherol is the most potent naturally occurring lipid soluble antioxidant⁶ and the choice of its chromanol head ensured rapid peroxy radical trapping. Tethering a BODIPY dye to the chromanol head both provided a fluorescent reporting element but also ensured that the probes retained the membrane partition characteristic of α -tocopherol.^{24,26,27}

Sensing in our previous designs exploited photoinduced electron transfer (PeT)²⁸ from the chromanol head to the BODIPY core; where PeT ensured effective deactivation of the probe. Upon scavenging of two lipid peroxy radicals, oxidation of the trap to a chromanone or chromoquinone deactivated PeT restoring the BODIPY emission (fluorogenicity).^{24,26,27} Despite a number of attempts however, we were not able to surpass ~80-fold and ~40-fold emission enhancements in homogeneous solution and model lipid membrane studies, respectively.²⁶ Greater emission enhancements would provide us with more certainty when detecting small differences in ROS production.

Optimum sensitivity was achieved in this work upon increasing the efficiency of PeT via tuning the redox properties of the BODIPY core. The tuning was achieved by removing the methyl groups at the 1 and 7 positions of the BODIPY. This modification increased the redox potential of the dye from -1.73 V (for the previously reported H₂BPMHC) to -1.41 V for the

newly designed chromophore (**H₄BPMHC**, see Figure 4.1), as determined from electrochemical experiments (see Chapter 3, Supporting Information Figure 3.8). To ensure membrane partitioning was not compromised, the methyl groups at the 3 and 5 position of the BODIPY core in **H₂BPMHC** were swapped with propyl-chlorides in **H₄BPMHC**. These moieties additionally provide a reactive handle for future modifications

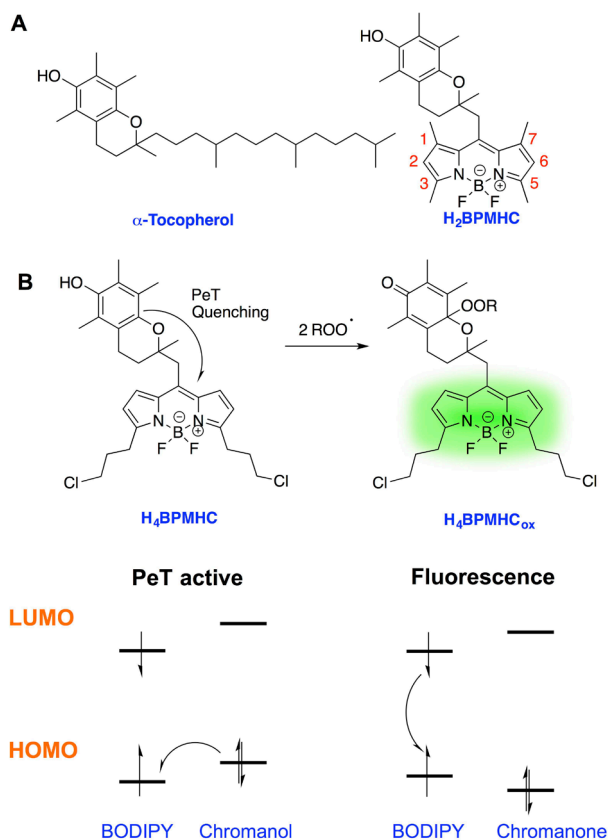


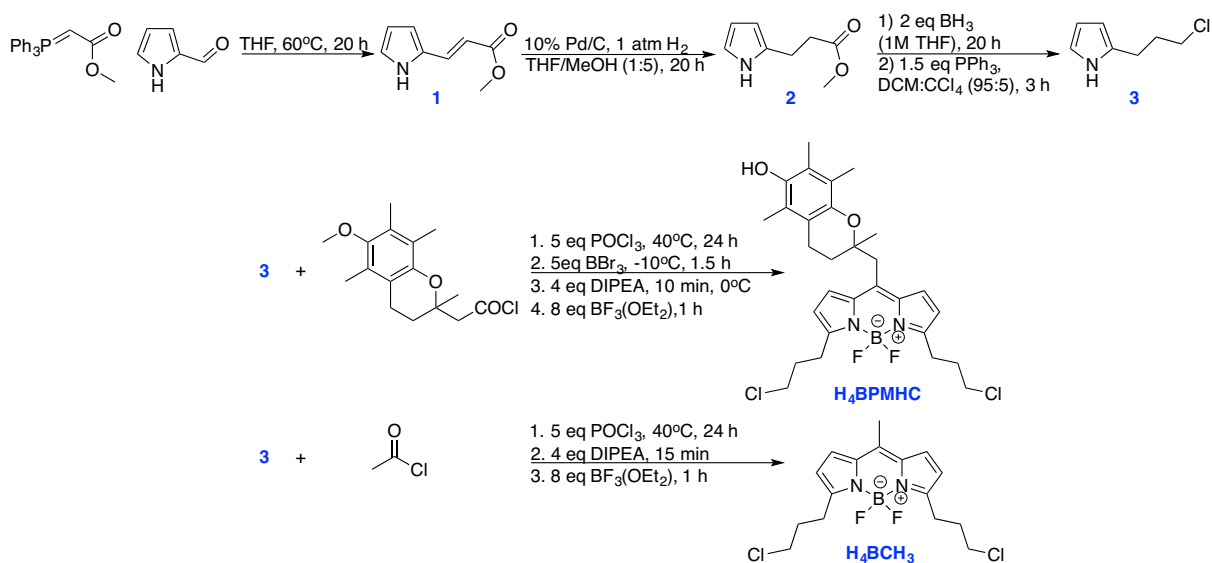
Figure 4.1 A) Structure of α -tocopherol and previously reported fluorogenic tocopherol analogue, **H₂BPMHC**. B) Proposed off/on sensing mechanism of the new fluorogenic probe, **H₄BPMHC** relying on PeT.

By providing a highly exergonic electron transfer reaction from the chromanol moiety to the BODIPY, we ensured that the fluorescence quantum yield of the BODIPY dye in the new probe was extremely low, $\phi_f \leq 0.001$, within detection error, prior to lipid peroxyl radical scavenging. This represents a $\sim 1,000$ -fold reduction in ϕ_f when compared to the parent BODIPY chromophore **H₄BCH₃**, (the BODIPY core in **H₄BPMHC**) with a $\phi_f = 0.94$. It

also sets the ceiling for fluorescence enhancement (and dynamic range) of the new probe in going from reduced to oxidized form at 1,000-fold (*vide infra*).

Synthesis of **H₄BPMHC** required for new pyrroles to be prepared, yet otherwise followed previously reported protocols²⁶ involving the condensation of two equivalents of the desired pyrroles with a chromanol acid chloride and subsequent deprotection of the chromanol moiety, deprotonation of the resulting chromanol-dipyrrin, and chelation with boron (see Scheme 4.1). The challenge in designing pyrrole **3** rested on the necessity to preserve the alpha-position of the pyrrole free, for condensation, while also affixing the reactive propyl chloride handle. Our synthesis of **3** comprised a set of 4 mild reactions that circumvented the need for protections. Starting from pyrrole-2-carboxaldehyde, we first performed a Wittig reaction with methyl (triphenylphosphoranylidene)acetate to add the 2 new carbons to form the propyl chain. The resulting alkenyl-ester, **1**, was then reduced over 2 steps (dehydrogenation and borane reduction) to give the desired alkyl-alcohol, followed by the Appel reaction to give the propyl-halogen, **3**. While all steps are reasonably high yielding, caution had to be followed in removing the solvent, as the pyrrole products are very volatile. With the new pyrrole in hand, our desired probe, **H₄BPMHC** was synthesised over 4 steps following our established protocol.²⁶ In addition, the fluorescent control, **H₄BCH₃**, was synthesised from **3** and acetyl chloride.²⁹

Scheme 4.1 Synthesis of **H₄BPMHC** and **H₄BCH₃**.



4.4.2 Spectroscopic properties

The absorption and fluorescence maxima, the extinction coefficient (ϵ), the fluorescence decay lifetime (τ_{dec}) and the fluorescence quantum yield (ϕ_f) for **H₄BPMHC**, its oxidized form (**H₄BPMHC_{ox}**, see details below for its generation) and the fluorescent control **H₄BCH₃** are listed in Table 4.1. Recorded absorption and fluorescence spectra (Figure 4.7) and maxima are in accordance with typical spectra/values for a BODIPY dye.^{29,30} The very rapid decay of **H₄BPMHC** precluded the measurement of a reliable τ_{dec} . Based on its low quantum yield, and the τ_{rad} value for the control compound, **H₄BCH₃** ($\tau_{\text{rad}} = \tau_{\text{dec}}/\phi_f \sim 6 \times 10^{-9}$ s), we predict $\tau_{\text{dec}} \sim 6 \times 10^{-12}$ s for **H₄BPMHC**. Similar τ_{dec} values ($\sim 5.6 \times 10^{-9}$) recorded for **H₄BPMHC_{ox}** and its control compound **H₄BCH₃** in turn indicated that oxidation fully restored the emissive properties of the BODIPY core, placing the emission enhancement at 1,000-fold, upon oxidation. While the emission quantum yield recorded for **H₄BPMHC_{ox}** at 0.700 is short of the expected ~ 0.940 (the value recorded for **H₄BCH₃**), the discrepancy may reflect a lack of full conversion to the oxidized product and/or partial degradation of the BODIPY core under the oxidation conditions utilized.

Table 4.1 Photophysical properties of the novel BODIPY dyes presented herein.

	Abs λ_{max} (nm)	Em λ_{max} (nm)	ϵ (cm ⁻¹ M ⁻¹)	τ_{dec} (ns)	ϕ_f
H₄BPMHC	509	520	82400	NA	0.001
H₄BPMHC_{ox}	509	520	NA	5.68	0.700
H₄BCH₃	502	516	78700	5.60	0.940

4.4.3 Reactivity with azo-initiators

In order to test the reactivity and validate the sensitivity of our new probe towards ROS, we subjected **H₄BPMHC** to peroxy radicals generated at a steady state while monitoring the fluorescence intensity enhancement. The intensity-time trajectories were recorded in the absence and, when stated, presence of competing antioxidants: either α -tocopherol or 2,2,5,7,8-pentamethyl-6-chromanol (PMHC) to record the fluorescence enhancement and the relative rate constants of **H₄BPMHC** vs α -tocopherol and PMHC. In our experiments,

peroxyl radicals were generated at a constant rate of $R_g = 9 \times 10^{-9} \text{ Ms}^{-1}$ via thermolysis at 37 °C of a 200 μM solution of the radical initiator, 2,2-azobis(4-methoxy-2,4-dimethyl valeronitrile) (MeO-AMVN), in air-equilibrated acetonitrile.^{26,31}

A fluorescence enhancement of 400 to 700-fold was recorded for **H₄BPMHC** in the presence of peroxyl radicals (Figure 4.2). This sensitivity is consistent with the deactivation of PeT following oxidation of the chromanol moiety. The larger enhancements observed in samples supplemented a priori with additional antioxidant (PMHC or α -tocopherol) are two-fold: 1) sacrificial scavenging of any radicals initially present in the solvent by the added antioxidant which would otherwise pre-activate the probe giving an artificially high initial fluorescence intensity and accordingly a reduced value for the enhancement²⁴ and 2) the inner filter effect due to the large absorbance of 10 μM **H₄BPMHC**.

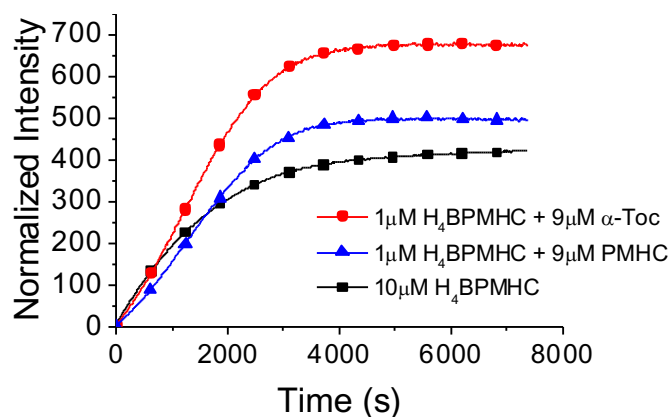


Figure 4.2 Fluorescence-time trajectories of **H₄BPMHC** (1 μM or 10 μM as indicated) in the presence of the radical initiator MeO-AMVN (200 μM) and supplemented with and without antioxidants (PMHC and α -tocopherol, 9 μM). Solutions were excited at 485 nm and emission was monitored at 520 nm. Fluorescence enhancement times, τ , were 2730 s, 2870 s, and 2460 s for **H₄BPMHC** and tocopherol, **H₄BPMHC** and PMHC, and 10 μM **H₄BPMHC** respectively.

The relative reactivity towards peroxyl radicals of **H₄BPMHC** and the competing antioxidants ($k_{\text{inb}}^{\text{H}_4\text{BPMHC}}/k_{\text{inb}}^{\text{TOH}}$) (where TOH stands for α -tocopherol or PMHC) was determined from a kinetic analysis based on Equation 4.1,²⁶ where I_∞ , I_t , and I_0 are the intensity of **H₄BPMHC** at the maximum, time t , and at $t = 0$ s and τ is the time required to fully consume the antioxidant load. The relative antioxidant activity determined for

H₄BPMHC is on par with that of both α -tocopherol and PMHC (Supplementary Information, Figure 4.8). At about 90% of the reactivity of the competing antioxidants, coupling the chromanol segment to the BODIPY moiety thus did not diminish the peroxy radical trapping reactivity of the former.

$$-\ln\left(\frac{I_{\infty}-I_t}{I_{\infty}-I_0}\right) = -\frac{k_{inh}^{H_4BPMHC}}{k_{inh}^{TOH}} \ln\left(1 - \frac{t}{\tau}\right) \quad \text{Equation 4.1}$$

4.4.4 Unmasking the influence of serum albumin in monitoring cell-membrane embedding probes

Prior to testing the sensitivity of **H₄BPMHC** in live cells under various levels of oxidative stress, and stimulated by a recent report illustrating the solubility and increased fluorescence of BODIPY dyes in the presence of bovine serum albumin (BSA),³² we investigated the effect of fetal bovine serum (FBS) on the partitioning of our BODIPY fluorophores into adherent cells. Here, partitioning is reflected by the fluorescence of our control dye, **H₄BCH₃**, observed in cells using fluorescence microscopy. This was a critical exercise to optimize staining conditions toward maximizing sensitivity.

HeLa cervical cancer cells (ATCC CCL-2) on fibronectin treated coverslips were used to compare the membrane partitioning of our fluorescent control BODIPY, **H₄BCH₃** (100 nM) when utilizing different imaging buffers -all containing 0.33% DMSO vehicle, including live cell imaging solution (LCS), and Dulbecco's Modified Eagles Medium (DMEM) supplemented with and without 10% FBS. The partitioning was recorded using widefield fluorescence (WF) microscopy. Frames 100 ms in duration were captured every minute over 30 minutes to minimize photo-bleaching from competing with the fluorescence increase due to partitioning of the dye into the cell.

Qualitatively, the presence of FBS resulted in a significant drop in intensity as may be observed in Figure 4.3 where images acquired at the same time intervals in each of the three buffers are displayed. Consistent with this observation, the corrected total cell fluorescence (CTCF) of the images acquired after 30 minutes for samples without FBS are similar (Supplementary Information, Figure 4.9A), while the CTCF of the sample containing FBS is 5

to 7-fold dimmer, indicating less dye partitioned into the cell in the presence of FBS. In all three buffers, staining of various organelle lipid membranes of the cell was clearly observed as is typical of the lipophilic BODIPY scaffold.³³⁻³⁵ Importantly, partitioning rate constants in all buffers were very similar (0.15-0.18 min⁻¹), taking about 20 minutes for the control dye to partition fully, as shown from the intensity-time trajectories fit to an exponential growth curve (Supplementary Information, Figure 4.10A). The dimmer intensity with FBS is thus not the result of kinetic control in partitioning. We may conclude that FBS while facilitating the solubility of the control dye, effectively prevented its partitioning into the cells by providing a competing hydrophobic environment for **H₄BCH₃** to reside into. This is consistent with the reports of BODIPY complexation by BSA.³²

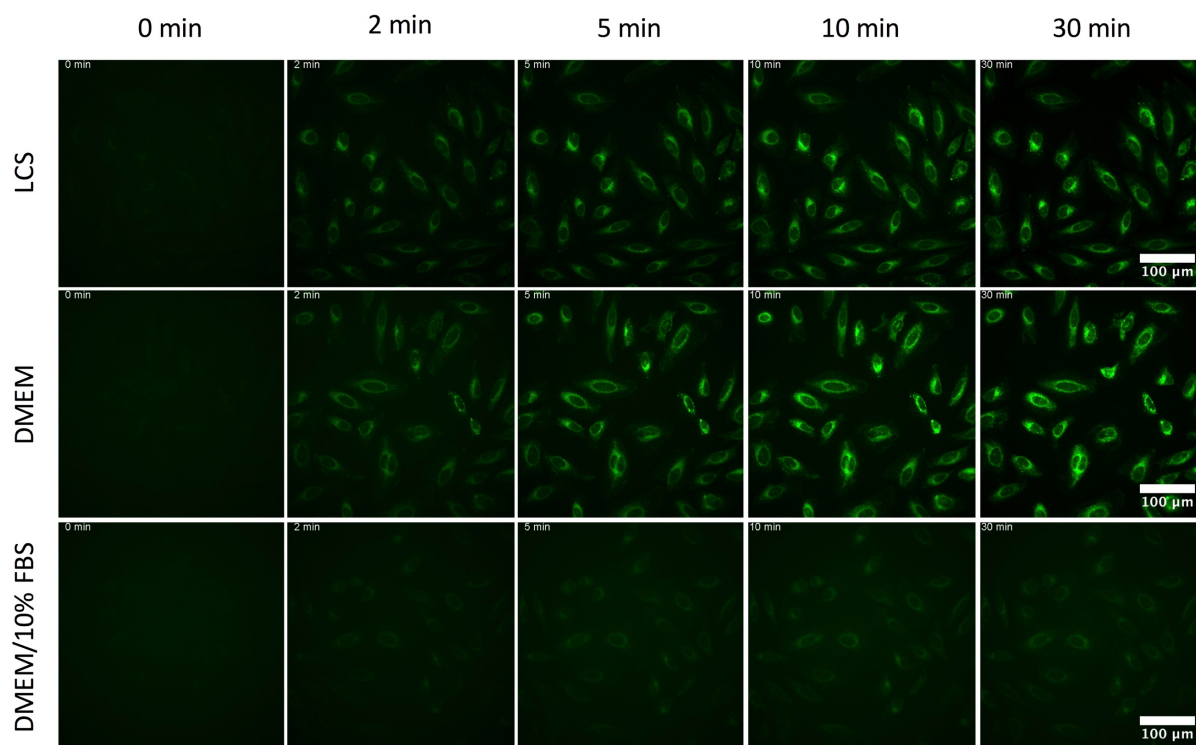


Figure 4.3 Images of HeLa cells acquired over 30 minutes upon the addition of 100 nM **H₄BCH₃** in LCS, DMEM or DMEM supplemented with 10% FBS. Images were acquired using widefield fluorescence microscopy.

That FBS in solution competes with cellular membranes for the lipophilic dye **H₄BCH₃** (and presumably also for the lipophilic fluorogenic probe **H₄BPMHC**) was additionally illustrated by a series of experiments where the staining solution of **H₄BCH₃** containing no FBS was removed, and addition of either fresh LCS, DMEM, or DMEM supplemented with 10% FBS took place. In the latter case, the control dye was rapidly depleted from the cell membranes, while only minor intensity reductions took place in the former two cases (no FBS added), see Figure 4.4. Final intensities of the solution containing 10% FBS were 50-fold lower than when FBS was not added (Figure 4.9B). Intensity-time trajectories of the partitioning out of **H₄BCH₃** are shown in Figure 4.10B and clearly indicate a rapid and significant drop in intensity in the presence of FBS.

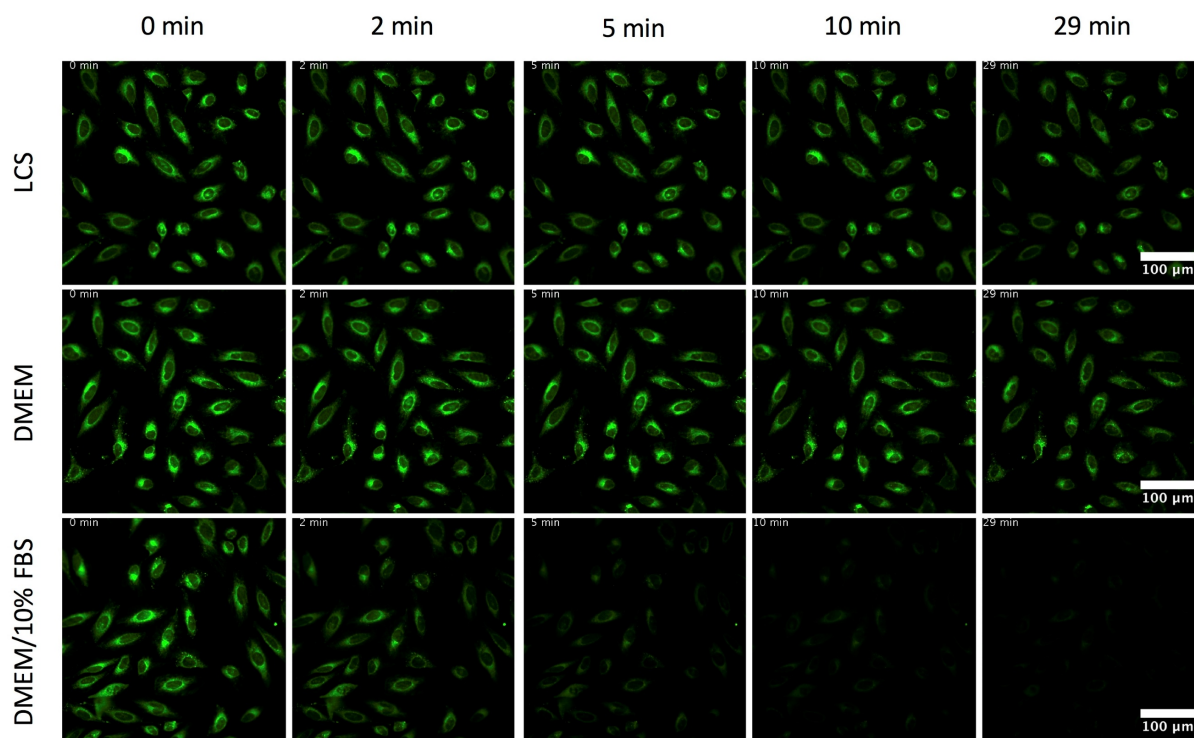


Figure 4.4 Images of HeLa cells acquired over 30 minutes upon the replacement of 100 nM **H₄BCH₃** in LCS, with fresh media (LCS, DMEM or DMEM supplemented with 10% FBS). Images were acquired using widefield fluorescence microscopy.

Previous imaging studies in DMEM supplemented with FBS precluded us from using dye concentrations below 1 μM . Lengthy incubation times (e.g. > 30 minutes) were additionally required. By utilizing buffers free from FBS, we reduce the incubation time thus preventing masking reactions occurring during the incubation period. Additionally, utilizing buffers free from FBS enables us to reduce the probe concentration, by at least one order of magnitude to 100 nM. This is key when small concentration of analytes, such as lipid peroxy radicals in this work (and concomitantly small amounts of probe) are expected to be produced (to react). Working with minimal amounts of the fluorogenic probe **H₄BPMHC** ensures maximizing signal to background, enabling us to observe fluorogenic antioxidant consumption in real-time upon production of trace amounts of peroxy radicals (*vide infra*).

Ultimately, incubation of **H₄BPMHC** and **H₄BCH₃** (100 nM) for 10 min in LCS in the absence of FBS provided optimal conditions in terms of signal to background. LCS was chosen as the incubation buffer for all subsequent experiments due to its low background fluorescence, and the relatively good cell viability when compared to unsupplemented DMEM.

4.4.5 Lipid peroxy radicals generated during cellular homeostasis and under fenton conditions

Armed with newly developed **H₄BPMHC** and working with optimized imaging conditions, we next sought to explore the antioxidant status of live cells both when exposed to high levels of oxidative stress in the form of lipid peroxy radicals generated via Fenton chemistry, but also under conditions of cellular homeostasis (no chemical stressors). We also explored how antioxidant loads in the form of chromanol compound, PMHC, affected the antioxidant status both under Fenton chemistry and in the absence of chemical stressors (see Figure 4.5).

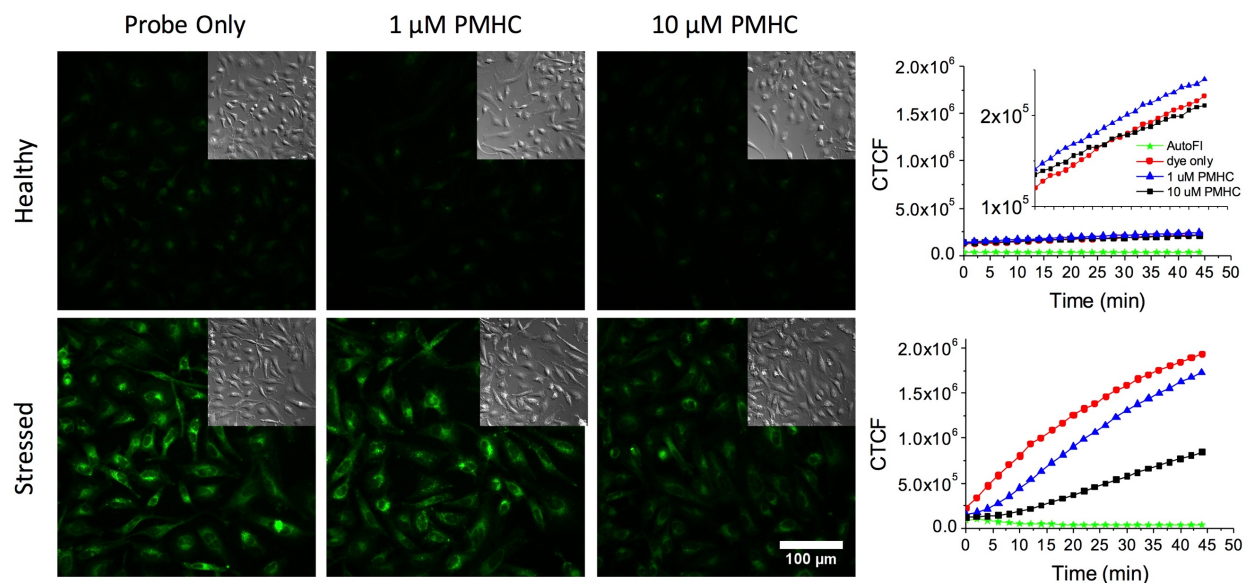
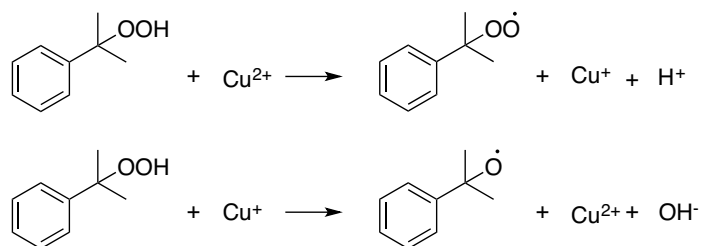


Figure 4.5 A) Images of HeLa cells in the presence of 100 nM H_4BPMHC (Probe) with/without PMHC acquired after 50 minutes of treatment with (stressed) or without (healthy) cumene hydroperoxide (100 μM) and copper sulfate (10 μM). Images were acquired using widefield microscopy. Inset shows compressed DIC images for the same region. B) Corrected total cell fluorescence vs time determined from images acquired over a 45 minute period with 100 nM H_4BPMHC in healthy cells and cells exposed to Fenton reagents.

HeLa cells were stained with a 100 nM solution of H_4BPMHC for 10 min, washed and the buffer replenished. A combination of cumene hydroperoxide (100 μM) and copper sulfate (10 μM) was used as a source of ROS under Fenton conditions. Cumene hydroperoxide reacts with copper via Fenton reaction to produce cumoxyl and cumoperoxyl radicals which may in turn lead to lipid peroxidation and the production of lipid peroxy radicals (see Scheme 4.2 for reaction).³⁶ Antioxidant additives, consisting of 1 μM and 10 μM solutions of PMHC pre-incubated for 30 min followed by cell staining for 10 min, and washing, were also studied with and without Fenton reagents. While one may argue that α -tocopherol should be the preferred choice, both PMHC and the latter have the same radical trapping reactivity, yet α -tocopherol has poor solubility and cell penetration. Thus, we use PMHC in our work, as a source of lipid soluble antioxidant. Unstained cells were imaged to determine the cell autofluorescence at the laser power and gain settings used.

Scheme 4.2 Formation of cumoperoxy and cumoxy radicals from cumene hydroperoxide in the presence of copper.



H₄BPMHC underwent a 30-fold enhancement in the CTCF value in the presence of the Fenton reagents, computed by comparing the sample before and after 50-minute incubation with the reagents (see Supporting Information section, Figure 4.11). A prominent yet smaller fluorescence enhancement of 24-fold and 10-fold was in turn recorded after 50 minutes for samples also stressed with the Fenton reagents, yet supplemented with 1 μM and 10 μM PMHC respectively when compared to time 0. (see Figure 4.11). Importantly, enhancements in the absence of Fenton reagents were smaller than 3-fold (*vide infra*). Further, no change in fluorescence was observed for our control dye, **H₄BCH₃** in the presence of either PMHC or Fenton reagents (Figure 4.6B). Close inspection of images acquired with 100 \times magnification following treatment with Fenton reagents for 50 minutes (see Supporting Information section, Figure 4.12) reveals that **H₄BPMHC** is localized in the various cell lipid membranes consistent with its lipophilic nature. A similar distribution is also apparent from the dim images prior to addition of Fenton reagents.

To provide a benchmark value for how much peroxy radical was trapped by **H₄BPMHC** after 50 min incubation with Fenton reagents (both with and without additive PMHC), we compared CTCF values for cells stained with **H₄BPMHC** vs **H₄BCH₃**. Under the assumption that both probes partition equally well within cells (i.e. their concentrations are similar), and that the lifetime of **H₄BPMHC_{ox}** in membranes is on par with that of **H₄BCH₃**, the CTCF recorded with **H₄BCH₃** would correspond to 100% conversion of **H₄BPMHC** to its oxidized, fully emissive, form upon trapping of two peroxy radicals. Figure 4.6 shows CTCF values normalized by frame exposure time and obtained under otherwise identical conditions. Samples containing 100 nM **H₄BPMHC** and supplemented with 0, 1 μM

and 10 μM PMHC achieved final intensities (and correspondingly, conversions) of 13%, 12% and 5.5%, respectively, relative to the intensities recorded with H_4BCH_3 . PMHC thus exerted a concentration dependent protective effect.

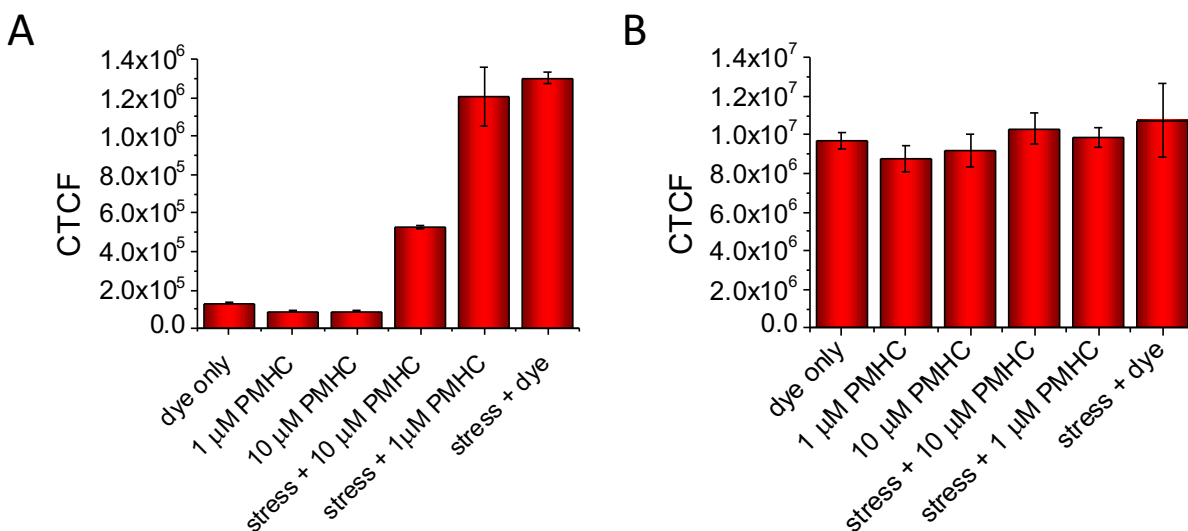


Figure 4.6 CTCF of H_4BPMHC (A) and H_4BCH_3 (B) in HeLa cells. Intensities were determined after 50 minutes of treatment with/without stressor. Dye = 100 nM in either H_4BPMHC or H_4BCH_3 , stressor = 100 μM cumene hydroperoxide and 10 μM copper sulfate. Images were acquired using widefield microscopy. CTCF of B was corrected by the exposure time used to match that of A.

CTCF Intensity-time trajectories were next retrieved from the data set by plotting the CTCF evolution with time for all conditions explored (Figure 4.5B). For cells bearing the Fenton reagents and no PMHC, the initial intensity increased in a linear fashion (reaching a 30-fold increase within 50 minutes). In contrast, for cells bearing the Fenton reagents and 1 μM PMHC, an induction period in fluorescence intensity was observed followed by a linear increase with a similar rate to that observed for the sample with no antioxidant additive. The observed induction period is a hallmark of inhibition of oxidation of H_4BPMHC by PMHC, under competitive kinetic conditions. The induction period was prominent (~ 10 min) when samples were supplemented with 10 μM PMHC, yet the intensity after the induction increased at a smaller rate than when no antioxidant was present indicating that inhibition was followed by retardation in the oxidation of H_4BPMHC .

Results of CTCF evolution with time underscore that PMHC, within the cellular milieu, is outcompeting **H₄BPMHC** in scavenging ROS produced by cumene hydroperoxide and copper. Qualitatively, similar results (induction periods) were previously observed in liposomes exposed to a source of peroxy radicals and stained with a less sensitive, yet equally reactive and lipophilic analogue of **H₄BPMHC**.²⁶ Our current work shows that PMHC, lacking a lipophilic tail, and thus provided with higher mobility within the cell membrane lipid milieu, is more effective in scavenging radicals at the cellular level than **H₄BPMHC** -and presumably α -tocopherol as **H₄BPMHC** and the latter are expected to have similar reactivities within the membrane.²⁶ While such an outcome had been described with model lipid membranes^{22,26} it is truly remarkable that within the complex cell environment it still holds.

An intriguing aspect, defying explanation, is the contrasting times required to oxidize **H₄BPMHC**, and comparatively, to consume the antioxidant additive PMHC. The time evolution of CTCF with Fenton reagents reveals that while 50 min were required to oxidize ~10% of the probe, ~5 min elapsed in the induction period with PMHC, for experiments where probe and antioxidant were incubated at 100 nM and 1 μ M, respectively. During the induction period, we postulate, all PMHC within the cell was depleted leading next to a temporal evolution characteristic of no PMHC. Should **H₄BPMHC** and PMHC have similar partitions within the cell lipid milieu, these numbers would indicate that 100-fold more PMHC reacts roughly in one tenth of the time than **H₄BPMHC**. This large difference conflicts with the 10-fold larger reactivity toward peroxy radicals recorded for PMHC vs both an analogue of **H₄BPMHC** and α -tocopherol, when in lipid membranes.²⁶ Alternatively, partitioning of PMHC within the cell is reduced compared to the probe, where upon incubation of both PMHC and **H₄BPMHC**, and following washing of the solution and refilling with fresh LCS buffer, PMHC would more readily escape cellular confinement given the lack of a lipophilic tail.

CTCF intensity-time trajectories acquired with 100 nM **H₄BPMHC** and no Fenton reagents in turn shed light on basal levels of lipid peroxy radicals produced during cellular homeostasis. In healthy cells, there was a notable gradual fluorescence increase with changes in CTCF values of 1.00×10^5 CTCF and 0.75×10^5 CTCF over 50 minutes for the samples

supplemented with either no or 1 μM PMHC, and for the sample with 10 μM PMHC respectively. In the context of the benchmark, emission intensity recorded under identical conditions for 100 nM **H₄BCH₃** -at a value of 1.00×10^7 CTCF- we may estimate that the amount of peroxy radicals produced under basal conditions over 50 min resulted in at most 1% of the probe being oxidized in a period of 50 min. If we approximate the concentration of dye inside a cell at 1.7 μM (see Supplementary Information, Section 4.7.3 for discussion), we may place the rate of production of lipid peroxy radicals under basal conditions at 33 nM/h within a cell (2 equivalents of ROS required to oxidize the probe). Regarding the smaller slope recorded for cells whose media was supplemented with 10 μM PMHC, we may postulate that excess PMHC suppressed the oxidation of **H₄BPMHC** in healthy cells. In line with PMHC protection, analysis of the fluorescence intensity also shows a noticeable difference in fluorescence between healthy samples pre-supplemented with PMHC vs those supplemented with no PMHC, about 2-fold larger for the latter, Figure 4.6A. Presumably some initial oxidation of **H₄BPMHC** may occur while incubation, washing and exploration of the chambers prior to image acquisition, where oxidation would be enhanced when no PMHC is present.

In closing, we may compile the above results to establish the sensitivity of **H₄BPMHC** within cells. Overall, a 40-fold fluorescence enhancement was observed between healthy cells pre-supplemented with PMHC, and cells exposed to Fenton reagents for 50 minutes without additional antioxidant. Considering that in the latter case there was only 13% conversion, a maximum enhancement would be placed at ~ 300 -fold. The discrepancy with the expected 1,000-fold enhancement may be rationalized in terms of pre-oxidation in the dark periods of the experiment. We note that should a 0.3% fraction of our pristine solution of **H₄BPMHC** undergo oxidation, and considering the enhancement is $\sim 1,000$ -fold in going from reduced to **H₄BPMHC_{ox}**, such a small conversion would account for an initial intensity 3-fold larger than that of pristine solution, and in turn a $1,000/3$ or ~ 300 value for the observed intensity enhancement.

4.5 Conclusion

Albeit lipid peroxy radicals have long been known to be formed at the cellular level,^{20,37} their elusive nature has prevented quantifying this highly reactive intermediate. Their physiological role has thus remained obscured, and that of α -tocopherol, its par excellence scavenger, controversial as an antioxidant.

By developing the highly sensitive fluorogenic α -tocopherol analogue, **H₄BPMHC**, we managed to overcome a major limitation in detecting trace amounts of lipid peroxy radicals, that is, that the initial signal is small enough that trace amounts of reaction can be monitored. The high imaging sensitivity we achieved is both the result of optimizing the construct, ensuring very rapid PeT takes place amply outcompeting emission by about 1,000-fold, and removing serum albumins, proteins that will otherwise scramble the distribution of lipophilic molecules including BODIPY dyes in general, and **H₄BPMHC** in particular. Thus, serum albumins may replenish fresh probe and remove oxidized emissive probe, ultimately masking lipid peroxidation. The latter results provide a note of caution when using lipophilic dyes in live cell imaging in the presence of FBS/BSA. Our work ultimately calls for the avoidance of FBS for cellular imaging of BODIPY fluorophores (and likely other lipophilic small molecule fluorophores) to gain better signal to background at low (nanomolar or submicromolar) concentrations.

Our results in live cells underscore the potential of **H₄BPMHC** to investigate the physiological relevance of lipid peroxy radical production during cell homeostasis and disease. The resulting large dynamic range of **H₄BPMHC** allowed us to not only discern healthy cells from cells treated with an onslaught of ROS, but more importantly allowed us to detect lipid peroxidation at basal levels and in the presence of additional antioxidant. Importantly, we showed undisputable evidence of the antioxidant role of Vitamin E *in vitro* as lipid peroxidation was suppressed in the presence of additional PMHC in HeLa cells under duress, and under normal cell culture conditions. The latter indicates potential complications that can arise from using cultured cells in experiments, especially when looking at the production of ROS. These experiments are typically conducted in the absence of antioxidants and the outcome of lipid peroxy radical formation, we believe, should be considered in interpreting results.

In closing, we note that while the chemistry of α -tocopherol and lipid peroxy radicals has been studied extensively in the last 35 years, their complex relationship in cellular mechanisms remains very much unclear. We strongly believe that imaging studies with sensitive fluorogenic probes capable of detecting subtle levels of lipid peroxidation, while also mimicking the reactivity of tocopherol, like **H₄BPMHC** reported herein, will ultimately help unravel the physiological role of both lipid peroxy radicals and α -tocopherol *in vivo*.

4.6 Experimental

4.6.1 Materials

HPLC grade solvents for spectroscopy and column chromatography were purchased through Fisher Scientific. MeO-AMVN was purchased from WAKO Pure Chemicals Ltd. Buffers, and growth media and other reagents for cell culture and staining were purchased through ThermoFisher Scientific. All other chemicals were supplied by Sigma-Aldrich, Co. and used without further purification.

4.6.2 Instrumentation

Absorption spectra were recorded using a Hitachi U-2800 UV-vis-NIR spectrophotometer. Luminescence spectra were recorded using a PTI QuantaMaster spectrofluorimeter using 1 cm \times 1 cm quartz cuvettes. Spectra were corrected for detector sensitivity. ¹H NMR and ¹³C NMR spectra were recorded on a Varian VNMRS 500 or a Bruker AVIIIHD 500 instrument at 500 and 126 MHz, respectively. Electrospray ionization (ESI) and atmospheric chemical ionization (APCI) mass spectra were measured on a Bruker maXis impact.

4.6.3 Time-based fluorescent enhancements with radical initiator

Time based fluorescent measurements were recorded on a PTI QuantaMaster spectrofluorimeter equipped with a four-position Peltier with motorized turret. 3 mL glass fluorimetry cells with 1 cm path lengths were used as sample cells. The excitation and emission slits were set to 1.2 nm. The temperature control was set to 37°C. Three samples containing

10 μM antioxidant load were prepared in acetonitrile (MeCN): 1) 10 μM **H₄BPMHC** 2) 1 μM **H₄BPMHC** and 9 μM α -tocopherol, and 3) 1 μM **H₄BPMHC** and 9 μM PMHC. Samples were excited at 485 nm and emission was collected at 520 nm. Initial fluorescence of the samples was measured, and samples were then spiked with 200 μM radical initiator, MeO-AMVN (2,2-azobis(4-methoxy-2,4-dimethyl valeronitrile)). Fluorescence was then recorded over time until the fluorescence intensity of all samples reached a maximum plateau.

4.6.4 Fluorescence quantum yield

Acetonitrile solutions of *meso*-acetoxymethyl-BODIPY dye²⁹ (H_2BOAc , $\phi_f=0.87$), or 8-phenyl pyrromethene fluoroborate (H_6BPh)³⁸ ($\phi_f = 0.013$) (structures in Figure 4.14) were used as standards to calculate the quantum yields of solutions of oxidized **H₄BPMHC** and **H₄BCH₃** or reduced **H₄BPMHC** respectively in MeCN. Solutions of **H₄BPMHC** were also supplemented with 5 μM PMHC to help to prevent any unwanted oxidation. Absorption and emission spectra of the dye standards and dyes of interest were measured at five different concentrations. 200 μM MeO-AMVN, a radical initiator, was added to **H₄BPMHC** to obtain **H₄BPMHC_{ox}** where the absorption and emission spectra were then measured once the maximum fluorescence intensity was reached. The integrated intensity versus absorbance were then plotted and fitted linearly. Quantum yields for the dyes with respect to the standard were obtained from Equation 4.2, where Φ_x , Δ , and η refer, respectively, to the fluorescence quantum yield, the slope obtained from the above-mentioned plot, and the solvent refractive index for the unknown (x) or standard (st) sample. Emission spectra were recorded for solutions using excitation and emission slits of 1.2 nm for solutions of H_2BOAc , **H₄BPMHC_{ox}** and **H₄BCH₃**, and 4 nm for solutions of H_6BPh and **H₄BPMHC**.

$$\phi_x = \phi_{st} \left(\frac{\Delta_x}{\Delta_{st}} \right) \times \left(\frac{\eta_x^2}{\eta_{st}^2} \right) \quad \text{Equation 4.2}$$

4.6.5 Fluorescence lifetime studies

The fluorescence lifetime measurements were carried out using a Picoquant Fluotime 200 Time Correlated Single Photon Counting setup employing a supercontinuum laser (WhiteLase SC-400-4, Fianium, Beverly, MA). Excitation wavelengths were spectrally separated from broadband emission by a computer controlled acousto-optical tunable filter (AOTF, Fianium). **H₄BPMHC_{ox}**, and **H₄BCH₃** were excited at 485 nm, and emission was collected at 520 nm and 516 nm respectively. The excitation rate was 10 MHz, and the detection frequency was less than 100 kHz. Photons were collected at the magic angle.

4.6.6 Microscopy

All fluorescence and differential interference contrast (DIC) imaging of HeLa cells were performed using either a wide-field objective-based total internal reflection fluorescence (TIRF) microscopy setup equipped with an oil-immersion objective (Nikon CFI SR Apochromat TIRF 100x, NA = 1.49) or a lower magnification wide-field microscopy setup equipped with an air objective (Nikon CFI Plan Apo VC 20x objective, NA = 0.75) consisting of an inverted microscope (Nikon Eclipse Ti) equipped with a Perfect Focus System (PFS). A stage-top incubator (Tokai Hit) was used to maintain the cells at 37°C (5% CO₂) in a humidified atmosphere. The excitation laser was 488 nm with powers of 0.09 mW (for 20x) and 0.04 mW (for 100x) measured out of the objectives where the beam was coupled into the microscope objective using a multiband beam splitter (ZT488/640rpc, Chroma Technology). The emission was spectrally filtered with an emission filter (ZET488/640m). For multi-channel imaging between the 488 channel and DIC, a motorized filter block turret was used. The fluorescence emission was collected through the same objective and captured on a back illuminated electron multiplying charge coupled device (EM-CCD) camera (Andor iXon Ultra DU-897).

4.6.7 Cell culture

HeLa cells (ATCC CCL-2) were cultured in Dulbecco's Modified Eagle Medium (DMEM) containing high glucose, L-glutamine, phenol red, and sodium pyruvate (Gibco),

supplemented with 10% fetal bovine serum (FBS) and 1% penicillin-streptomycin. Cells were maintained at 37 °C (5% CO₂) in a humidified atmosphere and were trypsinized and split 1/15 about twice a week when confluence of cells was reached. Cells were passaged a maximum of 30 times and tested for mycoplasma infection upon first passaging.

4.6.8 Cell imaging of H₄BCH₃

24 h prior to day of imaging, cells were plated on 35 mm glass imaging dishes (World Precision Instruments, Inc.) pre-coated with fibronectin (1 µg/cm²), in DMEM containing growth factors. After 24 h, cells were then washed twice with incubation buffer (LCS, DMEM or DMEM/10%FBS), followed by the addition of 1 mL of fresh incubation buffer. Cells were stained by the addition of 500 µL of the dye (300 nM) to give a final concentration of 100 nM in dye. The solution of dye was prepared from the addition of 5 µL of a 30 µM stock solution in DMSO. This overall 300-fold dilution was to ensure the percentage of DMSO in media was 0.33% (v/v). Images of the samples were then collected every minute (100 ms exposure time) over the course of 30 minutes.

4.6.9 Cell imaging of H₄BPMHC or H₄BCH₃ in healthy and stressed cells

24 h prior to imaging, 300 µL of 50 000 cells/mL were plated into each well of an 8-well ibidi-Treat µ-slide in DMEM containing growth factors. After 24 h, all wells were washed twice with LCS, and either loaded with 200 µL LCS, or 200 µL LCS containing either 1 µM PMHC or 10 µM PMHC. After 30 minutes, wells to be stained were loaded with 100 µL of a 300 nM stock of H₄BPMHC or H₄BCH₃ bringing the final concentration to 100 nM in dye, and incubated for 10 minutes. Wells were then washed with LCS and loaded with either 300 µL of LCS (wells to be maintained as healthy) or 200 µL of LCS (wells to be stressed later once slide is loaded onto the microscope). The slide was then loaded onto the microscope, where once fixed in place, 100 µL of LCS containing 300 µM cumene hydroperoxide and 30 µM copper sulfate was added to the wells to be stressed (100 µM and 10 µM final concentration of cumene hydroperoxide and copper sulfate respectively). All wells were then imaged every

2 minutes (300 ms and 70 ms exposure for **H₄BPMHC** and **H₄BCH₃** respectively) over the course of 50 minutes, where 3 single frames of each well were then taken.

4.6.10 Image analysis

All images were processed using the FIJI imaging processing package.³⁹ All quantifications were performed adapting a previously published protocol.⁴⁰ Equation 4.3 was used to calculate the corrected total cell fluorescence (CTCF):

$$CTCF = \frac{\text{IntDensity}_{\text{total cell area}} - (\text{Total Cell Area} \times \text{BkgFluorescence})}{N_{\text{cells}}} \quad \text{Equation 4.3}$$

where $\text{IntDensity}_{\text{total cell area}}$ is the integrated intensity of the pixels for all cells in the image, Total Cell Area is the number of pixels of all of the cells, BkgFluorescence is the mean fluorescence intensity per pixel for a region containing no cells and N_{cells} is the number of cells in the image. Measurements and errors reported are from the average and standard deviation CTCF obtained from at least 3 images per sample.

An ImageJ macro was utilized to identify the cells from the DIC image. First, a variance filter of radius five pixels was applied to the DIC image. The resulting image was converted to a binary image and the Fill Holes function was applied. The Analyze Particles function was next used to identify and fill any remaining holes smaller than 20 pixels² in the binary image, by setting their pixel values to 255. A dilate function was then applied. The binary image was then used to create a selection area for the region containing cells and the region without.

4.6.11 Quantifying concentration of probe in cells

HeLa cells were seeded at 5×10^4 cells/mL in a 10 cm petri dish (23.5 mL) and were allowed to grow for 24 h, approximately doubling in population (These concentrations and volumes were used to reflect the ratio of concentration:volume:surface area of the ibidi dishes used for imaging). Cells were then washed with LCS, and 23.5 mL of LCS containing 100 nM **H₄BCH₃** was added for 10 minutes. The fluorescence of the supernatant was then measured. Simultaneously, a 10 cm petri dish containing no cells (control) was treated the same way: 23.5

mL of LCS with 100 nM **H₄BCH₃** was added for 10 minutes. The fluorescence of this control was then measured and compared to the supernatant of the sample containing cells. Once the LCS solution was removed from the control dish, 2 mL of DMSO was then added and the fluorescence of this solution was measured to quantify the amount of dye which adhered to the dish. With these values in hand, the amount of dye which partitioned into cells was then quantified (see Section 4.7.3).

4.6.12 Synthesis

Methyl (E)-3-(1H-pyrrol-2-yl)acrylate (1). Pyrrole-2-carboxaldehyde (3.0 g, 0.031 mol) was dissolved in tetrahydrofuran (THF) (60 mL) under argon. Methyl (triphenylphosphoranylidene)acetate (12.6 g, 0.037 mol, 1.2 eq.) was added to the stirring solution and the temperature was increased to 60 °C. After 20 h the solvent was removed under reduced pressure. The resulting solid was loaded onto a silica flash column and eluted with 20% ethyl acetate in hexanes affording the clean white solid product (4.82 g, 97%). ¹H-NMR (500 MHz; CDCl₃): δ 9.56 (s, 1H), 7.64 (d, *J* = 15.9 Hz, 1H), 6.96 (q, *J* = 2.0 Hz, 1H), 6.60 (dd, *J* = 4.7, 2.6 Hz, 1H), 6.31 (q, *J* = 3.0 Hz, 1H), 6.16 (d, *J* = 15.9 Hz, 1H), 3.81 (s, 3H). ¹³C-NMR (126 MHz; CDCl₃): δ 168.9, 135.1, 128.5, 122.9, 114.7, 110.9, 110.5, 51.7 HRMS (ESI⁺) for C₈H₉NO₂Na (M+Na) calcd 174.0525, found 174.0522.

Methyl 3-(1-H-pyrrol-2-yl)propanoate (2). **1** (4.82 g, 0.031 mol) was dissolved in methanol/THF (5:1, 170 mL) in the presence of palladium on activated carbon (0.482 g, 10% wt/wt) under 1 atm of hydrogen. The reaction mixture was stirred for 20 h at room temperature after which it was filtered through celite. Solvent was then removed from the filtered solution very carefully since the product was volatile. Due to volatility, the exact mass of the product was not quantified since residual solvent was present, and was used without purification. ¹H-NMR (500 MHz; CDCl₃): δ 8.72 (s, 1H), 6.72 (td, *J* = 2.6, 1.6 Hz, 1H), 6.18 (q, *J* = 2.9 Hz, 1H), 6.01-5.99 (m, 1H), 3.77 (s, 3H), 2.99 (t, *J* = 7.1 Hz, 2H), 2.72 (t, *J* = 7.1 Hz, 2H). ¹³C NMR (126 MHz; CDCl₃): δ 174.4, 130.9, 116.9, 108.1, 105.4, 51.9, 34.4, 22.7 HRMS(APCI⁺ for C₈H₁₂NO₂) (M+H) calcd 154.08626, found 154.08618.

3-(1H-pyrrol-2-yl)propan-1-ol. 2 (0.031 mol) was dissolved in THF under argon at -78°C. Borane in 1M THF (6.2 mL, 2 eq) was added dropwise to the solution. The reaction mixture was allowed to warm to room temperature and stirred for 20 h. The reaction was then quenched with methanol, diluted with dichloromethane and washed twice with brine. Organic fractions were dried over anhydrous sodium sulfate and solvent was removed carefully under reduced pressure and used without further purification. ¹H-NMR (500 MHz; CDCl₃): δ 8.59 (s, 1H), 6.68 (td, *J* = 2.6, 1.6 Hz, 1H), 6.17 (d, *J* = 3.0 Hz, 1H), 5.97 (td, *J* = 1.6, 0.8 Hz, 1H), 3.69 (t, *J* = 6.2 Hz, 2H), 2.81 (s, 1H), 2.72 (t, *J* = 7.4 Hz, 2H), 1.92-1.86 (m, 2H). ¹³C NMR (126 MHz; CDCl₃): δ 132.0, 116.5, 108.1, 105.0, 62.1, 32.4, 24.1 HRMS (APCI for C₇H₁₀ON) (M-H) calcd 124.07679, found 124.07609.

2-(3-Chloropropyl)-1H-pyrrole (3). 3-(1H-pyrrol-2-yl)propan-1-ol (0.031 mol, assumed quantitative from previous step) was dissolved in dichloromethane/carbon tetrachloride (95:5, 150 mL) under argon. Triphenylphosphine (8.1 g, 0.031 mol, 1 eq.) was added in one portion. The reaction mixture was stirred for 3 h at 40 ° C. Solvent was then carefully removed under reduced pressure, and the resulting oil was loaded onto a silica flash column and eluted with ethyl acetate/hexanes (20%) affording an oil (2.15 g, 50% yield from compound **1**, over 3 steps). ¹H-NMR (300 MHz; CDCl₃): δ 8.01 (s, 1H), 6.71 (d, *J* = 1.4 Hz, 1H), 6.19 (d, *J* = 2.8 Hz, 1H), 6.00 (s, 1H), 3.60 (t, *J* = 6.3 Hz, 2H), 2.82 (t, *J* = 7.3 Hz, 2H), 2.10 (t, *J* = 6.9 Hz, 2H). ¹³C NMR (75 MHz; CDCl₃): δ 130.6, 116.6, 108.5, 105.5, 44.5, 32.5, 24.6 HRMS (APCI for C₇H₁₁ClN) (M+H) calcd 144.0580, found 144.0573.

8-((6-Hydroxy-2,5,7,8-tetramethylchroman-2-yl)-methyl)-1,5-di-(3-chloropropyl)-Pyrromethene Fluoroborate (H₄BPMHC). 2-(6-Methoxy-2,5,7,8-tetramethylchroman-2-yl)acetic acid²⁶ (0.19 g, 0.7 mol) was dissolved in thionyl chloride (1 mL) under argon and stirred at 50 °C for 1 h. The thionyl chloride was then removed by co-evaporation with toluene (15 mL, 5 times) and the flask was left on a vacuum pump overnight. The resulting acid chloride was then dissolved in 7 mL of dichloromethane under argon.

Phosphorus oxychloride (0.33 mL, 3.4 mol) was added dropwise followed by **3** (0.2 g, 1.4 mol) pre-dissolved in 2 mL of dichloromethane. The reaction mixture was stirred for 22 h at 35 °C. The mixture was then diluted with dichloromethane, washed with brine, and dried over sodium sulfate. Solvent was removed under reduced pressure. The resulting red oil was dissolved in dichloromethane under argon and cooled to -10 °C. Borontribromide (3.5 mL, 1M in dichloromethane, 3.5 mol) was added dropwise. The reaction mixture was allowed to slowly warm to room temperature over the course of 1.5 h when the reaction was quenched carefully with water. The solution was extracted with ethyl acetate and the organic fractions were washed with brine and dried over sodium sulfate. Solvent was removed under reduced pressure. The resulting red oil was dissolved in 5 mL of dichloromethane and 10 mL of toluene under argon at 0 °C. Diisopropylethylamine (0.49 mL, 2.8 mol) was added dropwise. After 10 minutes, Boron trifluoride diethyl etherate (0.69 mL, 6 mmol) was added dropwise and stirred for 1 h. The mixture was then quenched with water and extracted with ethyl acetate. The organic fractions were washed with brine and dried over sodium sulfate. Solvent was removed under reduced pressure. The resulting red solid was purified by flash column chromatography (30% ethyl acetate in hexanes) followed by further purification by a preparatory silica plate eluted in dichloromethane giving an orange film (30 mg, 8% yield). ¹H-NMR (500 MHz; CDCl₃): δ 7.12 (d, *J* = 4.2 Hz, 2H), 6.32 (d, *J* = 4.2 Hz, 2H), 4.25 (s, 1H), 3.62 (t, *J* = 6.6 Hz, 4H), 3.22-3.11 (m, 6H), 2.68 (qd, *J* = 13.3, 7.0 Hz, 2H), 2.22 (quintet, *J* = 7.3 Hz, 4H), 2.14 (s, 3H), 2.11 (s, 3H), 1.94 (s, 3H), 1.87 (t, *J* = 6.9 Hz, 2H), 1.28 (s, 3H). ¹³C NMR (126 MHz; CDCl₃): δ 159.5, 145.1, 144.8, 140.5, 136.1, 129.5, 122.9, 121.5, 118.6, 117.5, 116.6, 74.3, 44.3, 40.7, 33.0, 31.6, 26.1, 24.5, 20.7, 12.3, 12.2, 11.3 HRMS (ESI⁻) for C₂₉H₃₄BCl₂F₂N₂O₂ (M-H) calcd 561.2064 found 561.2076.

8-Methyl-1,5-di-(3-chloropropyl)-Pyrromethene Fluoroborate (H₄BCH₃). Acetyl chloride (0.05 mL, 0.7 mmol, 1 eq) was dissolved in dry dichloromethane (6 mL) under argon. Phosphorus oxychloride (0.33 mL, 3.5 mmol, 5 eq) was added dropwise to the solution followed by **3** (0.200 g, 1.4 mmol, 2 eq). The reaction mixture was then refluxed for 24 hours followed by dilution with dichloromethane and was then washed with brine. The organic

fraction was dried over sodium sulfate and solvent was removed under reduced pressure. The resulting residue was dissolved in dichloromethane (5 mL) and toluene (10 mL) at room temperature under argon. Diisopropylethylamine (0.49 mL, 2.8 mmol, 4 eq) was added dropwise and the solution was stirred for 15 minutes. Boron trifluoride diethyl etherate (0.69 mL, 6 mmol, 8 eq) was added dropwise and the solution was stirred for 1 h at room temperature. The solution was then filtered through a pad of silica eluted with dichloromethane followed by removal of solvent under reduced pressure. The resulting residue was purified using flash chromatography and eluted with hexanes/ethyl acetate (4:1) affording an orange solid (29 mg, 12%). $^1\text{H-NMR}$ (500 MHz; CDCl_3): δ 7.20 (d, $J = 4.1$ Hz, 2H), 6.39 (d, $J = 4.1$ Hz, 2H), 3.64 (t, $J = 6.6$ Hz, 4H), 3.16 (t, $J = 7.6$ Hz, 4H), 2.54 (s, 3H), 2.25 (quintet, $J = 7.3$ Hz, 4H). $^{13}\text{C NMR}$ (126 MHz; CDCl_3): δ 159.4, 141.3, 135.0, 127.4, 117.7, 44.3, 31.7, 26.1, 15.5 HRMS (ESI $^-$) for $\text{C}_{16}\text{H}_{18}\text{N}_2\text{BCl}_2\text{F}_2$ (M-H) calculated 357.09136, found 357.09181.

4.7 Supporting Information

The Supporting Information contains the radical scavenging competition analysis between **H₄BPMHC**, tocopherol and PMHC. It also contains extra data from cell imaging: intensities and time trajectories of **H₄BCH₃** in cells in different buffers, intensity of **H₄BPMHC** in the presence of Fenton reagents and PMHC, images of cells treated with **H₄BPMHC** taken with a 100 x objective, and DIC images of HeLa cells treated with **H₄BPMHC**. A discussion of how the concentration of **H₄BPMHC** was estimated is also presented.

$^1\text{H NMR}$ and $^{13}\text{C NMR}$ spectra for compounds **1-3**, 3-(1H-pyrrol-2-yl)propan-1-ol), **H₄BPMHC**, and **H₄BCH₃** may be found in the Appendix at the end of the thesis.

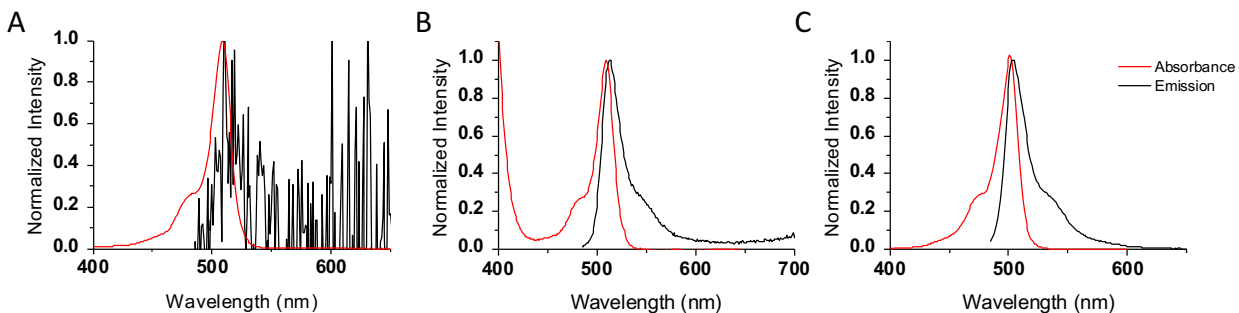


Figure 4.7 Absorption and emission spectra acquired in acetonitrile: A) H_4BPMHC , B) H_4BPMHC_{ox} C) H_4BCH_3 .

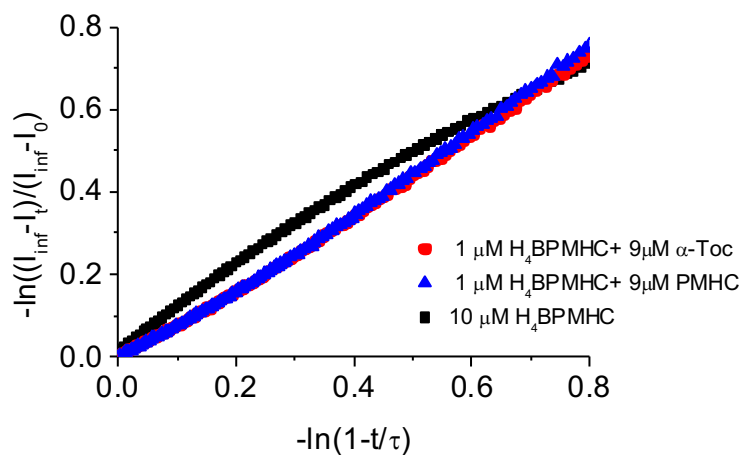


Figure 4.8 Plot of the rate analysis of Figure 4.2 using Equation 4.1. The relative rates determined from the slopes of the above plot (k_{H_4BPMHC}/k_{Toc} and k_{H_4BPMHC}/k_{PMHC}) were both 0.9.

4.7.1 Partitioning of H_4BCH_3 into cells in various buffers: Influence of serum albumins

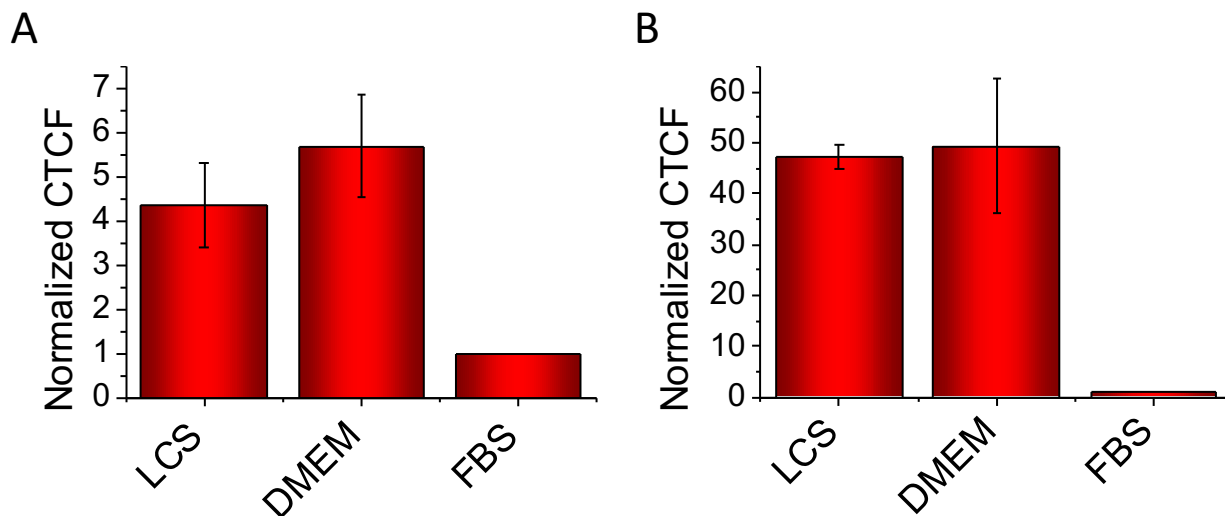


Figure 4.9 Normalized corrected total cell fluorescence (CTCF) of 100 nM H_4BCH_3 in HeLa cells. A) LCS, DMEM, and FBS intensities were determined from images acquired after 30 minutes of the dye partitioning in the respective buffers on a widefield microscopy setup. B) LCS, DMEM, and FBS intensities were determined after 30 minutes of the dye solution being removed and replaced with the respective buffer.

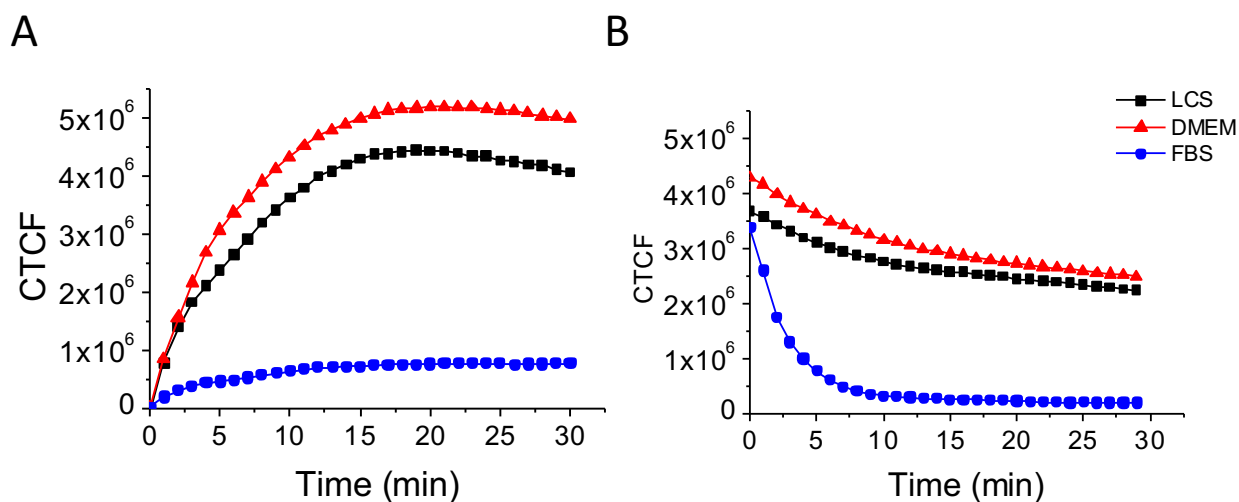


Figure 4.10 CTCF-time trajectories acquired during the partitioning of 100 nM H_4BCH_3 in HeLa cells. A) Trajectories acquired for the first 30 minutes of partitioning in the respective buffers. Curves were fit to an exponential growth curve according to Equation S4.1, where $k = 0.15, 0.16,$ and 0.18 for LCS, DMEM, and FBS respectively. B) Trajectories acquired for the first 30 minutes after

buffer exchange. Curves were fit to an exponential decay curve according to Equation S4.2, where $k = 0.093, 0.086,$ and 0.35 for LCS, DMEM, and FBS respectively.

$$y = A(1 - e^{-kt}) \quad \text{Equation S4.1}$$

$$y = y_0 + Ae^{-kt} \quad \text{Equation S4.2}$$

4.7.2 Imaging studies with H_4BPMHC

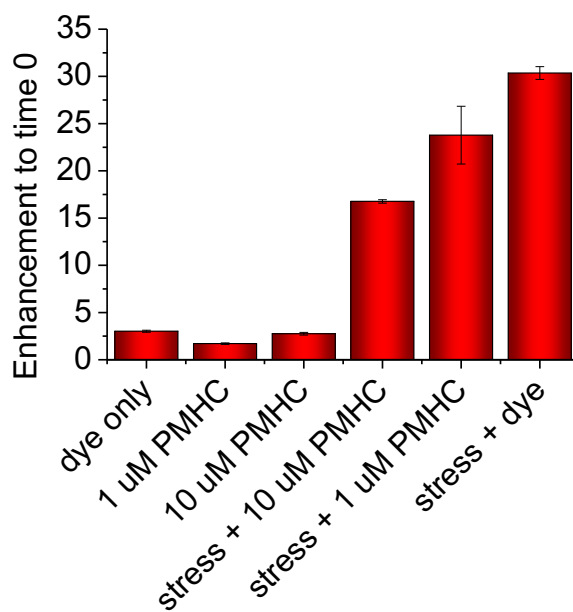


Figure 4.11 Relative fluorescence enhancement from time 0 of 100 nM H_4BPMHC in HeLa cells treated with/without PMHC and Fenton reagents after 50 minutes.

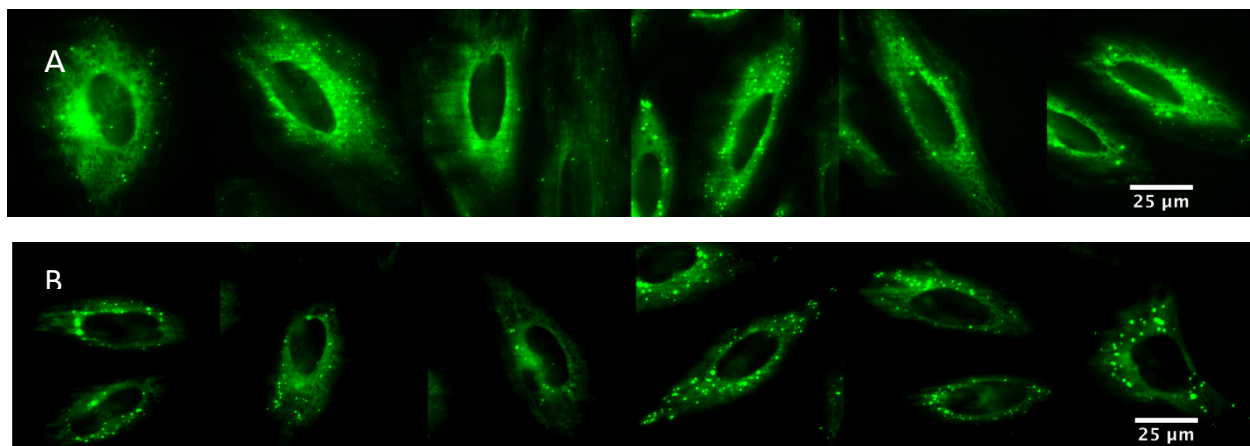


Figure 4.12 Images acquired with a TIRF setup of stressed (A) HeLa cells with 100 μM cumene hydroperoxide and 10 μM copper sulfate) and healthy (B) HeLa cells with 100 nM H_4BPMHC . The intensities of the healthy cells were increased 5-fold to better see the localization of the probe.

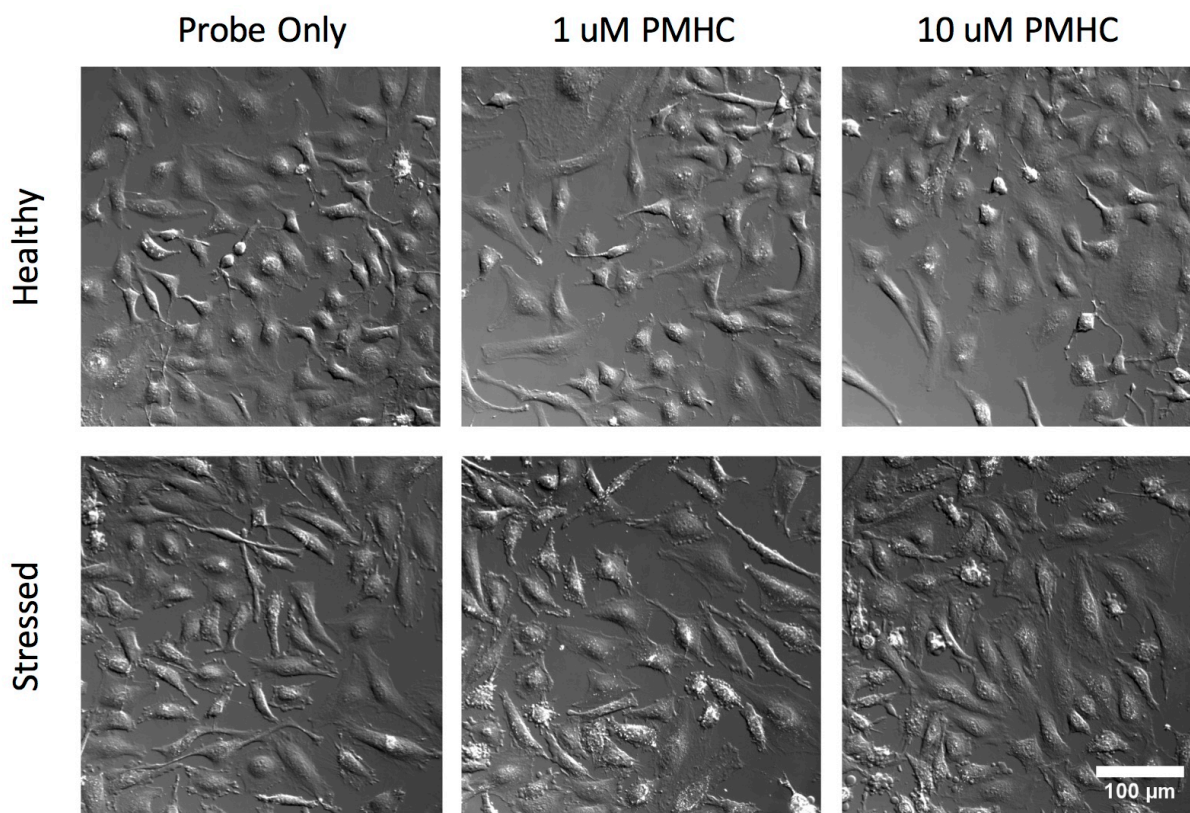


Figure 4.13 Corresponding DIC images to Figure 4.5A to show cell viability.

4.7.3 Approximation of concentration of dye in cells

According to the procedure described in Section 4.6.11, the fluorescence of the supernatant of the cells compared to the supernatant from the control sample (no cells) was 1% dimmer.

The fluorescence of the supernatant from the control sample was 50% dimmer than a stock of 100 nM H_4BCH_3 in LCS indicating 50% of the dye added to the control was in the LCS supernatant, and the rest was trapped to the petri dish which was recovered upon washing with DMSO. Thus, only 0.5% of the dye added to the plate, or 0.5 nM had partitioned into cells ($1\% \times 50\% \times 100$ nM). With this concentration in mind, we then calculated the concentration of dye in a single cell as follows:

- 0.5 nM dye in 23.5 mL is sequestered by cells: 1.1×10^{-11} mol of dye
- number of cells: 23.5 mL $\times 2$ (doubling in 24 h) $\times 5 \times 10^4$ cells/mL = 2.35×10^6 cells
- mol of dye per cell: 1.1×10^{-11} mol of dye / 2.35×10^6 cells = 5×10^{-18} mol/cell
- Volume of cell is about 3×10^{-12} L⁴¹ so concentration of dye per cell is: 1.7 μ M

If over 1 hour, 1% of dye reacted in unstressed cells: 17 nM/h

2 equivalents of ROS to light up probe: 33 nM/h ROS formation

4.7.4 Controls for determining quantum yields

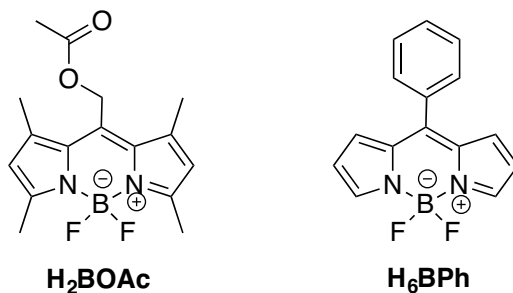


Figure 4.14 Structures of the dye standards used to determine fluorescence quantum yields.

4.8 References

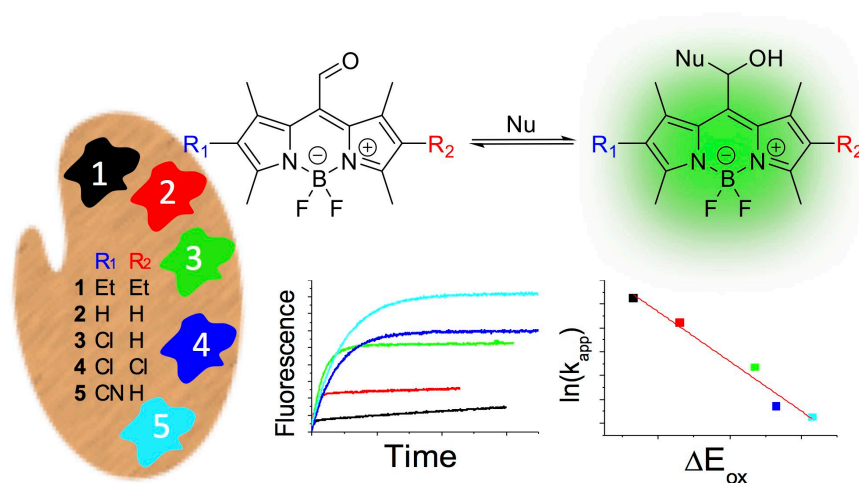
- (1) Evans, H. M.; Bishop, K. S. On the existence of a hitherto unrecognized dietary factor essential for reproductions *Science* **1922**, *56*, 650-651.
- (2) Tappel, A. L.; Zalkin, H. Inhibition of Lipid Peroxidation in Microsomes by Vitamin E *Nature* **1960**, *185*, 35-35.
- (3) Cummings, M. J.; Mattill, H. A. The Auto-Oxidation of Fats with Reference to Their Destructive Effect on Vitamin E *J. Nutr.* **1931**, *3*, 421-432.
- (4) Burton, G. W.; Le Page, Y.; Gabe, E. J.; Ingold, K. U. Antioxidant activity of vitamin E and related phenols. Importance of stereoelectronic factors *J. Am. Chem. Soc.* **1980**, *102*, 7791-7792.
- (5) Burton, G. W.; Ingold, K. U. Autoxidation of biological molecules. 1. Antioxidant activity of vitamin E and related chain-breaking phenolic antioxidants in vitro *J. Am. Chem. Soc.* **1981**, *103*, 6472-6477.
- (6) Burton, G. W.; Ingold, K. U. Vitamin E: application of the principles of physical organic chemistry to the exploration of its structure and function *Acc. Chem. Res.* **1986**, *19*, 194-201.
- (7) Traber, M. G.; Atkinson, J. Vitamin E, antioxidant and nothing more *Free Radic. Biol. Med.* **2007**, *43*, 4-15.
- (8) Galli, F.; Azzi, A.; Birringer, M.; Cook-Mills, J. M.; Eggersdorfer, M.; Frank, J.; Cruciani, G.; Lorkowski, S.; Ozer, N. K. Vitamin E: Emerging aspects and new directions *Free Radic Biol Med* **2017**, *102*, 16-36.
- (9) Singh, U.; Devaraj, S.; Jialal, I. Vitamin E, oxidative stress, and inflammation *Annu. Rev. Nutr.* **2005**, *25*, 151-174.
- (10) Barnham, K. J.; Masters, C. L.; Bush, A. I. Neurodegenerative diseases and oxidative stress *Nat Rev Drug Discov* **2004**, *3*, 205-214.
- (11) Dysken, M. W.; Sano, M.; Asthana, S.; Vertrees, J. E.; Pallaki, M.; Llorente, M.; Love, S.; Schellenberg, G. D.; McCarten, J. R.; Malphurs, J.; Prieto, S.; Chen, P.; Loreck, D. J.; Trapp, G.; Bakshi, R. S.; Mintzer, J. E.; Heidebrink, J. L.; Vidal-Cardona, A.; Arroyo, L. M.; Cruz, A. R.; Zachariah, S.; Kowall, N. W.; Chopra, M. P.; Craft, S.; Thielke, S.; Turvey, C. L.; Woodman, C.; Monnell, K. A.; Gordon, K.; Tomaska, J.; Segal, Y.; Peduzzi, P. N.; Guarino, P. D. Effect of vitamin E and memantine on functional decline in Alzheimer disease: the TEAM-AD VA cooperative randomized trial *JAMA* **2014**, *311*, 33-44.
- (12) Azzi, A.; Stocker, A. Vitamin E: non-antioxidant roles *Prog. Lipid Res.* **2000**, *39*, 231-255.
- (13) Azzi, A.; Gysin, R.; KempnÁ, P.; Munteanu, A.; Negis, Y.; Villacorta, L.; Visarius, T.; Zingg, J.-M. Vitamin E Mediates Cell Signaling and Regulation of Gene Expression *Ann. N.Y. Acad. Sci.* **2004**, *1031*, 86-95.
- (14) Boscoboinik, D.; Szewczyk, A.; Hensey, C.; Azzi, A. Inhibition of cell proliferation by alpha-tocopherol. Role of protein kinase C *J. Biol. Chem.* **1991**, *266*, 6188-6194.
- (15) Azzi, A. Molecular mechanism of alpha-tocopherol action *Free Radic Biol Med* **2007**, *43*, 16-21.
- (16) Bowry, V. W.; Ingold, K. U.; Stocker, R. Vitamin E in human low-density lipoprotein. When and how this antioxidant becomes a pro-oxidant. *Biochem. J.* **1992**, *281*, 341-344.
- (17) Mittal, M.; Siddiqui, M. R.; Tran, K.; Reddy, S. P.; Malik, A. B. Reactive Oxygen Species in Inflammation and Tissue Injury *Antioxid. Redox Signal.* **2014**, *20*, 1126-1167.
- (18) Wu, R. P.; Hayashi, T.; Cottam, H. B.; Jin, G.; Yao, S.; Wu, C. C.; Rosenbach, M. D.; Corr, M.; Schwab, R. B.; Carson, D. A. Nrf2 responses and the therapeutic selectivity of electrophilic compounds in chronic lymphocytic leukemia *Proc. Natl. Acad. Sci. U.S.A.* **2010**, *107*, 7479-7484.

- (19) Niki, E. Oxidative stress and antioxidants: Distress or eustress? *Arch. Biochem. Biophys.* **2016**, *595*, 19-24.
- (20) D'Autreaux, B.; Toledano, M. B. ROS as signalling molecules: mechanisms that generate specificity in ROS homeostasis *Nat Rev Mol Cell Biol* **2007**, *8*, 813-824.
- (21) Dickinson, B. C.; Chang, C. J. Chemistry and biology of reactive oxygen species in signaling or stress responses *Nat Chem Biol* **2011**, *7*, 504-511.
- (22) Niki, E.; Noguchi, N. Dynamics of Antioxidant Action of Vitamin E *Acc. Chem. Res.* **2004**, *37*, 45-51.
- (23) Oleynik, P.; Ishihara, Y.; Cosa, G. Design and Synthesis of a BODIPY- α -Tocopherol Adduct for Use as an Off/On Fluorescent Antioxidant Indicator *J. Am. Chem. Soc.* **2007**, *129*, 1842-1843.
- (24) Krumova, K.; Oleynik, P.; Karam, P.; Cosa, G. Phenol-Based Lipophilic Fluorescent Antioxidant Indicators: A Rational Approach *J. Org. Chem.* **2009**, *74*, 3641-3651.
- (25) Khatchadourian, A.; Krumova, K.; Boridy, S.; Ngo, A. T.; Maysinger, D.; Cosa, G. Molecular imaging of lipid peroxy radicals in living cells with a BODIPY- α -tocopherol adduct. *Biochemistry* **2009**, *48*, 5658-5668.
- (26) Krumova, K.; Friedland, S.; Cosa, G. How Lipid Unsaturation, Peroxyl Radical Partitioning, and Chromanol Lipophilic Tail Affect the Antioxidant Activity of α -Tocopherol: Direct Visualization via High-Throughput Fluorescence Studies Conducted with Fluorogenic α -Tocopherol Analogues *J. Am. Chem. Soc.* **2012**, *134*, 10102-10113.
- (27) Krumova, K.; Greene, L. E.; Cosa, G. Fluorogenic α -Tocopherol Analogue for Monitoring the Antioxidant Status within the Inner Mitochondrial Membrane of Live Cells. *J. Am. Chem. Soc.* **2013**, *135*, 17135-17143.
- (28) de Silva, A. P.; Gunaratne, H. Q. N.; Gunnlaugsson, T.; Huxley, A. J. M.; McCoy, C. P.; Rademacher, J. T.; Rice, T. E. Signaling Recognition Events with Fluorescent Sensors and Switches *Chem. Rev.* **1997**, *97*, 1515-1566.
- (29) Krumova, K.; Cosa, G. Bodipy Dyes with Tunable Redox Potentials and Functional Groups for Further Tethering: Preparation, Electrochemical, and Spectroscopic Characterization *J. Am. Chem. Soc.* **2010**, *132*, 17560-17569.
- (30) Loudet, A.; Burgess, K. BODIPY Dyes and Their Derivatives: Syntheses and Spectroscopic Properties *Chem. Rev.* **2007**, *107*, 4891-4932.
- (31) Barclay, L. R. C.; Ingold, K. U. Autoxidation of biological molecules. 2. Autoxidation of a model membrane. Comparison of the autoxidation of egg lecithin phosphatidylcholine in water and in chlorobenzene *J. Am. Chem. Soc.* **1981**, *103*, 6478-6485.
- (32) Jameson, L. P.; Smith, N. W.; Annunziata, O.; Dzyuba, S. V. Interaction of BODIPY dyes with bovine serum albumin: a case study on the aggregation of a click-BODIPY dye *PCCP* **2016**, *18*, 14182-14185.
- (33) Drummen, G. P. C.; van Liebergen, L. C. M.; Op den Kamp, J. A. F.; Post, J. A. C11-BODIPY581/591, an oxidation-sensitive fluorescent lipid peroxidation probe: (micro)spectroscopic characterization and validation of methodology *Free Radic. Biol. Med.* **2002**, *33*, 473-490.
- (34) Kowada, T.; Maeda, H.; Kikuchi, K. BODIPY-based probes for the fluorescence imaging of biomolecules in living cells *Chem. Soc. Rev.* **2015**, *44*, 4953-4972.
- (35) Lincoln, R.; Durantini, A. M.; Greene, L. E.; Martinez, S. R.; Knox, R.; Becerra, M. C.; Cosa, G. meso-Acetoxyethyl BODIPY dyes for photodynamic therapy: improved photostability of singlet oxygen photosensitizers *Photochem. Photobiol. Sci* **2017**, *16*, 178-184.
- (36) Halliwell, B.; Gutteridge, J. M. C. Oxygen toxicity, oxygen radicals, transition metals and disease *Biochem. J* **1984**, *219*, 1-14.
- (37) Murphy, M. P. How mitochondria produce reactive oxygen species *Biochem. J* **2009**, *417*, 1-13.

- (38) Kee, H. L.; Kirmaier, C.; Yu, L.; Thamyongkit, P.; Youngblood, W. J.; Calder, M. E.; Ramos, L.; Noll, B. C.; Bocian, D. F.; Scheidt, W. R.; Birge, R. R.; Lindsey, J. S.; Holten, D. Structural Control of the Photodynamics of Boron–Dipyrrin Complexes *J. Phys. Chem. B* **2005**, *109*, 20433-20443.
- (39) Schindelin, J.; Arganda-Carreras, I.; Frise, E.; Kaynig, V.; Longair, M.; Pietzsch, T.; Preibisch, S.; Rueden, C.; Saalfeld, S.; Schmid, B.; Tinevez, J.-Y.; White, D. J.; Hartenstein, V.; Eliceiri, K.; Tomancak, P.; Cardona, A. Fiji: an open-source platform for biological-image analysis *Nat Meth* **2012**, *9*, 676-682.
- (40) Gavet, O.; Pines, J. Progressive Activation of CyclinB1-Cdk1 Coordinates Entry to Mitosis *Dev. Cell* **2010**, *18*, 533-543.
- (41) Zhao, L.; Kroenke, C. D.; Song, J.; Piwnica-Worms, D.; Ackerman, J. J. H.; Neil, J. J. Intracellular water-specific MR of microbead-adherent cells: the HeLa cell intracellular water exchange lifetime *NMR Biomed.* **2008**, *21*, 159-164.

5 Development of a Fluorogenic Reactivity-Palette for the Study of Nucleophilic Addition Reactions Based on *meso*-Formyl BODIPY Dyes

Lana E. Greene, Richard Lincoln, Katerina Krumova, and Gonzalo Cosa, *To be Submitted*



5.1 Preface

*“Deep into that darkness peering, long I stood there, wondering, fearing, doubting, dreaming dreams no mortal
ever dared to dream before.”*

-Edgar Allan Poe

In Chapters 2-4 we discussed the development of fluorogenic probes capable of reporting redox reactions, antioxidant status, and lipid peroxidation in cells. In Chapter 5 the focus lies on the by-products of lipid peroxidation: aldehydes. In this regard, we have developed a palette of fluorogenic aldehydes, which upon nucleophilic attack become highly emissive.

Critical to fluorescent probe development is optimization of their utility in assaying the questions they were intended to answer (e.g. How much information can we extract from our experiments?). Here, we tackle this challenge through the development of a fluorescence based assay to monitor nucleophilic addition. This assay is comprised of a series of non-fluorescent *meso*-formyl BODIPY dyes previously synthesised in the Cosa laboratory which become fluorescent upon reaction with alcohols at different rates: ultimately forming a reactivity palette. The palette is assembled based on the increasing electrophilicity of the *meso*-formyl group, derived from tuning the substitution of the BODIPY core. We show that by exploring the photophysical properties (discussed in Chapter 1) of the reaction mixtures of our palette and added nucleophile, we can extract information on yield and types of products formed.

The reactivity palette approach discussed in this chapter, combined with the analysis of the reaction mixtures, aims to provide guidelines toward developing fluorogenic assays of reactivity in general, offering multiplex information, beyond fluorescence intensity. Furthermore, the fluorogenicity of these probes may be extended to the design of fluorogenic analogues of 4-hydroxynonenal to map alkylation *in vivo*.

5.2 Abstract

We describe herein a fluorescence-based assay to characterize and report on nucleophilic addition to carbonyl moieties and highlight the advantages a fluorescence based assay and multiplex analysis can offer. The assay relies on the fluorogenic properties of *meso*-formyl BODIPY dyes that become emissive following nucleophilic addition. A reactivity palette is assembled based on the increasing electrophilic character of five *meso*-formyl BODIPY compounds tested. We show that increasing rates of emission enhancement correlate with decreasing electrophilic character of the BODIPY dyes in the presence of an acid catalyst and nucleophile. These results are consistent with the rate limiting step involving activation of the electrophile. Increasing product formation are shown to correlate with the increasing electrophilic character of the BODIPY dyes, as expected based on thermodynamics. In addition to providing rates of reaction, analysis of the fluorescence parameters for the reaction mixtures, including emission quantum yields and fluorescence lifetimes, enable us to determine the extent of reactant conversion at equilibrium (in our case the estimated yield of a transient species), and the presence of different products, without the need for isolation. We anticipate that our reactivity palette approach, combined with the in-depth fluorescence analysis discussed herein, will provide guidelines toward developing fluorogenic assays of reactivity offering multiplex information, beyond fluorescence intensity.

5.3 Introduction

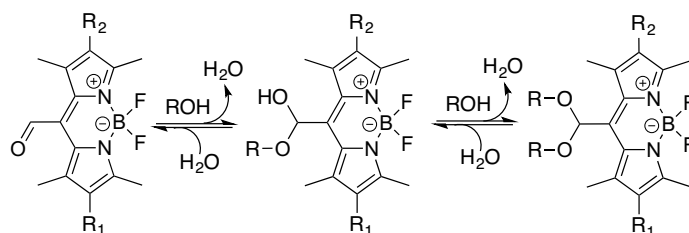
A significant effort has been devoted over the past decade toward developing fluorogenic probes for reaction screening.¹⁻⁶ A number of fluorescence based assays have been reported to monitor and study bond formation in a diverse set of reactions including aldol reactions,⁷⁻⁹ Mannich type reactions,¹⁰ Michael additions¹¹⁻¹³ and palladium catalyzed reactions.¹⁴⁻¹⁶ These assays, using fluorescence intensity as a marker, provide a rapid, *in situ* screening platform that is of simple application and requires minimum equipment investment.

We serendipitously uncovered that *meso*-formyl BODIPY dyes are non-emissive, yet their emission is readily restored following reaction with methanol.^{17,18} These dyes, we reasoned, would serve as uniquely sensitive probes of nucleophilic attack given that their

emission is undetectable before reaction (i.e., their emission quantum yield is nominally 0), but readily observable to the naked eye upon methanol addition.¹⁸ Given the ubiquitous nature of nucleophilic addition reactions in biology¹⁹⁻²² and in synthesis, the availability of a series of fluorogenic electrophiles would provide a simple, suitable tool to study nucleophile reactivity.

Here, we demonstrate that a reactivity palette may be assembled for nucleophilic addition screening comprised of electrophilic fluorogenic *meso*-formyl BODIPY dyes of increasing reactivity. We show that the rates of emission enhancement and the emission intensity measured for *meso*-formyl BODIPY dyes upon hemiacetal and/or acetal formation in the presence of various small alcohols, water and ethanedithiol (see Scheme 5.1), provide suitable markers to elaborate a reactivity scale and to determine the extent of reaction, respectively. We also highlight the valuable information a fluorescence assay may offer, with relative simplicity, beyond monitoring fluorescence intensity alone. Specifically we show the importance of monitoring the photophysical parameters of the reaction mixtures, including emission quantum yield and fluorescence lifetime, and of investigating the photophysical properties of the reaction products. Information on reaction yields, number of products and type of products formed, we show, may be gained upon inspecting these various photophysical properties.

Scheme 5.1 Expected products from the reaction of *meso*-formyl BODIPY and an alcohol (ROH).



We propose that our reactivity palette approach combined with the in-depth fluorescence analysis developed herein will be of general applicability toward developing additional fluorogenic assays (including high-throughput) on reactivity.

5.4 Results and Discussion

5.4.1 Rationale

Toward implementing a reactivity-scale, we conceived a fluorogenic reactivity-palette consisting of five electrophilic, non-emissive, *meso*-formyl BODIPY dyes, see compounds **1-5**, Figure 5.1.¹⁸ Nucleophilic addition and concomitant disruption of the formyl moiety deactivates an otherwise highly efficient non-radiative decay pathway for the excited state,^{17,18} rendering the probes emissive (Figure 5.2A). *meso*-Formyl BODIPY dyes thus provide highly sensitive substrates toward developing a fluorogenic palette.

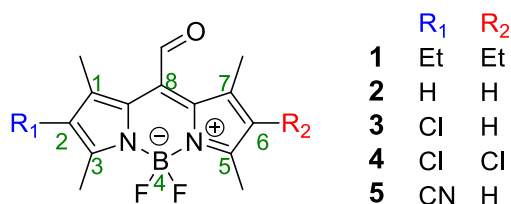


Figure 5.1 Structure of the *meso*-formyl BODIPY dyes used in this work. Numbering of the BODIPY core is shown in green.

To tune the electrophilic character of BODIPY dyes, substitution of the BODIPY core was performed with either electron rich or electron withdrawing groups at positions C2 and C6 of the dye. From a frontier molecular orbital (FMO) perspective, the reaction of a formyl group with a nucleophile involves orbital mixing between the highest occupied molecular orbital (HOMO) of the nucleophile and the lowest unoccupied molecular orbital (LUMO) of the formyl group. Substitution of BODIPY dyes with electron rich groups, destabilizing the LUMO, renders the formyl moiety less electrophilic. In turn, substitution by electron withdrawing groups, e.g. either chlorine atoms or nitriles and concomitant lowering of the LUMO renders the formyl group more susceptible to nucleophilic attack.

5.4.2 Reactivity

The reactivity of compounds **1-5** was tested in acetonitrile upon the addition of methanol where either a hemi-acetal or acetal may form. Steady state emission experiments were

conducted where fluorescence intensity enhancement immediately following addition of the nucleophile was monitored over time (every 12 s). While a trend in reactivity was apparent from results with compounds **1-5**, we also noticed large variations in re-runs of the experiments, possibly the result of traces of water affecting the ensuing kinetics of reaction. This observation prompted us to explore the addition of an acid catalyst in a controlled fashion working initially with compound **3**. We chose *p*-toluenesulfonic acid (*p*-TsOH) as an organic acid catalyst, as it is commonly used in the preparation of acetals.²³⁻²⁵ Reproducible results with *p*-TsOH enabled us to learn on equilibrium position and to obtain initial rates of reaction under a range of conditions.

Consistent with the reversible nature of the methanol addition, see Scheme 5.1, reaction of increasing amounts of methanol at constant concentrations of compound **3** and in the presence of *p*-TsOH as a catalyst resulted in increased intensities at $t = \infty$, i.e., once reaction has reached equilibrium, see Figure 5.2A. Under the assumption that conversion of the *meso*-formyl BODIPY is small (confirmed by the apparent fluorescence quantum yield experiments, *vide infra*) and working with large excess of nucleophile, one may then obtain a linear correlation between the concentration of methanol added and the intensity at $t = \infty$ (Figure 5.2B). Under the above working conditions, both the electrophile initial concentration, $[E]_0$, and the nucleophile concentrations used, $[Nu]_0$, remain fairly constant upon reaction. One may then show that the electrophile-nucleophile adduct concentration $[Nu-E]$, and thus the emission intensity, is proportional to the initial concentration of reactants used, see Equation 5.1.

$$K_{eq} = \frac{[Nu-E]}{[E]_0[Nu]_0} \quad \text{Equation 5.1}$$

In support of a pseudo first order reaction mechanism in the presence of excess nucleophile, the fluorescence intensity enhancement vs time curves followed an exponential behavior. Fitting the fluorescence intensity trajectories with an exponential growth curve according to Equation 5.2, next enabled us to obtain values for the pseudo first order rate constant k_{app} , where I_∞ is the fluorescence intensity at $t = \infty$ once reaction has reached equilibrium, and I_0 is the fluorescence intensity at $t = 0$. To our initial surprise, while the initial

rate of enhancement increased linearly with increasing methanol concentration, at large excess of nucleophile the rate of reaction became zero order on nucleophile concentration, as observed from the plateau in the plot of initial rate vs methanol concentration, see Figure 5.2C.

$$I(t) = I_{\infty} \times (1 - e^{-k_{app} \times t}) + I_0 \quad \text{Equation 5.2}$$

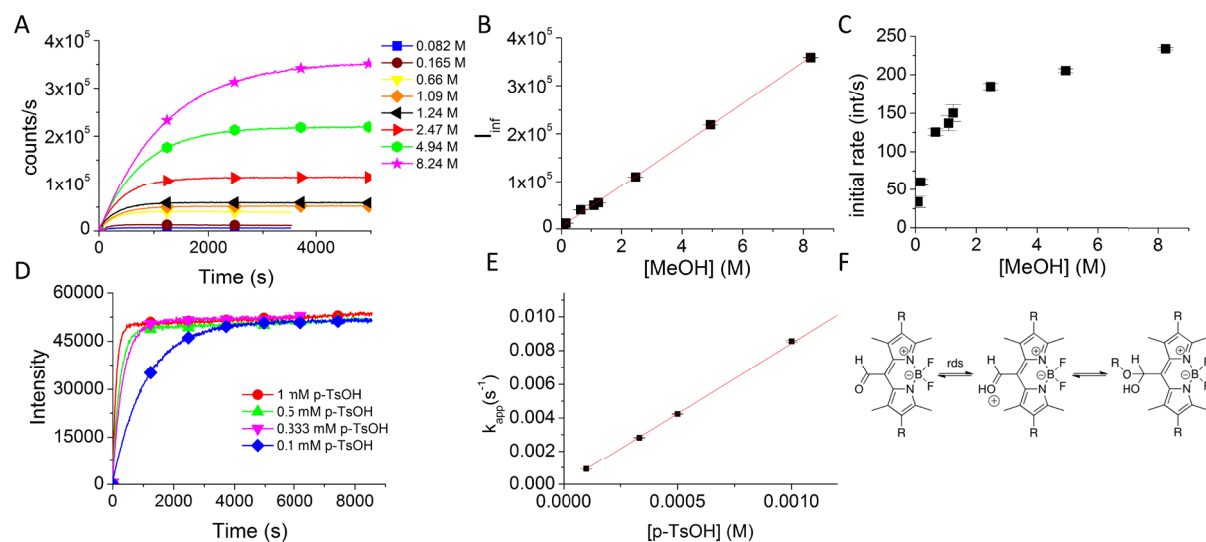


Figure 5.2 A) Intensity-time trajectories following the reaction of **3** ($4.5 \mu\text{M}$) with increasing methanol concentration at 21°C . B) Correlation between the intensity at infinite time (I_{∞}) obtained from fitting the intensity-time trajectories in panel A using Equation 5.2 and methanol concentration. C) Relationship of initial rate determined from panel A and methanol concentration. Error bars in y were obtained from the error associated with performing a linear fit on the initial increase of fluorescence enhancements in panel A. D) Intensity time trajectories following the reaction of $4.5 \mu\text{M}$ of **3** with 1.09 M methanol in acetonitrile with varying concentrations of *p*-TsOH at 21°C . E) Correlation between the apparent rate constants for **3** obtained from fitting the trajectories displayed in panel D with Equation 5.2 and *p*-TsOH concentration. Error bars were obtained from the error of the fitting with Equation 5.2. F) Equilibrium of *meso*-formyl BODIPY in the presence of an alcohol and an acid catalyst.

In order to understand the mechanism of nucleophilic addition to compound **3**, we next subjected **3** to increasing concentrations of *p*-TsOH in the presence of large nucleophile excess, 1.09 M methanol, where reaction is zeroth order in methanol, see Figure 5.2D. A linear correlation was observed between the concentration of *p*-TsOH and the apparent rate

constant (Figure 5.2E). The linearity suggests the formation of a catalyst activated aldehyde (protonation of the *meso*-formyl BODIPY) as the rate determining step, and thus a general-acid catalysis mechanism, see Figure 5.2F.

To test the reactivity of our palette, we monitored rates of intensity enhancement for compounds **1-5** in acetonitrile in the presence of 1.09 M methanol and 0.333 mM *p*-TsOH, see Figure 5.3A. A linear free energy relationship (LFER) analysis was conducted utilizing the natural logarithm of the ratio of measured apparent rate constant values (obtained according to Equation 5.2, relative to compound **1**) and the difference in oxidation potentials for compounds **1-5**, see Figure 5.3B.²⁶

Consistent with a rate limiting step involving activation via protonation of the *meso*-formyl BODIPY, we retrieved a negative slope for the LFER correlation. Electron donating groups on the BODIPY core stabilize the activated complex, where the larger electronic density in the BODIPY core increase the basicity and stabilize the protonated *meso*-formyl BODIPY dye. An energy raising by ca. 0.5 eV (~ 48 kJ/mol)¹⁸ for the oxidation potential of BODIPY dyes in going from electron releasing ethyl groups (compound **1**) to an electron withdrawing nitrile group (compound **5**) resulted in a drop by ca. 1 order of magnitude at 21°C for rate constants. The rate enhancement observed with decreasing oxidation potential, smaller than the 8 orders of magnitude expected at room temperature based on energy stabilization alone, indicates that the *meso*-formyl moiety, uncoupled from the BODIPY core as it is 90° from the BODIPY plane,¹⁷ is not nearly as affected by substitution of the BODIPY core.

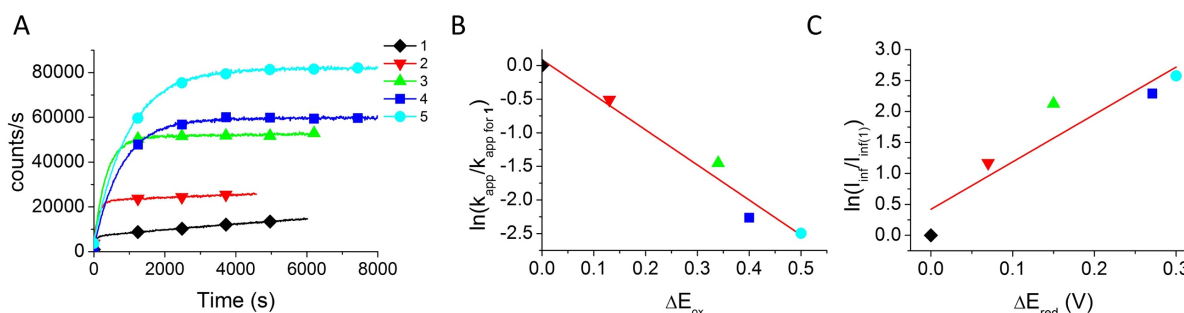


Figure 5.3 A) Intensity-time trajectories following the reaction of compounds **1** to **5** with 1.09 M methanol in acetonitrile supplemented with 0.333 mM of *p*-TsOH at 21°C. Dye concentrations were prepared such that their respective absorbance was 0.1 at the excitation wavelength used (i.e. 16

μM , $20 \mu\text{M}$, $4.5 \mu\text{M}$, $16 \mu\text{M}$ and $3 \mu\text{M}$ for dyes **1-5** respectively) B) Correlation between the ratio of apparent rate constants (k_{app}) and the difference in oxidation potentials (to compound **1**) in acetonitrile for the BODIPY dyes **1-5** vs ferrocene.¹⁸ Compound **1** k_{app} and oxidation potentials were used as a reference. C) Correlation between the ratio of intensities at infinite time (I_{∞}) and the difference in reduction potentials in acetonitrile for dyes **1-5** (to compound **1**) measured vs ferrocene.¹⁸ Compound **1** I_{∞} and reduction potentials were used as a reference.

To test the equilibrium position, we next utilized the maximum emission intensity reached for compounds **1-5** following reaction with methanol. In comparing emission intensities, we assumed that the emission quantum yield for each of the hemiacetal products formed with compounds **1-5** was similar. This is indeed the case with the emission quantum yield recorded for the *meso*-hydroxymethyl BODIPY dyes obtained following reduction of the formyl moiety.¹⁸

A new LFER with a positive slope was obtained when correlating the natural logarithm of the ratio of fluorescence intensity at $t = \infty$ (relative to compound **1**) for dyes **1-5** in the presence of 1.09 M methanol and *p*-TsOH, vs the difference in reduction potentials (relative to compound **1**) (LUMO energy values). We note that based on Equation 5.1, the intensity is proportional to the equilibrium constant under our experimental conditions. This LFER indicates that BODIPY cores bearing electron withdrawing groups favor product formation. The results are consistent with FMO considerations predicting the equilibrium position to be displaced toward products in the increasing order **1** < **2** < **3** < **4** < **5**. A 10-fold increase in product formation was recorded upon stabilizing the LUMO by ca. 0.3 eV (29 kJmol⁻¹) at 21°C.

We next tested the effect of nucleophiles on the rate of addition to our formyl dyes by monitoring compound **3** in the presence of various small alcohols, water and ethanedithiol (Figure 5.4). The formation of non-emissive *meso*-imines upon reaction of compounds **1-5** with amines precluded testing with this nucleophile substrate.¹⁷ Furthermore, amines are known fluorescence quenchers of BODIPY dyes.²⁷ All alcohols tested reacted at comparable rates ($k_{\text{app}} \sim 0.003 \text{ s}^{-1}$) and reached comparable fluorescence intensities ($\sim 50,000$ counts/s). This is not surprising given the general acid catalysis mechanism proposed (*vide supra*). We did observe however a ca-10-fold rate increase upon the use of water as a nucleophile what may be partly

due to a lowering of the pK_a of p -TsOH in the presence of water vs acetonitrile.^{28,29} The hydrate formation led to a very small emission enhancement indicating it is not a stable compound.

A ~ 10 -fold drop in reaction rate was recorded upon addition of ethanedithiol. The mismatch between the hard electrophile (formyl moiety) and the soft nucleophile (thiol) may alter the mechanism of reaction rendering the nucleophilic attack the rate determining step. We also observed a ca. 2-fold larger emission enhancement in the presence of ethanedithiol consistent with the larger stability of thioacetals (and presumably hemithioacetals) vs acetals (and hemiacetals).³⁰

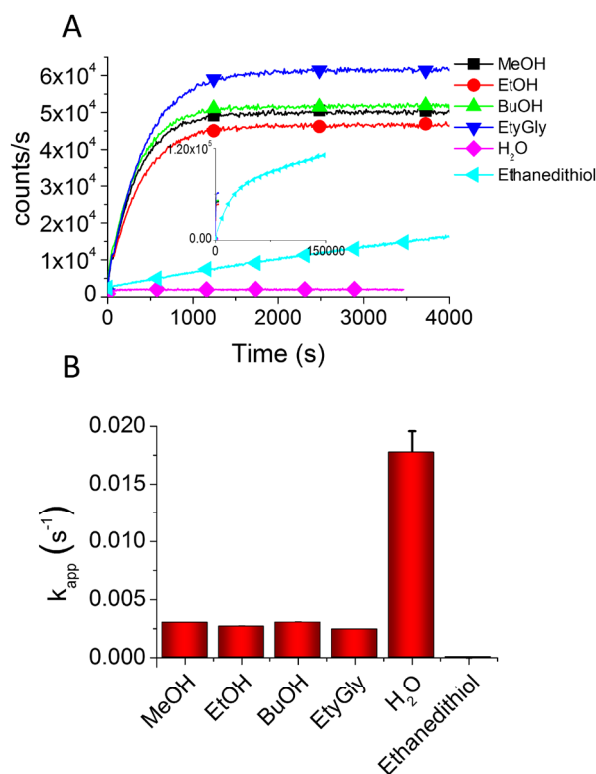


Figure 5.4 A) Intensity-time trajectories following the reaction of $4.5 \mu\text{M}$ of compound **3** and 1.09 M of methanol (MeOH), ethanol (EtOH), butanol (BuOH), ethylene glycol (EtyGly), water (H_2O) and ethanedithiol (EtSH_2) at 21°C in acetonitrile supplemented with 0.333 mM of p -TsOH. B) Apparent rate constants for the various nucleophiles tested were obtained from fitting the intensity-time trajectories in panel A with Equation 5.2. Error bars are from the fitting with Equation 5.2.

5.4.3 Equilibrium

In order to determine the product(s) formed in the reactions of our palette with various alcohol nucleophiles we prepared and isolated the *meso*-acetal BODIPY **6** from its precursor **5** (Figure 5.5A) by stirring at 80 °C with ethylene glycol in the presence of *p*-TsOH. Figure 5.5B shows the absorption and emission spectra of acetal **6** in ethylene glycol in comparison to those of **5** dissolved in ethylene glycol, where the hemiacetal and acetal may both form. The absorption and emission maxima of **5** (reacted) and **6** in this solvent were markedly different ($\lambda_{\text{abs}} = 502 \text{ nm}$ and $\lambda_{\text{em}} = 537 \text{ nm}$ vs $\lambda_{\text{abs}} = 514 \text{ nm}$ and $\lambda_{\text{em}} = 556 \text{ nm}$, respectively). The marked difference recorded between the spectra of the isolated acetal and the product obtained upon addition of ethylene glycol to compound **5** highlights the predominant formation of the hemiacetal (rather than acetal) in solutions of compound **5** in acetonitrile in the presence of either methanol or other alcohols studied herein (*vide supra*). A similar conclusion would also apply to reactions with the less electrophilic compounds **1-4**. The poor solubility of compounds **1-5** in acetonitrile/methanol mixtures precluded the use of NMR towards monitoring the reaction mixture. However, the use of mass spectrometry performed in methanol may be employed as a secondary method to confirm the generation of products.

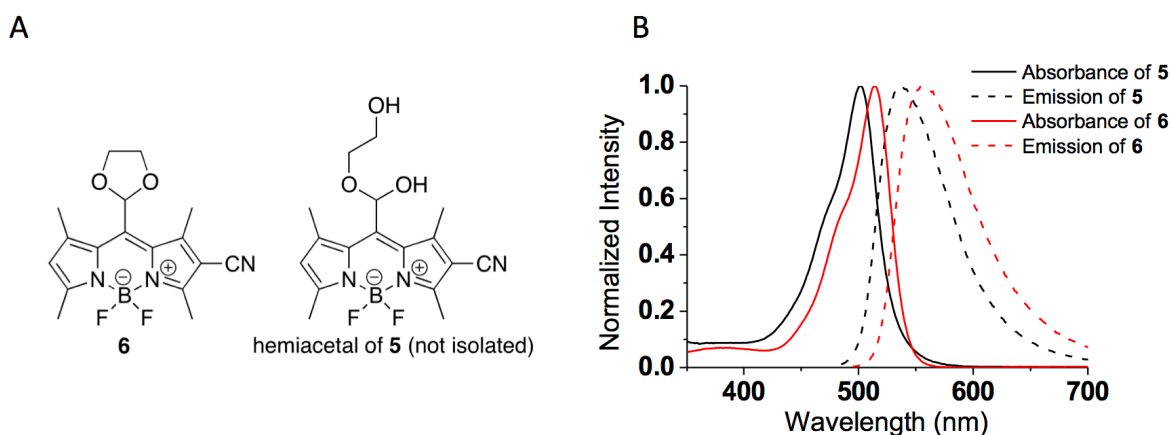


Figure 5.5 A) Structure of compound **6** and proposed structure of the major product of **5** dissolved in ethylene glycol. B) Absorption and emission spectra of **5** and **6** dissolved in ethylene glycol.

5.4.4 Photophysics of the reaction mixtures

We next revisited the final intensities reached at equilibrium for the various nucleophiles and compounds **1-5** studied herein to extract information on yields. In addition to providing a qualitative understanding on the extent of reaction completion at equilibrium, the emission intensities recorded, when combined with fluorescence quantum yields for the emissive products obtained and with their fluorescence decay rate constant values k_{dec} (or their reciprocal, fluorescence decay lifetimes τ_{dec}), may provide a quantitative yield of product formed in our palette upon reaction with nucleophiles without the need of product isolation. Specifically, by measuring the apparent emission quantum yield (Φ_f^{app}) of solutions of **1-5** in 1.09 M methanol with *p*-TsOH (0.333 mM) and estimating the actual emission quantum yield of the hemiacetals formed (Φ_f), one may estimate the product yield of hemiacetal, a transient species, from the ratio of the above two values, i.e., $yield = \Phi_f^{app}/\Phi_f$.

Comparison of the fluorescence of solutions of **1-5** in 1.09 M methanol and *p*-TsOH, with fluorescence from solutions of standard compounds whose emission quantum yield is known, (specifically ethyl substituted PM605 and the analogous H-substituted dye),¹⁸ yielded values of Φ_f^{app} for our palette **1-5** in methanol, see Table 5.1. While it is not possible to isolate a hemiacetal and directly measure its emission quantum yield, we obtained this parameter utilizing Equation 5.3 below by assuming that the radiative decay rate constant for these compounds is comparable to that of their *meso*-hydroxymethyl BODIPY analogues¹⁸ (i.e., $k_{rad} \sim 1 \times 10^8 \text{ s}^{-1}$), and by incorporating the τ_{dec} values measured for solutions of **1-5** in the presence of 1.09 M methanol and *p*-TsOH (Table 5.1). It is safe to estimate $k_{rad} \sim 1 \times 10^8 \text{ s}^{-1}$ for the hemiacetals considering that similar k_{rad} values were recorded for all *meso*-hydroxymethyl BODIPY analogues of compounds **1-5** ($+/-0.3 \times 10^8 \text{ s}^{-1}$) and for compound **6** (see Supplementary Information, Table 5.3). This value is also typically reported in the literature for BODIPY dyes.^{18,31} Tables 5.1 and 5.2 lists yields of reaction based on τ_{dec} and Φ_f^{app} for solutions of compounds **1-5** in methanol and *p*-TsOH, and also for compound **3** in the presence of various alcohols, water and ethanedithiol, and in the presence of *p*-TsOH. In line with our observations in Figure 5.4, the yield of hemi-acetal formed in the presence of various alcohols (Table 5.2) was independent on the nucleophile used. Furthermore, the low yields of

the hydrate (indicating its instability), and comparably high yield of hemi-thioacetal (indicating stability) are in agreement with the position of the expected equilibrium position.

$$\Phi_f = k_{rad} \times \tau_{dec} \quad \text{Equation 5.3}$$

Table 5.1 Photophysical properties of reaction mixtures for dyes **1-5** with 1.09 M methanol in acetonitrile and 0.333 mM *p*-TsOH.

Dye	τ_{dec} (ns) ^a	Φ_f^{app}	Φ_f^b	Yield (%) ^c
1	3.29	0.001	0.33	0.4
2	2.00	0.004	0.17	1.8
3	3.76 (76%) 2.08 (24%)	0.007	0.33	2.3
4	4.14	0.015	0.41	3.8
5	2.32 (62%) 0.96 (38%)	0.012	0.18	6.7

^aWeights of bi-exponential lifetimes are given based on their pre-exponential factors based on amplitude. ^bQuantum yield was calculated from τ_{dec} and an assumed k_{rad} of 10^8 s^{-1} using Equation 5.3. An average τ_{dec} based on the pre-exponential factors was used for biexponential lifetimes. ^cYield was calculated from the ratio of Φ_f^{app} and Φ_f .

Table 5.2 Photophysical properties of reaction mixtures of dye **3** in the presence of 1.09 M nucleophile (Nu) in acetonitrile and 0.333 mM *p*-TsOH.

Nu	τ (ns) ^a	Φ_f^{APP}	Φ_f^{b}	Yield (%) ^c
MeOH	3.85 (68%)	0.009	0.34	2.8
	2.59 (32%)			
EtOH	4.03 (83%)	0.008	0.37	2.1
	2.39 (17%)			
BuOH	4.27 (78%)	0.009	0.38	2.4
	2.61 (22%)			
EtyGly	4.03 (88%)	0.009	0.37	2.4
	1.69 (12%)			
H ₂ O	5.34 (64%)	0.001	0.42	0.14
	2.30 (36%)			
Et(SH) ₂	4.94 (47%)	0.05	0.26	18
	0.70 (53%)			

^aWeights of bi-exponential lifetimes are given based on their pre-exponential factors based on amplitude. ^bQuantum yield was calculated from τ_{dec} and an assumed k_{rad} of 10^8 s^{-1} using Equation 5.3. An average τ_{dec} based on the pre-exponential factors was used for biexponential lifetimes. ^cYield was calculated from the ratio of Φ_f^{APP} and Φ_f .

The above yield estimations based on photophysical properties assumed a sole product was formed, however, should an acetal and hemiacetal coexist, their intrinsic fluorescence lifetimes and emission quantum yields would enable a similar analysis, decoupling their contributions to the overall emission recorded, and providing a direct readout on the yield of each compound.

Importantly, we found that the hemiacetals formed from the symmetric BODIPYs (**1**, **2**, and **4**) gave mono-exponential lifetimes, whereas hemiacetals formed from the asymmetric BODIPYs (**3** and **5**) gave bi-exponential lifetimes as did compound **6** (Table 5.3). The two-component lifetimes for **3**, **5**, and **6** may be rationalized by the formation of atropisomers. The *meso*-position of the BODIPY core is sterically crowded due to the methyl groups at positions C1 and C7. This crowding has been shown to give rise to atropisomers from asymmetric BODIPYs.³² Since in compounds **3**, **5**, and **6** the BODIPY core is asymmetric, and the *meso*-position of the BODIPY is sterically hindered (preventing rotation) formation of 2

atropisomers is a plausible outcome. In our analysis we considered an average fluorescence decay lifetime based on the pre-exponential factors (amplitude) to estimate the yield for the atropisomer formation.

5.5 Conclusion

We have described herein a simple and rapid method and ensuing analysis for characterizing the reaction of nucleophiles with a series fluorogenic *meso*-formyl BODIPY dyes. Our off/on fluorogenic reactivity palette relies on nucleophilic addition to the formyl moiety that transforms the otherwise non-emissive *meso*-formyl BODIPY into an emissive *meso*-hemiacetal BODIPY. Our reactivity palette shows a linear free energy relationship between the reactivity and the oxidation potentials of the *meso*-formyl BODIPY dyes used, where the negative slope retrieved implies an acid catalyzed reaction. In turn, a LFER with a positive correlation between reduction potentials and reaction yield (proportional to the equilibrium constant under our experimental conditions) highlights the product stabilization with lowering of the LUMO of the reacting electrophile. The lifetimes and apparent quantum yields recorded for the palette upon reaction with nucleophiles allow for an estimation of the reaction yield of the transient hemiacetal species and the number and types of fluorescent products formed without need for product isolation. In general, we anticipate that the analysis described herein will be of broad application to fluorescent based assays especially when the formation of more than one product is expected.

5.6 Experimental Section

5.6.1 Materials

HPLC grade solvents for spectroscopy were purchased from Fisher Scientific. All other chemicals were purchased from Sigma-Aldrich, Co. and were used without further purification.

5.6.2 Instrumentation

Absorption spectra were recorded using a Hitachi U-2800 UV-vis-NIR spectrophotometer. Luminescence spectra were recorded using a PTI QuantaMaster spectrofluorimeter using 1 cm × 1 cm quartz cuvettes and corrected for detector sensitivity. ¹H NMR and ¹³C NMR spectra were recorded on a Varian VNMRS 500 instrument at 500 and 126 MHz, respectively. ESI mass spectra were measured on a Thermo Scientific Exactive Orbitrap.

5.6.3 Time based fluorescent enhancements

Time based fluorescent measurements were recorded on a PTI QuantaMaster spectrofluorimeter equipped with a four-position Peltier with motorized turret. 3 mL glass fluorimetry cells with 1 cm path lengths were used as sample cells. The excitation and emission slits were set to 2 nm. The temperature control was set to 21 °C. Solutions of dyes **1-5** in acetonitrile (3 mL final volume) were prepared in cuvettes at concentrations such that each solution had an absorbance of 0.1 at the excitation wavelength (i.e. 16 μM, 20 μM, 4.5 μM, 16 μM and 3 μM for dyes **1-5** respectively). Each solution was supplemented with 0.333 mM *p*-TsOH (unless otherwise indicated). When ready to measure intensity over time, the nucleophile of interest (1.09 M, unless otherwise specified) was added to each cuvette (final volume 3 mL). Compounds **1**, **3**, and **4** were excited at 500 nm and their emission was collected at 560 nm. Compounds **2** and **5** were excited at 475 nm and their emission was collected at 538 nm. The emission was background corrected with an acetonitrile blank.

5.6.4 Fluorescence quantum yield

Acetonitrile solutions of *meso*-acetoxymethyl-BODIPY dyes:¹⁸ H₂BOAc or PM605 were used as standards to calculate the apparent quantum yields of reaction mixtures of dyes **1-5** in acetonitrile treated with 1.09M methanol and 0.333 mM *p*-TsOH (following equilibration monitored via fluorescent enhancement), and the quantum yield of **6** in acetonitrile. Absorption and emission spectra of the *meso*-acetoxymethyl-BODIPY dyes and **6** were measured at five different concentrations. Since fluorescence of **1-5** is very sensitive to

concentration, only single emission and absorbance spectra were measured following reaction completion. The integrated intensity versus absorbance were then plotted and fitted linearly. Relative apparent quantum yields of fluorescence for reaction mixtures of dyes **1-5** and quantum yield of dye **6** with respect to the standard were obtained from Equation 5.4, where Φ_x , Δ , and η refer, respectively, to the fluorescence quantum yield, the slope obtained from the above-mentioned plot, and the solvent refractive index for the unknown (x) or standard (st) sample. Emission spectra were recorded for solutions using excitation and emission slits of 1.4 nm.

$$\phi_x = \phi_{st} \left(\frac{\Delta_x}{\Delta_{st}} \right) \times \left(\frac{\eta_x^2}{\eta_{st}^2} \right) \quad \text{Equation 5.4}$$

5.6.5 Fluorescence lifetime studies

The fluorescence lifetime measurements were carried out using a Picoquant Fluotime 200 Time Correlated Single Photon Counting setup employing a supercontinuum laser (WhiteLase SC-400-4, Fianium, Beverly, MA). Excitation wavelengths were spectrally separated from broadband emission by a computer controlled acousto-optical tunable filter (AOTF, Fianium). Compounds **2**, **5**, and **6** were excited at 475 nm, and compounds **1**, **3** and **4** were excited at 500 nm. The excitation rate was 10 MHz, and the detection frequency was less than 100 kHz. Photons were collected at the magic angle. An instrument response function (IRF) was measured with colloidal silica beads and was used to deconvolute the time profile of the excitation source from the emission decay. Reduced chi-squared statistics were employed to determine good fits to bi-exponential decays.

5.6.6 Synthesis

Compounds **1-5** were prepared according to literature procedures¹⁸ where spectroscopic data matched those of the reported materials.

8-(1,3-dioxolane)-2-cyano-1,3,5,7-tetramethyl pyrromethene fluoroborate (6). Compound **5** (50 mg, 0.17 mmol) was dissolved in dry toluene (5 mL) under argon. Ethylene glycol (0.5 mL) and *p*-toluenesulfonic acid (3 mg, 0.015 mmol, 0.09 equiv) were added and the solution was stirred for 4 days at 80 °C. The solution was then diluted with ethyl acetate, washed 2 times with saturated sodium bicarbonate and washed once with brine. The organic layer was dried over anhydrous sodium sulfate and solvent was removed under reduced pressure. The title compound was purified using flash column chromatography with hexanes:ethyl acetate (1:1) giving an orange residue (9.5 mg, 17%). ¹H NMR (500 MHz; CDCl₃): δ 6.27 (s, 1H), 6.02 (s, 1H), 4.27-4.24 (m, 2H), 4.06-4.03 (m, 2H), 2.62 (s, 3H), 2.59 (s, 3H), 2.44 (s, 3H), 2.40 (s, 3H). ¹³C NMR (126 MHz; CDCl₃): δ 164.9, 154.6, 147.6, 141.7, 136.9, 136.4, 129.4, 126.3, 115.2, 104.0, 98.1, 77.2, 65.0, 17.3, 15.52, 15.45, 13.6 HRMS (ESI) for C₁₇H₁₇N₃O₂BF₂ (M-H) calculated: 344.13874, found: 344.13933.

5.7 Supporting Information

¹H NMR and ¹³C NMR spectra for compound **6** may be found in the Appendix at the end of the thesis.

Table 5.3 Photophysical properties of dye **6**.

Dye	Solvent	Φ_f	τ (ns) ^a	k_{rad} (s ⁻¹)	k_{nr} (s ⁻¹)
6	EtGly	0.16	1.67 (72%)	1×10^8	6×10^8
			0.81 (28%)		
6	MeCN	0.09	0.82 (68%)	1×10^8	1×10^9
			0.28 (32%)		

5.8 References

- (1) Chan, J.; Dodani, S. C.; Chang, C. J. Reaction-based small-molecule fluorescent probes for chemoselective bioimaging *Nat Chem* **2012**, *4*, 973-984.
- (2) Xia, B.; Gerard, B.; Solano, D. M.; Wan, J.; Jones II, G.; Porco Jr, J. A. ESIPT-Mediated Photocycloadditions of 3-Hydroxyquinolinones: Development of a Fluorescence Quenching Assay for Reaction Screening *Org. Lett.* **2011**, *13*, 1346-1349.
- (3) Shaughnessy, K. H.; Kim, P.; Hartwig, J. F. A Fluorescence-Based Assay for High-Throughput Screening of Coupling Reactions. Application to Heck Chemistry *J. Am. Chem. Soc.* **1999**, *121*, 2123-2132.
- (4) Dickinson, B. C.; Huynh, C.; Chang, C. J. A Palette of Fluorescent Probes with Varying Emission Colors for Imaging Hydrogen Peroxide Signaling in Living Cells *J. Am. Chem. Soc.* **2010**, *132*, 5906-5915.
- (5) Matsumoto, T.; Urano, Y.; Takahashi, Y.; Mori, Y.; Terai, T.; Nagano, T. In Situ Evaluation of Kinetic Resolution Catalysts for Nitroaldol by Rationally Designed Fluorescence Probe *J. Org. Chem.* **2011**, *76*, 3616-3625.
- (6) Liu, J.-B.; Liu, L.-J.; Dong, Z.-Z.; Yang, G.-J.; Leung, C.-H.; Ma, D.-L. An Aldol Reaction-Based Iridium(III) Chemosensor for the Visualization of Proline in Living Cells *Sci. Rep.* **2016**, *6*, 36509.
- (7) Katsuyama, I.; Chouthaiwale, P. V.; Akama, H.; Cui, H.-L.; Tanaka, F. Fluorogenic probes for aldol reactions: tuning of fluorescence using π -conjugation systems *Tetrahedron Lett.* **2014**, *55*, 74-78.
- (8) Mase, N.; Ando, T.; Shibagaki, F.; Sugita, A.; Narumi, T.; Toda, M.; Watanabe, N.; Tanaka, F. Fluorogenic aldehydes bearing arylolefinyl groups: turn-on aldol reaction sensors for evaluation of organocatalysis in DMSO *Tetrahedron Lett.* **2014**, *55*, 1946-1948.
- (9) Guo, H.-M.; Tanaka, F. A Fluorogenic Aldehyde Bearing a 1,2,3-Triazole Moiety for Monitoring the Progress of Aldol Reactions *J. Org. Chem.* **2009**, *74*, 2417-2424.
- (10) Guo, H.-M.; Minakawa, M.; Tanaka, F. Fluorogenic Imines for Fluorescent Detection of Mannich-Type Reactions of Phenols in Water *J. Org. Chem.* **2008**, *73*, 3964-3966.
- (11) Tanaka, F.; Thayumanavan, R.; Barbas, C. F. Fluorescent Detection of Carbon-Carbon Bond Formation *J. Am. Chem. Soc.* **2003**, *125*, 8523-8528.
- (12) Chen, J.; Jiang, X.; Carroll, S. L.; Huang, J.; Wang, J. Theoretical and Experimental Investigation of Thermodynamics and Kinetics of Thiol-Michael Addition Reactions: A Case Study of Reversible Fluorescent Probes for Glutathione Imaging in Single Cells *Org. Lett.* **2015**, *17*, 5978-5981.
- (13) Umezawa, K.; Yoshida, M.; Kamiya, M.; Yamasoba, T.; Urano, Y. Rational design of reversible fluorescent probes for live-cell imaging and quantification of fast glutathione dynamics *Nat Chem* **2017**, *9*, 279-286.
- (14) Song, F.; Garner, A. L.; Koide, K. A Highly Sensitive Fluorescent Sensor for Palladium Based on the Allylic Oxidative Insertion Mechanism *J. Am. Chem. Soc.* **2007**, *129*, 12354-12355.
- (15) Stauffer, S. R.; Hartwig, J. F. Fluorescence Resonance Energy Transfer (FRET) as a High-Throughput Assay for Coupling Reactions. Arylation of Amines as a Case Study *J. Am. Chem. Soc.* **2003**, *125*, 6977-6985.
- (16) Rozhkov, R. V.; Davisson, V. J.; Bergstrom, D. E. Fluorogenic Transformations Based on Formation of C-C Bonds Catalyzed by Palladium: An Efficient Approach for High Throughput Optimizations and Kinetic Studies *Adv. Synth. Catal.* **2008**, *350*, 71-75.
- (17) Lincoln, R.; Greene, L. E.; Bain, C.; Flores-Rizo, J. O.; Bohle, D. S.; Cosa, G. When Push Comes to Shove: Unravelling the Mechanism and Scope of Nonemissive meso-Unsaturated BODIPY Dyes. *J. Phys. Chem. B* **2015**, *119*, 4758-4765.

- (18) Krumova, K.; Cosa, G. Bodipy Dyes with Tunable Redox Potentials and Functional Groups for Further Tethering: Preparation, Electrochemical, and Spectroscopic Characterization *J. Am. Chem. Soc.* **2010**, *132*, 17560-17569.
- (19) LoPachin, R. M.; Gavin, T.; Petersen, D. R.; Barber, D. S. Molecular Mechanisms of 4-Hydroxy-2-nonenal and Acrolein Toxicity: Nucleophilic Targets and Adduct Formation *Chem. Res. Toxicol.* **2009**, *22*, 1499-1508.
- (20) Perluigi, M.; Coccia, R.; Butterfield, D. A. 4-Hydroxy-2-Nonenal, a Reactive Product of Lipid Peroxidation, and Neurodegenerative Diseases: A Toxic Combination Illuminated by Redox Proteomics Studies *Antioxid. Redox Signal.* **2012**, *17*, 1590-1609.
- (21) Galligan, J. J.; Rose, K. L.; Beavers, W. N.; Hill, S.; Tallman, K. A.; Tansey, W. P.; Marnett, L. J. Stable Histone Adduction by 4-Oxo-2-nonenal: A Potential Link between Oxidative Stress and Epigenetics *J. Am. Chem. Soc.* **2014**, *136*, 11864-11866.
- (22) Avonto, C.; Chittiboyina, A. G.; Rua, D.; Khan, I. A. A fluorescence high throughput screening method for the detection of reactive electrophiles as potential skin sensitizers *Toxicol. Appl. Pharmacol.* **2015**, *289*, 177-184.
- (23) Wenkert, E.; Goodwin, T. E. 4-Formyl-2-cyclohexenone derivatives *Synth. Commun.* **1977**, 409-415.
- (24) Mansilla, H.; Regás, D. Simple Method for the Preparation of Dimethyl Acetals from Ketones with Montmorillonite K 10 and p-Toluenesulfonic Acid *Synth. Commun.* **2006**, *36*, 2195-2201.
- (25) Ohrlein, R.; Schwab, W.; Ehrler, R.; Jaeger, V. 3-Nitropropanal and 3-nitropropanol: preparation of the parent compounds and derivatives *Synthesis* **1986**.
- (26) Edwards, J. O. Correlation of relative rates and equilibria with a double basicity scale *J. Am. Chem. Soc.* **1954**, *76*, 1540-1547.
- (27) Loudet, A.; Burgess, K. BODIPY dyes and their derivatives: syntheses and spectroscopic properties *Chem Rev* **2007**, *107*, 4891-4932.
- (28) Guthrie, J. P. Hydrolysis of esters of oxy acids: pKa values for strong acids; Brønsted relationship for attack of water at methyl; free energies of hydrolysis of esters of oxy acids; and a linear relationship between free energy of hydrolysis and pKa holding over a range of 20 pK units *Can. J. Chem.* **1978**, *2342-2353*.
- (29) Eckert, F.; Leito, I.; Kaljurand, I.; Kütt, A.; Klamt, A.; Diedenhofen, M. Prediction of acidity in acetonitrile solution with COSMO-RS *J. Comput. Chem.* **2009**, *30*, 799-810.
- (30) Wuts, P. G. M.; Greene, T. W. In *Greene's Protective Groups in Organic Synthesis*; John Wiley & Sons, Inc.: 2006, p 431-532.
- (31) Durantini, A. M.; Greene, L. E.; Lincoln, R.; Martínez, S. R.; Cosa, G. Reactive Oxygen Species Mediated Activation of a Dormant Singlet Oxygen Photosensitizer: From Autocatalytic Singlet Oxygen Amplification to Chemically Controlled Photodynamic Therapy *J. Am. Chem. Soc.* **2016**, *138*, 1215-1225.
- (32) Kolemen, S.; Cakmak, Y.; Kostereli, Z.; Akkaya, E. U. Atropisomeric Dyes: Axial Chirality in Orthogonal BODIPY Oligomers *Org. Lett.* **2014**, *16*, 660-663.

6 Conclusions and Outlook

“Nothing in life is to be feared, it is only to be understood. Now is the time to understand more, so that we may fear less.”

-Marie Curie

6.1 Conclusions and Contribution to Original Knowledge

In the 21st century, revolutionary collaborative efforts, such as the Human Protein Atlas¹ and BRAIN Initiative,² have embarked to map the human body at the molecular level. In the spirit of Marie Curie’s words, the ultimate goal of these efforts is to understand the complex processes occurring in and amongst cells. With this understanding, we may engineer effective therapeutics, and even halt disease before its symptoms manifest. Our contribution to this ‘ultimate goal’ is the development of unique and sensitive probes to decipher, from a chemical standpoint, the complex relationship existing between antioxidant status, and physiological phenomena, reconciling the chemistry with the biology of lipid peroxidation and reactive oxygen species (ROS).

This thesis describes the design and development of a palette of bio-inspired fluorogenic probes, whose sensitivity were optimized to provide a large dynamic range. With these sensitive probes in hand, we developed novel assays to underpin both the reactivity and the formation of transient species both in ensemble experiments (semiquinones, hemiacetals, and ROS) and in live cells (ROS).

In Chapter 2, the development of a fluorogenic analogue of ubiquinone to reversibly report on redox reactions is described. The design of H₂B-Q exploited photoinduced electron transfer (PeT) to garner the desired fluorogenicity. Due to the high electron acceptor nature of quinones, we chose to design a probe which would be quenched in the oxidized (quinone) state, and that would be fluorescent in the reduced (quinol) state. Challenges in handling quinones and quinols were overcome in the synthesis, by primarily working with a phenol

precursor, and selectively oxidizing to the quinone and subsequent reduction to the quinol at later stages in the synthesis. While H₂B-Q has reduced sensitivity in polar solvents, in non-polar solvents the sensitivity is excellent exhibiting a 200-fold fluorescence enhancement upon reduction. We demonstrated the redox reversibility of the probe both chemically and electrochemically, as well as its direct and indirect antioxidant behaviour through its reaction with peroxy radicals and its synergistic reaction with tocopheroxyl radicals, validating H₂B-Q as a suitable fluorogenic analogue of ubiquinone. This probe provides us with a unique opportunity to study redox reactions of quinones in non-polar solvents, which is currently underway in our laboratory. Our overall strategy provides guiding rules for the future design and synthesis of related quinone analogues.

Chapter 3 describes our efforts to rationalize PeT efficiency in BODIPY-tocopherol analogues within the context of Marcus Theory of electron transfer. While previous generations of fluorogenic BODIPY-tocopherol probes prepared in our laboratory have been instrumental in monitoring ROS within lipid membranes, we were confronted with the challenge of achieving the optimum sensitivity needed to detect subtle levels of lipid peroxidation. Our quest to improve the sensitivity of these probes thus led us to investigate the effect that substitution of the BODIPY core and of the linker length between the BODIPY and tocopherol moiety both have on the rate constant for photoinduced electron transfer k_{PeT} . Using DFT and electrochemical measurements, the thermodynamic driving force for PeT was estimated for a library of BODIPY-tocopherol constructs. Fluorescence quantum yields, rationalized as a means to estimate k_{PeT} , provided us with a measure of PeT efficiency. Within the library of BODIPY-tocopherol probes studied (over a 400 mV redox window, and 2 linker lengths differing by 2.8 Å), we observed fluorescence enhancements ranging from 20-fold to nearly 1000-fold. By effectively competing with radiative decay, we may achieve excellent sensitivity upon judicious choice of linker and substitution. Furthermore, our studies underscore the sensitivity ceiling one may achieve in our fluorogenic BODIPY-tocopherol probes.

With the knowledge acquired from the work in Chapters 2 and 3, Chapter 4 describes the methodology behind detecting basal levels of lipid peroxidation in live cells. The high

reactivity of ROS had previously circumvented its detection and quantification in cells under homeostasis. Our fundamental challenge was thus detection of trace amounts of ROS, with minute concentrations of fluorogenic probe, and with enough signal to detect over background. Our strategy revolved around utilization of our new, highly sensitive, fluorogenic analogue of tocopherol, H₄BPMHC, capable of undergoing 1,000-fold fluorescence enhancement upon scavenging peroxy radicals. Our analysis of fluorescence intensity and fluorescence-time trajectories of images acquired with H₄PMHC indicates that the rate of production of lipid peroxy radicals in HeLa cells under basal conditions is approximately 33 nM/h and provides undisputable evidence on the antioxidant role of α -tocopherol. These results highlight the potential of H₄BPMHC to investigate the physiological relevance of lipid peroxidation during cell homeostasis and disease, and to unravel the physiological role of both lipid peroxy radicals and α -tocopherol *in vivo*.

The work presented in Chapter 5 highlights the multiplex information that can be gleaned from a simple fluorescence assay by studying the photophysical properties of the reaction mixtures assayed. Here, a reactivity palette was assembled which becomes emissive upon nucleophilic addition. We showed, via analysis of fluorescence-time trajectories, that rates of reaction correlated with decreasing electrophilicity in the presence of an acid catalyst confirming a general-acid catalyst mechanism. Furthermore, through analysis of the fluorescence intensities, lifetimes, and quantum yields, we showed that product formation correlated with increasing electrophilicity, and approximated the extent of reaction conversion at equilibrium (in our case of a transient hemiacetal species). Ultimately, this chapter provides guidelines for fluorescence assay development and showcases, through an in-depth fluorescence analysis, that a simple fluorescence assay may provide information on reaction mechanism, rate, and conversion.

6.2 Outlook and Future Directions

By virtue of the cyclical nature of fluorogenic probe development, improvement of the probes discussed in this thesis is a natural direction to proceed. We may improve the sensitivity of the probes by increasing PeT efficiency, we may improve their synthesis by increasing yield

and decreasing steps, and the utility by adding elements to target organelles, enhance reactivity, tune emission colour, or improve solubility. From the design strategies discussed in these chapters, it is relatively straightforward to expand the palette of fluorogenic bio-inspired molecules to further our understanding of the multiple reactions occurring in cells (eg. dopamine oxidation in neurons, electron transfer mediated by plastoquinone in plants).

6.2.1 Improving H₂B-Q for targeting mitochondria and use in biological applications

In Chapter 2 we discussed the development of a redox-reversible, fluorogenic analogue of ubiquinone. This probe showed excellent fluorescence sensitivity in non-polar solvents and is currently being used in our laboratory to understand proton-coupled electron transfer reactions of quinones in organic solvents in the presence and absence of protic solvents. However, the poor sensitivity of this probe in polar solvents and hence biological milieu prevents its utility in studying the reactions ubiquinone undergoes in biological applications. Furthermore, there is no functionality in H₂B-Q to target the mitochondrion, where the electron transfer reactions of ubiquinone occur.

The lack of sensitivity in polar solvents is due to fluorescence quenching by both redox states of the quinoid moiety, that is, not only the quinone, but the dihydroquinone moiety may quench the BODIPY emission via PeT. Polar solvents facilitate electron transfer from the reduced, quinol moiety to the BODIPY dye (photoreduction of BODIPY) by stabilizing the charge transfer and the formation of the radical ion pair. The redox properties of the BODIPY core are thus not optimally tuned for PeT occurring from the quinone moiety only. Designing PeT systems with the quinone/quinol redox couple is challenging since the quinone is an excellent electron acceptor, and the quinol is a very good electron donor. The substituents of the BODIPY core of H₂B-Q are thus not sufficiently electron rich to prevent electron transfer from the quinol moiety in polar solvents.

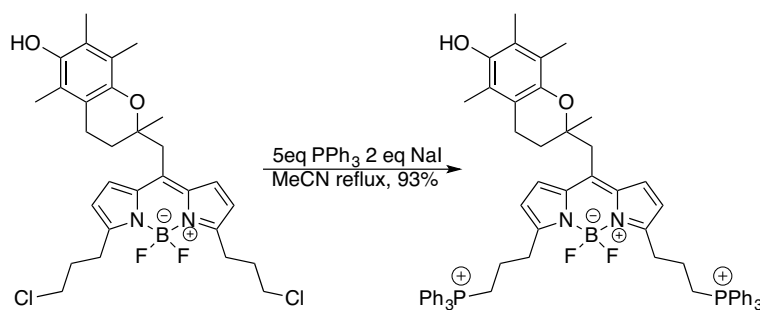
New efforts may be made to design a more electron rich BODIPY core to facilitate electron transfer to the quinone moiety, but inhibit electron transfer from the quinol moiety. Additionally, by adding a reactive handle, similar to that described in Chapter 4 for H₄BPMHC,

we may generate an easy opportunity to target the mitochondrion by substituting with triphenylphosphine.^{3,4}

Following the synthesis of a new generation of H₂B-Q, experiments in cells or isolated mitochondria can be performed. In addition, we posit that single molecule spectroscopy may be exploited to visualize single redox turnovers in newly prepared ubiquinone analogues.

6.2.2 Targeting H₄BPMHC to mitochondria for studying ROS accumulation and production in Alzheimer's disease

The highly sensitive fluorogenic tocopherol analogue, H₄BPMHC, described in Chapter 4 is poised for further modifications to target organelles. Ongoing work in our lab, and in collaboration with the group of Professor Claudio Cuello at McGill University, is being done to better understand the association of ROS with the onset of Alzheimer's disease. Oxidative stress has been observed in late stages of Alzheimer's disease, yet where and when oxidative stress initiates in those suffering from Alzheimer's is not known. It is postulated that amyloid- β peptides, whose accumulation is a key characteristic in patients with Alzheimer's, induces oxidative stress.⁵ Indeed, there is evidence showing the interaction of amyloid- β peptides with mitochondria, where it may inhibit the electron transport chain and cause a cascade of reactions leading to production of ROS.⁶ Having a sensitive ROS probe targeting the mitochondrion would help address this hypothesis. Due to the propyl halogen on the core of the BODIPY of H₄BPMHC, addition of a mitochondrial targeting triphenylphosphonium group is straightforward and has been successfully accomplished (Scheme 6.1). Work is underway in our laboratory to optimize cell imaging with this new probe, including both healthy but also pathological cell lines.

Scheme 6.1 Synthesis of H₄-mito-BPMHC from H₄BPMHC.

To better understand and characterize the stages of Alzheimer's disease, the Cuello group has developed a transgenic rat model of Alzheimer's disease.⁷ With the new probe in hand, we are currently working with the Cuello group to detect subtle ROS differences in both isolated mitochondria and brain slices of the transgenic rat model, vs of a wild-type rat. Through this collaboration, we hope to decipher the role of amyloid- β peptides and mitochondria in the generation of lipid peroxyl radicals and initiation of oxidative stress in Alzheimer's disease.

6.2.3 Expanding the palette to fluorogenic analogues of biological molecules of interest

The probe design strategies described in this thesis can be applied to the development of other biological molecules of interest. Quinones/quinols are ubiquitous molecules in biological systems. These molecules, like ubiquinone, generally have multi-faceted roles and carry out redox reactions in the cell. Such molecules include plastoquinone (redox mediator in plants), Vitamin K (redox mediator, and cofactor in blood coagulation), and dopamine (neurotransmitter). The general strategy used to prepare H₂B-Q may be used to develop similar probes based on the biomolecules listed here. A fluorogenic plastoquinone may be used to monitor electron transfer reactions in photosystems, a fluorogenic Vitamin K may be used to understand its dual role as electron carrier and cofactor,⁸ and a fluorogenic dopamine may be used to visualize neurotransmitter oxidation and its implication in diseases such as Parkinson's.

The design strategy used in the development of the *meso*-formyl BODIPY dyes for nucleophile screening discussed in Chapter 5 may be applied to develop fluorogenic bio-

aldehydes. Recently in our lab, we have initiated the development of a fluorogenic analogue of 4-hydroxynonenal (4-HNE) which exploits the same quenching mechanism as the one shown for *meso*-formyl BODIPYs. As described in Chapter 1, 4-HNE is a toxic by-product of lipid peroxidation which may undergo reaction with biological nucleophiles such as cysteine residues and DNA bases. Similarly to the *meso*-formyl dyes, upon reaction with a nucleophile such as cysteine, the 4-HNE analogue becomes highly emissive. We are currently working on the cell-imaging of this new probe, as well as working in conjunction with the Cuello group to discern the ability to clear lipid derived electrophiles, such as 4-HNE, between transgenic and wild type rats.

6.2.4 State-of-the-art fluorescence imaging methods

Single molecule and super resolution techniques such as STORM (stochastic optical reconstruction microscopy),⁹ STED (stimulated emission depletion microscopy)^{10,11} PALM (photoactivated localization microscopy)^{12,13} and NASCA (nanometer accuracy by stochastic chemical reactions)¹⁴ will become necessary to study ROS production and electron transfer reactions in mitochondria. Single molecule techniques are especially critical when visualizing redox-reversible molecules such as H₂B-Q. Single redox turnovers would not be noticed in ensemble experiments where an average intensity would mask dynamic interconversions, thus requiring the sensitivity of single molecule spectroscopy (SMS) to observe individual turnovers. Indeed, SMS electrochemical techniques are currently being explored in our laboratory to visualize single redox events, and NASCA techniques are being explored to visualize alkylation events of our fluorogenic 4-HNE analogue in cells. Other techniques such as fluorescence lifetime imaging microscopy (FLIM) should also be considered as they provide unique opportunities to quantify ROS buildup. The considerable difference in lifetimes observed for our tocopherol probes between reduced and oxidized states may allow us to determine the ratio of oxidized to reduced species within a cell via FLIM, essentially exploring the weight of lifetimes as a means to develop a ratiometric method.

Through the development of improved fluorogenic probes, and improved techniques and assays, we aim to gain an understanding of the complex interplay between ROS and

antioxidants, as well as the complex redox reactions that take place in living systems. Understanding how these reactions work and how to improve our strategies will allow us to ultimately reconcile the chemistry of these systems with their biology.

6.3 References

- (1) Uhlén, M.; Fagerberg, L.; Hallström, B. M.; Lindskog, C.; Oksvold, P.; Mardinoglu, A.; Sivertsson, Å.; Kampf, C.; Sjöstedt, E.; Asplund, A.; Olsson, I.; Edlund, K.; Lundberg, E.; Navani, S.; Szigartyo, C. A.-K.; Odeberg, J.; Djureinovic, D.; Takanen, J. O.; Hober, S.; Alm, T.; Edqvist, P.-H.; Berling, H.; Tegel, H.; Mulder, J.; Rockberg, J.; Nilsson, P.; Schwenk, J. M.; Hamsten, M.; von Feilitzen, K.; Forsberg, M.; Persson, L.; Johansson, F.; Zwahlen, M.; von Heijne, G.; Nielsen, J.; Pontén, F. Tissue-based map of the human proteome *Science* **2015**, 347.
- (2) Jorgenson, L. A.; Newsome, W. T.; Anderson, D. J.; Bargmann, C. I.; Brown, E. N.; Deisseroth, K.; Donoghue, J. P.; Hudson, K. L.; Ling, G. S. F.; MacLeish, P. R.; Marder, E.; Normann, R. A.; Sanes, J. R.; Schnitzer, M. J.; Sejnowski, T. J.; Tank, D. W.; Tsien, R. Y.; Ugurbil, K.; Wingfield, J. C. The BRAIN Initiative: developing technology to catalyse neuroscience discovery *Philosophical Transactions of the Royal Society B: Biological Sciences* **2015**, 370.
- (3) Murphy, M. P.; Smith, R. A. J. Targeting Antioxidants to Mitochondria by Conjugation to Lipophilic Cations *Annu. Rev. Pharmacol. Toxicol.* **2007**, 47, 629-656.
- (4) Krumova, K.; Greene, L. E.; Cosa, G. Fluorogenic α -Tocopherol Analogue for Monitoring the Antioxidant Status within the Inner Mitochondrial Membrane of Live Cells. *J. Am. Chem. Soc.* **2013**, 135, 17135-17143.
- (5) Butterfield, D. A.; Sultana, R. Methionine-35 of A β (1-42): Importance for Oxidative Stress in Alzheimer Disease *J. Amino Acids* **2011**, 2011, 1-10.
- (6) Devi, L.; Prabhu, B. M.; Galati, D. F.; Avadhani, N. G.; Anandatheerthavarada, H. K. Accumulation of Amyloid Precursor Protein in the Mitochondrial Import Channels of Human Alzheimer's Disease Brain Is Associated with Mitochondrial Dysfunction *J. Neurosci.* **2006**, 26, 9057.
- (7) Wanda Carolina Leon, F. C., Vanessa Partridge, Simon Allard, Maria Teresa Ferretti, Arald Dewilde, Freya Vercauteren, Ramtin Atifeh, Adriana Ducatzenzeler, William Klein, Moshe Szyf, Leena Alhonen, A. Claudio Cuello A novel transgenic rat model with a full alzheimer's - Like amyloid pathology displays pre - Plaque intracellular amyloid - β - Associated cognitive impairment *J. Alzheimers Dis* **2010**, 20, 113-126.
- (8) Belzile, M.-N.; Godin, R.; Durantini, A. M.; Cosa, G. Monitoring Chemical and Biological Electron Transfer Reactions with a Fluorogenic Vitamin K Analogue Probe *J. Am. Chem. Soc.* **2016**, 138, 16388-16397.
- (9) Rust, M. J.; Bates, M.; Zhuang, X. Sub-diffraction-limit imaging by stochastic optical reconstruction microscopy (STORM) *Nature methods* **2006**, 3, 793-795.
- (10) Hell, S. W.; Wichmann, J. Breaking the diffraction resolution limit by stimulated emission: stimulated-emission-depletion fluorescence microscopy *Opt. Lett.* **1994**, 19, 780-782.
- (11) Klar, T. A.; Hell, S. W. Subdiffraction resolution in far-field fluorescence microscopy *Opt. Lett.* **1999**, 24, 954-956.
- (12) Betzig, E.; Patterson, G. H.; Sougrat, R.; Lindwasser, O. W.; Olenych, S.; Bonifacino, J. S.; Davidson, M. W.; Lippincott-Schwartz, J.; Hess, H. F. Imaging intracellular fluorescent proteins at nanometer resolution *Science* **2006**, 313, 1642-1645.
- (13) Hess, S. T.; Girirajan, T. P.; Mason, M. D. Ultra-high resolution imaging by fluorescence photoactivation localization microscopy *Biophys. J.* **2006**, 91, 4258-4272.

(14) Roeffaers, M. B. J.; De Cremer, G.; Libeert, J.; Ameloot, R.; Dedecker, P.; Bons, A.-J.; Bückins, M.; Martens, J. A.; Sels, B. F.; De Vos, D. E.; Hofkens, J. Super-Resolution Reactivity Mapping of Nanostructured Catalyst Particles *Angew. Chem. Int. Ed.* **2009**, *48*, 9285-9289.

7 Appendix

“The chemists are a strange class of mortals, impelled by an almost insane impulse to seek their pleasures amid smoke and vapor, soot and flame, poisons and poverty; yet among all these evils I seem to live so sweetly that may I die if I were to change places with the Persian king.”

Johann Joachim Becher

This chapter includes ^1H and ^{13}C NMR spectra for all novel compounds prepared and presented in this thesis:

Chapter 2:

- 3,4-dimethoxy-2-hydroxy-6-methylbenzaldehyde (**2**) ^1H -NMR spectrum, 300 MHz; CDCl_3 , ^{13}C -NMR spectrum, 75 MHz, CDCl_3 (Page 187).
- 3-(2-(E)-vinyl-5,6-dimethoxy-3-methylphenol)-1,5,7-tetramethyl-8-H-pyrromethene fluoroborate (**H₂B-phenol**) ^1H -NMR spectrum, 500 MHz; CDCl_3 , ^{13}C -NMR spectrum, 126 MHz; CDCl_3 (Page 188).
- 3-(2-(E)-vinyl-5,6-dimethoxy-3-methyl-1,4-quinone)-1,5,7-tetramethyl-8-H-pyrromethene fluoroborate (**H₂B-Q**) ^1H -NMR spectrum, 500 MHz; CDCl_3 , ^{13}C -NMR spectrum, 126 MHz; CDCl_3 (Page 189).
- 3-(2-(E)-vinyl-5,6-dimethoxy-3-methyl-1,4-quinol)-1,5,7-tetramethyl-8-H-pyrromethene fluoroborate (**H₂B-QH₂**) ^1H -NMR spectrum, 500 MHz; CDCl_3 , ^{13}C -NMR spectrum, 126 MHz; CDCl_3 (Page 190).

Chapter 3:

- 8-Acetoxymethyl-3,5-dimethyl Pyrromethene Fluoroborate (**H₄MeBOAc**) ^1H -NMR spectrum, 500 MHz; CDCl_3 , ^{13}C -NMR spectrum, 126 MHz, CDCl_3 (Page 191).
- 8-Hydroxymethyl-3,5-dimethyl Pyrromethene Fluoroborate (**H₄MeBOH**) ^1H -NMR spectrum, 500 MHz; CDCl_3 , ^{13}C -NMR spectrum, 126 MHz, CDCl_3 (Page 192).
- 8-((±)-6-Hydroxy-2,5,7,8-tetramethylchromane-2-carbonyloxy)-methyl-3,5-dimethyl Pyrromethene Fluoroborate (**H₄MeBTOH**) ^1H -NMR spectrum, 500 MHz; CDCl_3 , ^{13}C -NMR spectrum, 126 MHz, CDCl_3 (Page 193).
- 8-((±)-6-Hydroxy-2,5,7,8-tetramethylchromane-2-carbonyloxy)-methyl-2,6-dichloro-1,3,5,7-tetramethyl Pyrromethene Fluoroborate (**Cl₂BTOH**) ^1H -NMR spectrum, 500 MHz; CDCl_3 , ^{13}C -NMR spectrum, 126 MHz, CDCl_3 (Page 194).

- 8-((6-Hydroxy-2,5,7,8-tetramethylchroman-2-yl)-methyl)-2,6-diethyl-1,3,5,7-tetramethyl Pyrromethene Fluoroborate (**Et₂BPMHC**) ¹H-NMR spectrum, 500 MHz; CDCl₃, ¹³C-NMR spectrum, 126 MHz, CDCl₃ (Page 195).
- 8-((6-Hydroxy-2,5,7,8-tetramethylchroman-2-yl)-methyl)-2,6-dichloro-1,3,5,7-tetramethyl Pyrromethene Fluoroborate (**Cl₂BPMHC**) ¹H-NMR spectrum, 500 MHz; CDCl₃, ¹³C-NMR spectrum, 126 MHz, CDCl₃ (Page 196).

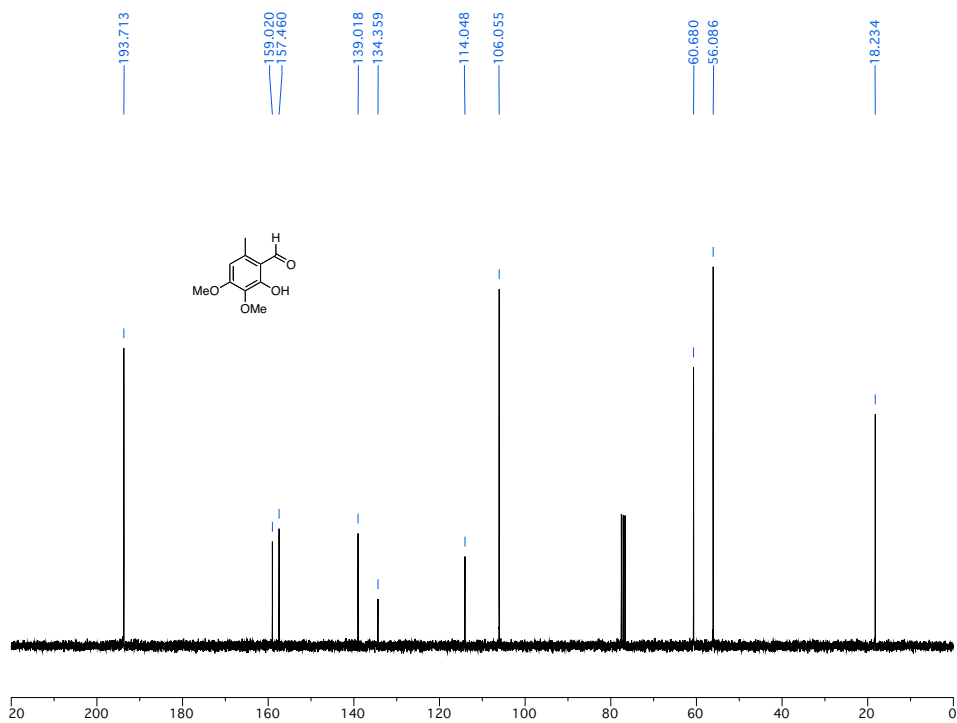
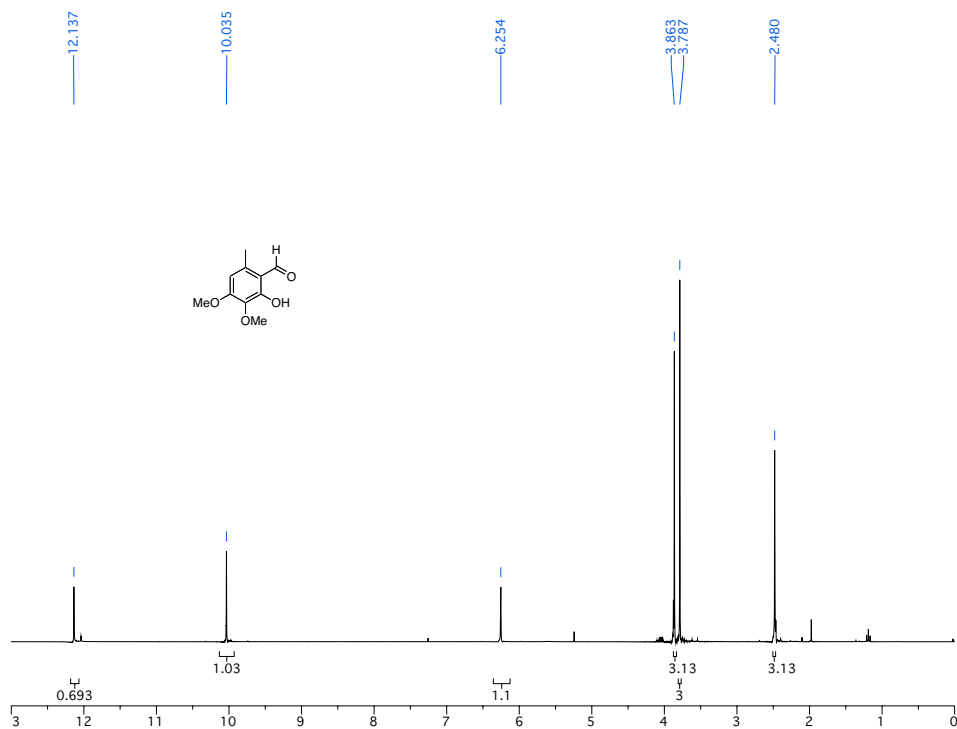
Chapter 4:

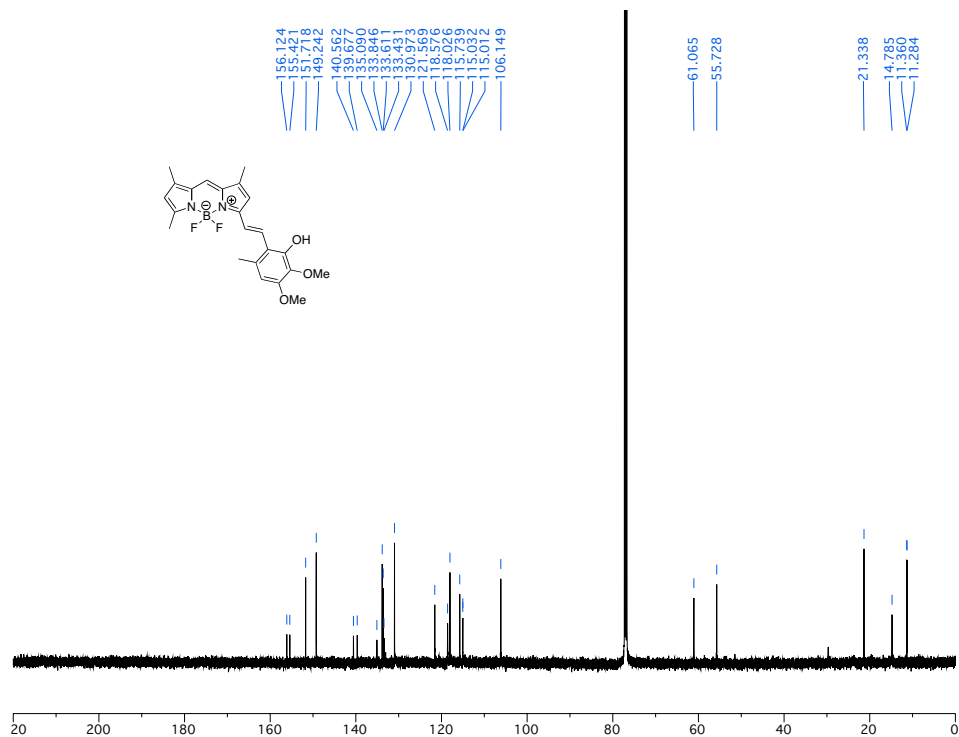
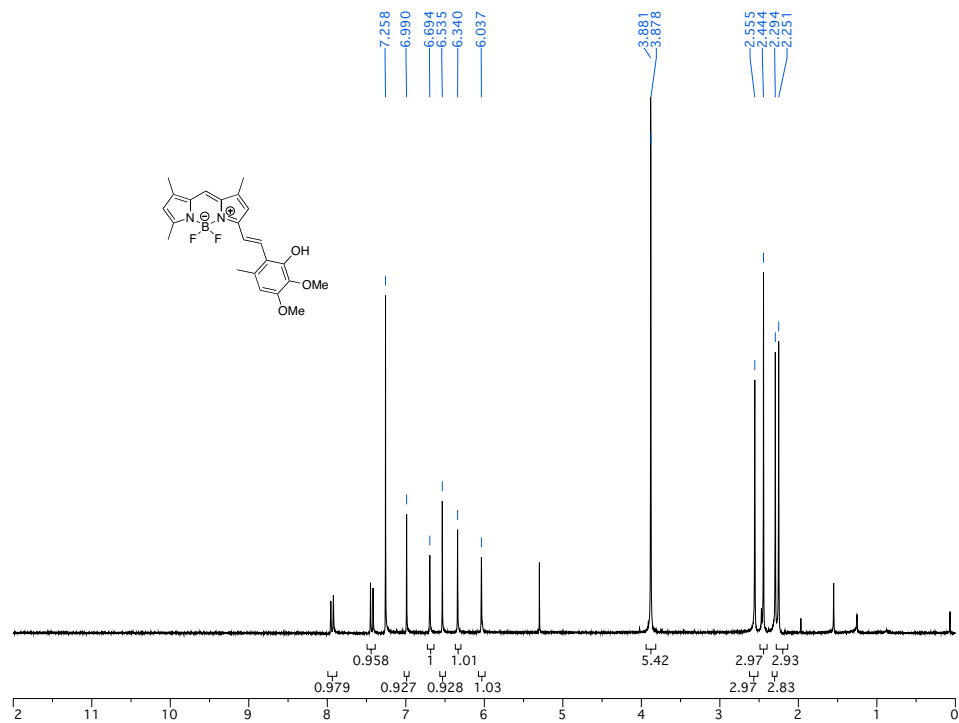
- Methyl (E)-3-(1H-pyrrol-2-yl)acrylate (**1**). ¹H-NMR spectrum, 500 MHz; CDCl₃, ¹³C-NMR spectrum, 126 MHz; CDCl₃ (Page 197).
- Methyl 3-(1-H-pyrrol-2-yl)propanoate (**2**). ¹H-NMR spectrum, 500 MHz; CDCl₃, ¹³C-NMR spectrum, 126 MHz; CDCl₃ (Page 198).
- 3-(1H-pyrrol-2-yl)propan-1-ol. ¹H-NMR spectrum, 500 MHz; CDCl₃, ¹³C-NMR spectrum, 126 MHz; CDCl₃ (Page 199).
- 2-(3-Chloropropyl)-1H-pyrrole (**3**). ¹H-NMR spectrum, 500 MHz; CDCl₃, ¹³C-NMR spectrum, 126 MHz; CDCl₃ (Page 200).
- 8-((6-Hydroxy-2,5,7,8-tetramethylchroman-2-yl)-methyl)-1,5-di-(3-chloropropyl)-Pyrromethene Fluoroborate (**H₄BPMHC**). ¹H-NMR spectrum, 500 MHz; CDCl₃, ¹³C-NMR spectrum, 126 MHz; CDCl₃ (Page 201).
- 8-Methyl-1,5-di-(3-chloropropyl)-Pyrromethene Fluoroborate (**H₄BCH₃**). ¹H-NMR spectrum, 500 MHz; CDCl₃, ¹³C-NMR spectrum, 126 MHz; CDCl₃ (Page 202).

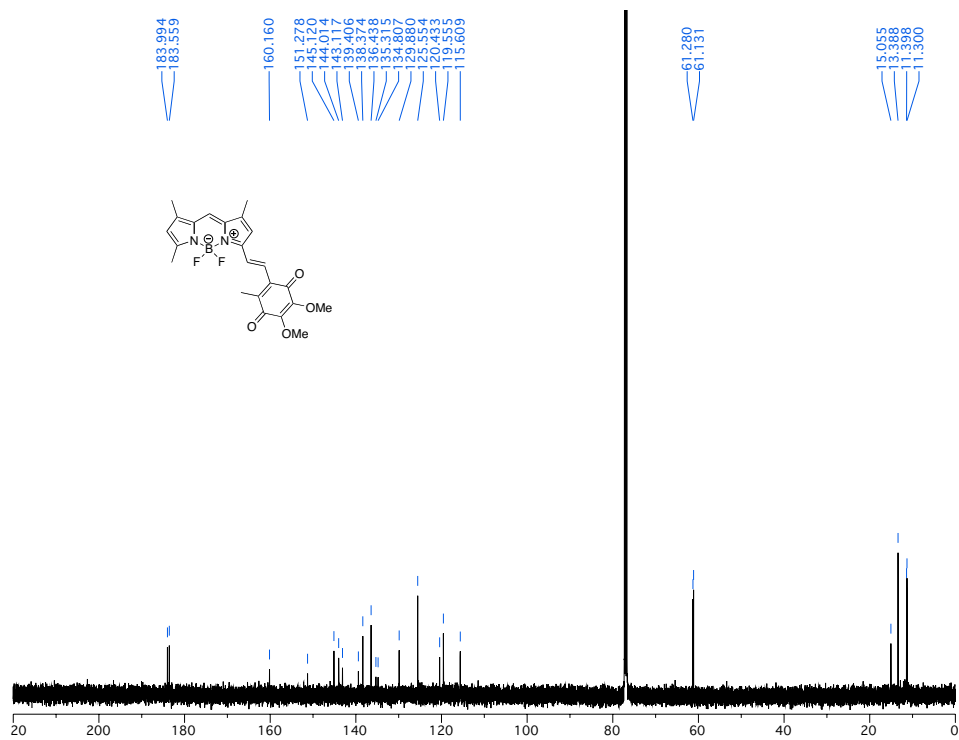
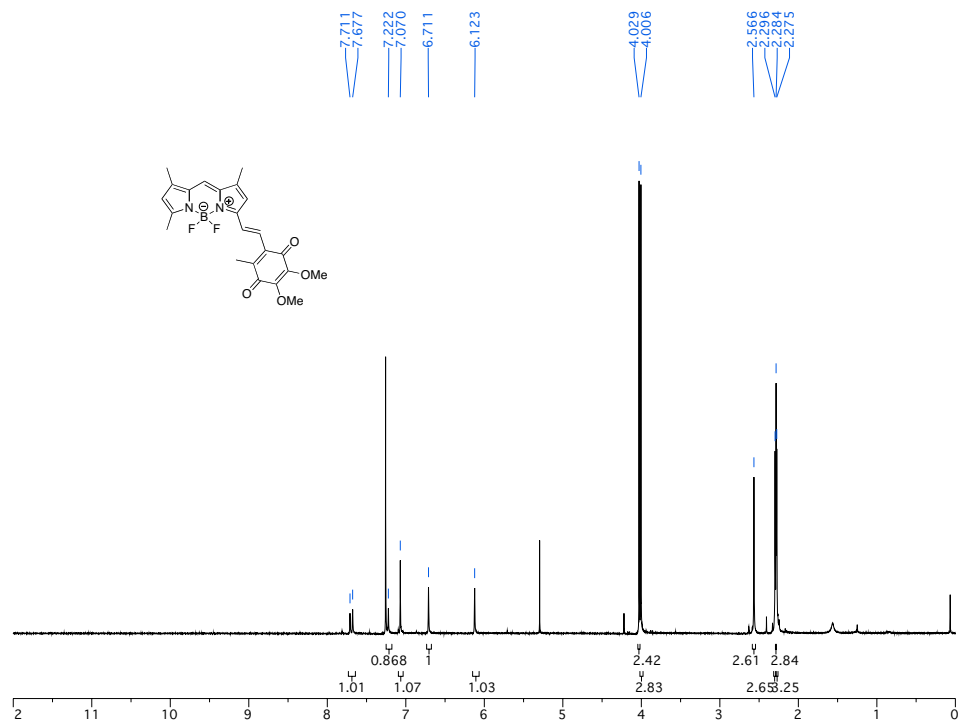
Chapter 5:

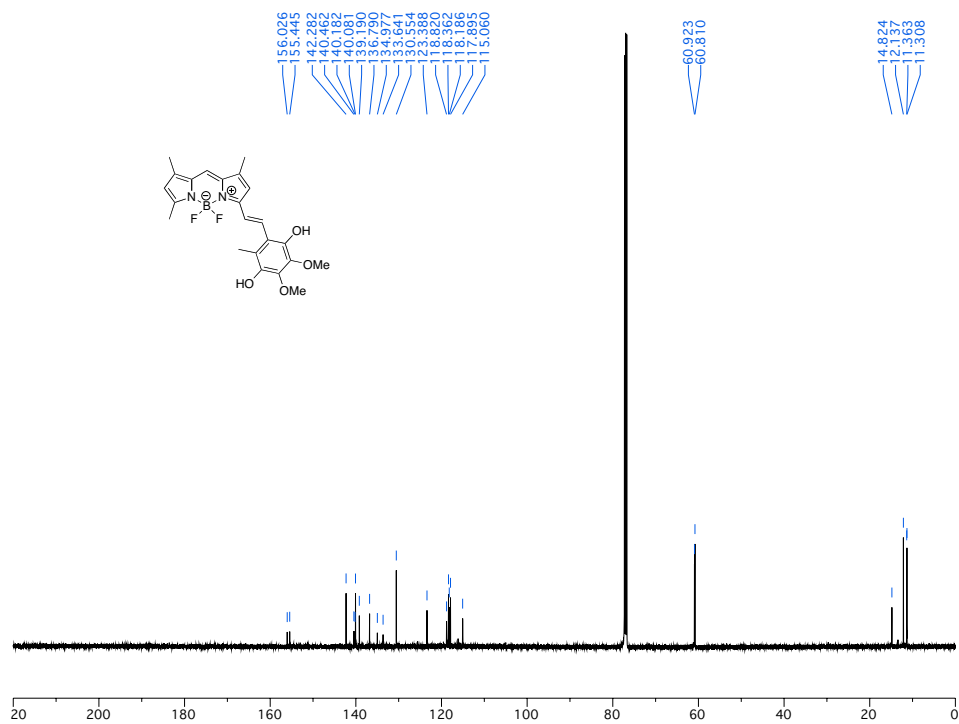
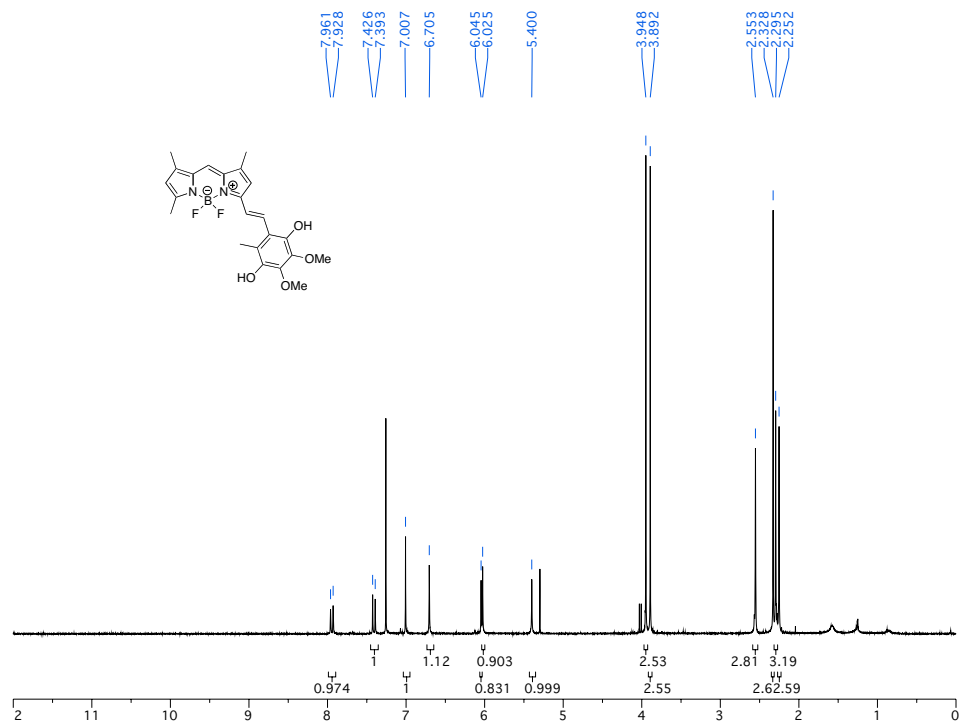
- 8-(1,3-dioxolane)-2-cyano-1,3,5,7-tetramethyl Pyrromethene Fluoroborate (**6**) ¹H-NMR spectrum, 500 MHz; CDCl₃, ¹³C-NMR spectrum, 126 MHz; CDCl₃ (Page 203).

7.1 Appendix Chapter 2

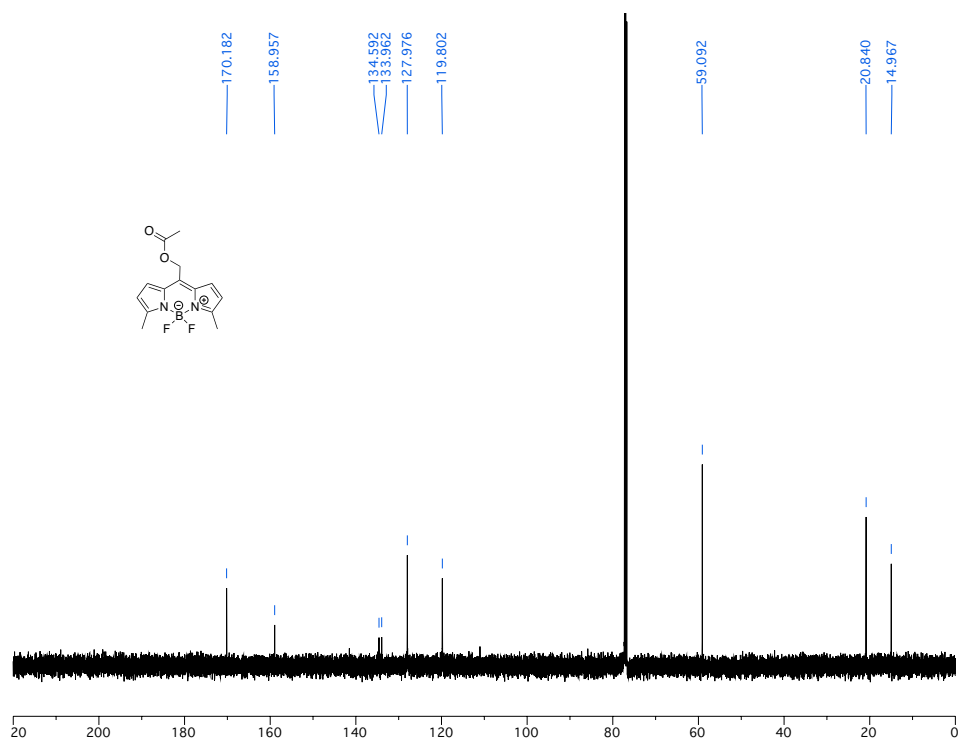
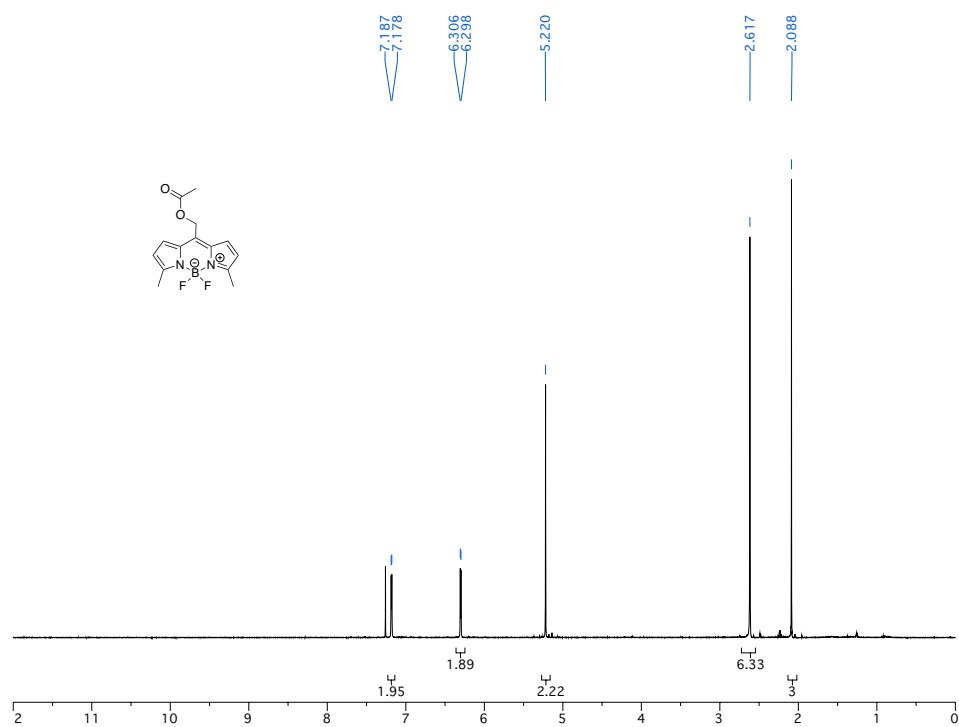


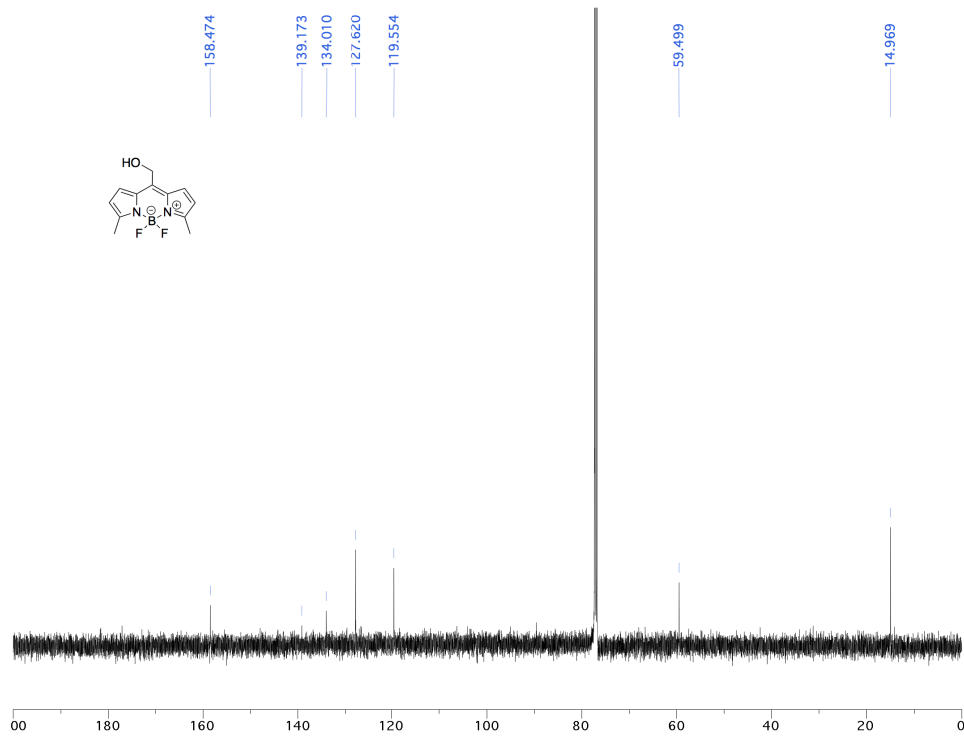
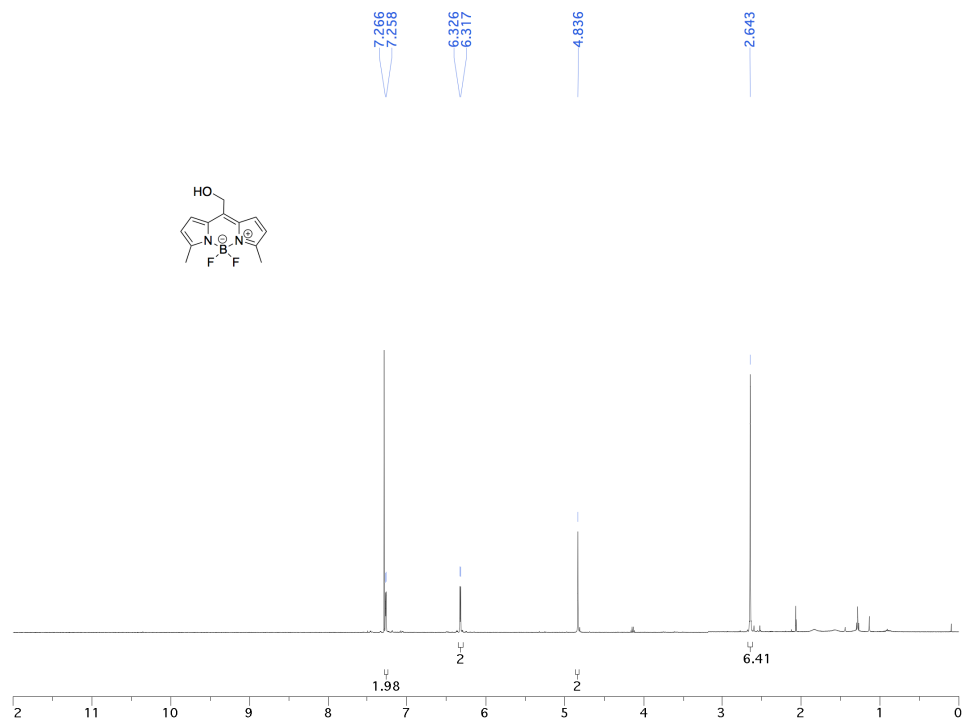


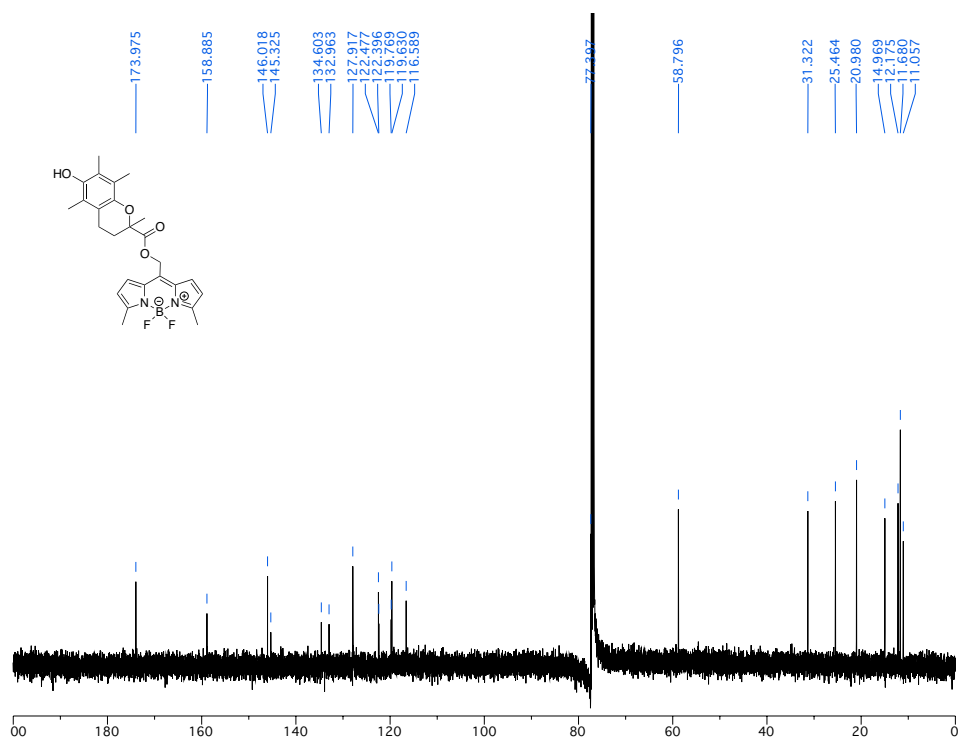
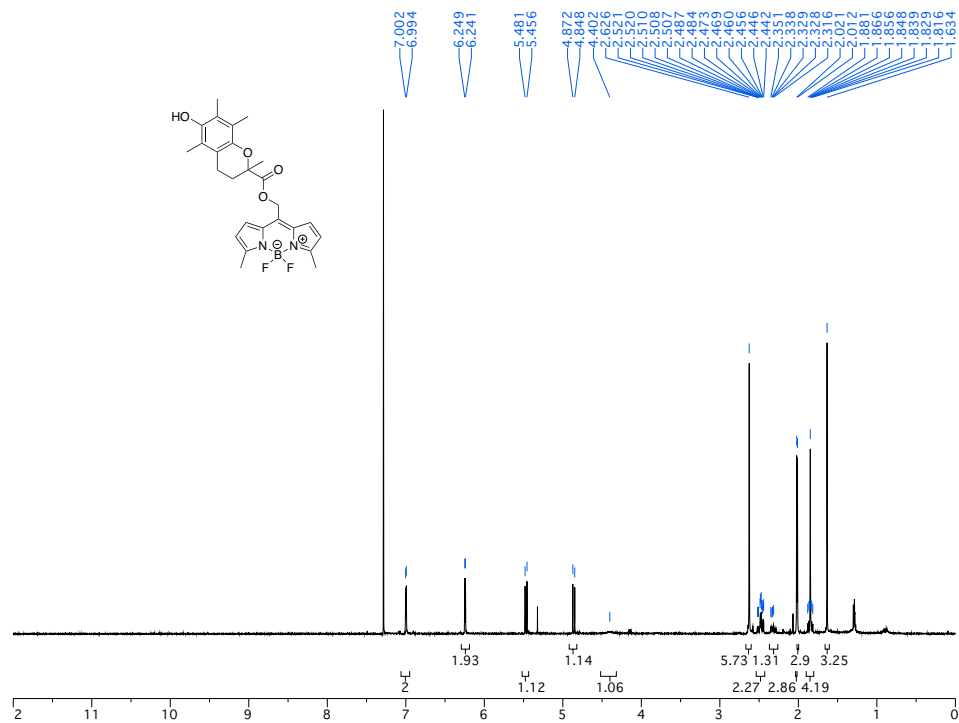


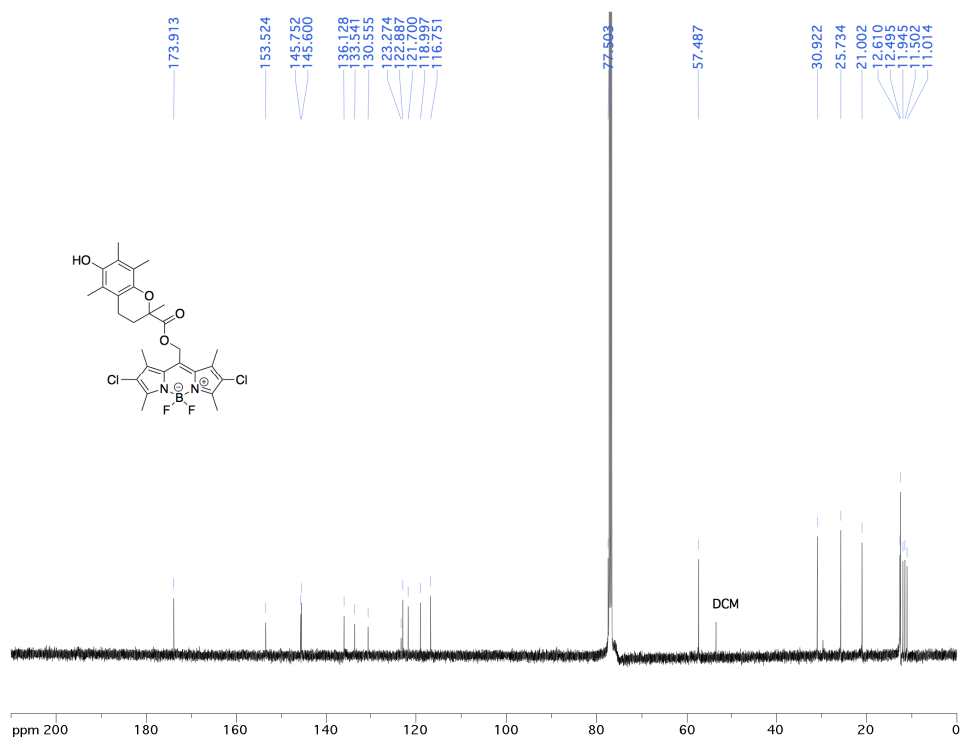
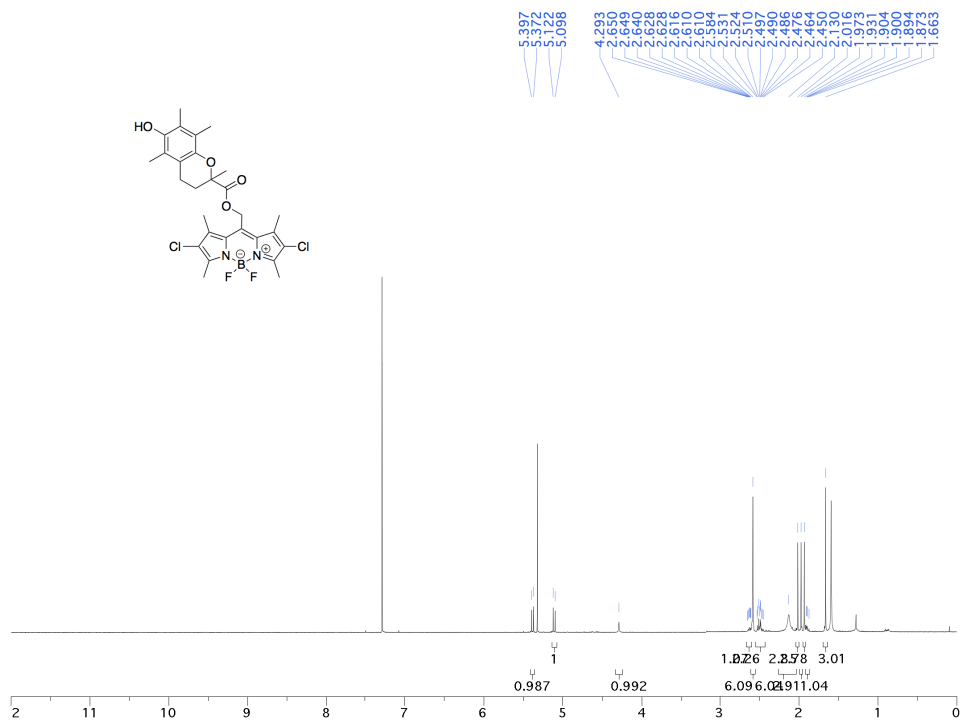


7.2 Appendix Chapter 3

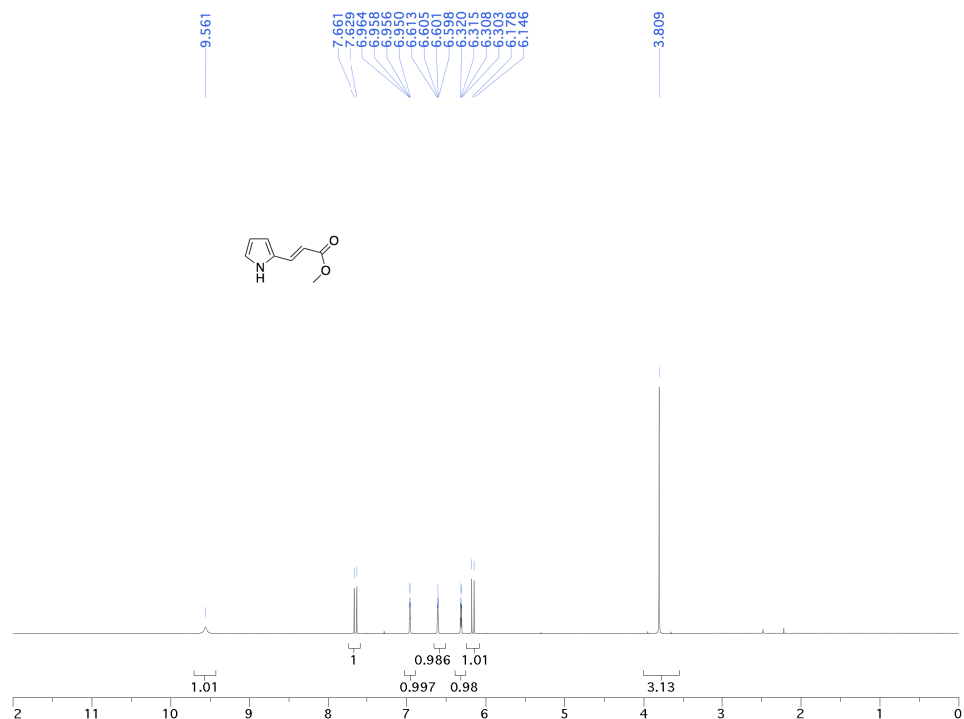


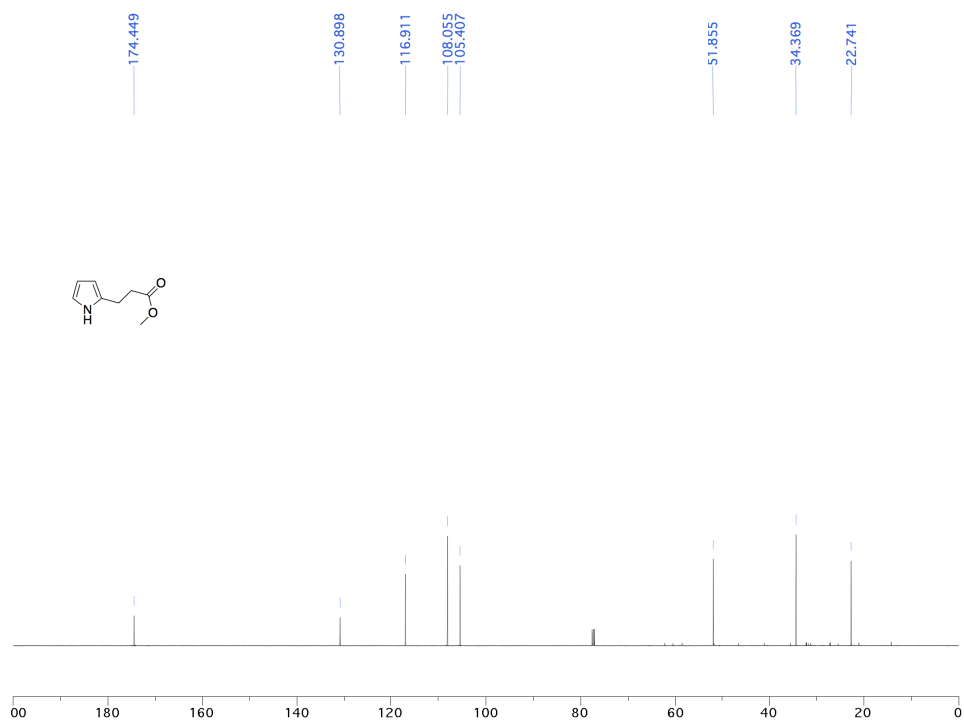
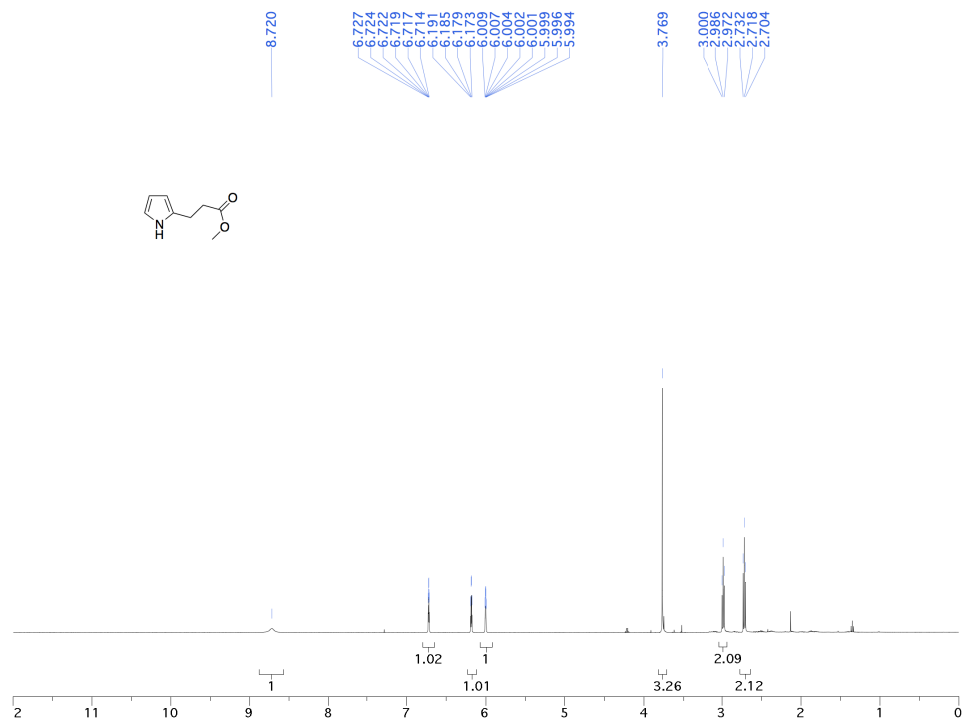


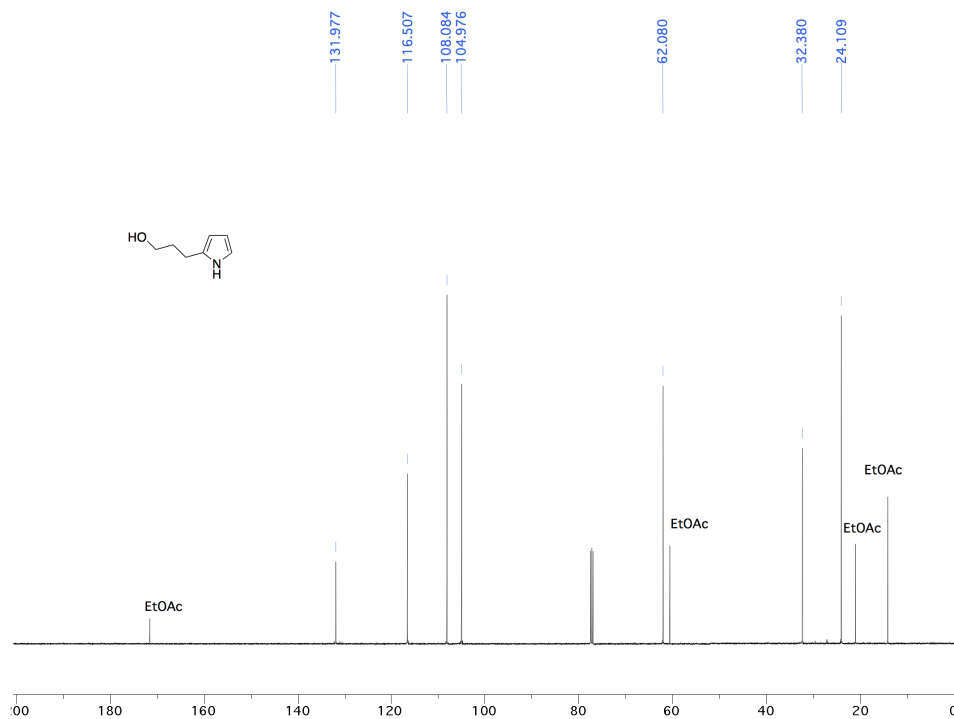
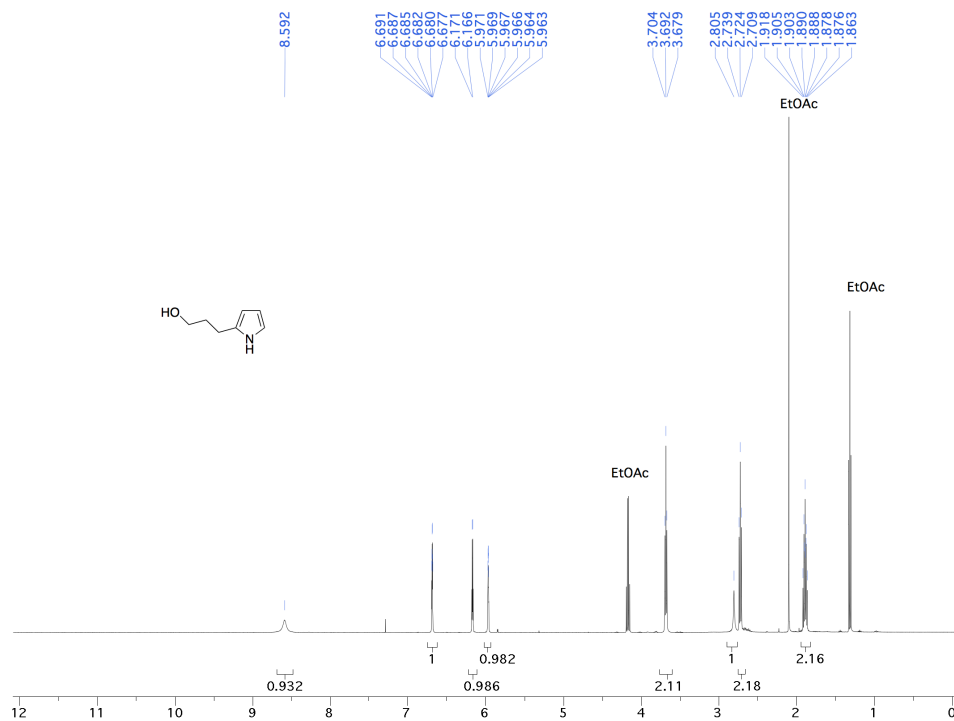


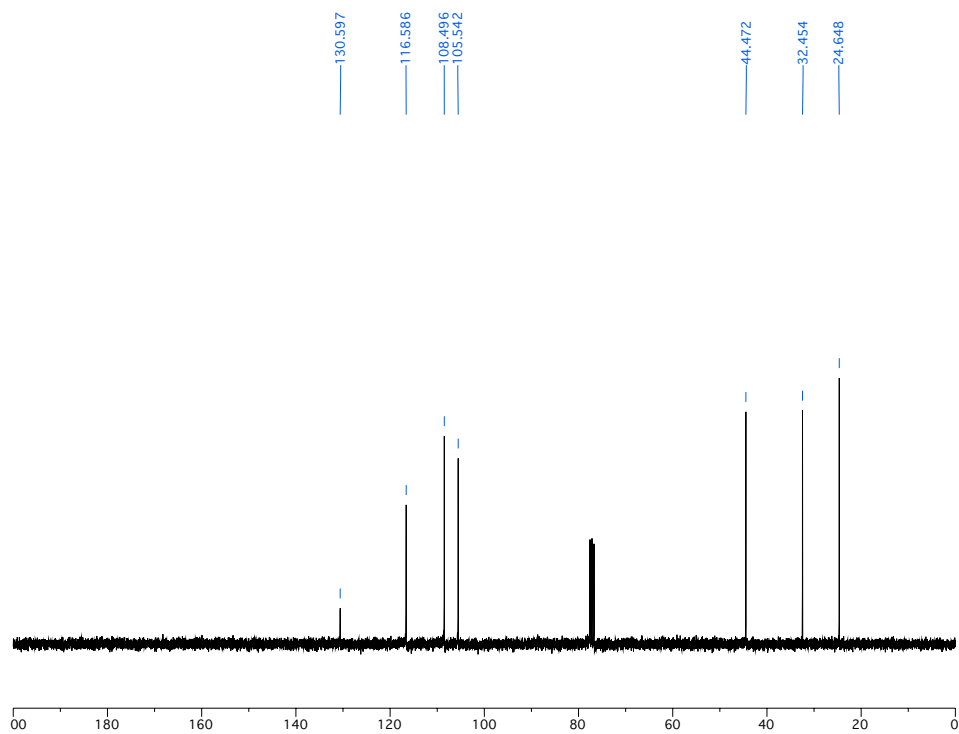
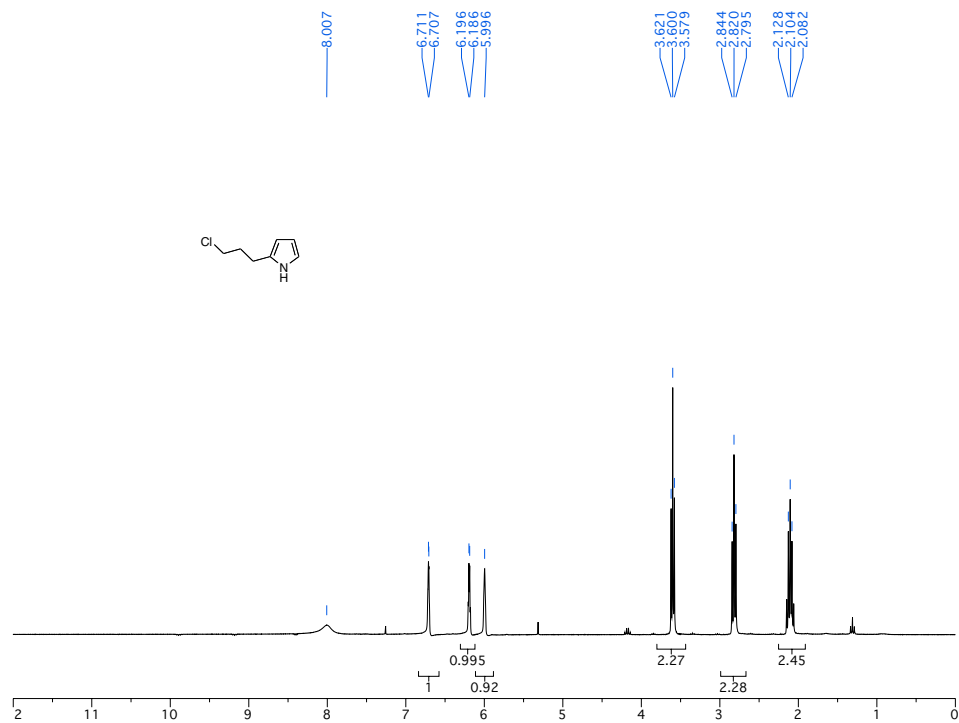


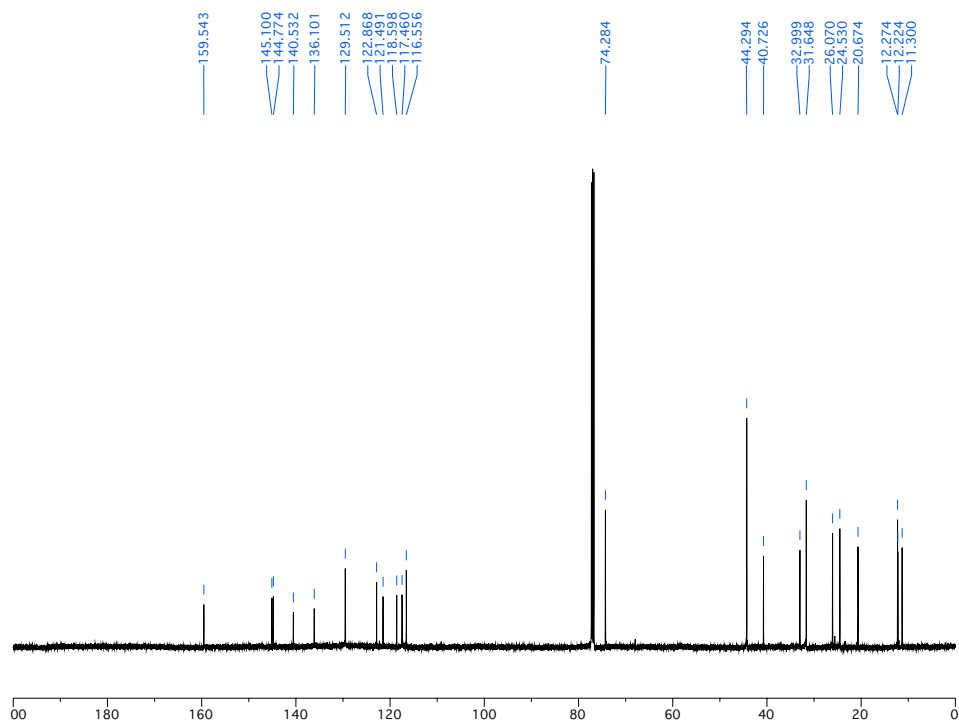
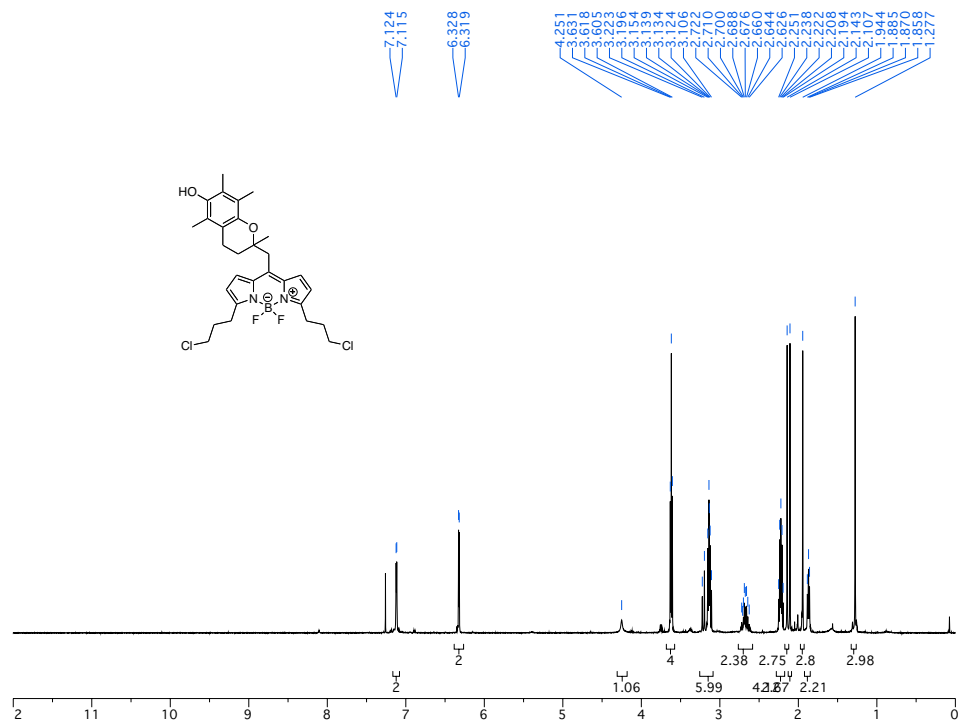
7.3 Appendix Chapter 4

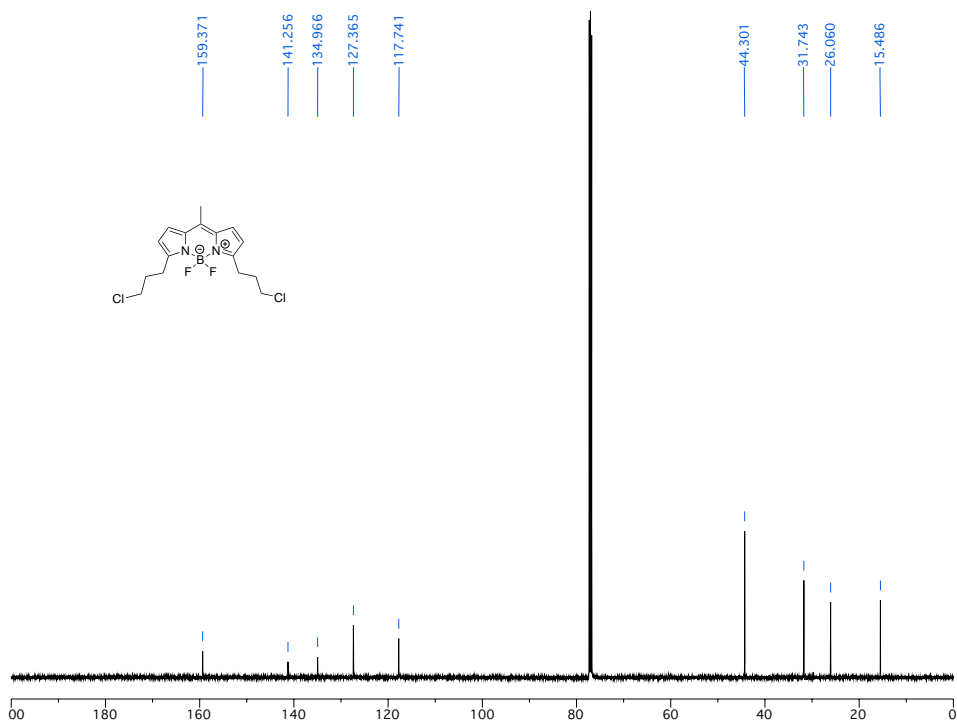
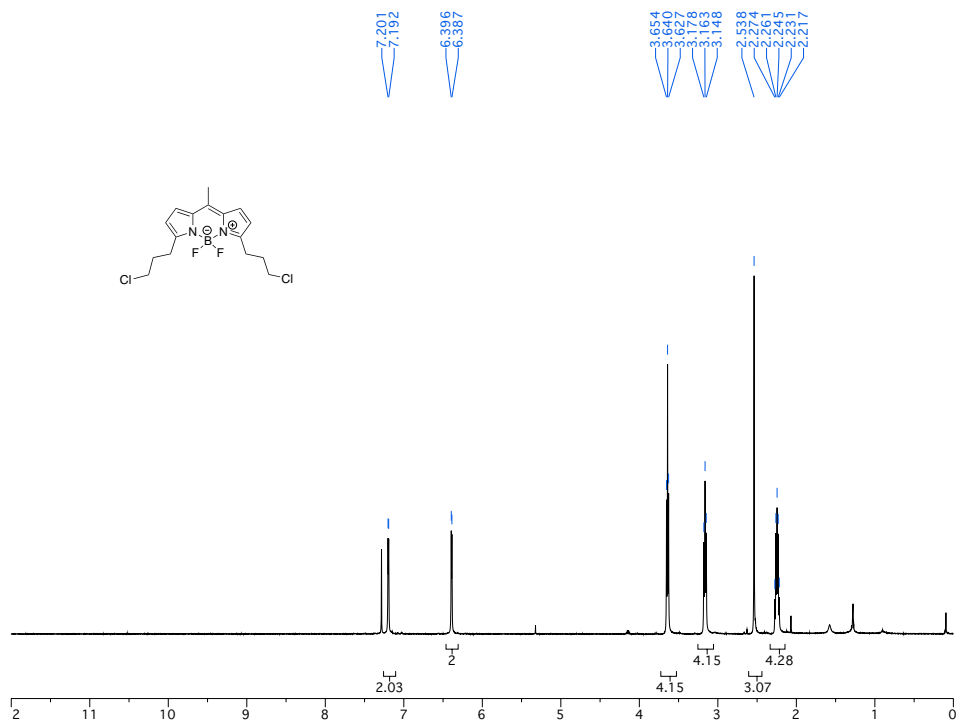












7.4 Appendix Chapter 5

